PROBING THE RELATIONSHIP BETWEEN MAGNETIC AND TEMPERATURE STRUCTURES WITH SOFT X-RAYS ON THE MADISON SYMMETRIC TORUS

by

Meghan B. McGarry

A dissertation submitted in partial fulfillment of

the requirements for the degree of

Doctor of Philosophy

(Physics)

at the

University of Wisconsin – Madison

2013

Date of final oral examination: May 24, 2013

The dissertation is approved by the following members of the Final Oral Committee:
Daniel den Hartog, Research Professor, Physics
John Sarff, Professor, Physics
Ellen Zweibel, Professor, Physics
Chris Hegna, Professor, Physics
Paul Wilson, Professor, Engineering Physics
John Goetz, Senior Scientist, Physics

Abstract

An innovative new soft x-ray (SXR) diagnostic has been developed for the Madison Symmetric Torus that provides measurements of tomographic emissivity and electron temperature (T_e) via the double-foil technique. Two measurements of electron temperature from SXR emission are available, one from the ratio of the emissivities through thin and thick filters as mapped onto magnetic flux surfaces, and the other directly from the ratio of two foils sharing a single line-of-sight. The SXR measurements have been benchmarked against Thomson Scattering electron temperature during high current, improved confinement discharges, and show excellent agreement. The SXR diagnostic has been used to investigate whether the source of emissive structures seen during high-current improved confinement discharges is due to localized increase in electron temperature, electron density (n_e), or effective atomic number (Z_{eff}). Although the emissivity structures are correlated to the magnetic configuration of the discharges, direct-brightness T_e measurements do not typically show a clear T_e structure, indicating a general upper limit of $\sim 15-20\%$ on any possible localized increase in T_e. In most shots, the flux-surface reconstructed T_e shows no indication of T_e structure. However, in one discharge with a very large tearing mode amplitude (15 Gauss), measurements and modeling indicate that the structure has a localized increase of 20-180 eV in T_e. The structure cannot be explained by a localized enhancement of n_e. A second case study with a multiple-helicity magnetic spectrum indicates that a ring of enhanced SXR emission at 0.4 normalized radius is caused by impurity accumulation.

There is no evidence of a T_e structure, and the structure cannot be explained with a model assuming only enhancement in n_e. If caused by impurities alone, the structure has a 58% increase in Z_{eff} compared with the core region. For the first time, the SXR diagnostic has also been combined with Al^{11+} impurity measurements to normalize the aluminum contribution to the SXR emission spectrum and demonstrate that the filter thicknesses used for the diagnostic do not pass aluminum line radiation. The new SXR T_e and tomography diagnostic will continue to provide insight into the relationship between magnetic structures and electron temperature in improved confinement plasmas.

Acknowledgments

It has been a long nearly-eight years, filled with temptations that Fate could not resist: *I'd never* . . . move somewhere so cold as Wisconsin . . . be in grad school longer than six years . . . change research groups . . . build a diagnostic from scratch . . . have a child in grad school . . . have a *second* child in grad school . . .. Nonetheless, sometimes Fate provides the richer path, and I would not trade my time here in Madison. I am grateful for many people who have guided me along the way.

First and foremost, thank you Paolo Franz, for being a mentor and expert in every physics topic even remotely related to x-rays in plasmas. You are lucky to have the perfect adviser role - all of the scientific guidance with none of the administrative tedium. Your patience when I insist on proving to myself what you have learned from years of experience is greatly appreciated. I'm sorry to say I still haven't learned Italian, though not for lack of your efforts to teach me.

A thank you of parallel importance to my actual adviser Daniel Den Hartog. You rescued my from my ill-fated first attempt at research, and thereby rescued my dream of getting my Ph.D. Your unflagging support for me both as a scientist and a parent has been invaluable, and I will never forget it.

Thank you to John Goetz, my unheralded third adviser. You have been my sounding board, my moral support, and the only person I've ever met who might be more obsessed with the weather than myself.

Thank you to Mark Thomas, Mikhail Reyfman, Jay Johnson, and the entire

MST team. Without your help, I would never have been able to build the SXR diagnostic from the ground up while beating the noise right back down. Your expertise, dedication, persistence, kindness and collective sense of humor have made MST a truly great place to work.

Thanks are also in order for the many people outside of UW Madison who have helped me define my career. Laura Grego and David Wright, you have shown me a path to my dream career and have been invaluable guides. Exposure to science policy through the summer symposium has motivated me to push through the hardest parts of grad school. Thank you also to my mentors from Chandra: Pat Slane, Bill Forman, and Jan Vrtilek. Without your advice, I never would have considered moving to the great City of Madison. Pat, you are the best mentor a person could hope to have. Bill, I should have listened more closely to your advice. And Jan, you introduced me to Laura and to UCS, and helped me to find my path.

Of course the past eight years would have been bleak without the company of great friends. Jake and Bob, you gave me double-friendship by also giving me Kirsten and Betsy. Kyle, Zane, and Doug, it turns out they were right, we should have listened to all those Christmas Colloquium jokes about MST'ers. But I'm glad we were in it together. Christie, Tyler, Mat, Brian, Aongus, Nick and Mike, you finished so long ago that you could probably have graduated again by now, and I miss you all. Jessica, I never needed a friend so badly as when Charlie walked into Amelia's life, and I found a kindred spirit in you. Alaine, I there is not a place far enough away to stand in the way of our friendship, but please don't move to the Moon because I'd never be able to convince Brett to visit.

Thank you to my entire family, who have been eternally supportive, if somewhat baffled, by this odyssey. Mom, Kenny, Dad, Donna, I am so grateful for all of your love, support, and visits. If only we could just remove all those silly states in between Wisconsin and California and put them somewhere else. Bryan, I know can count on you to always be there for me, to find the absolute most logical solution and then to lighten my mood when it proves somewhat unpalatable.

Thank you to my beautiful daughters Amelia and Isabel. Amelia, you have endured my crabbiness for so long that you may have forgotten it could be any other way. Isabel, I am amazed that I could love anyone so deeply as to overlook this much lost sleep. You both bring such joy into my life, and anchor me to what is really important.

Finally, **Thank You** to my husband. Brett, this undertaking proved longer and harder than either of us imagined it could. You are my Oak. I never would have made it without your love, support, and patience for my endless complaints. If only I could promise you a lifetime of riches in return.

In memory of

Doris Vasold

(January 12, 2013)

Contents

List of Figures

List of Tables

Chapter 1

Introduction

Magnetic confinement devices seek to harness the energy source of the sun, fusion, in a laboratory environment. Fusion requires a combination of high temperature and density, as well as a large collisional cross-section. These can be expressed as the Lawson criterion for sustained fusion. For deuterium-tritium plasmas, the Lawson criterion requires thermal energies around 10 keV [1]. In the sun, confinement of high energy particles is achieved via gravity, however this is not possible on Earth. In the laboratory, confinement can instead be achieved using magnetic fields and a toroidal geometry. Although particles generally follow field lines, they do not follow them precisely, and are impacted by several types of drift forces. Additionally, instabilities can be triggered by free-energy from gradients in the pressure and current profiles [2]. Instabilities and drifts combine to make confinement a serious obstacle to controlled laboratory fusion.

In sufficiently hot plasmas, electrons emit x-ray radiation. Because electrons follow magnetic field lines, their x-ray radiation provides an indication of the internal magnetic structure in the plasma. Additionally, x-ray radiation is also an indication of electron temperature. As a result, x-ray emission is an excellent tool to aid in the study of plasma confinement and stability.

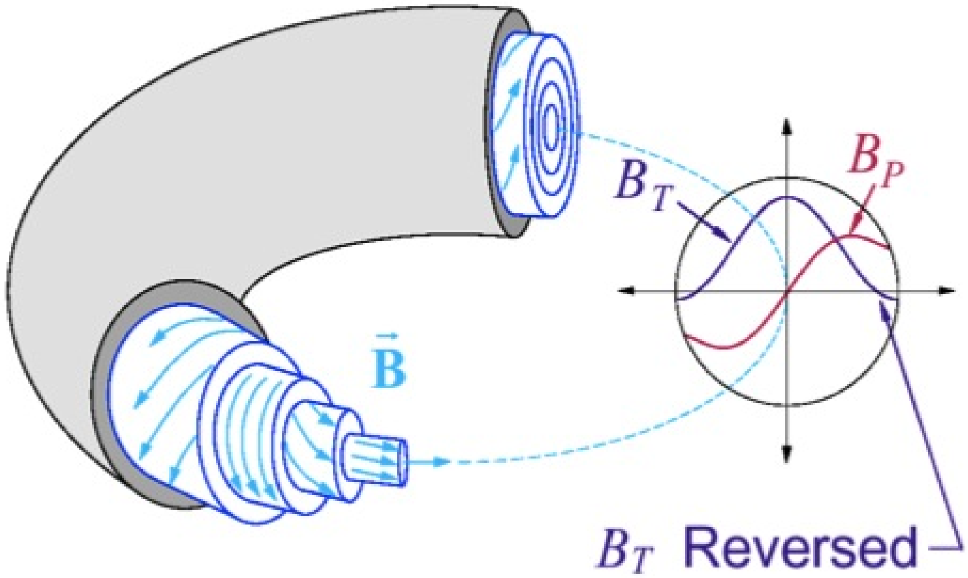

Figure 1.1: Schematic of the magnetic field topology in MST. Note the magnetic field is purely toroidal in the core and has a reversal surface where the field becomes completely poloidal. The toroidal component continues to reverses direction as it reaches the edge of the plasma.

This thesis uses soft x-ray (SXR) emission to study both the magnetic structure and electron temperature in a plasma. The first Chapter provides an overview of the magnetic tearing modes in the Madison Symmetric Torus (MST) (§1.1), explains how x-rays can be used as indicators of magnetic structure (§1.2), provides a brief history of SXR diagnostics on other devices (§1.3), and introduces the SXR diagnostic on MST (§1.4). §1.5 provides an overview of the remainder of this thesis.

1.1 Introduction to the Madison Symmetric Torus

The Madison Symmetric Torus (MST) is a magnetic confinement device that uses a reversed-field pinch (RFP) configuration. Figure 1.1 shows the magnetic configuration of the device. The reversed field pinch is so-called due to the fact that the toroidal component of the magnetic field at the edge points opposite its orientation in the core. This configuration conserves helicity while minimizing energy, and generates a dynamo whereby the magnetic flux is self-sustaining [3]. The RFP configuration leads to a set of resonant magnetic surfaces that occur where the safety factor (q) is a rational number:

$$q(r) = \frac{rB_t}{RB_p} \tag{1.1}$$

where r and R are the minor and major radii of MST, respectively, and B_t and B_p are the toroidal and poloidal magnetic fields. The poloidal coordinate traces the vessel when a vertical slice is taken, while the toroidal coordinate traces the vessel in the horizontal cross-section. These resonant surfaces occur because the fluctuation wave vector ($\vec{k}$) is perpendicular to the magnetic field ($\vec{B}$):

$$\vec{k} \cdot \vec{B} = 0 \tag{1.2}$$

This condition can be written as:

$$\frac{mB_p}{r} + \frac{nB_t}{R} = 0 \tag{1.3}$$

where m and n are the poloidal and toroidal wave numbers, respectively. Ata resonant surface, q can then be written as:

$$q_s(r) = -\frac{m}{n} \tag{1.4}$$

At these resonant surfaces, fluctuations in the magnetic field cause the field lines to tear apart and reconnect into closed 'island' surfaces, as illustrated in Figure 1.2. These islands are also called magnetic flux surfaces, and have magnetic field lines that wrap around the torus without breaking. A flux surface creates a natural confinement

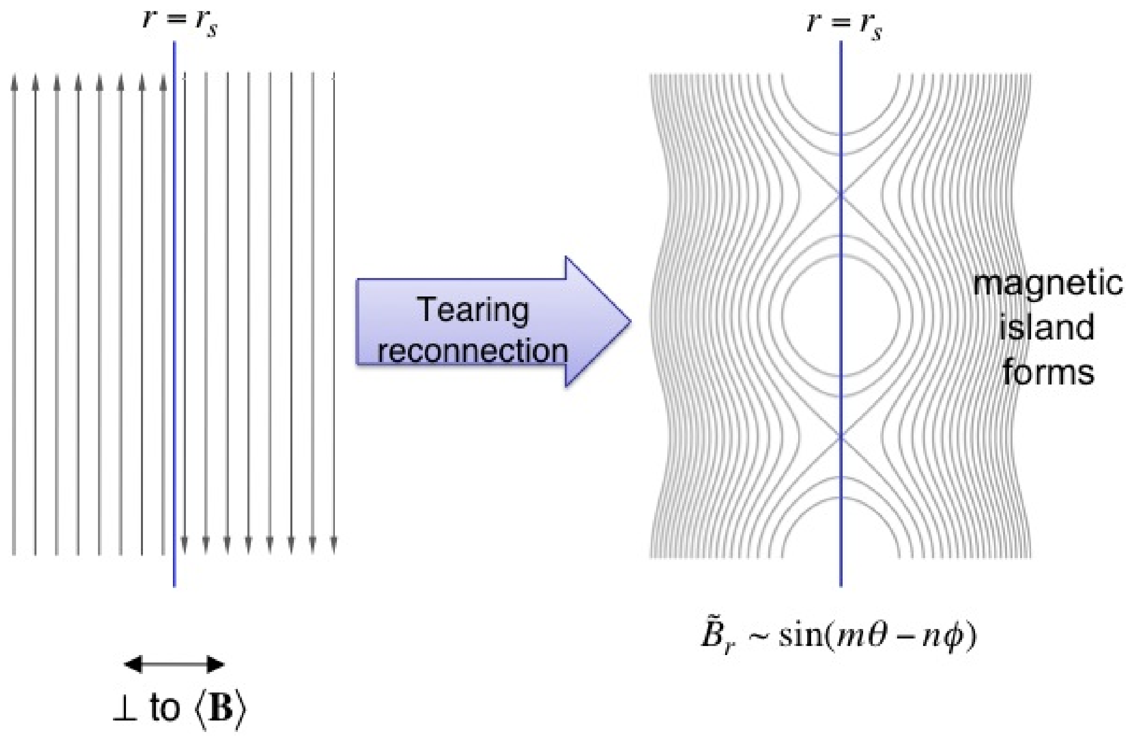

Figure 1.2: Schematic showing the generation of a tearing mode at a resonant magnetic surface $r = r_s$. The left-hand side shows a perturbation to the equilibrium magnetic field, while the right-hand side shows the configuration created by the resonant fluctuation $\tilde{B}$.

of particles and energy, since temperature will equilibrate along the field lines much more quickly than across the field lines.

1.1.1 Magnetic Measurements on MST

Magnetic fluctuations create an electromotive force (emf) in MST that contributes to the total parallel current density ($J_{||}$):

$$E_{||} + \left\langle \tilde{v} \times \tilde{b} \right\rangle_{||} = \eta J_{||} \tag{1.5}$$

where $\tilde{v}$ and $\tilde{b}$ are fluctuations in the fluid flow and magnetic field, $E_{||}$ is the parallel electric field, and η is the plasma resistivity. This emf acts as a dynamo electric field that drives the RFP [4]. Due to the importance of the dynamo in the RFP, it is critical to measure the fluctuating magnetic fields.

Poloidal (B_θ) and toroidal (B_ϕ) components of the magnetic field are measured on MST using a toroidal array of 64 coils located at 241° poloidal. Poloidal angle starts from the outboard mid-plane and increases moving upward toward the inboard mid-plane. The toroidal locations are equally spaced, beginning at the transformer (0°), where ϕ is defined in a left-handed coordinate system, increasing counter-clockwise (looking down from above). The signals are decomposed into Fourier components to define a mode amplitude ($|B|$), phase (δ), and velocity for m=1, $n \geq 5$ magnetic fluctuations. (The series is cutoff below $n = 5$ which it corresponds to the largest rational value of q accessible in the MST geometry):

$$|B(r,\theta,\phi,t)| = a_{mn}(t)\, cos(m\,\theta + n\,\phi(t)) + b_{mn}(t)\, sin(m\,\theta + n\,\phi(t)) \tag{1.6}$$

This can be written as:

$$|B| = C_{mn}\, cos(m\theta + n\phi - \Phi) \tag{1.7}$$

where $\Phi = arctan\,\frac{b_{mn}}{a_{mn}}$. For m=1 modes on MST, the poloidal dependence is wrapped into the measured phase, which is:

$$\delta = \Phi - m\theta \tag{1.8}$$

These equations can be used to understand the location of magnetic island o-points with respect to the SXR diagnostic. The requirement for an o-point at the origin of the coordinate system defined by the magnetics (0° T, 241° P) is:

$$\phi = \frac{\delta}{n} \tag{1.9}$$

Applying the definition $q = \frac{\phi}{\theta} = \frac{m}{n}$, the poloidal location (θ_{SXR}) of the magnetic o-point for an $m = 1, n$ mode at the toroidal location of the SXR diagnostic ($\phi_{SXR} = 90°$) is:

$$\theta_{SXR} = n\phi_{SXR} - \delta + 241 \tag{1.10}$$

Equation 1.10 is used throughout this thesis to compare the poloidal location of m=1 modes at the SXR diagnostic as measured by the magnetic array to the location seen in the SXR emission. MST also has a poloidal array of coils, however, these have not been as well-aligned, so calculations of mode phase in this thesis use the toroidal array exclusively. Care must be taken with analysis if a dominant mode locks early in the plasma. Calibration of the magnetics signal is performed early in the discharge, before 15 ms. If the plasma locks before 15 ms, the resulting amplitude measurement can be corrupted (although the phase is typically OK). In this case, the mode analysis code must be re-run by hand for an earlier period when no m=1 modes have locked. For more detailed information on mode analysis in MST, see the internal document *Magnetic Mode Analysis in MST*, by Darren Craig [5], as well as Tim Tharp's thesis [6].

1.1.2 Modes of Operation in the RFP

The RFP has several distinct operational configurations that result in different types of plasmas. These configurations are achieved by controlling the electric and magnetic field profiles. The standard configuration is highly repeatable and features sawtooth crashes, which are a manifestation of the dynamo. This thesis focuses on two special magnetic configurations in MST that reduce stochasticity and lead to improved confinement and higher electron temperature. Improved confinement can be achieved by minimizing the energy in all magnetic tearing modes, or by concentrating the plasma energy into a single dominant tearing mode that allows for healing of the flux surfaces.

1.1.2.1 Standard Plasmas

It is typical to have multiple tearing modes growing within an RFP plasma. Figure 1.3 shows the radial profile of the resonant surfaces in MST, as well as a schematic of an $m/n = (1/7)$ magnetic mode (where the mode wraps seven times poloidally in one toroidal pass). In this type of *multiple helicity* (MH) plasma, free energy from the peaked current-profile allows mode growth in multiple resonant modes [7, 8]. If adjacent magnetic islands, i.e. the *(1/6)* and *(1/7)* modes, grow sufficiently large in radial extent, they will begin to overlap. Overlapping islands create stochasticity, which results in poor confinement when there are no well-defined flux-surfaces and particles migrate outward. Growth of parallel current relative to magnetic field strength ($J_{||}/B$) moves the plasma away from a relaxed state until it becomes unstable and non-linear interactions trigger a reconnection event. Magnetic reconnection flattens the parallel current profile and returns the plasma to a relaxed state by reducing the total magnetic energy. This *sawtooth* cycle of growth and reconnection repeats every few milliseconds, and confinement is very poor.

1.1.2.2 Improved Confinement

MST can be run in a configuration called pulsed parallel current drive (PPCD), which reduces all resonant mode amplitudes and improves confinement. In PPCD, the current density profile is flattened by inductively controlling the parallel current profile. When current gradients at the edge of the plasma are reduced, core modes that are driven by this gradient will also be reduced [9, 10]. This configuration eliminates the typical cycle of fluctuation growth followed by sawtooth events [11]. Tearing

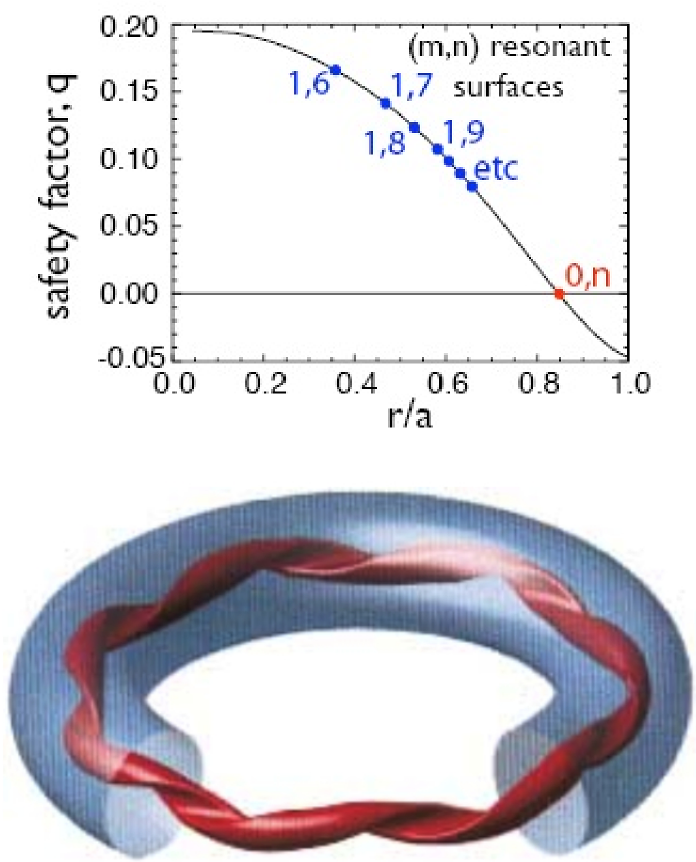

Figure 1.3: (Top) Safety factor as a function of normalized radius for standard MST configuration. (Bottom) Schematic showing the magnetic topology (or flux surface) for a m=1,n=7 magnetic mode.

mode growth is also suppressed so that the modes no longer overlap, reducing magnetic stochasticity. Global electron thermal diffusion is reduced to 2 m^2/s, electron temperature can exceed 2 keV, and energy confinement times reach up to 12ms [12]. This increase in energy confinement and electron temperature creates a dramatic increase of soft x-ray emission, increasing signal levels by a factor of 100 compared with standard plasmas. Due to the large signals, PPCD plasmas are an excellent candidate for study with the soft x-ray double-filter diagnostic.

1.1.2.3 Single Helical Axis (SHAx)

Concentration of energy into a single tearing mode occurs in the *single helical axis*, or SHAx state. A SHAx state is an extension of a quasi-single helicity (QSH) state, where the energy of the fluctuation becomes concentrated in a single magnetic tearing mode and the energy in the remaining modes is reduced. Typically in a QSH plasma, the dominant mode will grow to occupy ∼10% of the plasma volume [13]. In some cases, the dominant mode grows beyond this limit. If it becomes sufficiently large then it overtakes the magnetic axis of the plasma. The magnetic axis merges with the island core, and a new magnetic configuration, SHAx, emerges with a substantially shifted core. SHAx plasmas have been observed in the RFX reversed field pinch, where they have generated improved confinement [14]. In a SHAx plasma, the dominant mode becomes large while secondary resonant modes simultaneously become smaller [15]. In MST, evidence for the healed magnetic flux surfaces characteristic of SHAx have been observed, but no improved confinement or increase of electron temperature has yet been measured [16]. SHAx-like magnetic structures arise in MST during non-reversed plasmas, when MST is configured so that the toroidal magnetic field is forced to zero at the wall [17]. At high current, rotation halts as the dominant n=5 mode saturates, which is referred to as *locking*.

1.2 X-rays As a Probe of Magnetic Structure

Given the importance of magnetic field structure in plasma control, it is useful to be able to measure not only the field at the edges but also to get a picture of the magnetic topology throughout the plasma. X-ray emission from the plasma tracks magnetic structure, and so x-rays offer a method of probing the internal workings of the plasma. What follows is a brief description of the types of radiation a soft x-ray diagnostic will measure. A more detailed description of x-ray emission, is given in *Radiative Processes In Astrophysics* [18].

1.2.1 X-ray Emission 'Images' Flux Surfaces

X-ray emission derives from the charged particles in the plasma, so it stands that the motion of these particles can be tracked via soft x-rays. As a first approximation, electrons in a plasma follow magnetic field lines. The magnetic structure is defined by ideal MHD to be a function of pressure:

$$\vec{J} \times \vec{B} = \nabla P \tag{1.11}$$

where J is current density, B is magnetic field, and P is pressure. Using the vector identity $\vec{A} \cdot \vec{B} \times \vec{C} = \vec{A} \times \vec{B} \cdot \vec{C}$, it can be shown that:

$$\vec{J} \cdot (\vec{J} \times \vec{B}) = \vec{B} \cdot (\vec{J} \times \vec{B}) = 0 \tag{1.12}$$

$$\vec{J} \cdot \nabla P = \vec{B} \cdot \nabla P = 0 \tag{1.13}$$

Equation 1.13 demonstrates that there is no pressure gradient along the direction of current density or the magnetic field. Therefore the pressure is constant along field lines. Since the magnetic field lines in a plasma define flux surfaces, it is equivalent to say that *pressure is constant along a flux surface*. The ideal gas law then relates pressure and temperature (T) through density (n) and the Boltzmann constant (k_B):

$$P = nk_B T \tag{1.14}$$

Parallel diffusion is much faster than perpendicular diffusion, so temperature quickly equilibrates along magnetic flux surfaces. Therefore, it can be said that flux surfaces are surfaces of constant temperature, pressure, and current density. Because x-ray emission comes from electrons as they move along the flux surface, the x-ray emission then provides an 'image' of the magnetic structure of the plasma. In fact, the correlation between internal magnetic structures and soft x-ray emission was first shown experimentally in 1974 by von Goeler et al [19].

1.2.2 Bremsstrahlung Radiation

Plasmas emit many types of electromagnetic radiation. Cyclotron radiation, for example, occurs when electrons are accelerated by a magnetic field. The typical field strength on MST is $\sim$ 0.5 Tesla, which creates cyclotron emission in the microwave portion of the electromagnetic spectrum at a wavelength of 1cm. On the other hand, the primary source of X-rays in MST is bremsstrahlung, or braking radiation. Free-free bremsstrahlung radiation occurs as an electron is accelerated as it passes through the field of an ion. The power (P) radiated by a single electron is given by the Larmor equation:

$$P = \frac{e^2 a^2}{6\pi\epsilon_o c^3} \tag{1.15}$$

where e is the charge of the electron, a is the acceleration, and c is the speed of light. Using the Coulomb force to find the acceleration of the electron as it passes by an ion $Z \cdot e$, the power as a function of distance (r) becomes:

$$P = \frac{2}{3}\left(\frac{e^2}{4\pi\epsilon_o}\right)^3 \frac{Z^2}{c^3 m_e^2}\frac{1}{r^4} \tag{1.16}$$

To determine the total power radiated per unit volume of particles, the power per particle must be multiplied by the number of collisions per particle and the density (n). The number of collisions is the distance traveled divided by the mean free path of the particle, or $2\pi n b^2 db$. b is the distance of closest approach between the electron and ion, or impact parameter.

$$P_n = \frac{2}{3}\left(\frac{e^2}{4\pi\epsilon_o}\right)^3 \frac{n_e n_i\, Z^2}{c^3 m_e^2} \int_{b_{min}}^{\infty} \frac{2\pi}{b^2}\, db \tag{1.17}$$

For a given velocity v, b_{min} can be estimated using the Heisenberg uncertainty principle as $b_{min} = \hbar/2m_e v$. Because plasmas have a multiple different ion species, introduce

$$Z_{eff} = \frac{\sum_i n_i Z_i^2}{n_e} \tag{1.18}$$

Assuming a Maxwellian distribution of electrons, the total power radiated per unit volume becomes:

$$P(E)\, dE = \frac{8\pi}{3}\left(\frac{e^2}{4\pi\epsilon_o}\right)^3 \frac{n_e^2\, Z_{eff}}{\hbar c^3 m_e^{3/2}}\, T_e^{-1/2}\, e^{-E/T_e}\, dE \tag{1.19}$$

Integrating over all energies, the functional dependence of the power radiated becomes:

$$P(E) \propto n_e^2\, Z_{eff}\, T_e^{1/2}\, e^{-E/T_e} \tag{1.20}$$

1.2.3 Line and Recombination Radiation

The other two main sources of electromagnetic radiation in the soft x-ray regime are line and recombination radiation. In line radiation, bound electrons absorb energy and are excited either through collisions or due to photon absorption. As the electrons decay back into lower levels, they radiate away energy in the form of emission at a specific photon energy. Line radiation is a complicated phenomenon depending on atomic structure and quantum energy levels and requires great effort to model accurately. However, for known transitions, it is possible to create a simple model for the line radiation in the form of a Gaussian peak added to the background bremsstrahlung spectrum. In this model of line radiation, one needs only to estimate the energy and amplitude of the emission line, as well as its width.

Recombination radiation occurs when an ion recaptures a free electron, pulling it into a bound quantum state. The atom captures the electron and emits a photon from the excess energy of the original free electron, resulting in a discontinuous increase to the spectrum. The emitted photons create a step in the spectrum at the ionization energy of the atom (where the amplitude of the step is determined by the recombination rate). Together, line and recombination radiation can generate a large fraction of the total emission spectrum. However, with proper choice of filters to remove line radiation and avoid recombination steps, the total power radiated can be considered a function of density, electron temperature, and effective atomic mass.

1.2.4 A Double-Filter Technique to Measure Electron Temperature

When the SXR emission source is well-understood, it is possible to decouple the contribution of density in the soft x-ray emissivity, thereby providing a measurement of electron temperature. Specifically, for a plasma with bremsstrahlung continuum emission and a Maxwellian electron distribution, (where any impurity lines have been filtered out), electron temperature can be measured using the two-color or double-foil technique [20]. The double-foil technique calculates electron temperature by taking the ratio of SXR signals through two different filters coming from a single location in the plasma [21]. The measured SXR emissivity ε due to bremsstrahlung radiation in the plasma is given by

$$\varepsilon_{obs} = K \int_E dE\, A(E)\, T(E, Be) \left\{ \frac{Z_{eff}\, n_e^2(r)}{\sqrt{T_e(r)}} e^{-\frac{E}{T_e(r)}} \right\} \tag{1.21}$$

For a given energy E, K is a constant, $A(E)$ is the absorption function of the detector, and $T(E, Be)$ is the transmission function of a beryllium filter with thickness Be. n_e and T_e are the electron density and temperature, respectively. Density is not a function of energy, so it follows that the ratio of the emissivities from the same part of the plasma through two different beryllium filter thicknesses are each a function of the electron temperature in that region [20]. The precise relation between the ratio and the temperature is a polynomial function whose coefficients are found by modeling the bremsstrahlung radiation for many plasma temperatures [21, 22].

In the case where the two beryllium filters have shared lines-of-sight, the line integral is the same for both and the two-color technique can be applied directly to the brightness measurement:

$$f(L) = \int_L dL \varepsilon \tag{1.22}$$

$$R = \frac{f_1}{f_2} = \frac{\int_l \varepsilon_1(T_e)\, d\vec{l}}{\int_l \varepsilon_2(T_e)\, d\vec{l}} \tag{1.23}$$

Because temperature is not a line-integrated quantity, this temperature cannot be de-convolved into components from individual regions along the line-of-sight. Rather, this temperature represents the characteristic electron temperature for the Maxwellian distribution being sampled along the line-of-sight. For equilibrium plasmas, this corresponds to the hottest temperature along the line. In plasmas containing temperature structures however, the mapping of this temperature is somewhat more complex. For a more detailed discussion, see §2.3.3.

1.3 History of SXR Diagnostics for Plasmas

The technique of tomography in plasmas was originally adapted from medical imaging tomography, such as that used in CAT and MRI diagnostics [23]. Tomography provides a non-perturbative method of imaging internal structures. Initially, x-ray tomography in plasma experiments was achieved using a single array of detectors. Measurements provided insight into the magnetic topology of the plasma, but could be inverted only by making assumptions based on symmetry or plasma rotation [24, 25, 26]. However, in the 1980's, Alcator C became the first experiment to build two separate arrays and combine the data using the Cormack-Bessel method [27]. 2D tomographic reconstructions were used to study mode dynamics, impurity diffusion, and pellet injection. Large tokamaks such as JET, as well as reversed field pinches and stellarators, soon followed suit [28, 29, 30]. The first tomography system on MST was developed using arrays of surface barrier detectors in the early 1990's [31]. This diagnostic was designed utilizing individual portholes for each detector, so the limited number of unique chords affected the quality of the reconstructions.

At the same time, single array x-ray systems were also being used for double-foil temperature measurements. By 1987, TFTR was making time-resolved multi-chord temperature measurements of electron temperature [32]. Double foil temperature was also pursued at RFX, first with single-chord measurements [22, 33], and then with multi-chord capability by 2006 [34].

Recently, tomography and double-foil techniques have been combined to provide two separate estimates of electron temperature. Tomographic and double-foil temperature measurements were combined using a tangential viewing multi-chord system developed at NSTX in 2007. That system provides direct double-foil T_e profile measurements and can also be used to make T_e maps from reconstructed emissivity by assuming symmetry and applying a one-dimensional Abel inversion [35]. However, the new SXR Tomography and Double-Foil diagnostic on MST represents the first diagnostic to make full use of both the direct double-foil technique and tomographic reconstruction from multiple angles, eliminating the need for assumptions of symmetry.

1.4 SXR Measurements on MST

A silicon photodiode SXR tomography diagnostic was first installed on MST in 2001. Originally comprised of one array of diodes at a single poloidal location, the diagnostic was expanded to eventually include 4 poloidally separated arrays of 20 diodes each, for a total of 80 lines-of-sight [36]. This diagnostic provided tomographic reconstruction of SXR emissivity. Tomographically reconstructed temperature was first measured in the core-region of MST in 2006 [37]. Attempts to expand T_e measurements beyond the core region led to the discovery of artifacts in the measurement that mimicked temperature islands. As a result, a new diagnostic was developed that both addressed limitations in the original SXR design and also added a new capability for direct line-of-sight T_e measurements using the double-foil technique [38, 39].

The new double-foil SXR diagnostic has four individual probes at a single toroidal angle and poloidal locations separated by 90° intervals. Each probe contains two columns of 10 diodes, separated by 5mm toroidally, such that their cones-of-sight overlap in the plasma. The two columns look through different filter thicknesses, so that a given volume of plasma is sampled in two energy ranges along the same line-of-sight. As a result, each probe provides a radial profile measurement of T_e via the double-filter technique. The probes are located so that two probes combine for a near-vertical profile measurement, while the other two probes combine for a near-horizontal profile.

Since each of the four probes contains 10 lines-of-sight looking through the same filter thickness and the probes are separated by 90° intervals, tomographic capability is retained. In fact, this improvement in angular distribution over the previous system results in improved tomographic reconstruction. The new design also extends the field-of-view to the edge of the SXR emission region to improve the reconstructions and reduce artifacts. Furthermore, thin filter measurements and thick filter measurements can be independently reconstructed. The double-foil technique is then applied to the ratio of the reconstructed emissivities to give a 2D map of T_e throughout the poloidal cross-section. As a result, the new double-foil diagnostic provides two separate measurements of electron temperature in the plasma, in addition to SXR emissivity.

MST also has two other diagnostics that measure soft x-rays. The x-ray spectroscopy diagnostic consists of six silicon photodiode detectors to measure 2-10 keV x-rays, plus 12 CdZnTe crystal detectors that measure 10-300 keV x-rays [40]. Each detector is combined with a shaping amplifier that outputs a voltage proportional to the incident x-ray energy. As a result, this diagnostic measures the x-ray spectrum of MST in the 2-300 keV spectral range. The hard and soft-x-ray detectors are positioned on MST to provide radial profile measurements of the x-ray spectrum.

Finally, MST has two individual surface barrier x-ray detectors that look at the core of MST through two different beryllium filters. Designated *Be1* (25μm) and *Be2* (51μm), these detectors are a standard diagnostic on MST and are therefore always turned on. Their stability over many years provides an excellent mechanism for comparing plasma shots to find similar x-ray behavior. (See Ref. [31] for a description of the detectors). The ratio of these two signals has been previously used as a proxy for electron temperature evolution in the core region by normalizing to single-point Thomson scattering measurements [41]. However, due to the thin filters and known line radiation contamination, this detector cannot be reliably used for absolute temperature measurement.

1.5 Thesis Overview

This thesis describes the development of the new double-foil SXR diagnostic and its use for measurement of electron temperature in MST. Chapter 2 introduces the source of x-ray emission in plasmas and describes an emission model used extensively for simulations throughout this thesis. This Chapter explains the tomographic reconstruction technique and the double-foil technique for electron temperature measurement. It describes how the SXR emission model can be combined with these techniques to provide estimates of uncertainty, and explains their limitations.

Chapter 3 describes the hardware of the original SXR diagnostic on MST and its limitations for temperature measurement. It uses the SXR emission model described in the previous Chapter to investigate the source of artifacts in the temperature measurement. This series of simulations provide insight into the geometric limitations of the diagnostic and how they could be overcome with design improvements.

Chapter 4 introduces the new SXR double-filter diagnostic that resulted from the work described in Chapter 3. Several additional features are added into the new diagnostic to substantially expand its capabilities. The SXR emission model is used again to demonstrate the improvement provided by the new design. Finally, the Chapter describes in some detail several hurdles in implementation that resulted from the new design. Specifically, sensitivity to magnetic pickup became unacceptable at high gain levels and several modifications were undertaken to reduce it. A more detailed characterization of magnetic pickup is found in Appendix A.

Chapter 5 describes physics results through a sampling of measurements that highlight the capabilities of the new double-foil diagnostic. An integrated data analysis approach is used, incorporating Thomson Scattering, FIR, and magnetics measurements. The SXR diagnostic is also used to measure the plasma spectrum in combination with the CHERS measurement of Al^{11+} impurity density. The full horizontal and vertical direct-brightness T_e profiles are benchmarked against the Thomson scattering T_e during high-current PPCD. Flux surface mapping of T_e indicates the presence of a ΔT_e structure in a shot with a large locked dominant tearing mode. In contrast, a multiple-helicity discharge shows evidence for impurity accumulation in the mid-radius.

Chapter 6 summarizes the results of this thesis. It also proposes further avenues of research. Building upon this thesis, it suggests future run campaigns during non-crash-heated PPCD with additional diagnostics to measure J_r and Z_{eff}. It also advocates a Bayesian approach to uncertainty estimation. Other interesting physics questions are posed regarding the nature of crash-heated PPCD compared to non-crash-heated PPCD, during both rotating and locked discharges. Finally, the SXR T_e and tomography diagnostic should be used to search for ΔT_e structures in single-helical-axis (SHAx) plasmas.

Chapter 2

SXR Emission and Electron Temperature

Soft X-ray emission is a useful tool for probing the plasma. It represents the magnetic flux geometry in the plasma, and incorporates electron temperature, density, and impurity content. A critical tool in developing a SXR diagnostic is a model to understand how these plasma parameters intersect to explain the measured SXR emission. This model can be combined with a specific tomography diagnostic and machine geometry to create a simulated SXR brightness profile. A simulated brightness profile has many applications, it is used to: optimize the design of the diagnostic upgrade, provide a measure of confidence in the tomographic reconstruction technique, and calculate the ratio-temperature relations that are applied to measurements when determining electron temperature directly from brightness measurements. An accurate SXR emissivity model can also be used in combination with some combination of measured SXR brightness, electron temperature, or effective atomic number (Z_{eff}) to constrain the remaining parameters.

Section 2.1 describes the SXR emission model used on MST. The model is based on bremsstrahlung emission but also incorporates line and recombination radiation, as well as non-maxwellian effects. Section 2.2 describes the Cormack-Bessel technique for tomographic reconstruction. Tomographic reconstruction converts line-integrated brightness measurements into emissivity. This technique can be applied to both the model and the actual data to generate 2D 'images' of the plasma flux surfaces. Section 2.3 explains the double-foil technique for converting SXR measurements to electron temperature. The double-foil technique can be applied to tomographically reconstructed emissivity to make a 2D map of tomographic T_e. With the new diagnostic on MST, it can also be applied directly to the line-integrated brightness to make profile measurements of direct-brightness (DB) T_e. The DB T_e measurement generally represents the hottest temperature along the line-of-sight. Finally, §2.4 discusses limitations to the double-foil technique that arise due to the Aluminum impurity content on MST.

2.1 The Soft X-Ray Emission Model

The SXR emission model used in this thesis was originally developed at RFX and is designed to simulate the expected SXR emission from a plasma given a specific set of plasma parameters [42, 43]. The simplest application calculates the bremsstrahlung radiation (ε) created by a plasma in the energy range (E) of interest, as a function of electron temperature (T_e) and density (n_e):

$$\varepsilon = \int_E dE \left\{ \frac{Z_{eff}\, n_e^2(r)}{\sqrt{T_e(r)}} e^{-\frac{E}{T_e(r)}} \right\} \tag{2.1}$$

The RFX model applies this SXR emission equation to a flux surface geometry, as shown in Figure 2.1. In this geometry, Δa is the shift of the magnetic axis with respect to the geometric axis O, Δh is the shift of the last closed flux-surface, and the flux surfaces ρ are centered on a point shifted $\Delta\rho$. Because a bremsstrahlung-only model is sometimes insufficient to describe plasmas in MST, simple approximations for line radiation and recombination radiation have been added. Additionally, a pa-

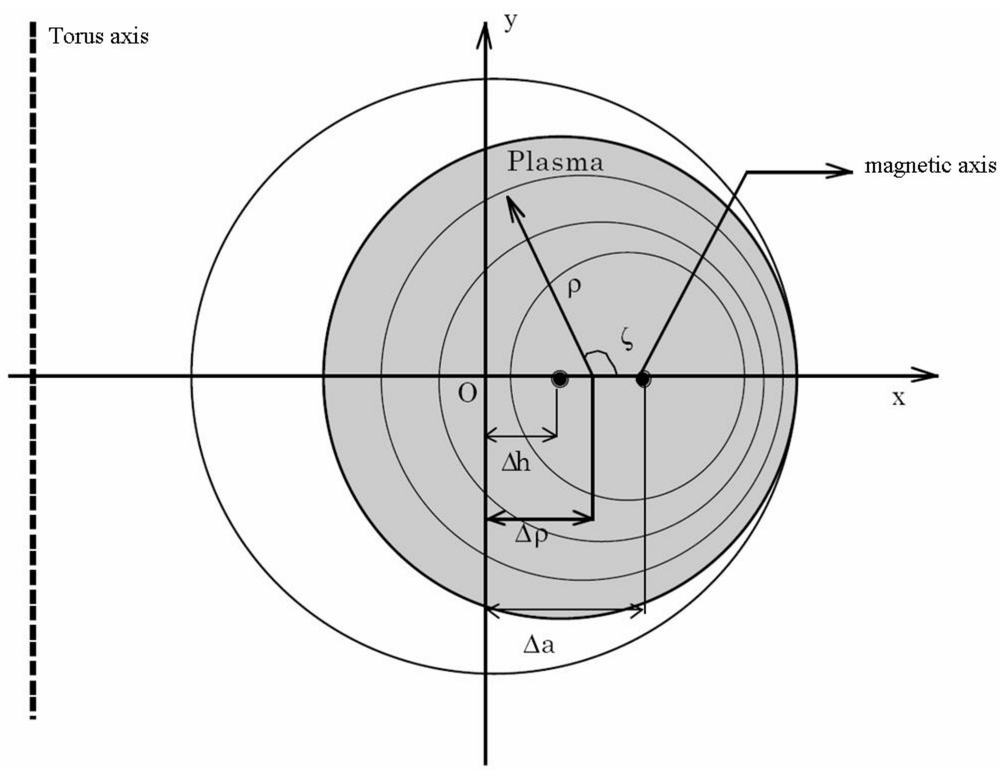

Figure 2.1: Schematic of the flux-coordinate system used in the SXR model, courtesy of F. Bonomo [42]

rameter called 'enhancement factor' has been included which can account for any non-Maxwellian contributions to the electron distribution.

2.1.1 The Bremsstrahlung Model

The simplest soft x-ray (SXR) model estimates the soft x-ray emission from a plasma due to only bremsstrahlung radiation. The model restricts the calculation to the x-ray energy range of interest by incorporating the filter and detector silicon thicknesses. To simulate a symmetric plasma, the model takes user-specified temperature and density radial profiles as power-law functions in the form:

$$f(r) = f(0)(1 - (r/a)^A)^B \tag{2.2}$$

where r/a is normalized to the minor radius of the vessel. Both the magnetic axis and the the last closed flux surface in the plasma can be shifted away from the geometric center of the machine. Examples of equilibrium T_e and n_e profiles can be seen in Figures 5.19 and 5.20, respectively. Additionally, perturbations on an equilibrium system can be included. Figure 2.2 shows examples of an equilibrium plasma, a plasma with a 'bean' shaped temperature island, and a plasma with a single helical axis (SHAx) temperature structure. A plasma with an island has a magnetic geometry comprised of an axisymmetric portion as well as a separate healed flux-surface that appears as a helical island structure. In a SHAx configuration, the magnetic configuration of the island overtakes the magnetic core, and a new helical geometry is formed [44]. (For a detailed description of these two configurations, refer to §1.1.2). Specifically, temperature 'islands', and density 'rings' are modeled as gaussian structures of the form:

$$T_e(r) = T_e(0)\,(1 - (r/a)^\alpha)^\beta + \Delta T_e\, e^{-(\delta r_T - r)^2/2\Delta r_T^2} e^{-(\delta\theta - \theta)^2/\Delta\theta^2} \tag{2.3}$$

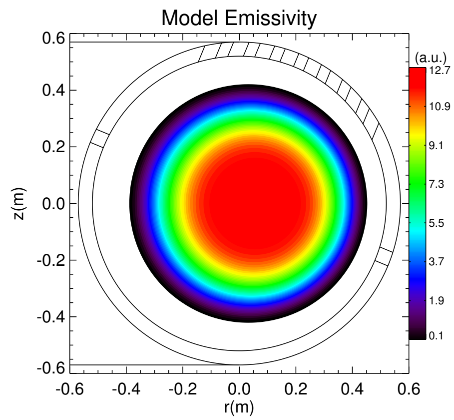

(a) Equilibrium

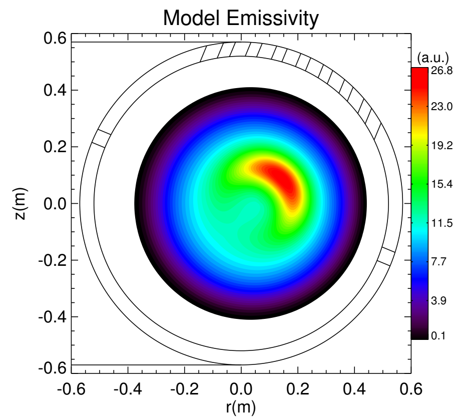

(b) Island

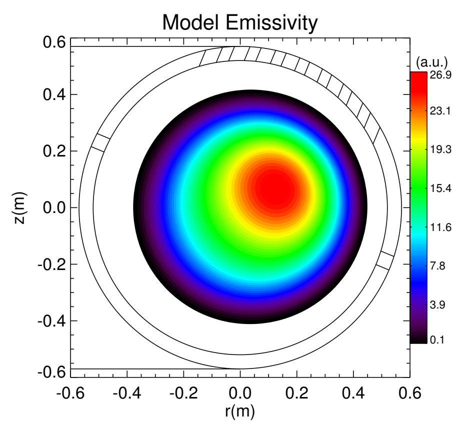

(c) Single Helical Axis (SHAx)

Figure 2.2: Simulated SXR emissivity for a 1.5 keV plasma (top left), with an added temperature island (top right), or an added SHAx-like temperature structure (bottom). Plasma parameters $T_e(0)$=1.5 keV, α=4.5, β=1.0, γ=4.5, Δa=0.06 m, Δh=0.02 m; Island parameters ΔT_e=$T_e(0)$ * 0.35, θ=45°; (island: r=0.25, δr_T=0.10, $\Delta\theta$=65°); (SHAx: r=0.20, δr_T=0.35, $\Delta\theta$=0°).

$$n_e(r) = n_e(0)\,(1 - (r/a)^{\gamma}) + \Delta n_e\, e^{-(\delta r_n - r)^2/2\Delta r_n^2} \tag{2.4}$$

In Equation 2.3, $T_e(0)$ is the value at the center of the plasma, a is the minor radius, α and β are the power-law exponents describing the shape of the profile. ΔT_e is the amplitude of the temperature perturbation. The island is modeled as the product of two gaussians in r and θ, where Δr_T and $\Delta\theta$ are the radial and poloidal widths of the temperature perturbation. δr_T and $\delta\theta$ are the radial and poloidal location of the center of the perturbation. Temperature structures can also be modified to model SHAx structures by setting the width of the angular extent to zero. (This models the island as a single gaussian centered at (r, θ)).

Equation 2.4 describes the density profile with the same types of parameters. Density perturbations however, are not constrained helically and so create a perturbation symmetric about the center axis of the plasma (i.e. a ring), rather than a localized poloidal structure, so no angular component is needed [45]. Alternatively, the density or temperature profile can be described as an array of individual radial points. This feature allows the use of measured profiles from the Thomson Scattering or FIR diagnostics on MST to be incorporated into the model.

The assumption of pure bremsstrahlung radiation from a Maxwellian electron distribution is not always sufficient. In addition to atmospheric impurities, the MST vacuum vessel is made of aluminum, so the actual plasmas often do not emit pure hydrogen bremsstrahlung radiation. Aluminum ions add line and recombination radiation, and change the effective atomic number of the plasma. The SXR emission model now includes simple models to account for these variations.

2.1.2 Line and Recombination Radiation

Line radiation and recombination steps have been added into the SXR emissivity model. The recombination step is defined by the energy at which it occurs and the relative strength of the radiation compared to the bremsstrahlung model. Line radiation is parameterized by specifying the energy of the radiation line, amplitude relative to the bremsstrahlung background, line width, and the potential energy of the emitting ion. Both these effects are modeled very primitively and require estimates of the scale of the emission. However, they are still quite useful. In MST for example, hydrogen-like aluminum has radiation steps at 2.1 and 2.3 keV, and line radiation at 1.48 keV [46]. For example, Figure 2.3 shows the simulated brightness profile seen through thin Be filters (50 μm) for a high current plasma with a core temperature of 1.5 keV. In this case, hydrogen-like aluminum radiation causes increased SXR emission, which tends to broaden the profile near the edges as compared with a hydrogen bremsstrahlung-only plasma.

2.1.3 Effective Atomic Number (Z_{eff})

Variation in the effective atomic number (Z_{eff}) in the plasma can be modeled as a radial profile. The model defines a general enhancement as a function of 4 points ($r_1 - r_4$) and two amplitudes ($enh = [A_1, A_2]$). The amplitudes are added to the emission in exponential form:

$$\varepsilon = e^{ln\left(\frac{n_e^2}{E\sqrt{T_e}}\right)} * e^{-E/T_e} * e^{ln(1+ENH)} \tag{2.5}$$

so that an enhancement factor of zero results in the un-enhanced emission. From $r/a = 0$ to r_0, there is no enhancement. From $r_1 - r_2$ the profile has zero enhancement. From $r_2 - r_3$ the profile increases from zero $-A_1$. Finally from $r_3 - r_4$ the profile

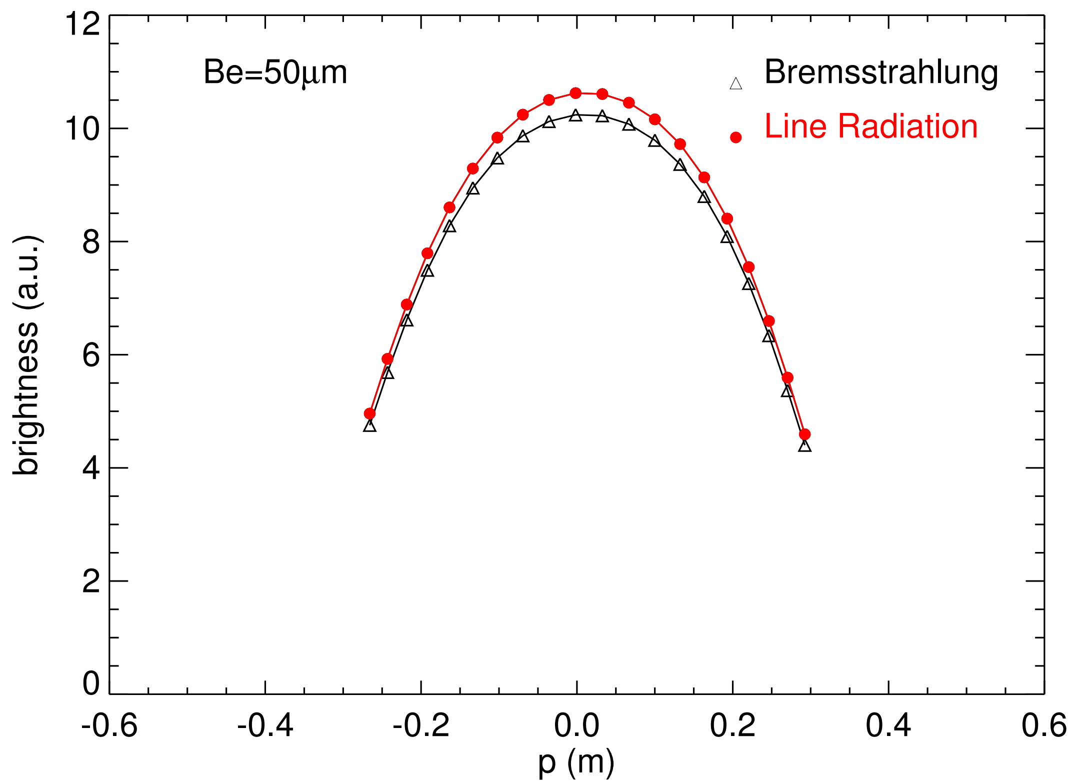

Figure 2.3: Simulated brightness profile for a 1.5 keV plasma with (circles) and without (triangles) a Kα Aluminum radiation line. The radiation lines increase emission in the area where they are ionized, which in this case is the core. As a result, the profile is somewhat peaked.

increases to A_2. From r_4 to $r/a = 1$, the profile decreases back to zero enhancement.

2.1.4 Electron Distribution

There is evidence that the electron distribution on MST is not always a pure Maxwellian. Figure 2.4 shows the x-ray spectrum as measured with the hard and soft x-ray detectors for a 500 kA PPCD plasma. For a purely Maxwellian plasma with an electron temperature of 2 keV, there should be negligible x-rays beyond about 15 keV [47]. However, previous studies have detected x-ray emission out to $\sim$ 150keV [48]. This enhanced x-ray emission is likely due to fast electrons, which create a non-Maxwellian tail in the electron distribution. Although there has not yet been evidence of non-Maxwellian emission observed in the energy range accessible by the SXR tomography and T_e diagnostic, it is worthwhile to consider the possibility. Therefore, parameters have been added the SXR emission model to simulate a non-Maxwellian tail on the electron distribution in the plasma. Plotted on a log scale, the spectrum of a pure Maxwellian electron distribution is linear and decreasing as energy increases. A non-Maxwellian contribution creates a "knee" in the distribution, causing the higher energy component to have a more shallow slope. In the model, the non-Maxwellian tail is parameterized by the energy at which the non-Maxwellian contribution begins to affect the plasma (the position of the "knee"), and the relative strength of the effect (the slope of the "knee"). Generally speaking, a non-Maxwellian tail enhances the SXR radiation preferentially at the high energy tail, making the plasma appear hotter than it actually is.

2.2 Tomographic Reconstruction

The SXR model calculates plasma emissivity, but the measured quantity from the plasma is SXR brightness. To compare the modeled emissivity with the mea-

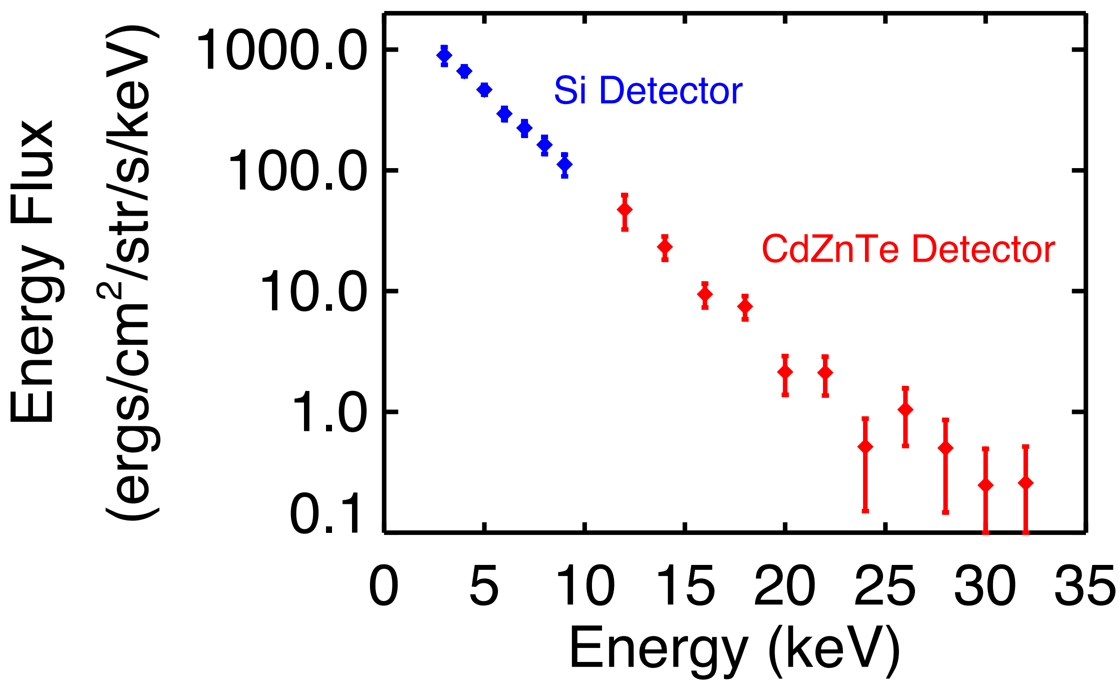

Figure 2.4: X-ray spectrum for a canonical 500kA PPCD plasma as measured by the SXR and HXR diagnostic. A pure Maxwellian spectrum for a 2.0 keV plasma such as this one should have negligible x-ray emission beyond 15 keV. The presence of additional x-rays in the high energy region of this plot indicate a non-Maxwellian tail in the electron distribution, likely caused by runaway electrons. (Plot courtesy of D. Clayton [47]).

sured data, the model can be integrated along each line-of-sight, to create simulated brightness profiles. Alternatively, the measured SXR brightness can be tomographically reconstructed to find the emissivity contributed from each part of the plasma. Additionally, simulated plasma emissivity can be integrated into brightness, then tomographically reconstructed back into emissivity to test the robustness of the mathematical technique. The mathematical methods for converting between brightness and emissivity provide an estimate of the uncertainties in the measurements.

2.2.1 SXR Brightness

The SXR emission model is combined with the geometry of actual SXR probes to simulate the expected measured SXR brightness for individual lines-of-sight. Each individual diode measures a unique brightness based on its geometry. A simulated brightness profile including all diodes in a probe can be used to optimize new designs. It can also be used in combination with measured brightness to examine the role of impurities, density, or temperature in the SXR emission.

The measured brightness $f(L)$ integrated over energy E begins with the plasma emissivity (ε):

$$f(L) = f_g \int_E \int_L dE\, A(E)\, T(E, Be)\, \varepsilon(E)\, dl \tag{2.6}$$

It incorporates the transmission of the Be filters $T(E, Be)$, the absorption of the photodiode $A(E)$, as well as the geometric factor defined by the cone of sight of the diode f_g:

$$f_g = \frac{A_d\, A_{ph}}{4\pi d^2}\, cos^4\gamma \tag{2.7}$$

A_d is the detector area, A_{ph} is the pinhole area, d is the distance from the pinhole plane to the detector plane, and γ is the angle between the line-of-sight and the normal vector of the detector plane [49].

The Be filter transmission and Si photodiode absorption are both governed by the attenuation function:

$$T(t, Be, E) = e^{-t\mu(E)} \tag{2.8}$$

for a material thickness (t) and absorbing coefficient μ specific to each material [21]. For a material with atomic number Z, μ is defined for each wavelength λ (in Angstroms) as:

$$\mu = c * (\lambda^a) * (Z^b) \tag{2.9}$$

The coefficients a, b, c are tabulated in Bardet [50] for both beryllium and silicon. Silicon is calculated in three separate energy ranges to account for discontinuities in the transmission function at the L1 and K-shell transitions.

Figure 2.5 shows sensitivity curves of the SXR detector, accounting for two typical beryllium filter thicknesses (400 and 800 μm), as well as the silicon thickness of the photodiode (35 μm). $T(E)A(E)$ represents the fraction of incident photons that will be detected as a function of energy. Incident photons from ~2-10 keV will pass through the beryllium and be absorbed by the silicon, resulting in a detection. Photons below ~2 keV do not have enough energy to pass through the filters, while photons above ~10 keV are so energetic that they pass through the silicon photodiode undetected.

2.2.2 Cormack Bessel Technique

The plasma emissivity is calculated from the measured (or simulated) SXR brightness through tomographic reconstruction. A tomographic reconstruction uses the measured brightness along many chords to determine how much emission is coming from each point in the plasma. The result is a two-dimensional map of SXR emission in a poloidal cross-section. On MST and RFX, tomographic reconstruction is done

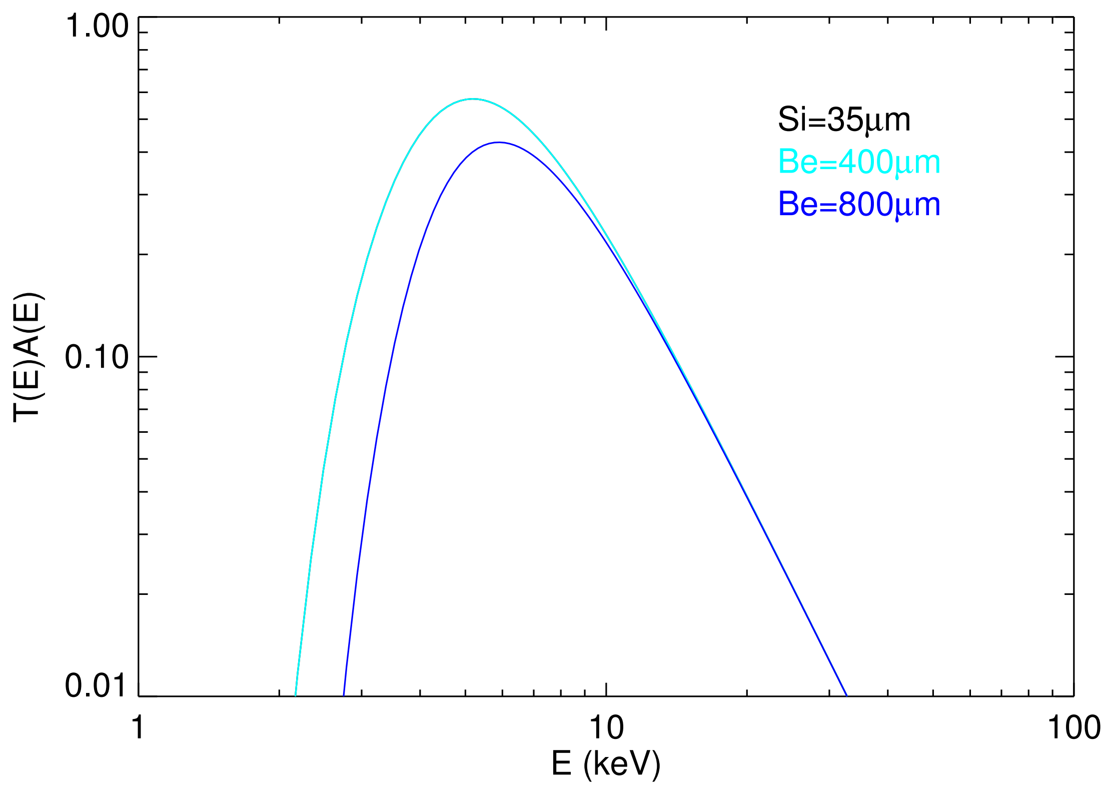

Figure 2.5: Sensitivity curve showing the fraction of incident photons that will be detected as a function of energy, including both the transmission curve of beryllium and the absorption curve of silicon for the thicknesses used in the actual SXR detectors. Light blue is the sensitivity curve for a 400 μm beryllium foil with a 35 μm silicon photodiode. Dark blue uses the same silicon thickness for a beryllium foil of 800 μm. The detected signal comes from ~2-10 keV photons.

using the Cormack-Bessel technique. A brief description of the method is given here, more detail is available in Franz [49]. The brightness (f) and emissivity (g) are defined as:

$$f(p,\phi) = \int_{L(p,\phi)} g(r,\theta)\, dl \tag{2.10}$$

Emissivity is defined in the standard poloidal r, θ coordinate system. Brightness is defined by impact parameter p and impact angle ϕ. Figure 2.6 illustrates the relationship between the two coordinate systems. The impact parameter is the shortest distance from a line-of-sight to the center of the plasma, while ϕ is the angle of p.

The Cormack approach [51, 52] applies a truncated Fourier series to the brightness and emissivity:

$$f(p,\phi) = \sum_{m=0}^{M} \left[f_m^c(p)\, cos(m\phi) + f_m^s(p)\, sin(m\phi)\right] \tag{2.11}$$

$$g(r,\theta) = \sum_{m=0}^{M} \left[g_m^c(r)\, cos(m\theta) + g_m^s(r)\, sin(m\theta)\right] \tag{2.12}$$

The truncation is based on the number of unique measurement chords. The Cormack method relates equations 2.11 and 2.12:

$$g_m^{c,s}(r) = -\frac{1}{\pi}\frac{d}{dr}\int_r^1 \frac{r\, f_m^{c,s}(p)\, T_m(p/r)\, dp}{p\sqrt{p^2 - r^2}} \tag{2.13}$$

$T_m(p/r)$ are Tchebychev polynomials. By expanding the Fourier components over a truncated set of Bessel functions, the boundary condition of zero emissivity at the edge is met [53, 54]:

$$g_m^l(r) = J_m(\lambda_m^{l-1} r) \tag{2.14}$$

where $\lambda_m^{l-1} r$ is the lth zero of the mth order Bessel function $J_m(z)$. Equation 2.13 can

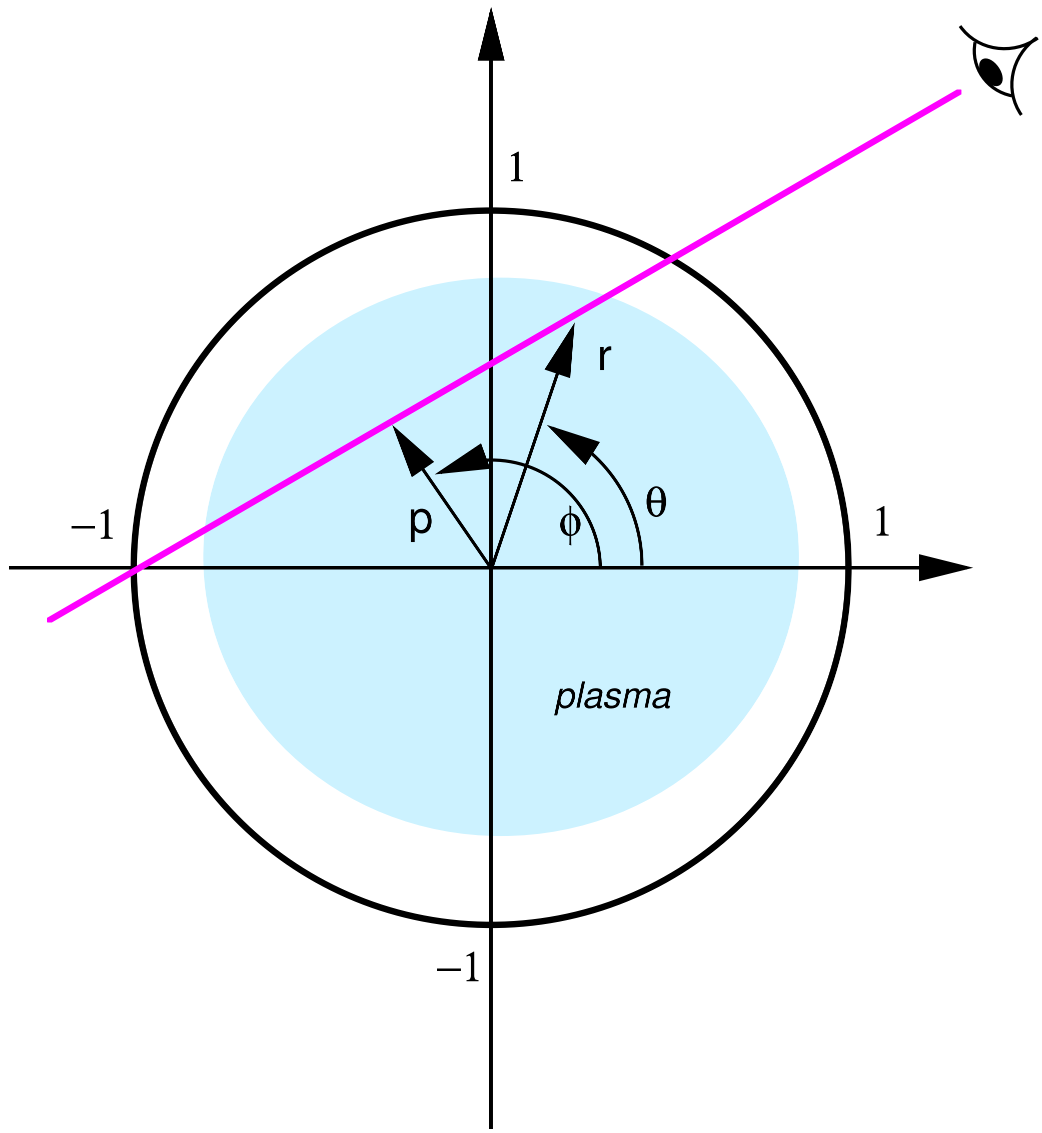

Figure 2.6: Relationship of the brightness coordinates p and ϕ to the emissivity coordinates r and ρ. Impact parameter p is the standard coordinate used in SXR T_e profile plots as well. (Plot courtesy of F. Bonomo [42]).

now be represented as a matrix of the form:

$$\mathbf{f} = \mathbf{W} \cdot \mathbf{g} \tag{2.15}$$

The matrix $\mathbf{W}$ defines the geometry of the system, so that the emissivity vector $\mathbf{g}$ is solved when brightness $\mathbf{f}$ is measured. Singular value decomposition (SVD) is then applied to the solution:

$$\| \mathbf{r} \|_2 = \| \mathbf{W} \cdot \mathbf{g} - \mathbf{f} \|_2 = \sqrt{\sum_i \mathbf{W} \cdot \mathbf{g} - \mathbf{f}_i} \tag{2.16}$$

When the residual $\| \mathbf{r} \|_2$ becomes smaller than some specified value, then the reconstruction is complete. The result is a two-dimensional map of reconstructed emissivity everywhere in the plasma, as well as the line-integrated brightness that the detectors would see based on the emissivity map (referred to as 'reconstructed brightness').

2.2.3 Alternative Reconstruction Techniques

This analytical solution to mapping emissivity has worked well for the SXR system [37]. It is also possible to develop a tomographic reconstruction using other techniques, namely by a finite element method or a hybrid of the two. In the finite element method, the poloidal cross-section is cut into discrete pixels of constant flux, and the pixel size and shape is constrained by the overlap of the measurement chords. Alternatively, the hybrid method applies the finite element approach to the radial components, creating nested circular regions in which the angular harmonics are solved analytically [55]. In addition to the analytical approach, both the finite element and hybrid methods were applied to the SXR tomography system at RFX. All three techniques successfully reproduced island structures in the emissivity, but the analytical approach is much less computationally intensive [56]. As a result, the Cormack-Bessel technique is used exclusively in the MST tomography analysis.

2.2.4 Using Simulated Brightness as a Measure of Uncertainty

The SXR emission model is a useful tool for understanding the uncertainties in the tomographic reconstruction. Tomographic reconstruction has many parameters that can be varied when fitting the data (i.e. the Fourier expansion m in $sin(m\theta)$ and $cos(m\theta)$, the Bessel function truncation l, and the residual $\parallel \mathbf{r} \parallel_2$ set in the single value decomposition). Therefore, a method for determining a 'good fit' is needed. The tomographic reconstruction begins with a measured line-integrated brightness measurement and then calculates the SXR emissivity at each point in the plasma. By adding up all the reconstructed emissivity passing through a line-of-sight, the 'reconstructed brightness' is calculated. If the reconstruction is accurate, then the reconstructed brightness should match the measured brightness for all the probes. If the reconstruction is poor, the reconstructed brightness will not match the measured brightness in one or more probes. This feedback provides confidence that the chosen reconstruction parameters are a good fit to the data.

Even if the reconstruction parameters are ideal, it is still difficult to estimate the uncertainty of a tomographic reconstruction. Simple estimates of error such as Poisson statistics do not apply to the raw data, because individual photons are not being measured. Therefore, the reconstruction itself should be used to estimate the uncertainty. The SXR emission model can be used to calculate the ideal emissivity for a specified plasma. (This model plasma will approximate the actual plasma if measured T_e and n_e profile measurements are used.) Given the model emission, the uncertainty in the reconstruction can be estimated by varying the reconstruction parameters and comparing the deviation in the reconstructed emissivity to the model emissivity.

2.3 The Double-Foil Technique for T_e Measurement

Measurement of SXR brightness already provides SXR emissivity, which is a proxy for magnetic structure in the plasma. However, even more information can be gleaned from the measurement using the double-foil, or two-color, technique. This technique relies on the fact that individual electrons in a plasma do not all have a single energy at a given plasma temperature. Rather, a single T_e is comprised of electrons with a range of different energies, defined by a distribution function. Because the beryllium in the SXR diagnostic acts as a band-pass energy filter, different filters looking at the same distribution of electrons will measure different brightnesses. The difference between these measured energy bands can then be used to calculate the characteristic T_e of the electron distribution. Therefore, if SXR emission from the same plasma is measured with two different beryllium filters, the electron temperature of the plasma is determined.

The double-foil technique begins with the assumption that SXR emission from the plasma is due to bremsstrahlung radiation and the plasma has a Maxwell-Boltzmann (often referred to as simply a Maxwellian) electron distribution. The Maxwell-Boltzmann distribution function describes the motion of particles in a gas as a function of the temperature T of the gas using a statistical treatment. The likelihood f of a particle having a specific energy E is described by:

$$f(E) = \sqrt{\frac{E}{\pi kT}}\, e^{-E/kT} \tag{2.17}$$

Figure 2.7 shows the general distribution of energies within a Maxwell-Boltzmann

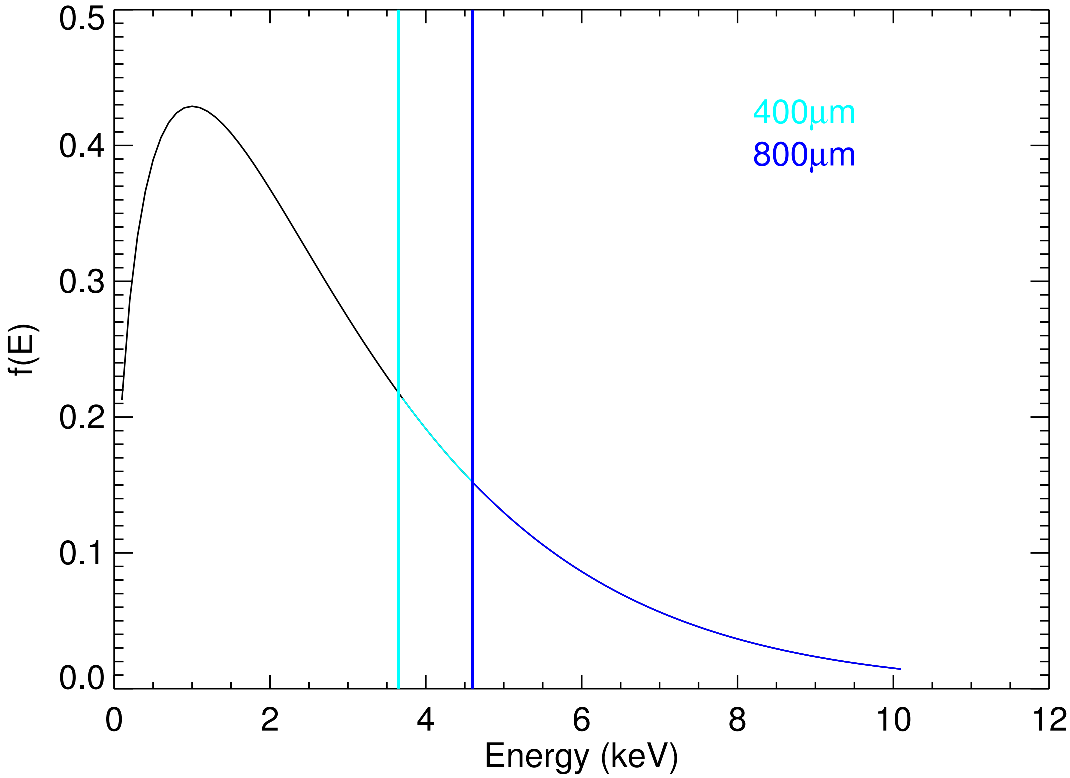

Figure 2.7: Distribution function for a Maxwellian plasma with an electron temperature of 2.0 keV. The region to the right of the light blue line denotes x-ray energies measured through a 400 μm beryllium foil, while the region to the right of the dark blue line denotes x-ray energies measured through an 800 μm beryllium foil. (Vertical lines are the 1/e cutoff energy for each filter). The ratio of these two measurements is used to calculate the temperature of the plasma.

gas with a temperature 2.0 keV. Assume a pure Bremsstrahlung plasma with a density n_e and atomic number Z_{eff}. (That is, for a plasma where all radiation is caused by electrons accelerating through the electric field of an ion, with no line or recombination radiation). The measured x-ray radiation from this distribution of electrons (ε_{obs}) as a function of energy E, including the transmission functions defined in Figure 2.5, is:

$$\varepsilon_{obs} = \int_E dE\, A(E)\, T(E, Be) \left\{ \frac{K\, Z_{eff}\, n_e^2(r)}{\sqrt{T_e(r)}} e^{-\frac{E}{T_e(r)}} \right\} \tag{2.18}$$

where K is a constant, and $A(E)$ and $T(E, Be)$ are the absorption and transmission functions for the silicon photodiode and beryllium filter (Equation 2.8). The two colored regions in Figure 2.7 denote the energies that can be measured through two different filters, where the line defines the the $1/e$ minimum cutoff energy for the filter thickness. The region to the right of the light blue line denotes x-ray energies measured through a 400 μm beryllium foil, while the region to the right of the dark blue line denotes x-ray energies measured through an 800 μm beryllium foil. The ratio of emissivities through these two filters is defined as:

$$R = \frac{\varepsilon_1}{\varepsilon_2} \tag{2.19}$$

The density and effective atomic number from equation 2.18 are independent of energy and therefore the same for both beryllium filters, so the ratio is a function of only the energies accessed by each filter and the temperature of the plasma $R(E, T)$.

To determine electron temperature in the plasma from the measured SXR emission, a library of ratios is created. Using Equations 2.8, 2.18, and 2.19, the expected ratio for x-rays from electrons a with temperature T is calculated for a specific pair of filters. This calculation is done for many temperatures, until a function $R(T)$ is

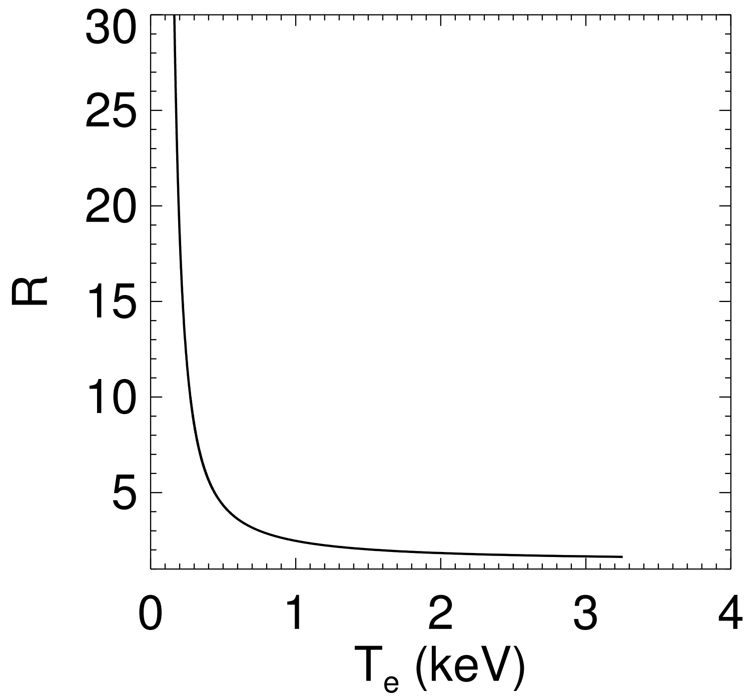

Figure 2.8: Typical curve showing the polynomial dependence between T_e and the ratio R for Be filters with thicknesses 408 and 821μm. The electron temperature in the plasma is determined by applying this relationship to the measured emissivity ratio of through the two filters.

built. Figure 2.8 shows a typical ratio curve for a pair of foils that are approximately 400 and 800 μm thick. With this library in place, the ratio of measured SXR emissivity between two foils is converted to an electron temperature for that region of the plasma. Because SXR emission is a function of n_e, Z_{eff}, and T_e, there is not a particular lower-limit to measurable T_e with this filter set, but historically the diagnostic has been sensitive to plasmas with $T_e > 500$ eV.

2.3.1 Tomographic Temperature

The measured values of SXR emissivity on MST come from tomographic reconstruction of the raw SXR brightness measurement, as described in §2.2.2. Figure 2.9 is a simulation showing the emissivity at every point in the plasma calculated by tomographically reconstructing the SXR brightness through a thin foil (i.e. 400 μm) and a thick foil (i.e. 800 μm). The ratio library contains a curve for every geometrical point in the plasma, so by taking the ratio of emissivities at each point in the poloidal view, a 2D tomographically reconstructed temperature is found (Figure 2.10). This technique has been previously applied to experimental data on MST to determine the electron temperature in the core region of the plasma [37]. However, the technique is very sensitive to small variations in the measured brightness (see §2.4 for details) and so works best for rather smooth profiles with large signal levels (i.e. equilibrium plasmas or well-measured island structures).

2.3.2 The Direct-Brightness Method

In addition to tomographic temperature, in certain geometries the double-foil technique can also be applied directly to the SXR brightness measurement. If the thin and thick filters look through the same line-of-sight, then the *Direct-Brightness (DB) Method* can be used.

The direct SXR brightness f is a line-integrated emissivity measurement along a line-of-sight (l):

$$f(l) = \int_l dl\, \varepsilon \tag{2.20}$$

Taking the ratio of the brightnesses of the two filters directly:

$$R = \frac{f_1}{f_2} = \frac{\int_l \varepsilon_1(T_e)\, d\vec{l}}{\int_l \varepsilon_2(T_e)\, d\vec{l}} \tag{2.21}$$

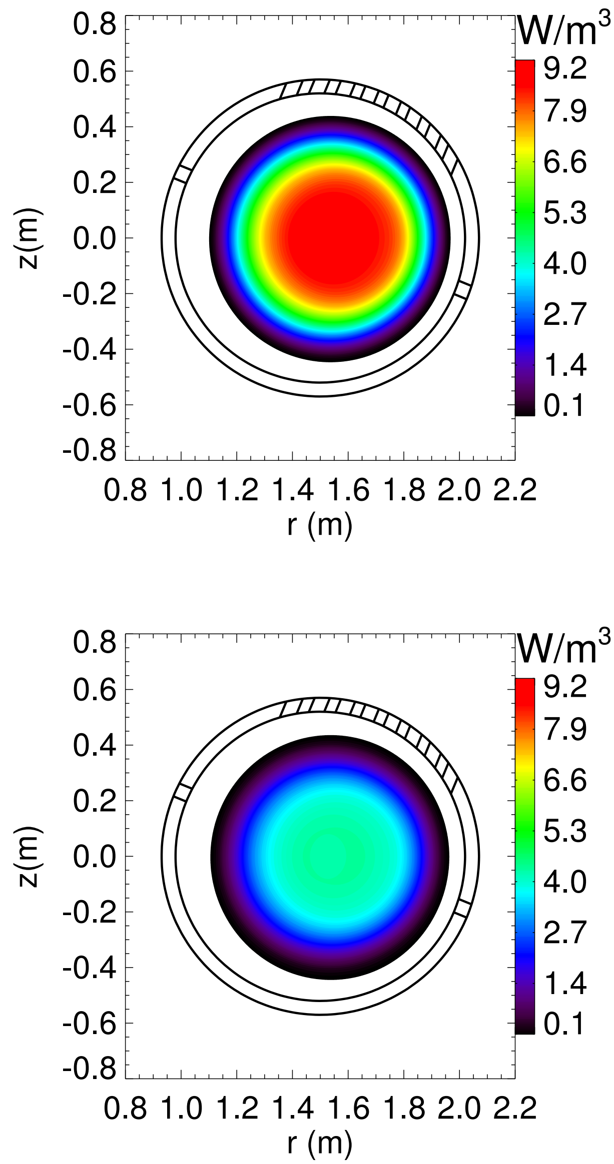

Figure 2.9: Tomographically reconstructed emissivity from simulated SXR brightness measured through a $\sim$400 μm Be foil (top) and an $\sim$800 μm Be foil (bottom) for a 1.5 keV equilibrium plasma, with the same contour scaling.

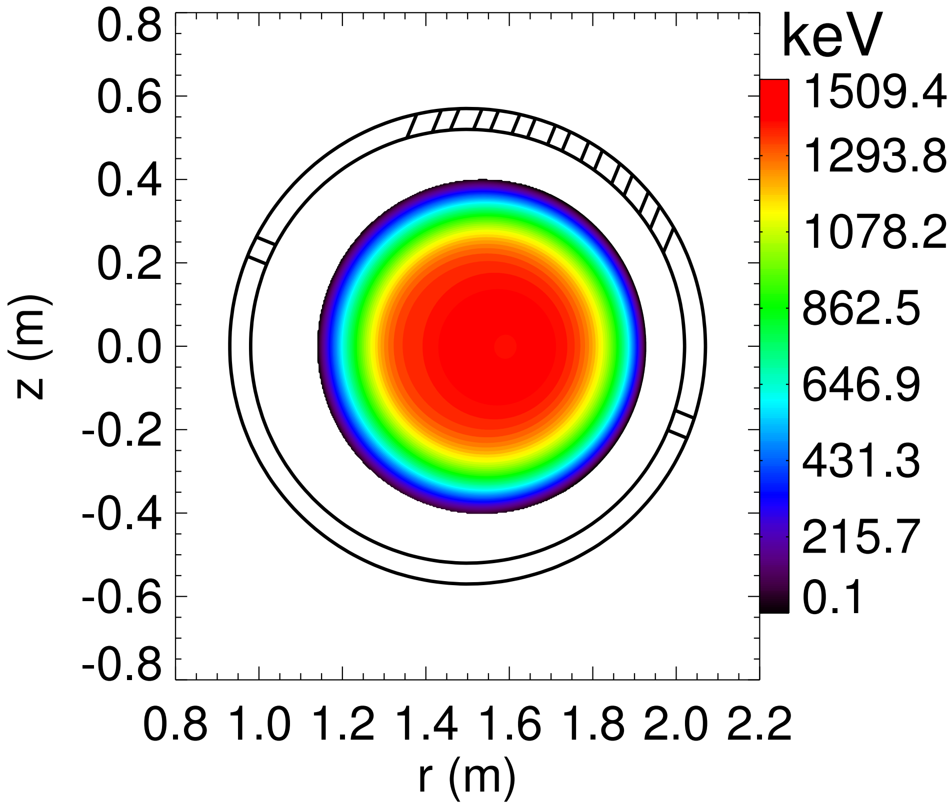

Figure 2.10: Tomographic T_e obtained by taking the ratio of the reconstructed thin and thick filter emissivities for a modeled 1.5 keV equilibrium plasma (Figure 2.9). The tomographic T_e technique provides a 2D map of temperature in a poloidal cross-section of the plasma.

If the thin foil and the thick foil measurements both come from the same line-of-sight, then the line integrals of the numerator and denominator in Equation 2.21 are the same. The integral over line-of-sight integrates density and atomic number, which are independent of energy. Therefore these contributions will again drop out of the ratio. Temperature is also a function of location in the plasma, and so it is unique to each line-of-sight. Therefore, the ratio curves calculated for pure emissivity in §2.3 cannot be used here, and a new set of ratio curves must be calculated for each individual line-of-sight. Once the ratio versus temperature curves are calculated for the line-of-sight, they are applied to the measurement to determine T_e. In the case of the direct-brightness measurement, a single brightness measurement leads to a single T_e along a line-of-sight.

The DB T_e does not represent an integral of individual temperatures along a line-of-sight in the way that brightness is an integral of emissivities however, because temperature is not an integrated quantity. Instead, the temperature calculated by this method is something of a weighted average. For symmetric plasmas, the temperature represents the hottest temperature along the line-of-sight. The following simulations were calculated beginning with the emissivity contours shown in Figure 2.2. Each simulation begins with a 1500 eV plasma (plasma parameters defined in Equations 2.3-2.4 and Figure 2.1 are α=4.5, β=1.0, γ=4.5, Δa=0.06 m, Δh=0.02 m).

Figure 2.11 shows temperature measured by each chord of SXR-D, (with a centered pinhole), for the equilibrium case of a flat T_e profile (plasma parameters $T_e(0)$=1.5 keV, α=4.5, β=1.0, γ=4.5, Δa=0.06 m, Δh=0.02 m). Each line-of-sight of the probe is traced in red. The blue circle along each chord represents the hottest temperature of the model along that chord. The green triangle represents the temperature measured when the direct-brightness technique is applied to the model. The purple

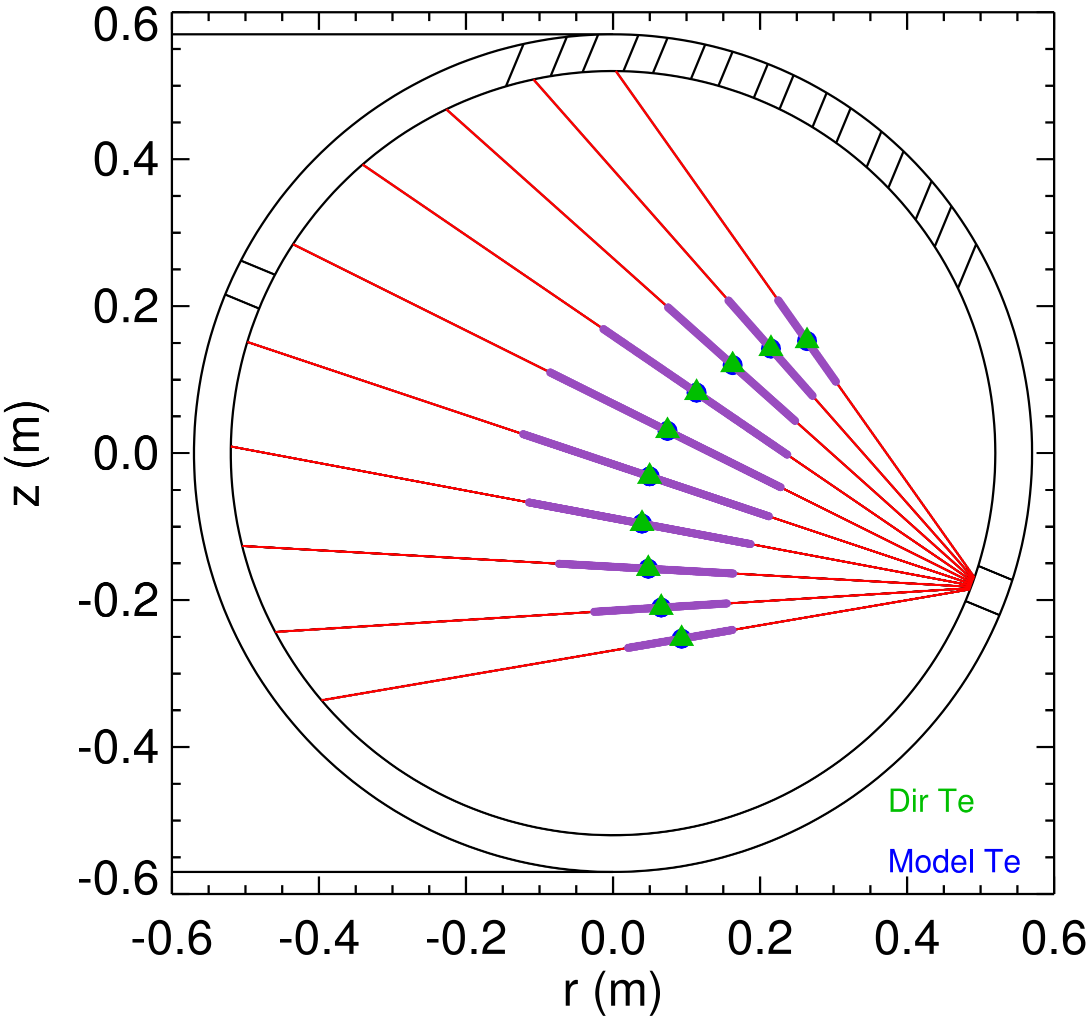

Figure 2.11: Lines-of-sight for SXR-D, showing the location of DB T_e (green triangle) as well as the actual hottest temperature along the chord (blue circle) for an equilibrium plasma. The purple regions along each chord show where the model temperature is within 1% of the direct-brightness temperature. In an experiment, a measurement of DB T_e with a systematic ambiguity of 1% could be attributed to any area in the purple region of the given chord. In an equilibrium plasma, DB T_e measures the hottest temperature region along the chord.

regions show any points along the chord where the model temperature is within 1% of the DB temperature. So if an experimental measurement of DB T_e was measured for a given chord then the effective 'location' of that temperature in the plasma could be anywhere shown in purple, with a systematic uncertainty of 1%. Increasing the uncertainty bounds lengthens the purple region. For the equilibrium case, the direct-brightness method truly represents the hottest temperature along the line-of-sight.

Figures 2.12 and 2.13 again show the DB T_e along each chord of SXR-D with a centered pinhole, but this time for a SHAx plasma and a plasma with an island, respectively (island parameters ΔT_e=Te(0) * 0.35, θ=45°; SHAx: r=0.20, δr_T=0.35, $\Delta\theta$=0°; island: r=0.25, δr_T=0.10, $\Delta\theta$=65°). For these simulations, the $R(T_e)$ library is created using the same island structure as seen in the emissivity. The shape of a SHAx structure is easily accommodated here and so again the direct-brightness temperature represents the hottest temperature along the chord. On the other hand, for an island, there are multiple discrete regions with the same temperature along some chords. As a result, the DB T_e measurement does not distinguish a unique region. Figure 2.14 plots the profile measurement for this simulation and clearly shows that in island cases, DB T_e will slightly underestimate the actual temperature of the structure.

2.3.3 Direct-Brightness T_e Accuracy

Section §2.3.2 demonstrates that when the plasma parameters are known *apriori*, the direct-brightness method correctly measures the hottest temperature along the line-of-sight for equilibrium and SHAx plasmas, and is accurate to within $\sim$ 5% for island structures. In experimental conditions however, the exact plasma parameters are not known *apriori*. How will this impact the DB T_e measurement?

The $R(Te)$ library is made by averaging the $R(Te)$ curves for a peaked and flat temperature and density profile (α=2.0, α=10.0). The uncertainty introduced by not

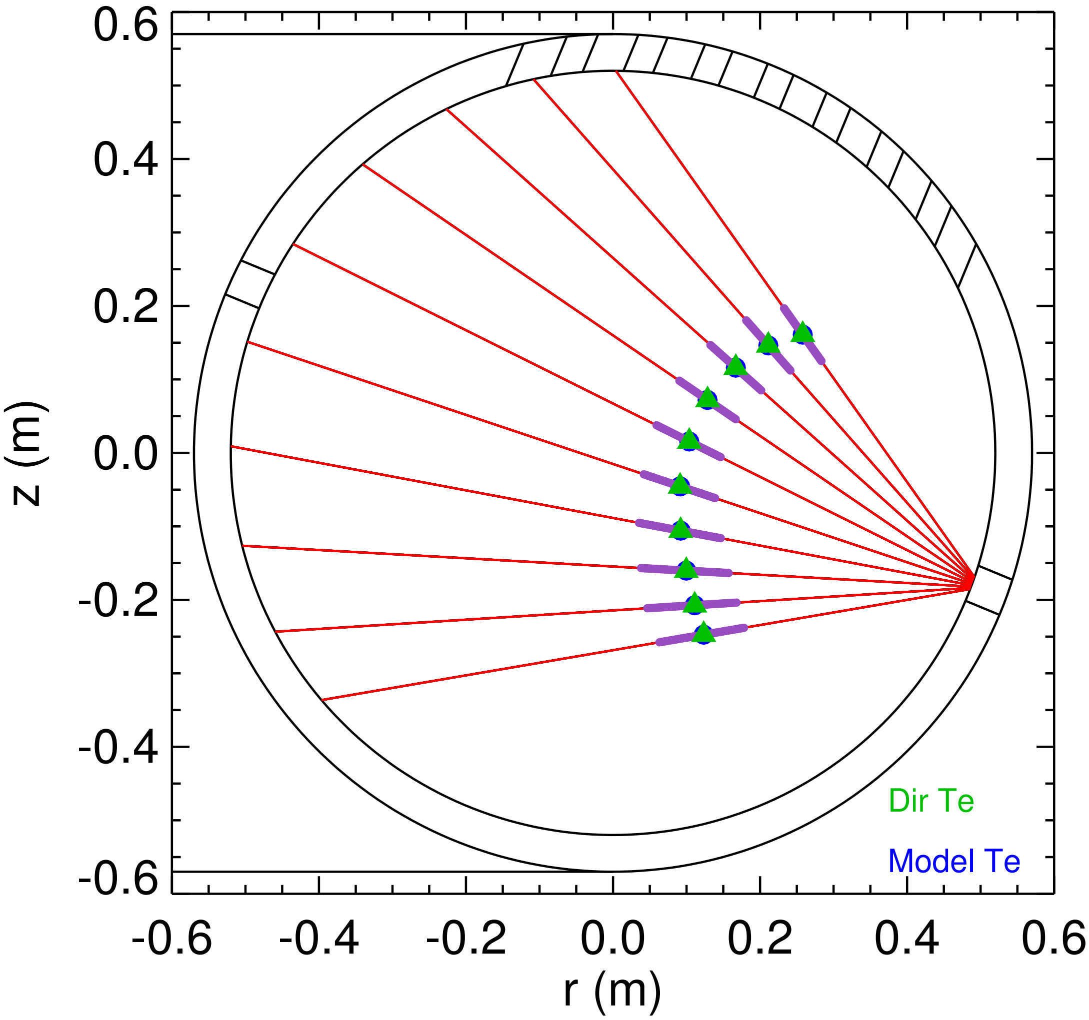

Figure 2.12: Lines-of-sight for SXR-D, showing the location of DB T_e (green triangle) as well as the actual hottest temperature along the chord (blue circle) for SHAx plasma, using a $T_e(R)$ library containing an island. The purple regions along each chord show where the model temperature is within 1% of the direct-brightness temperature. Because the SHAx structure is similar to an equilibrium plasma, DB T_e continues to represent the hottest temperature region along the chord.

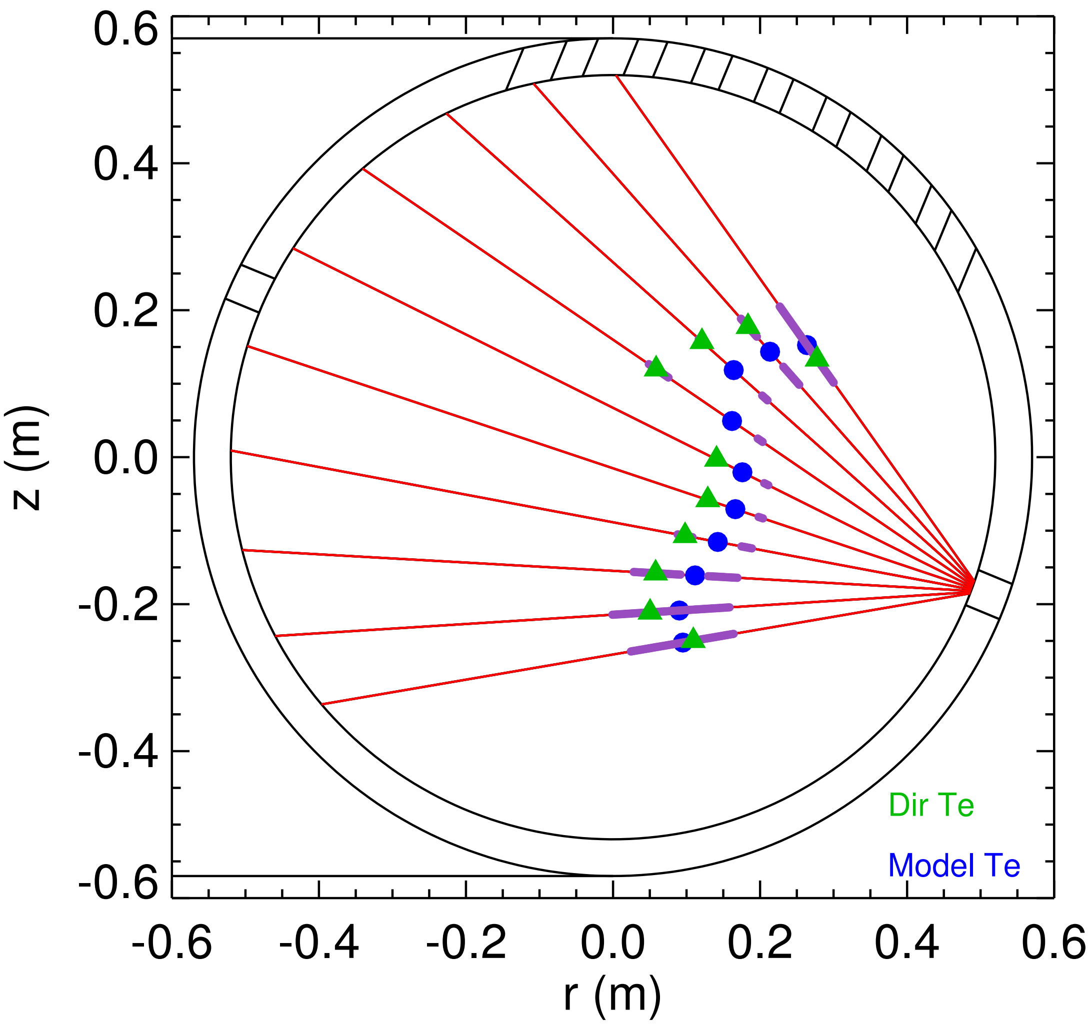

Figure 2.13: Lines-of-sight for SXR-D, showing the location of DB T_e (green triangle) as well as the actual hottest temperature along the chord (blue circle) for a plasma with an island, using a $T_e(R)$ library containing an island. The purple regions along each chord show where the model temperature is within 1% of the direct-brightness temperature. DB T_e for the island structure is not quite the hottest temperature along the chord. Particularly in chords that look through the angled part of the bean, (i.e. the 4th chord from the top), the chord looks through two distinct regions of the island that have the same temperature.

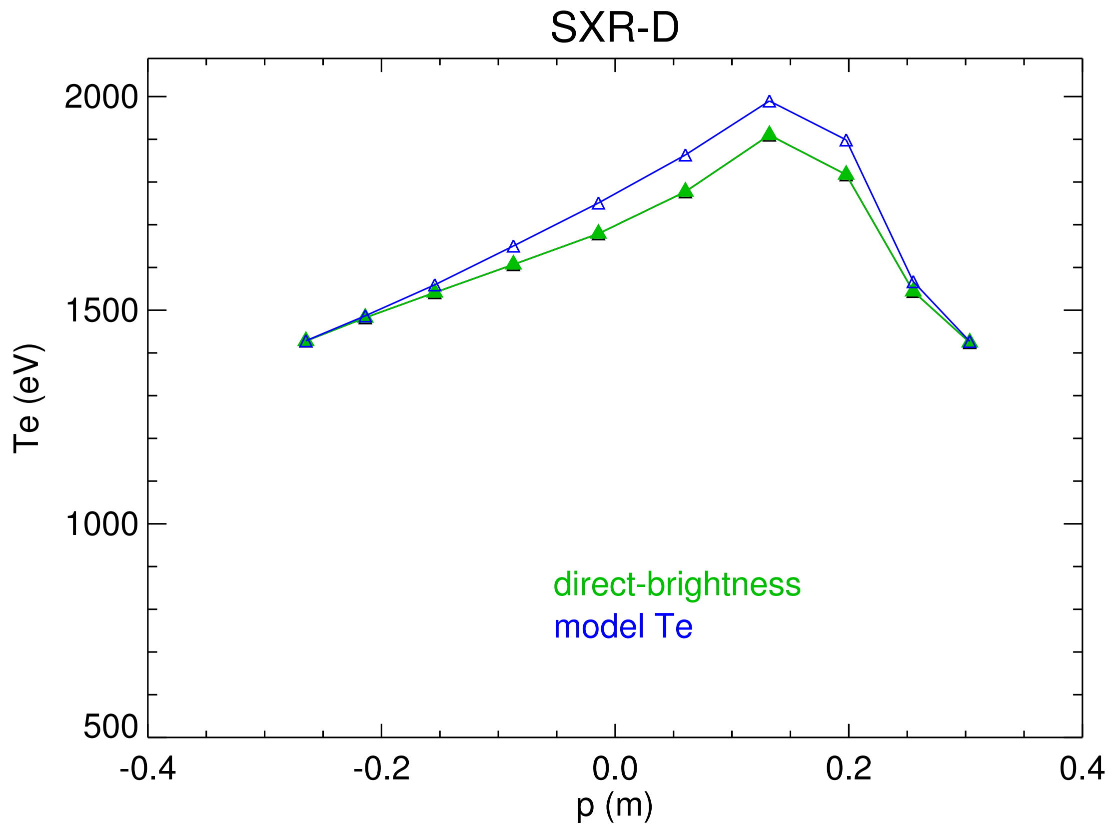

Figure 2.14: Profile of DB T_e (filled green) compared with the model T_e (unfilled blue) for SXR-D in a plasma with a T_e island. DB T_e (based on island model) for the island structure is not quite the hottest temperature along the chord, and underestimates the actual hottest temperature by $\sim 5\%$.

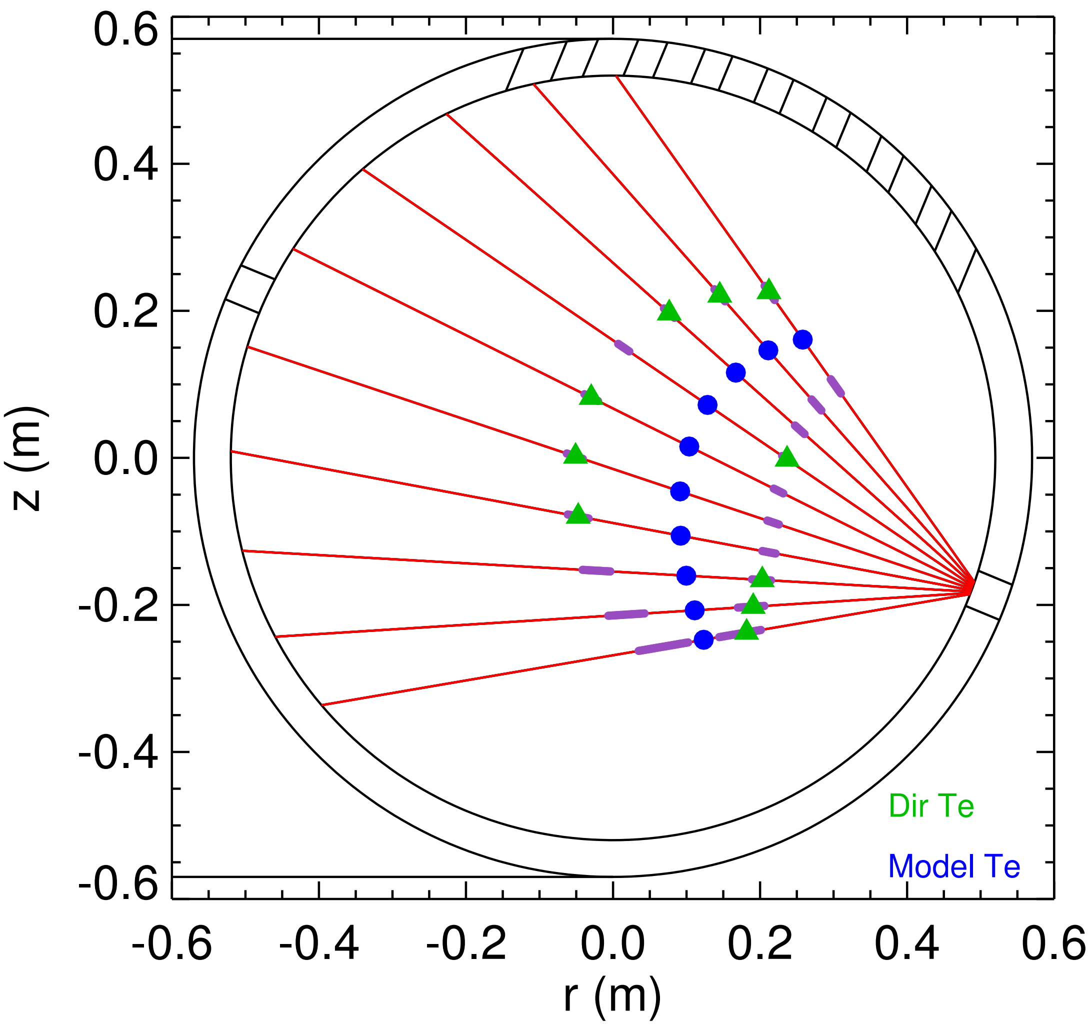

Figure 2.15: Lines-of-sight for SXR-D, showing the location of DB T_e (green triangle) as well as the actual hottest temperature along the chord (blue circle) for SHAx plasma. In this case, the $R(T_e)$ library assumes an equilibrium plasma *apriori* while the modeled plasma has a structure. The purple regions along each chord show where the model temperature is within 1% of the direct-brightness temperature.

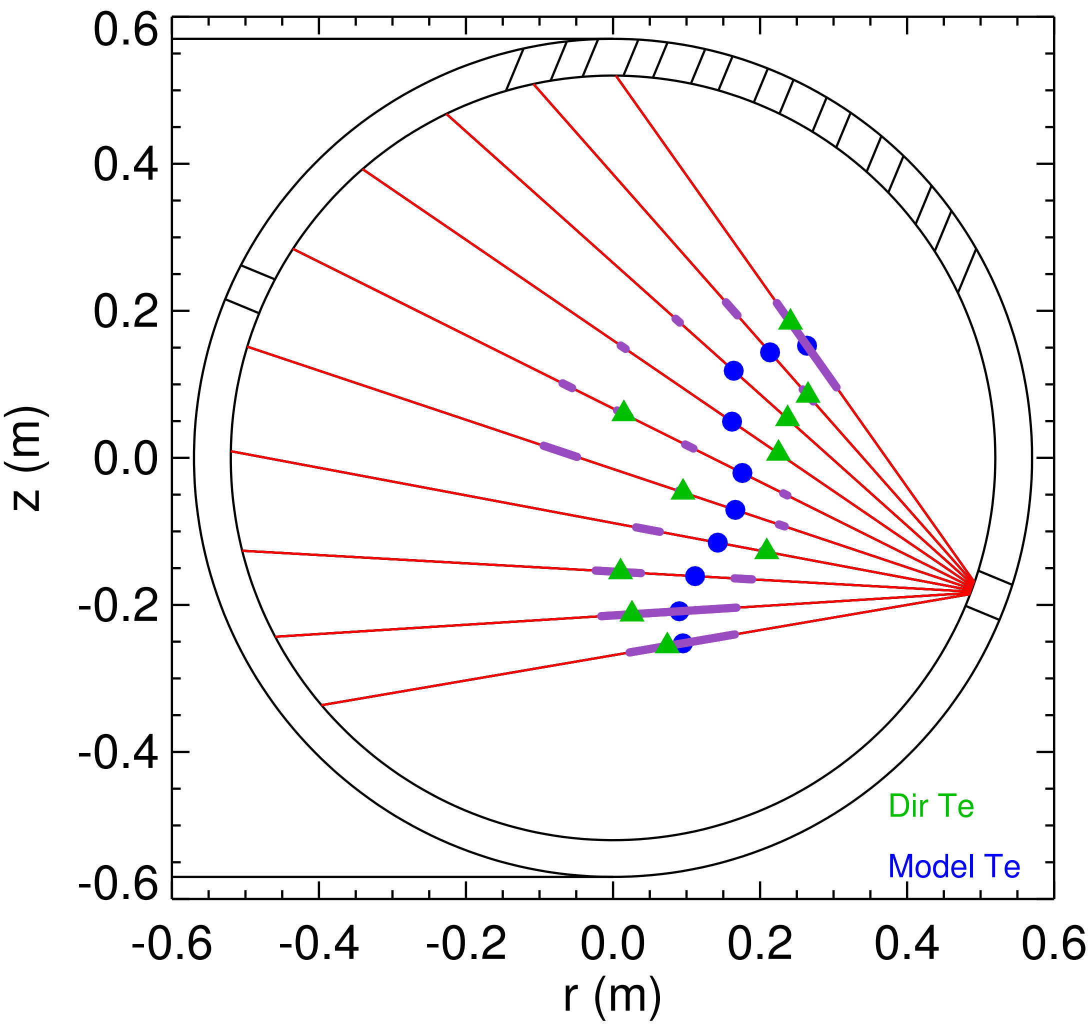

Figure 2.16: Lines-of-sight for SXR-D, showing the location of DB T_e (green triangle) as well as the actual hottest temperature along the chord (blue circle) for a plasma. In this case, the $R(T_e)$ library assumes an equilibrium plasma *apriori* while the modeled plasma has a structure. The purple regions along each chord show where the model temperature is within 1% of the direct-brightness temperature.

knowing the precise profile for T_e is just a few eV on a 1-2 keV plasma. If the plasma shifts (Δa, Δh) are not properly included, then the direct brightness temperature loses accuracy near the edge of the plasma (as the slope increases), but this effect is also less than $\sim 1\%$. The largest introduction of error occurs when an island structure is not accounted for in the $R(T_e)$ library. Figures 2.15 and 2.16 show simulations of DB T_e measured by SXR-D with a centered pinhole for plasmas with SHAx or islands, respectively, when the $T_e(R)$ model does not assume an island structure. Instead, the calculation applies the equilibrium library to the data. DB T_e is the green triangle, while the actual hottest temperature along the chord as blue circles. The purple region of each line is the portion where the temperature of the plasma is within 1% of DB T_e.

Figures 2.17 and 2.18 provide a profile view of the temperature measurement for these two cases. In the profile view it is clear that that the DB T_e is systematically lower than the actual hottest temperature along the chord by $\sim 10-15\%$. Despite the inaccuracy in amplitude, the direct-brightness temperature does accurately determine the existence and location of both types of island. Figure 2.19 show the DB T_e profiles for SHAx islands in various poloidal locations. In this plot, the black part of the profile shows the chords from SXR-C, while the cyan part of the profile shows the chords from SXR-D (both with the standard offset pinhole). The green line represents the hottest model temperature along each chord. (The profiles from the two probes do not line up perfectly because a shared impact parameter is not exactly equal to a shared plasma location). The technique is able to identify the region of the island at all angles.

For the best temperature estimate for shots of interest, an iterative process can be used. A first DB T_e calculation that assumes an equilibrium plasma will identify the

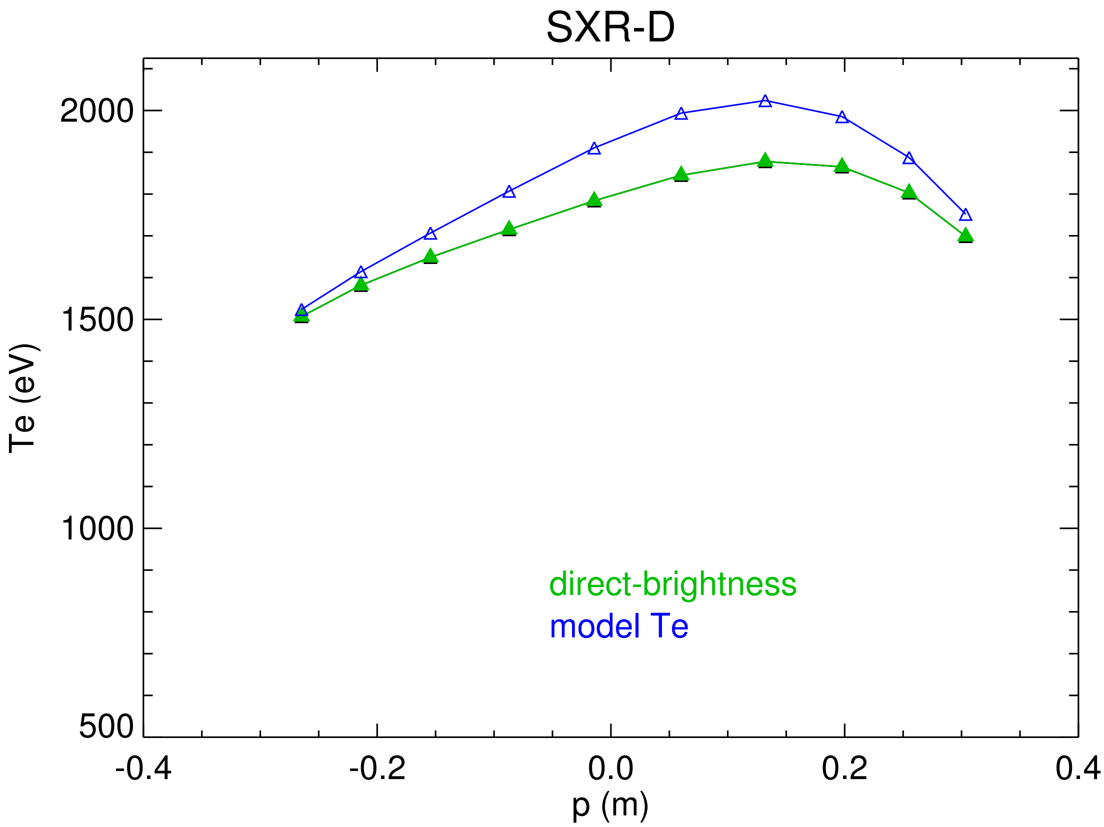

Figure 2.17: Profile of DB T_e (filled green) compared with the model T_e (unfilled blue) for SXR-D in a SHAx plasma. DB T_e (based on equilibrium model) for the SHAx structure is not quite the hottest temperature along the chord, and underestimates the actual hottest temperature by $\sim 10\%$.

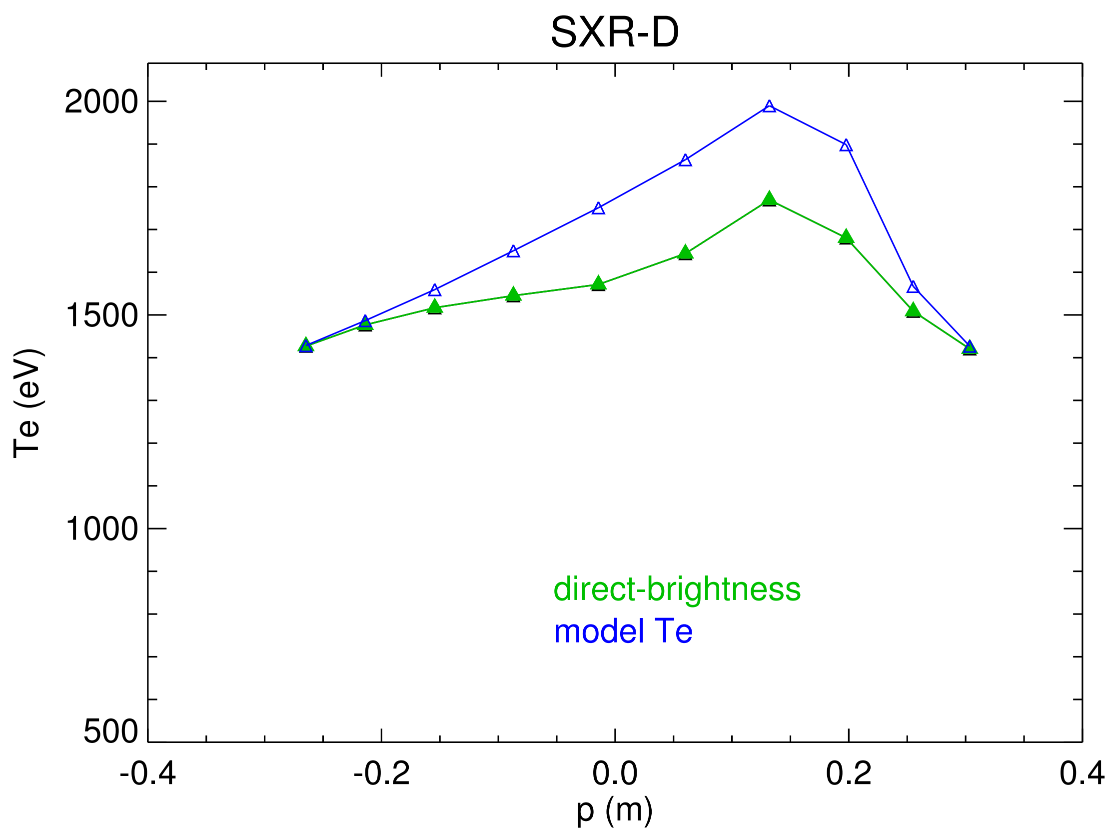

Figure 2.18: Profile of DB T_e (filled green) compared with the model T_e (unfilled blue) for SXR-D in a plasma with an island. DB T_e (based on equilibrium model) for the island is not quite the hottest temperature along the chord, and underestimates the actual hottest temperature by $\sim 15\%$.

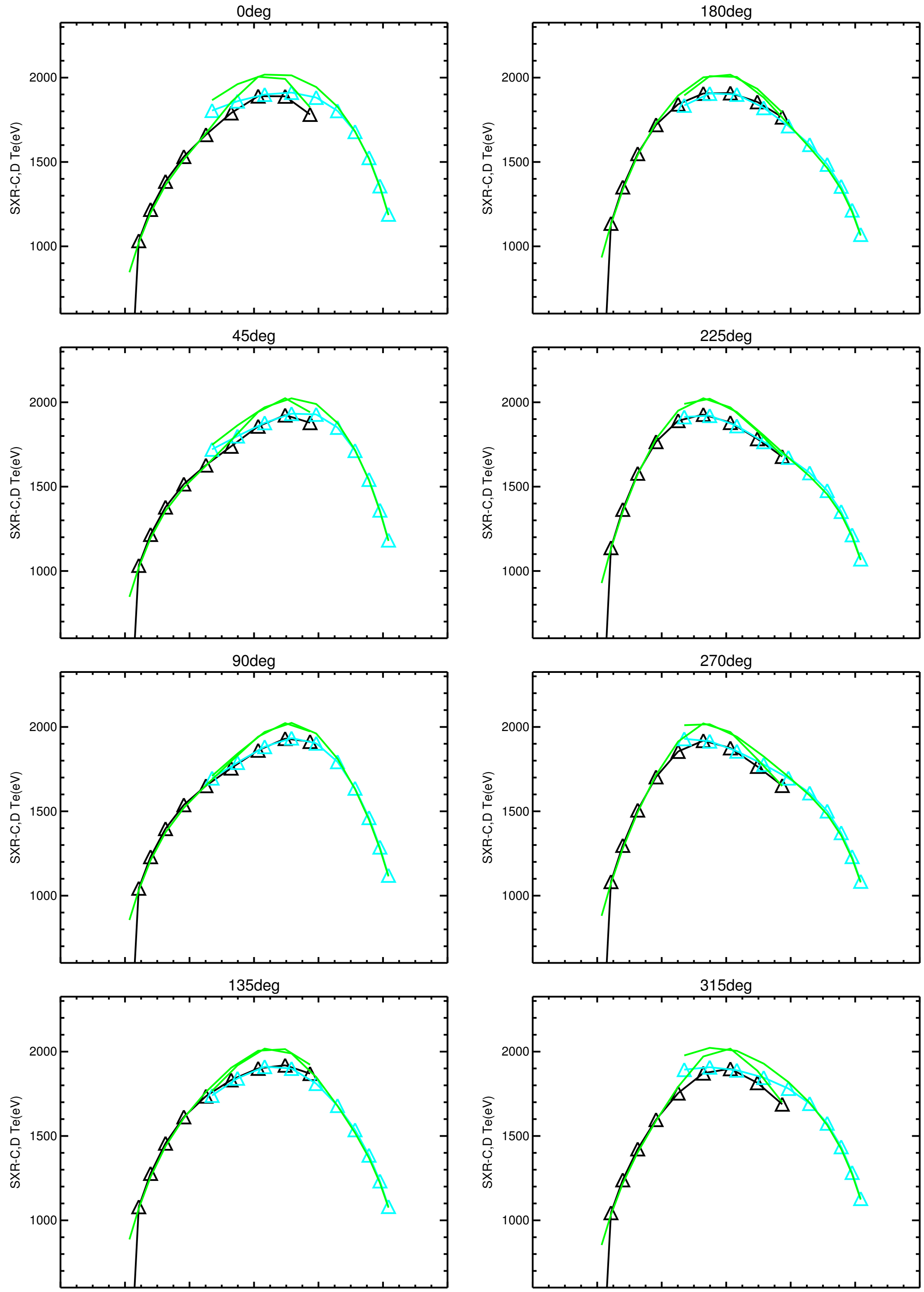

Figure 2.19: Simulated DB T_e profiles for SXR-C (black) and SXR-D (cyan) for the same SHAx plasma shown in Figure 2.17, where the $R(T_e)$ curves assume an equilibrium shape. In each plot, the poloidal location of the island is specified in the title. The green trace shows the hottest model temperature along each chord. The island is clearly shown in each measurement, although its amplitude is systematically underestimated.

existence and general location of any island. A subsequent iteration, folding an island at the same location into the model, will improve the temperature estimate. The first iteration must be done with an equilibrium library, because previous simulations have shown that applying an $R(T_e)$ library containing an island to an equilibrium plasma leads to artificial 'islands' in the calculated DB T_e. Experimental measurements from the magnetic arrays can also be used to confirm the location of island structures.

2.3.4 Direct-Brightness T_e Uncertainty Estimate

In addition to the inherent under-estimate of DB T_e due to the nature of the line-integrated measurement, there are also experimental uncertainties. There are two main sources of uncertainty: electronic noise in the measured signals ($errT_{noise}$) and systematic uncertainty due to hardware geometry and assumptions in the ratio technique ($errT_{systematic}$). The direct-brightness temperature is described as $T_e \pm errT$, where:

$$errT = errT_{noise} + errT_{systematic} \tag{2.22}$$

The uncertainty of the raw brightness measurements is taken from the electronic noise in the system. Although the data is digitized at 500 kHz, the amplifier bandwidth is substantially less than this at all gains (see Table 4.1 for the bandwidth at each gain). Therefore, the data is down-sampled to the bandwidth of the amplifier before any calculations. The uncertainty is then calculated using the standard deviation (σ) value of the electronic noise during the period just before the shot. During the plasma, there is an increase in the σ of the signal. The plasma σ is not used as the uncertainty because true variations in plasma signal should not be mistaken for noise, but it is possible that the plasma does create some additional electronic noise that is not captured in the pre-plasma σ value.

There are several small systematic sources of error due to the physical hardware design. Changing angle of incidence as a function of diode board position means that diodes at the edge will have slightly thicker effective silicon thickness. This effect creates a $\sim 3\%$ divergence between the measured and expected brightness at the edges of the diode board for a 1500 eV plasma. This effect applies to both thin and thick filter brightnesses, so the resulting T_e also varies by $\sim 3\%$ near the edge. Additionally, the beryllium foils are each measured to $\pm$ 1 μm and then are stacked (5 foils for the 421 μm filter, and 9-10 foils for 857 μm filter). Therefore, the beryllium filter thickness has an overall uncertainty of $\sim 1\%$.

Finally, the systematic uncertainty due to the n_e and T_e profile assumptions in the $R(T_e)$ introduces a discrepancy between the model and the data. In fact, these profiles vary from shot-to-shot, which introduces a discrepancy between the model and data. This uncertainty is quantified by generating simulated data with a known profile (flat versus peaked) and then applying the $R(T_e)$ library based on the opposite profile. Simulations have shown that even with an extreme mismatch between the $R(T_e)$ library profiles and the data it is being applied to, the resulting temperature is less than $\sim 1\%$ different from the simulated value.

To calculate the total error in the DB T_e, first the errors from the brightness measurements are folded into the ratio calculation, then the systematic uncertainties are added. Beginning with the thin ($S1$) and thick ($S2$) filter signals, low and high errors are defined by applying the $T_e(R)$ curves to the range of signal plus noise:

$$errT_{low} = T_e\left(\frac{S1 - \sigma_1}{S2 + \sigma_2}\right) \tag{2.23}$$

$$errT_{high} = T_e\left(\frac{S1 + \sigma_1}{S2 - \sigma_2}\right) \tag{2.24}$$

The total systematic uncertainty in the measurement, including profile variation as well as Si and Be thickness, is estimated to be $\pm 2\%$. Combining this uncertainty with the total noise in T_e from the original signals, the total error in the temperature measurement becomes:

$$T_e \pm [0.02 * T_e + 0.5 * (errT_{high} - errT_{low})] \tag{2.25}$$

In practical terms, the total uncertainty in the temperature measurement ends up being about $5 - 10\%$ in the lowest-noise cases during high-current PPCD.

2.4 Thick Filter Limitation on the Double-Foil Technique

Implementation of the double-foil technique is reliant upon the assumption that the plasma has a Maxwellian electron distribution and emits only bremsstrahlung continuum radiation in the energy range of interest. (In theory, it is possible to apply the double-foil technique to plasmas with non-bremsstrahlung contributions to the SXR emission, but only if those components have been well characterized. In practice, line and recombination radiation are dependent on the impurity density profile in addition to the electron temperature, and MST is unable to measure the full radial profile of impurity density.) On MST, the requirement of bremsstrahlung-only radiation is met by using beryllium foils to filter the measured energies. Typical impurities on MST include atmosphere-related elements such as nitrogen, oxygen, and argon, as well as material-components such as boron, carbon, and aluminum from hardware. Line radiation from low-atomic number (Z) elements is typically in the EUV energy range, below 1 keV, which is easy to block with thin Be filters. Higher Z elements such as aluminum, however, have lines in the energy range of interest for SXR diagnostics, as described in §2.1.2. To avoid this radiation, thick Be filters must be chosen, with the thinnest filter being at least 400 μm (see §5.2.1 for experimental verification of this limit).

There are two important consequences of this thick filter requirement for MST. First, thick filters mean lower general signal-to-noise, which obviously impacts the quality of the data. In practice, the minimum signal that can be converted into a measurable temperature is about 0.5 W/m^2. In fact, at this limit signals must be averaged over 0.5-1.0 ms to reduce noise to acceptable levels, reducing the effective bandwidth of the system to ∼1.0 kHz. This translates to a requirement of very hot or very dense plasma conditions on MST. Typically, these signal levels are exceeded only for 600 kA F=0 plasmas or >400 kA PPCD plasmas (with densities around $\sim 0.5 - 0.7x10^{13}cm^{-3}$) with amplifier gains of $10^7 - 10^9$. (In high-current PPCD, signal levels exceed 10 W/m^2, and temperature measurements can be made at higher effective bandwidth, >30-50 kHz). Of course, if one is interested in emissivity and SXR T_e is not required, thinner filters (i.e. 40 μm) will provide signals in standard plasmas with currents as low as 250 kA.

The second consequence of the thick filters is that the match between the shape of the ratio curve and the experimental data cannot be optimized. Figure 2.20 shows R(T_e) curves for an idealized pair of foils with 100 and 900 μm foils (top), compared with the standard set of 400 and 800 μm Be foils (bottom). In the idealized case, the thin and thick filters are chosen so that the 'elbow' of the curve is centered near the expected electron temperature, 1-2 keV. The elbow is the ideal region of the curve to be accessing because it has a fairly constant slope. In this region, a step in temperature corresponds to a similarly scaled step in ratio. Outside this region the plot becomes asymptotic, so that a very small change in one parameter leads to a very large change in the other parameter. The actual filter case of 400 and 800 μm foils illustrates this point. In the expected temperature region of 1-2 keV, the curve is already flattening out, so that very small changes in the measured ratio turn into large changes in T_e. In an ideal system, this is not a concern, but in practice this means the calculated temperature is sensitive to noise in the measured signal.

Figure 2.21 illustrates the radial variation in ratio for a typical (simulated) plasma in MST (in both a horizontal and vertical plasma cross-section). In the top case, again with the idealized filter pair of 100/900 μm, the measured ratio varies by $\sim$30% the maximum value across the profile. In contrast, for the typical 400/800 μm foils (bottom), the measured ratio only varies by $\sim$15%. The ideal 100/900 μm foils would be less sensitive to noise and would provide better temperature measurements. However, because of the Aluminum radiation lines, the minimum foil thickness on MST is 400 μm. An increase in the upper-foil thickness beyond $\sim$800 μm is also infeasible because such a thick filter would reduce the signals too much.

2.5 Conclusions

Understanding of SXR line-integrated brightness measurements are greatly aided by the use of a SXR emission model. The model creates simulations of radiation that is generated at each individual point in the plasma from electron-ion interactions. The model includes bremsstrahlung, line, and recombination radiation and can account for non-maxwellian electron distributions. The model emissivity is integrated into brightness and then used as a simulated diagnostic to study diagnostic design and measured uncertainties. Measured or simulated brightness is converted into two-dimensional emissivity using tomographic reconstruction. Reconstructed emissivity is an indirect measurement and standard estimates of uncertainty cannot be applied. Instead, the SXR emission model is used with various parameters and estimates of measured noise to provide an understanding of the uncertainty in the tomographic reconstruction.

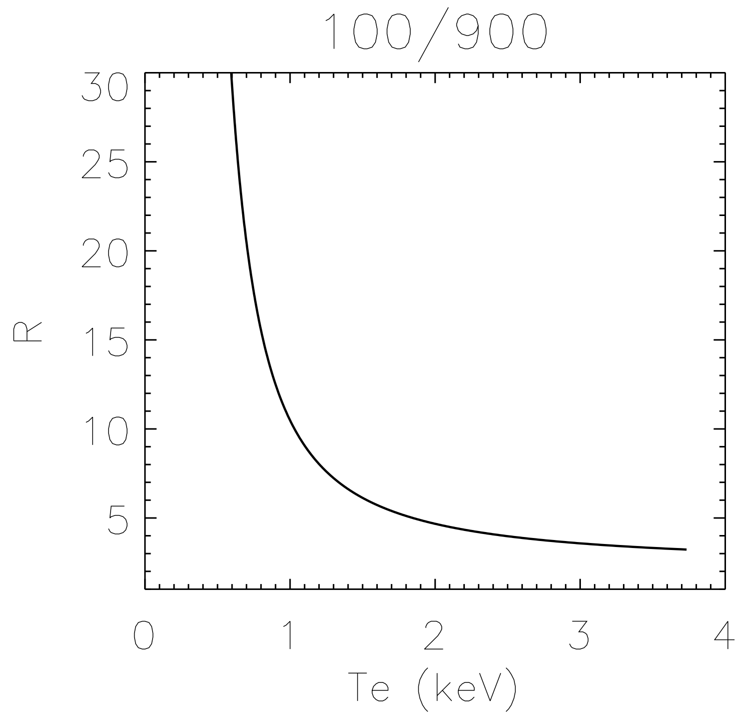

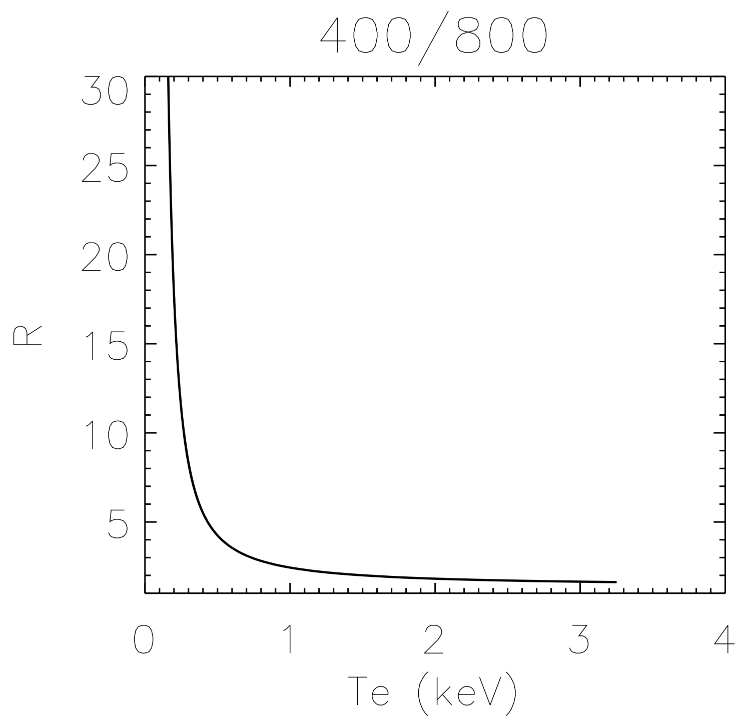

Figure 2.20: Temperature versus ratio curves for an idealized pair of 100/900 μm foils (top) compared with the curve for the typical 400/800 μm foils used on MST (bottom). The idealized foils are chosen so that the 'elbow' of the curve covers the temperature range of interest (i.e. 1-2 keV). This provides the best balance of sensitivity and stability in the calculation.

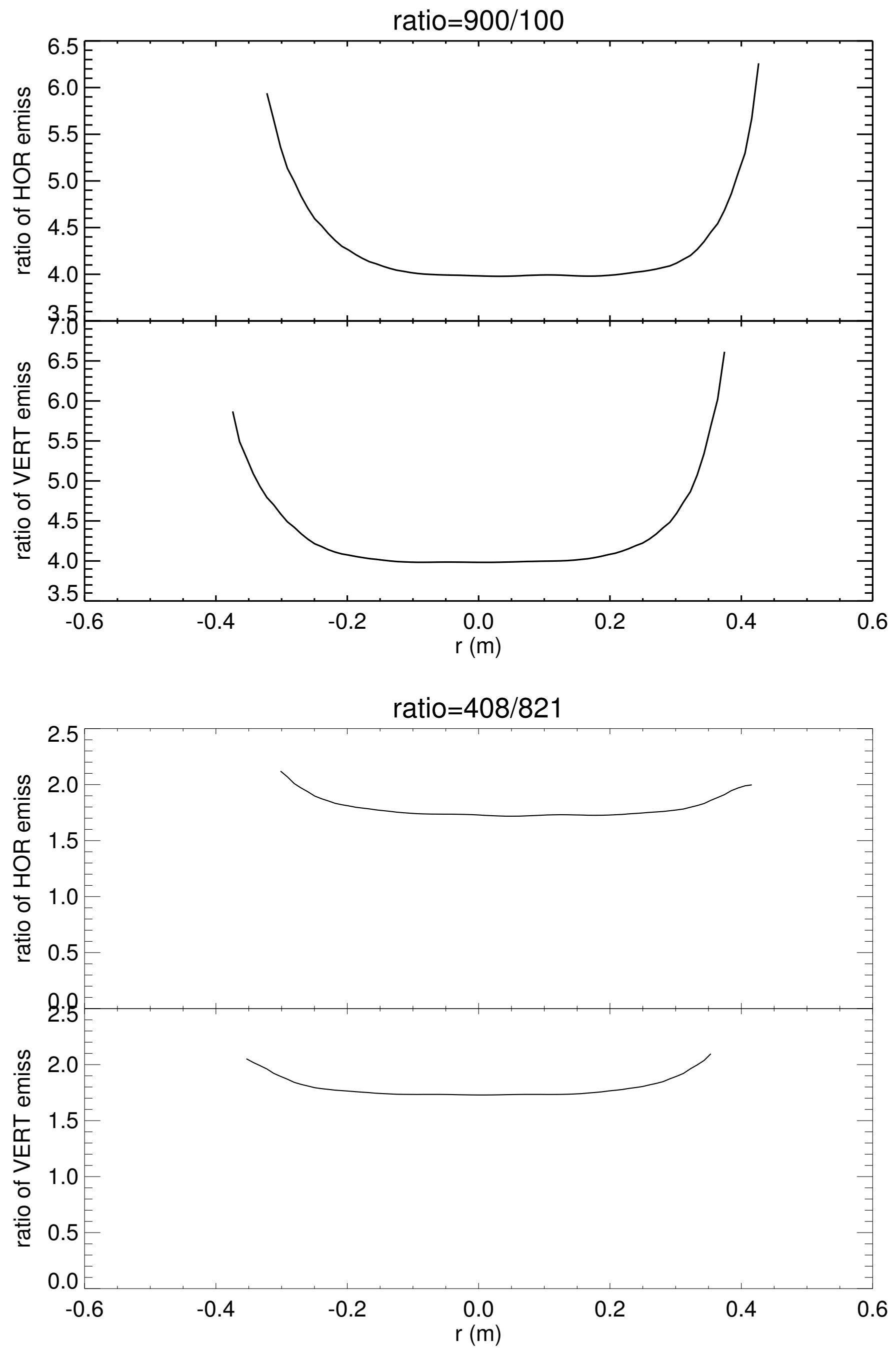

Figure 2.21: Vertical and horizontal cross-sections of the simulated ratio in the plasma for the ideal 100/900 μm filters (top) versus typical MST 400/800 μm filters (bottom). The ratio for the ideal case varies by $\sim$30% across the plasma radius, while the value for the typical MST case varies by only $\sim$15%. Unfortunately due to aluminum contamination and signal to noise constraints, the best choice for MST cannot not optimized for R vs T_e sensitivity.

SXR emission is converted to electron temperature measurements either through tomographically reconstructed emissivity or directly from the brightness measurement via the double-foil technique. Tomographic temperature is a 2D temperature map, while DB T_e are profiles of approximately the hottest temperature along each line-of-sight. In fact, the actual temperature is not well-defined. In equilibrium and SHAx plasmas, a large portion of a chord is all the same temperature. In plasmas with islands, distinct flux surfaces in the core and in the island both have the same temperature, and so there is an ambiguity about the measurement. The precision of DBT_e in non-equilibrium plasmas is improved by an iterative process in which a first fit assumes an equilibrium plasma and then islands are added into the R(T_e) curves in response to the first fit.

The double-foil technique is limited by the aluminum impurity content in MST. Aluminum impurity radiation around 1.5-2.3 keV contaminates signals if thin filters are used, so all filters on MST must be at least 400 μm thick. The thick filters reduce the overall signal levels such that the technique may only be used in hot plasmas, such as high current F=0 or PPCD conditions. The thickness is also not optimized for the ratio curve, so the technique is somewhat more sensitive to noise than in an idealized case. Despite these limitations, the technique can be used to resolve island or SHAx structures in both tomographic T_e and direct-brightness T_e.

Chapter 3

Limitations of the Previous SXR Tomography Diagnostic

A SXR tomography diagnostic was first installed on MST in 2001. Over the course of six years, the number of probes, number of detector channels, types of diodes, and types of amplifiers were optimized for SXR emissivity measurements [57, 36]. These measurements worked well and led to insights about the magnetic structure of MST plasmas. Beginning in 2006, the diagnostic was also used in 'double-foil' mode to measure electron temperature. The application of the double-foil technique to reconstructed emissivity measured core electron temperature, but was too mathematically unstable to accurately measure temperature across the full profile of the SXR emission. Investigation of this limitation led to the discovery of oscillations in the tomographic reconstruction that were too small to affect reconstructed emissivity but destabilized the temperature measurement. This Chapter describes the source of these oscillations and the fundamental limitations of the original diagnostic, which motivated development of a new SXR T_e and tomography diagnostic. Section 3.1 describes the SXR tomography diagnostic in use on MST from 2001 to 2011. §3.2 uses simulations of the diagnostic to show the oscillations that appear in the temperature calculation. Finally, §3.3 details various attempts to eliminate the oscillations and presents the best possible configuration for the 300° toroidal location.

3.1 Original Diagnostic

The SXR tomography diagnostic on MST, (in its final configuration beginning in 2007), was comprised of four individual probes located at -45°, +45°, +75°, and +165°poloidal, all at 300° toroidal. Each probe had one 20-channel photodiode array with a 35μm thick silicon base (IRD device AXUV20ELM). (Iterations of the diagnostic prior to 2006 had fewer viewing chords.) Each probe looked through a beryllium foil whose thickness could be changed depending on the specific run campaign. From 2002-2011, the beryllium foils were curved so that each diode looked through the exact same beryllium thickness. (In earlier data, the foil holders were flat, so the varying beryllium thickness depending on diode location had to be accounted for in the analysis software). A schematic of the electronics layout is shown in Figure 3.1. The electronics included the diodes inside the probe body, linear transimpedance amplifiers (TLA) to convert from current to voltage at high gain, and isolation amplifiers to separate the MST ground from the digitizer ground. The TLA had adjustable gain of $10^5, 10^6, 10^7$, while the isolation amplifiers supplied a second stage gain of 1, 2 or 5x. The amplified signals were sent to Joerger 1612 digitizers and sampled at 500 kHz. A detailed hardware description and history of the diagnostic can be found at http://paolo.franz.net/MST/.

In particular, note that the original diagnostic had individual cathode signals with a shared anode across all 20 diodes. All the cabling was coaxial, with the cathode signal on the inner wire and the anode signal on the shield. The anode signal was tied to MST ground at the diode array. The cathode and grounded anode wires used two-pin asymmetric LEMO connectors (part number FFA.0S.CLAC42) at the vacuum feedthrough (part number SWH.0S.302.CLLPV). The grounded anode was carried through the TLA and to the isolation amplifiers. The isolation amplifiers broke the ground connection between MST and the CAMAC rack, which would have otherwise created a ground loop. The CAMAC ground was supplied not through the digitizers but at a breakout panel converting from RG58 BNC to RG174 single-ended LEMO. The digitizer itself was in high-impedance differential mode, meaning that the digitizer subtracted the pin signal (cathode) from the shield signal (anode, in this case CAMAC ground). The digitizer inputs were set with standard impedance of $100k\Omega$. The main drawback to this layout is that by having all diode anodes tied to one another, an internal ground loop was created. This made the system susceptible to pickup noise.

The four probes were used in a series of configurations. The lines-of-sight for their last configuration is shown in Figure 3.2. In *tomography mode*, all four probes used the same thickness beryllium filter, enabling a 4-probe tomographic inversion. In *two-color mode*, SXR-1 and 2 were outfitted with one set of filters (typically the 'thin' filters), while SXR-3 and SXR-4 were outfitted with a different set of filters (typically the 'thick' filters). In this configuration, tomographic inversions were done separately for each pair of probes, so that the resulting emissivity maps could be converted to temperature using the double-foil technique (for details on the double-foil technique, see section §2.3). Finally, during the transition to the new T_e diagnostic, only SXR-3 and SXR-4 remained available, so a series of data was taken in *two-probe tomography* mode. This configuration had thin foils (44μm) in both probes and of course had only a single 2-probe tomographic inversion available.

The original SXR tomography diagnostic has been extremely valuable in the RFP. Tomographically reconstructed emissivity maps have provided a wealth of information about magnetic structure and evolution. Emissivity has been correlated to m=0 and m=1 magnetic fluctuations during PPCD [58]. The diagnostic has success-

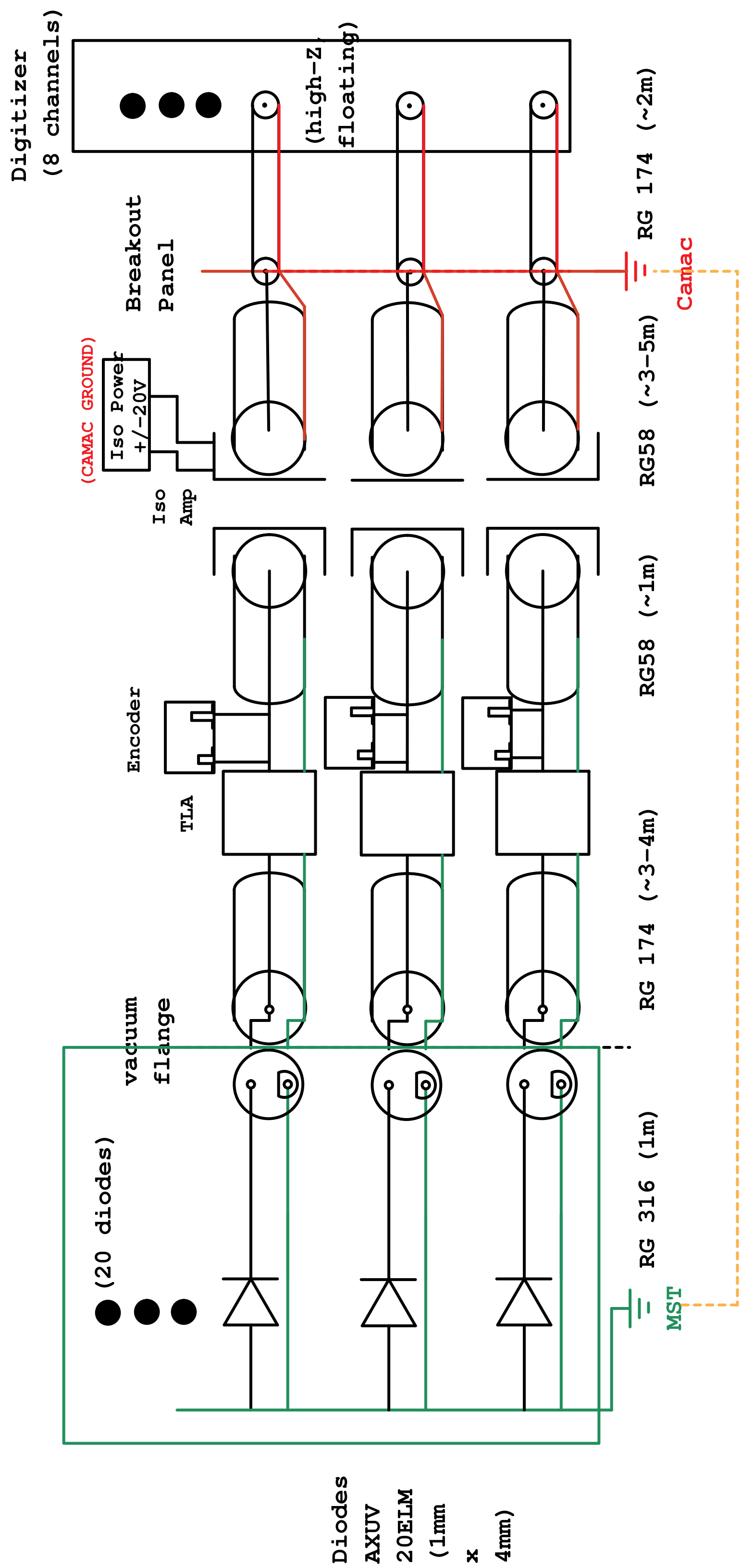

Figure 3.1: Ground layout for the SXR tomography system in use until June 2011. Note that all 20 diodes share a common anode that is tied to MST ground.

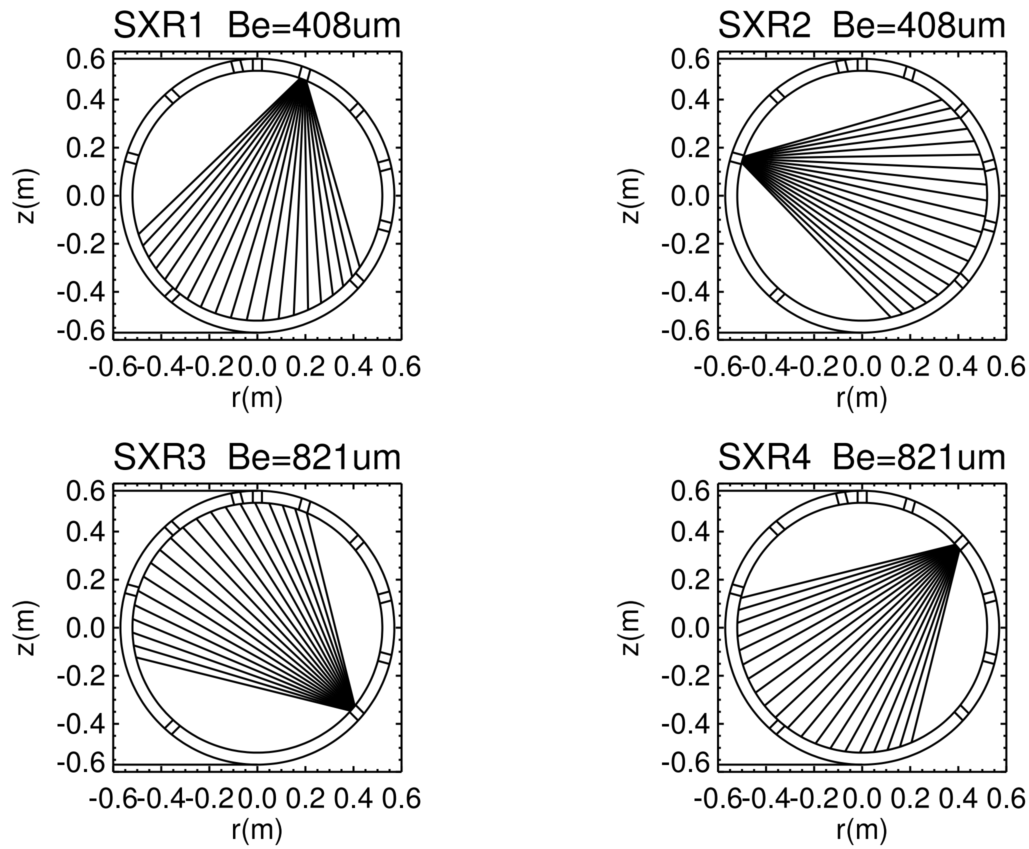

Figure 3.2: Porthole assignments and field-of-view of original diagnostic from 2008-2011, at 300° toroidal. Each probe is labeled with its name and the thickness of beryllium foil used in the simulations throughout this Chapter.

fully measured multiple magnetic islands in the core during PPCD [59]. Quasi-single helicity structures have also been identified and studied during standard discharges [49]. Most recently, the SXR tomography diagnostic has helped to identify plasmas containing a single helical axis (or SHAx) [16]. Tomographic reconstruction from soft x-ray emission is a reliable and highly successful means of accessing the internal dynamics of the plasma.

3.2 Limitation As a Temperature Diagnostic

Attempts were made to extend the capabilities of the original SXR tomography diagnostic to include electron temperature measurements. Applying the two-color technique to the tomographically reconstructed emissivity, the temperature in the core of the plasma was measured for a high current PPCD plasma in 2006 [37]. However, attempts to apply the technique more widely were unsuccessful. Outside the core region of the plasma, oscillating structures were frequently seen that did not seem physical. Figure 3.3 shows the measured brightness profiles for a 500kA PPCD plasma. The black triangles are the measured values for SXR-1 and SXR-3, while the blue triangles are the measured values for SXR-2 and SXR-4. The emissivity calculated from tomographic reconstruction has been integrated along each line-of-sight to create a reconstructed brightness. This serves as a check on the quality of the reconstruction. Here, the reconstructed brightnesses are shown as green dots. Figure 3.4 shows that the reconstructed emissivities are not smooth. The variation can be seen in the reconstructed brightness as very small deviations from the measured brightness, on the scale of expected SXR noise level. The tomographically reconstructed temperature is shown in Figure 3.5. The full tomographic T_e is a 2D map like emissivity. The profile view is created by plotting the T_e calculated for each point in the vessel along a vertical line from the bottom to the top (mid-cylinder) at the geometric center.

The T_e profile clearly shows structure across the plasma. Unfortunately, this structure is likely an artifact of the variations in emissivity because the characteristic electron temperature profile for a PPCD plasma is quite flat. With variation at this level, it is impossible to know whether a true plasma structure is being identified.

By investigating this phenomenon through simulations with the SXR model, it was found that the oscillations were an artifact of the tomographic temperature method. Figures 3.6-3.9 demonstrate the origin of these oscillations using simulated equilibrium plasma with flat temperature ($\alpha = 4.5$) and density ($\gamma = 4.0$) profiles. (Refer to section 2.1.1 for a description of modeled profile power-law parameters α and γ.) Figure 3.6 shows the simulated brightness profile (black diamonds), along with the brightness calculated from the tomographically reconstructed emissivity (green dots) for each probe. Figure 3.7 shows the reconstructed emissivity for each pair of probes. There is no evidence of oscillations in the emissivity map, and the reconstructed brightness matches the simulated brightness very well.

However, closer inspection of the simulated data reveals troubling features. Figure 3.8 plots cross-sections of the emissivity map from Figure 3.7. For each point along a line drawn through the vacuum vessel, the value of the emissivity is plotted. The top plot shows a horizontal cross-section (i.e. the outboard midplane) for the emissivity. The reconstructed emissivity from SXR-1 and SXR-2 is shown in black, while the reconstructed emissivity from SXR-3 and SXR-4 is shown in red. For comparison, the emissivity used in the original model (before any reconstructions) is also plotted. Blue is the model emissivity through the thin filters (SXR-1, SXR-2), and green is the model emissivity through thick filters (SXR-3, SXR-4). The bottom plot shows the same set of data, but for a vertical cross-section (mid-cylinder). Comparing the model emissivity to the tomographic reconstruction, discrepancies are seen. There are small

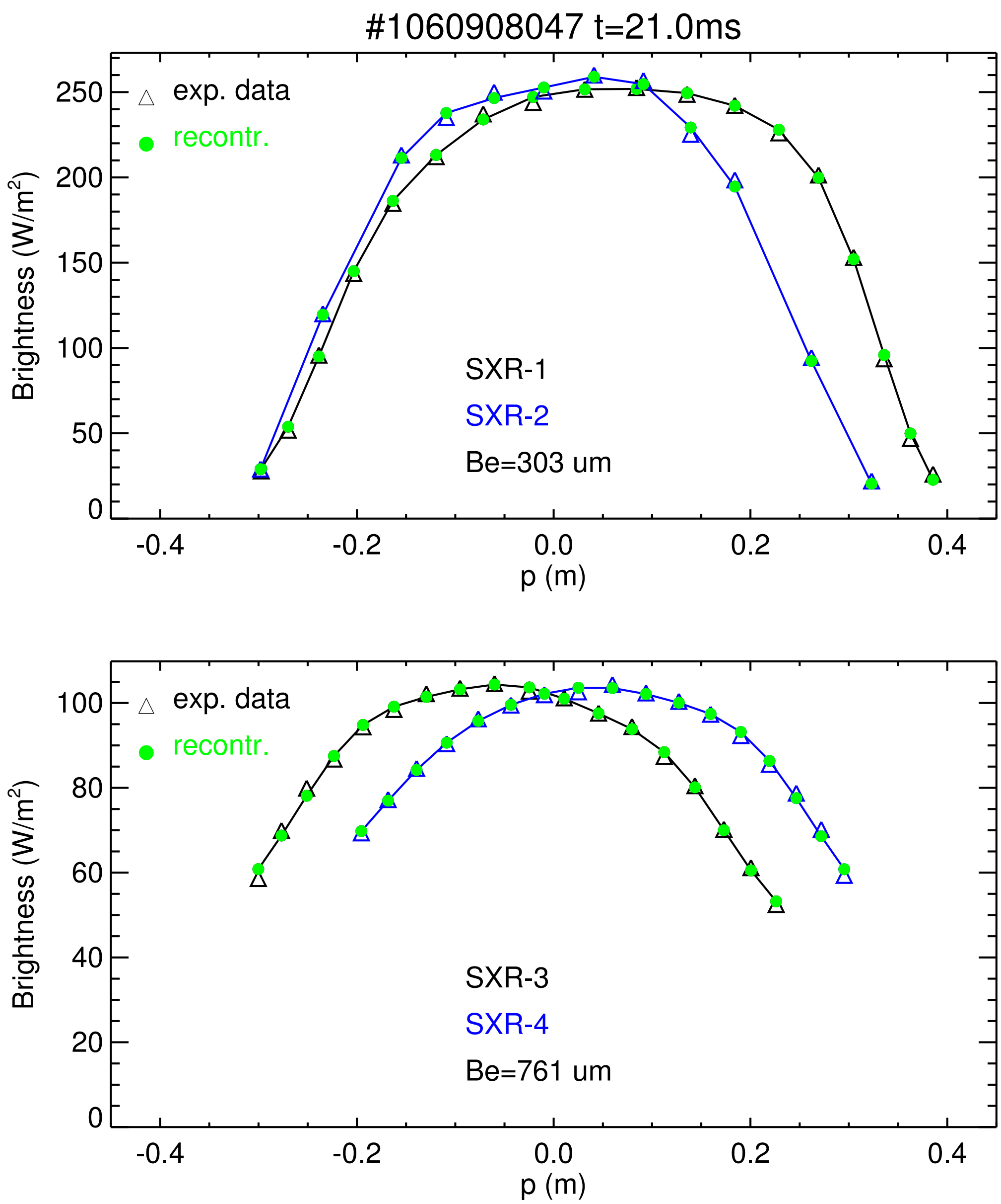

Figure 3.3: Measured brightness for SXR-1,3 (black) and SXR-2,4 (blue) in triangles. Overlaid circles (green) are the brightnesses calculated by integrating tomographically reconstructed emissivity along the line-of-sight. In this shot, SXR-1,2 use a 331 μm Be foil, while SXR-3,4 use a 706μm foil. There are small discrepancies in the reconstruction due to noise in the measured signals. (The shot number and time are recorded in the title.)

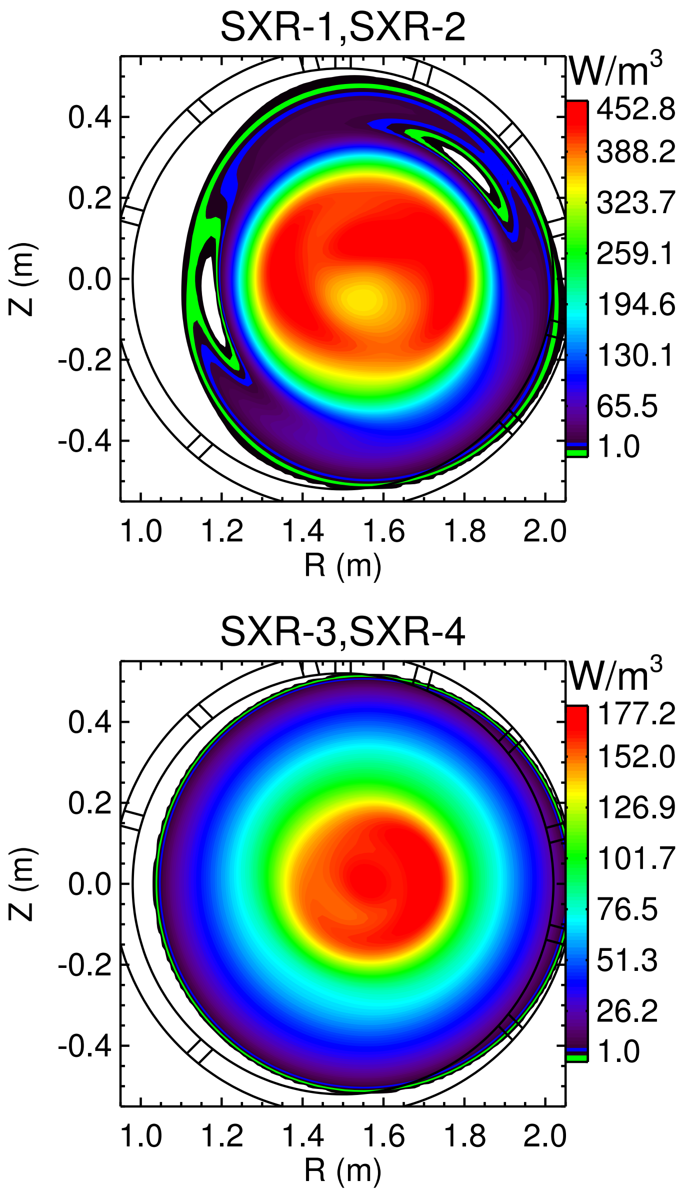

Figure 3.4: Reconstructed emissivities for shot 1060908047 thin filter probes (top), and thick filter probes (bottom). The reconstructions have some variation due to noise in the measured signal.

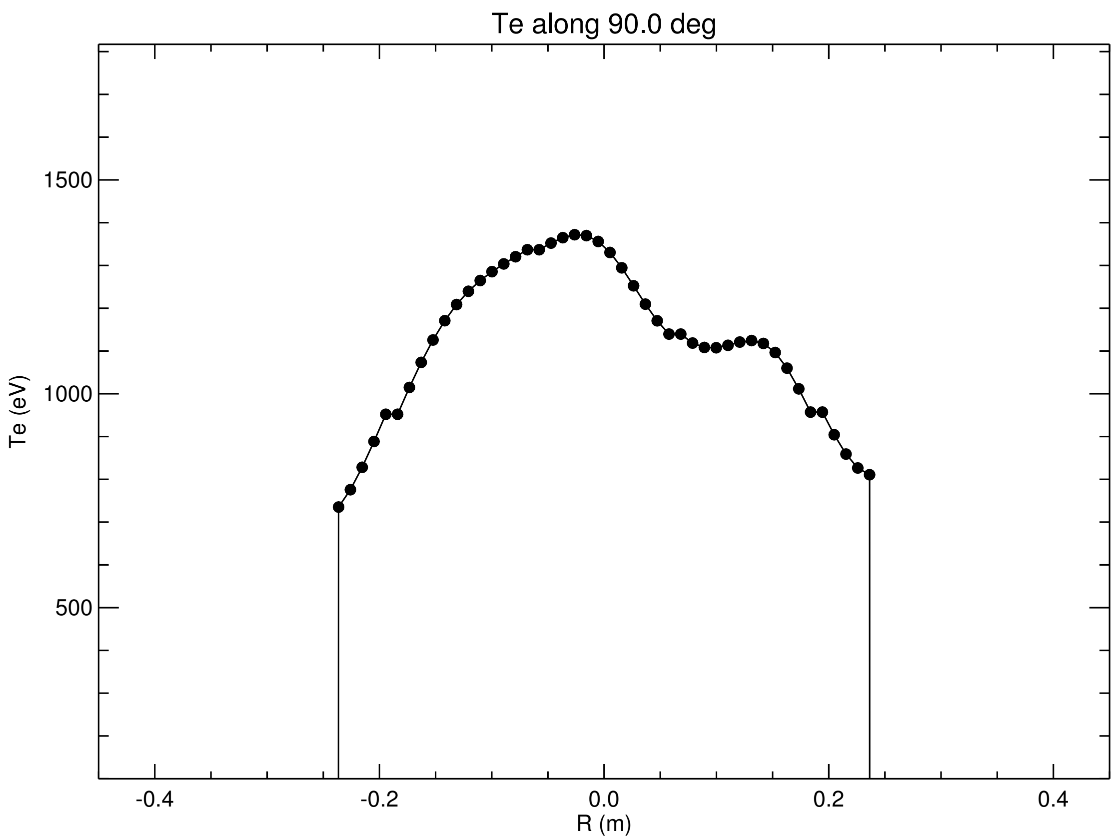

Figure 3.5: Tomographic temperature calculated from the ratio of the emissivities in Figure 3.4. The full tomographic T_e is a 2D map like emissivity, while the profile is created by plotting the T_e calculated for each point in the vessel along a vertical line from the bottom to the top (i.e. 90° from the outboard midplane).

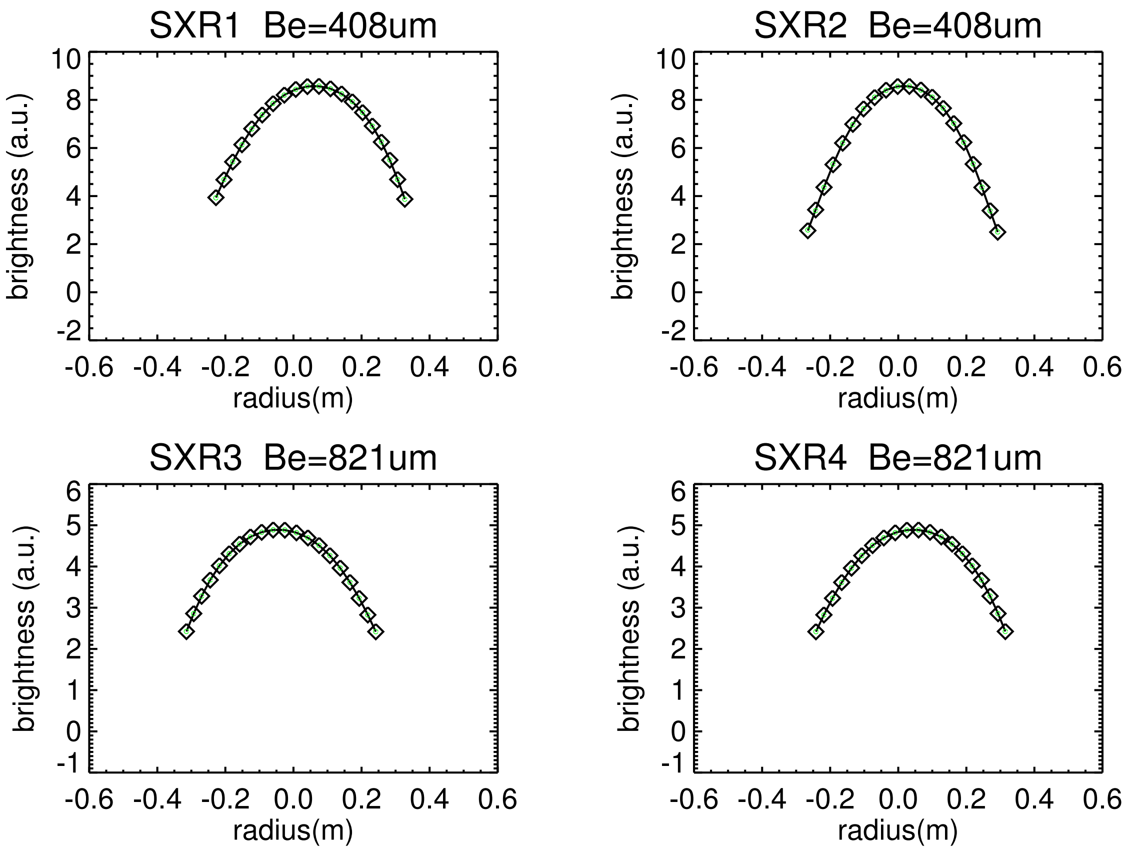

Figure 3.6: The modeled brightness profile (black diamonds) compared to the line integration of tomographically reconstructed emissivity (green dots). In this simulation, SXR-1,2 have 408μm Be filters, while SXR-3,4 have 821μm filters. Note that the field-of-view of the detectors is narrow and leaves large regions unmeasured near the edge of the plasma.

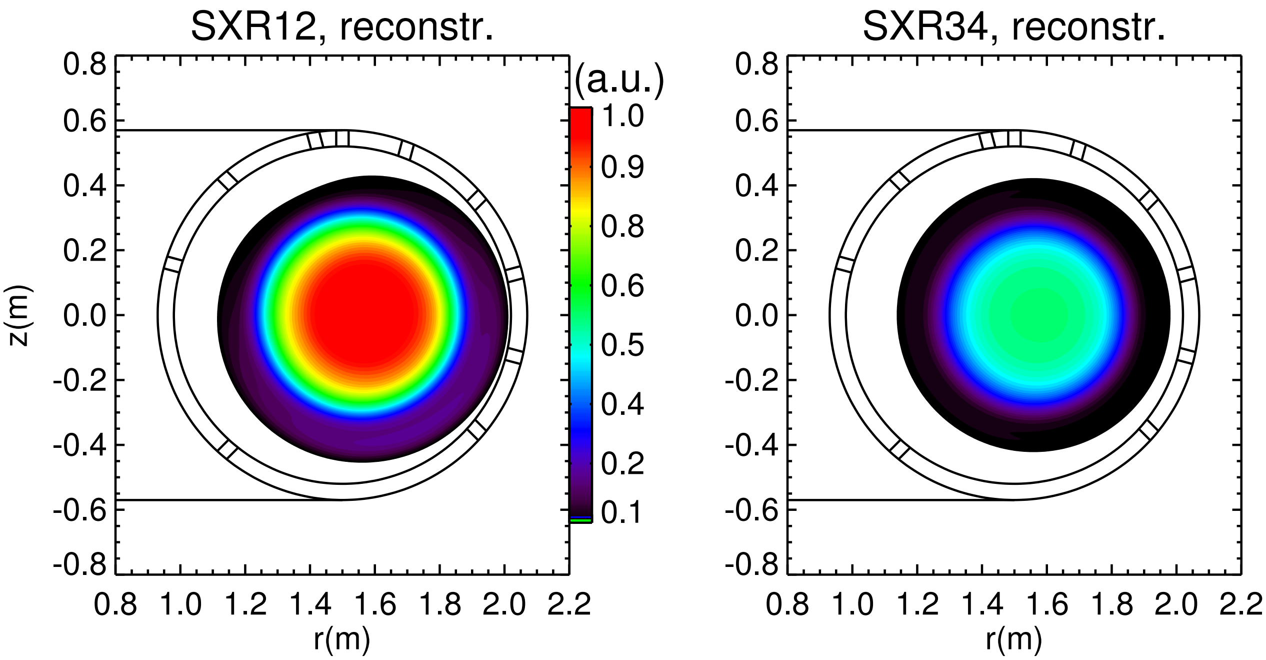

Figure 3.7: Tomographically reconstructed emissivities of the brightness modeled in Figure 3.6 using SXR-1,2 (left) and SXR-3,4 (right) to determine the measured plasma emissivity as seen through thin and thick Be filters, respectively. The intensity scale is normalized to the maximum value of the thin filter. The contour plot, like the reconstructed brightness, seem to match the modeled data well.

oscillations in the reconstruction in the core region, and there are large discrepancies at the edge.

Figure 3.9 is a profile of the tomographic temperature. Tomographic temperature (in black) is found by calculating the ratio of the thin-foil emissivity to the thick-foil emissivity at every point in the 2D emissivity map. The ratio is then converted into temperature using the calculated $T_e(R)$ curves (for details on the T_e calculation, see section §2.3). Like the emissivity plots previously, here a profile of the reconstructed temperature along a horizontal cross-section in the plasma is shown for clarity. The temperature profile used by the model input into this simulation is shown in green. A comparison of the model to the reconstruction again shows large discrepancies near the edges of the plasma. More concerning however, is that the oscillations have propagated into the core region of the plasma, where the model and reconstructed emissivity matched almost perfectly.

Why does the temperature profile have so much structure, when the reconstructed brightness profile (Figure 3.6) looks smooth? The answer lies in the lack of viewing chords near the edge of the plasma. As will be shown in the following sections, if the brightness profile is not sampled all the way to zero, then its shape is not well-constrained. If there is insufficient data at the edge of the plasma, the reconstruction is free to create any (non-physical) shape necessary in that region such that the line-integrated brightness remains true to the data. This problem is not apparent in the emissivity contours (Figure 3.7) because the error in the Cormack-Bessel reconstruction is very small. However, this deviation from the model can be seen if emissivity is viewed as a cross-section. The oscillations are then greatly amplified in the tomographic temperature because the temperature is calculated by taking the ratio of the two emissivities. As a result, the oscillations in emissivity SXR-1,2 multiply

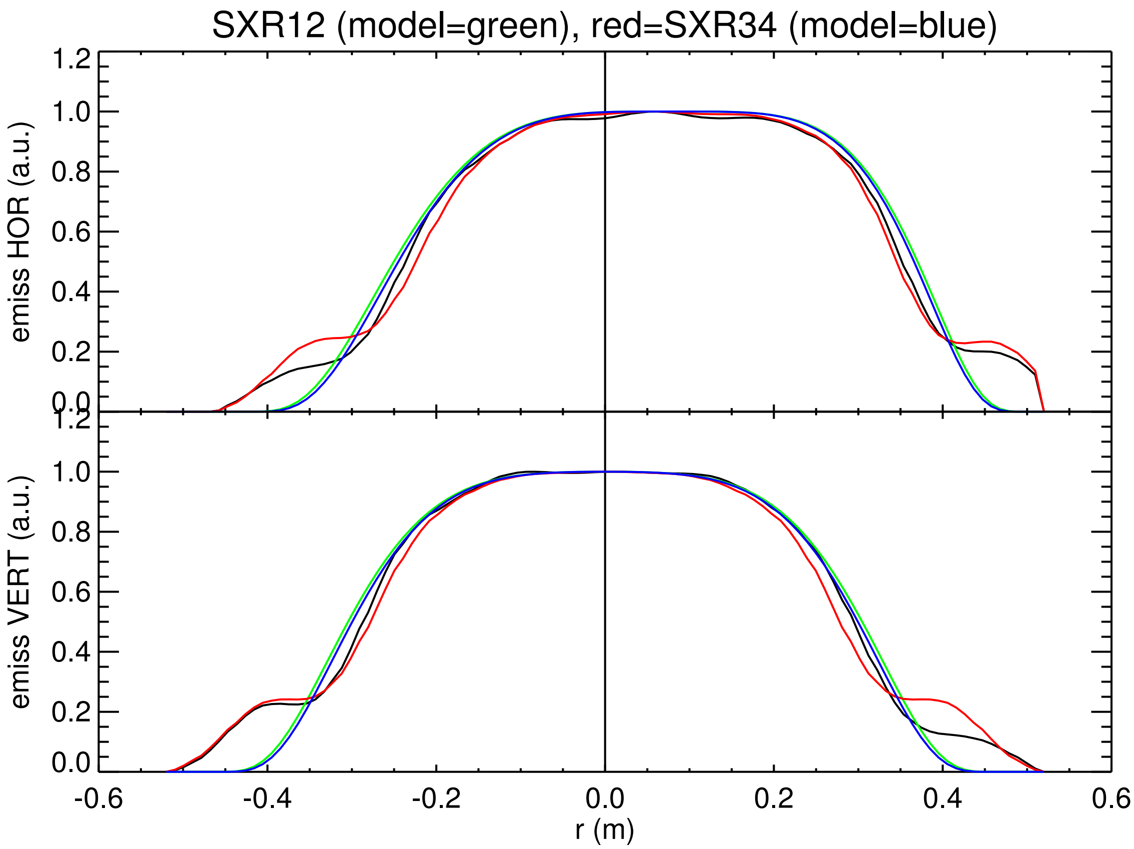

Figure 3.8: Horizontal (top) and vertical (bottom) cross-sections of the reconstructed emissivity from the modeled case in Figure 3.6. In each plot, the emissivity input into the model for the thin filter is green, while the model emissivity through the thick filter is blue. The tomographically reconstruction of SXR-1,2 results in the 'measured' emissivity plotted in black, and the 'measured' emissivity for SXR-3,4, normalized to the thin filter maximum, is shown in red. The model and reconstruction deviate near the edge of the plasma where the brightness profile is not well-defined.

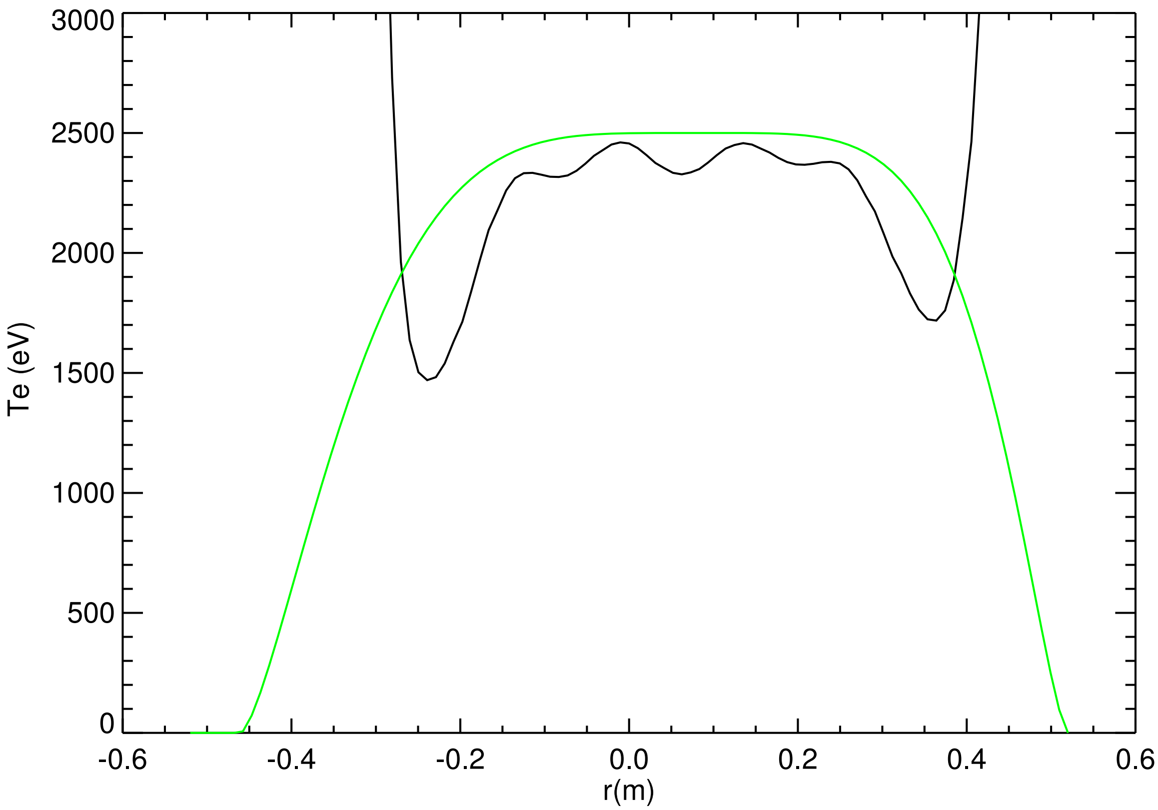

Figure 3.9: A cross-section of the tomographic temperature for this simulation. The full tomographic temperature is a 2D map like emissivity. For clarity, a horizontal cross-section of this reconstructed temperature is plotted in black. The temperature profile defined by the model input in the simulation is plotted in green. As with the emissivity cross-section, discrepancies are clearly seen near the edge of the plasma. A bigger problem is that this instability has propagated into the core of the plasma, creating artifacts on the same scale as potential magnetic structures.

with the oscillations from emissivity SXR-3,4, completely undermining the integrity of the tomographic temperature.

3.3 Attempts to Eliminate Oscillations

An obvious explanation for a tomographic reconstruction containing artifacts is the geometry of the system. Too few chords or too few poloidal probe positions will result in poorly constrained reconstructions, leading to artifacts. A comparison to the well-behaved SXR tomography system at RFX led to some insights [56]. Figures 3.10-3.12 show the field-of-view, brightness profile, and reconstructed emissivity cross-section for the same simulated plasma shown in Figures 3.6-3.9, but in RFX. Although the RFX device is not setup to make a 2D tomographic temperature measurement, it does produce 2D tomographic emissivity reconstructions, which are sufficient to predict oscillations in a temperature profile. The main difference between the SXR diagnostic at RFX-mod and the one at MST is the viewing coverage near the edges of the plasma. Specifically, RFX has chords that view all the way to zero x-ray emission. This creates a well-defined brightness profile with a constrained slope to zero, unlike on MST. The benefit to this field-of-view is clearly seen in Figure 3.12. Plasma coverage in the radial direction (accessed by the 'VERT' probes) completely covers the plasma to out to zero brightness signal. Correspondingly, the horizontal reconstructed emissivity profile (green) matches the modeled emissivity (black) almost perfectly. Plasma coverage in the Z direction (accessed by the 'HOR' probe) on the other hand, does not quite go to zero brightness. Although this does create a slight mismatch between model and reconstruction in the vertical profile, it is much smaller than the mismatch on MST. In fact, the increasing mismatch with reduced edge coverage as seen between RFX and MST suggests that this is the source of oscillations in T_e.

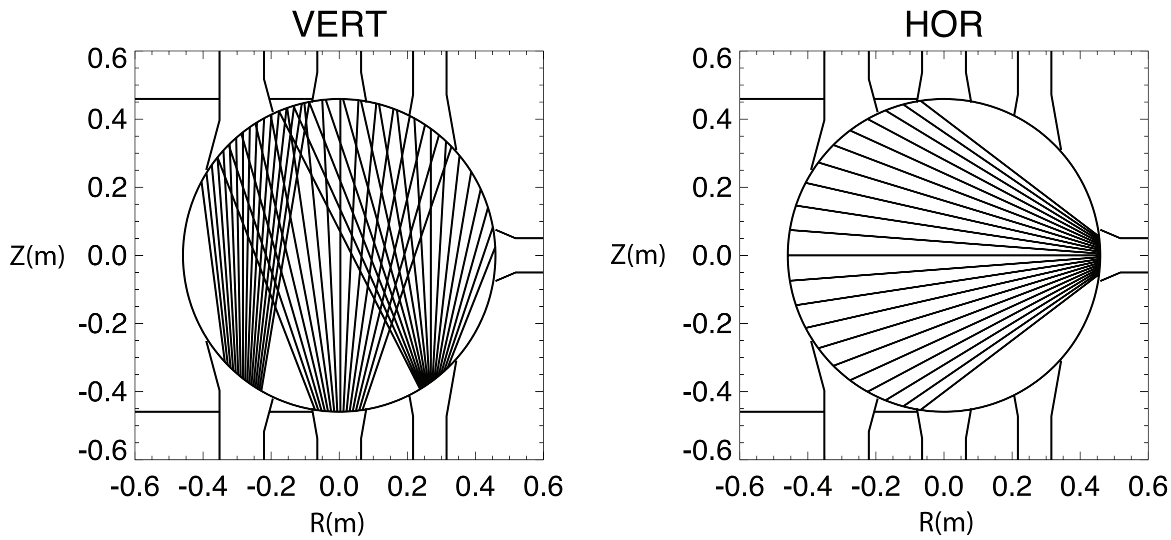

Figure 3.10: Field-of-view for the SXR tomography diagnostic on RFX-mod. Unlike the original diagnostic on MST, the RFX design includes good coverage at the edge of the plasma.

3.3.1 Null Chords

Given the insight that brightness needs to be measured to the edge, fake chords outside the viewing region were added to the simulation to see if the oscillation could be addressed without modifying the hardware. Four null chords were placed on each side of the profile with zero emission, and a fifth chord was placed halfway between the null chord and first real chord in impact parameter, with a value determined by the slope between these two points. The results of this test can be seen in Figures 3.13-3.15. Comparing the shape of the brightness profile in 3.13 to that in the well-sampled RFX simulation (3.11) suggests that this solution will not be effective. The profile as defined in this simple model has a very different slope near the edge compared to the true brightness profile. As expected, the null-chord is not sufficient to properly constrain the reconstruction, and oscillations persist in the emissivity and temperature profiles (Figures 3.14-3.15).

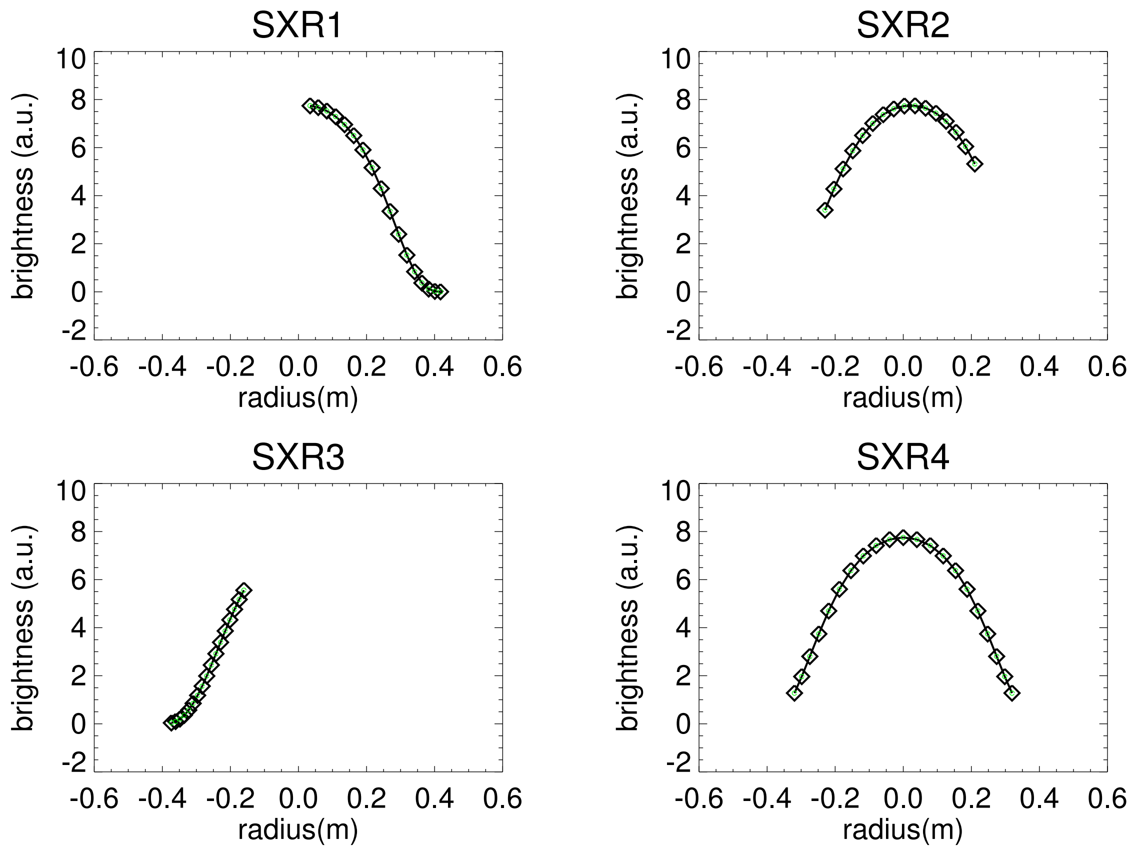

Figure 3.11: Simulated brightness profile (diamonds) compared to tomographic reconstruction of the simulation (dots) for the RFX diagnostic. SXR-1 represents the right-most vertical probe, and the remaining probes are numbered in clockwise order from there. Notice that the combined vertical brightness profile is defined all the way to zero signal, and the vertical brightness profile is nearly defined all the way to zero.

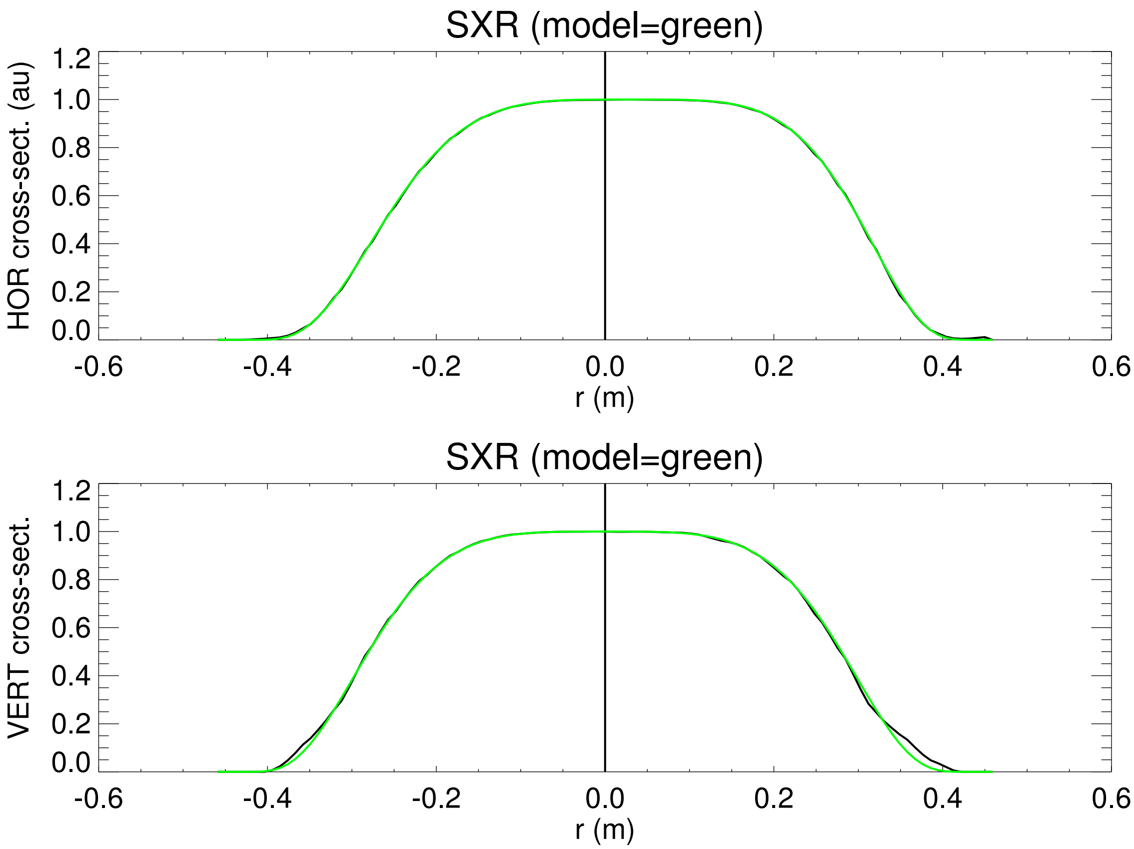

Figure 3.12: Cross-sections (black) of the tomographically reconstructed emissivity for the plasma using the RFX diagnostic, normalized to the thin filter maximum. As with the MST simulation, the cross-section is calculated from the full 2D tomographic emissivity by plotting the emissivity values along a horizontal (top) or vertical (bottom) line through the plasma. Green shows the emissivity defined in the model for the same points. Reconstructed emissivity on RFX-mod does not suffer from oscillations due to the well-defined slope of the brightness profile at the edge of the plasma.

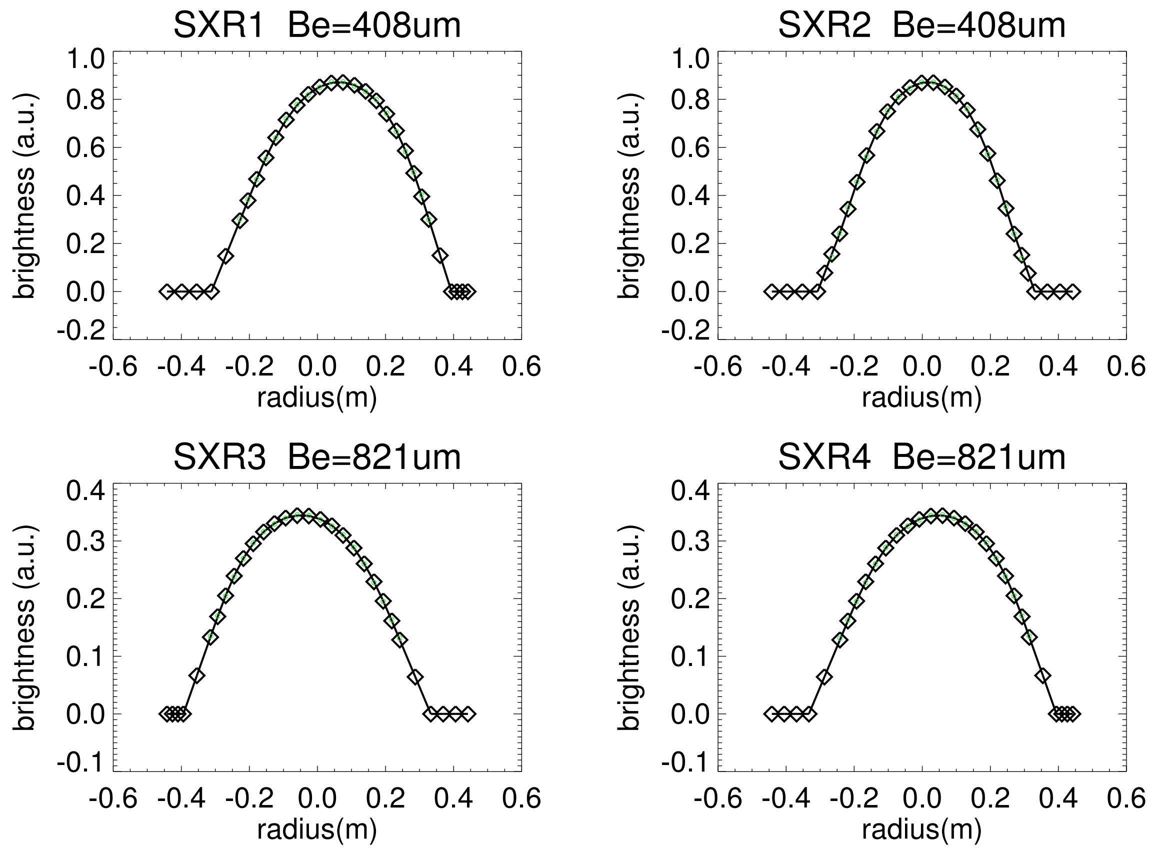

Figure 3.13: Simulated brightness profile (black) for the MST diagnostic with the addition of 5 null chords on each side of the field-of-view. Four of the null chords are defined to measure zero emission, and the fifth null chord is given a value half way between zero and the brightness of the first regular line-of-sight. The reconstructed brightness for actual lines of sight is shown in green. This simulation created a well-defined region of zero-brightness, but the profile shape is not consistent with that of a real plasma.

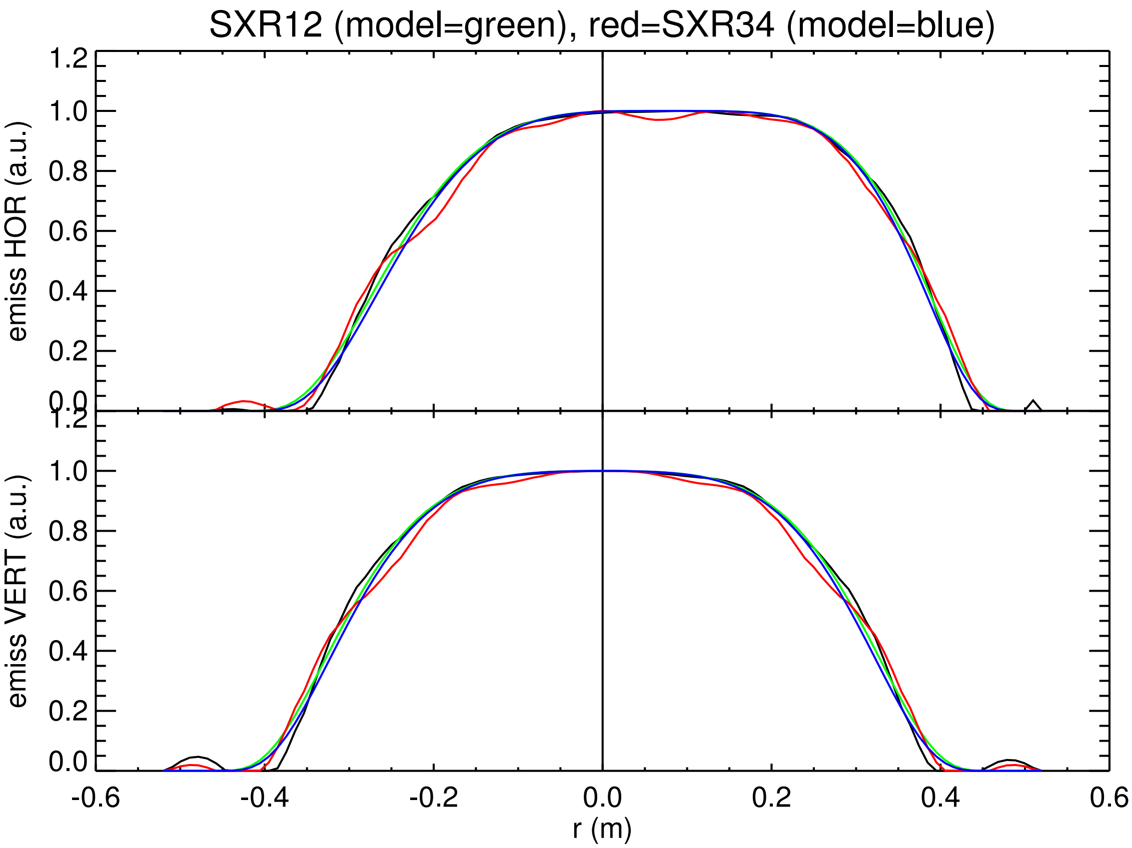

Figure 3.14: Horizontal (top) and vertical (bottom) cross-sections of the reconstructed emissivity, with the addition of the null chords. In each plot, the emissivity input into the model for the thin filter is green, while the model emissivity through the thick filter is blue. The tomographically reconstruction of SXR-1,2 results in the 'measured' emissivity plotted in black, and the 'measured' emissivity for SXR-3,4 is shown in red. The model and reconstruction match better at the edge of the plasma with the null chords, but substantial oscillations are seen in the core region. This is likely due to the reconstruction having difficulty matching the non-physical shape of the brightness profile.

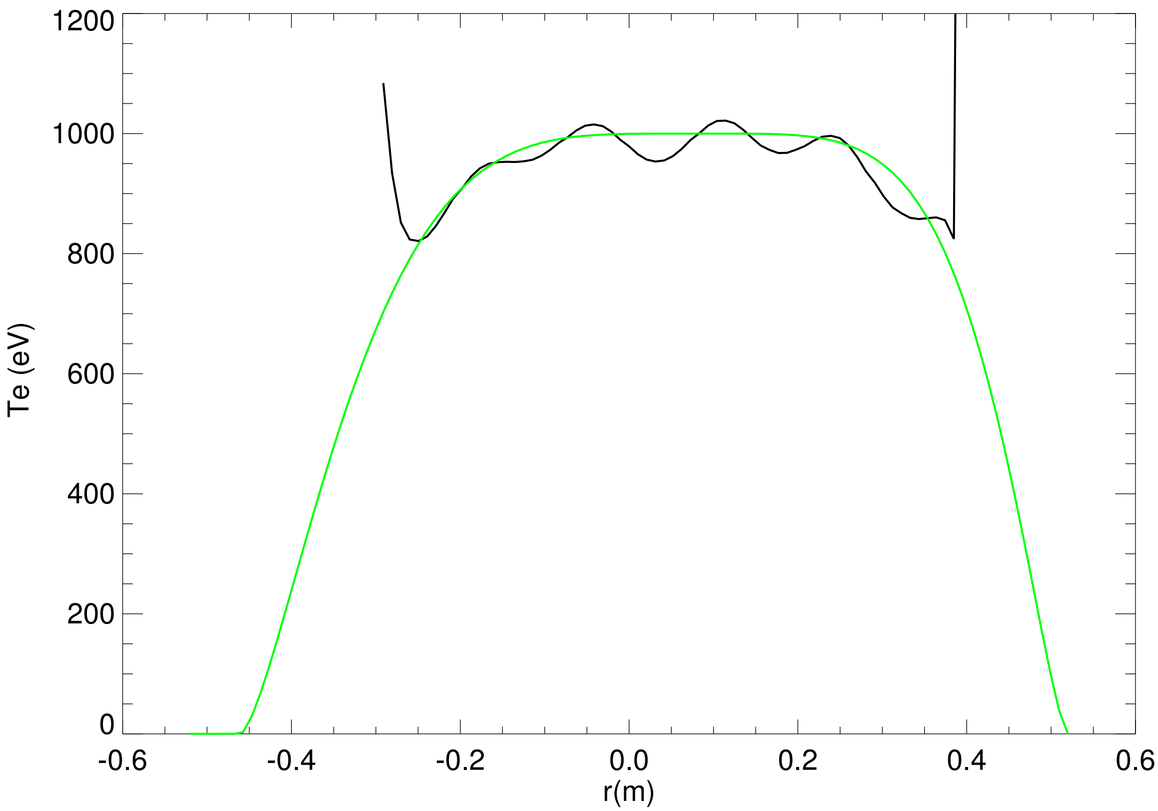

Figure 3.15: A horizontal cross-section of the tomographic temperature for the simulation including null chords. The temperature profile defined by the model input in the simulation is plotted in green. Again, discrepancies are clearly seen both near the edge of the plasma and in the core region.

3.3.2 Increased Sampling

Simulations were run to investigate both the effect of increasing the number of chords in each probe (improving the spatial resolution) and also increasing the total number of probes at this toroidal location (improving the angular sampling coverage). Figure 3.16 shows the layout for a simulation where the number of chords was tripled in each probe over the same angular extent, with existing chords in red and added chords in black. Figure 3.17 shows another simulated geometry where the total number of probes was increased from four to eight, maintaining a total of 20 chords per probe. The original probes are at 45°, 75°, 165°, and 315° poloidal, while the additional probes are at 15°, 105°, 135°, and 225° poloidal. Neither of these two simulations eliminated oscillations, indicating that the tomographic reconstruction is not under-specified.

3.3.3 Extending the Field-of-View

As expected, the largest reduction in oscillations came by extending the field-of-view of the diodes so that the brightness profile is well-sampled all the way to zero brightness. Figure 3.18 shows the geometry for which the oscillations were nearly eliminated in equilibrium plasmas. The quality of the reconstruction was stable for many temperature profiles ranging from quite narrow to very broad ($\alpha = 1.5 - 6.0$).

The best geometry configuration at 300°, with extended viewing angle, provides excellent tomographic reconstruction of emissivity and temperature in equilibrium plasmas. This configuration features a pinhole-to-diode distance of 8mm (rather than the original distance of 15mm) to widen the field-of-view, and has SXR-1,2 (thin filter) at 75 and 165°P, while SXR-3, 4 (thick filter) are located at 45, 105°P. Figures 3.19 - 3.21 show the brightness profiles, reconstructed emissivity cross-sections, and

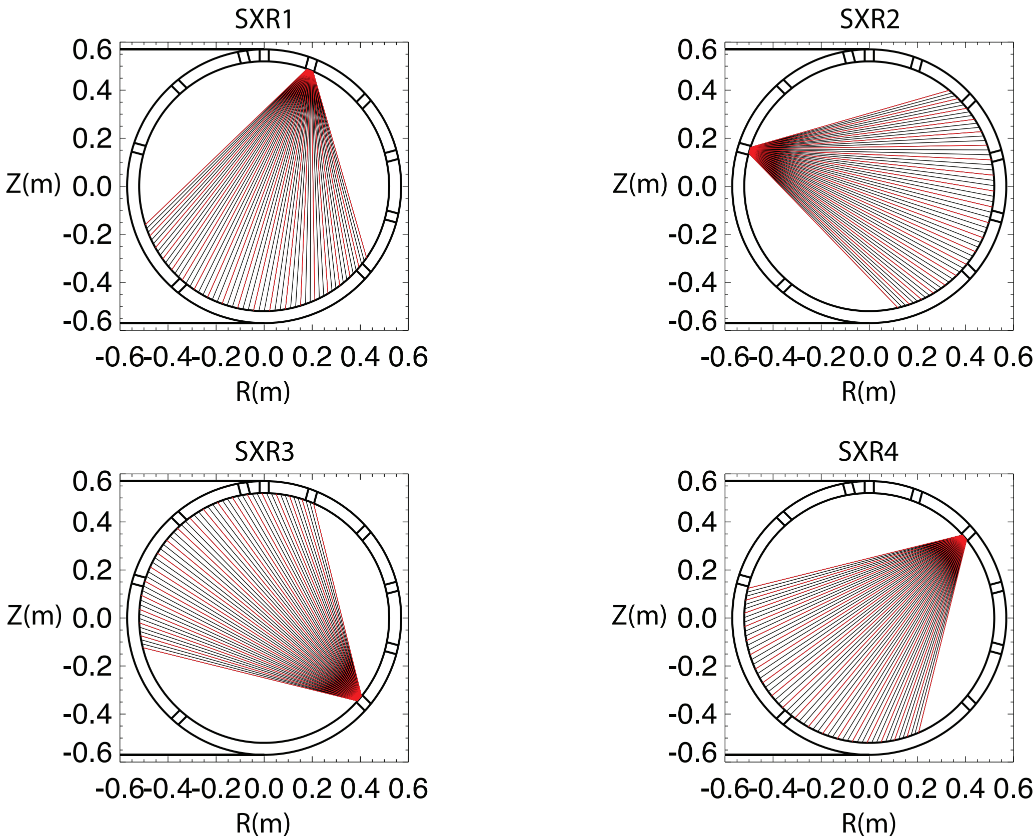

Figure 3.16: Field-of-view for a simulation where forty additional chords (red) were interleaved with the chords of the existing probes (shown in black). The increased spatial resolution of the system did not eliminate the oscillation.

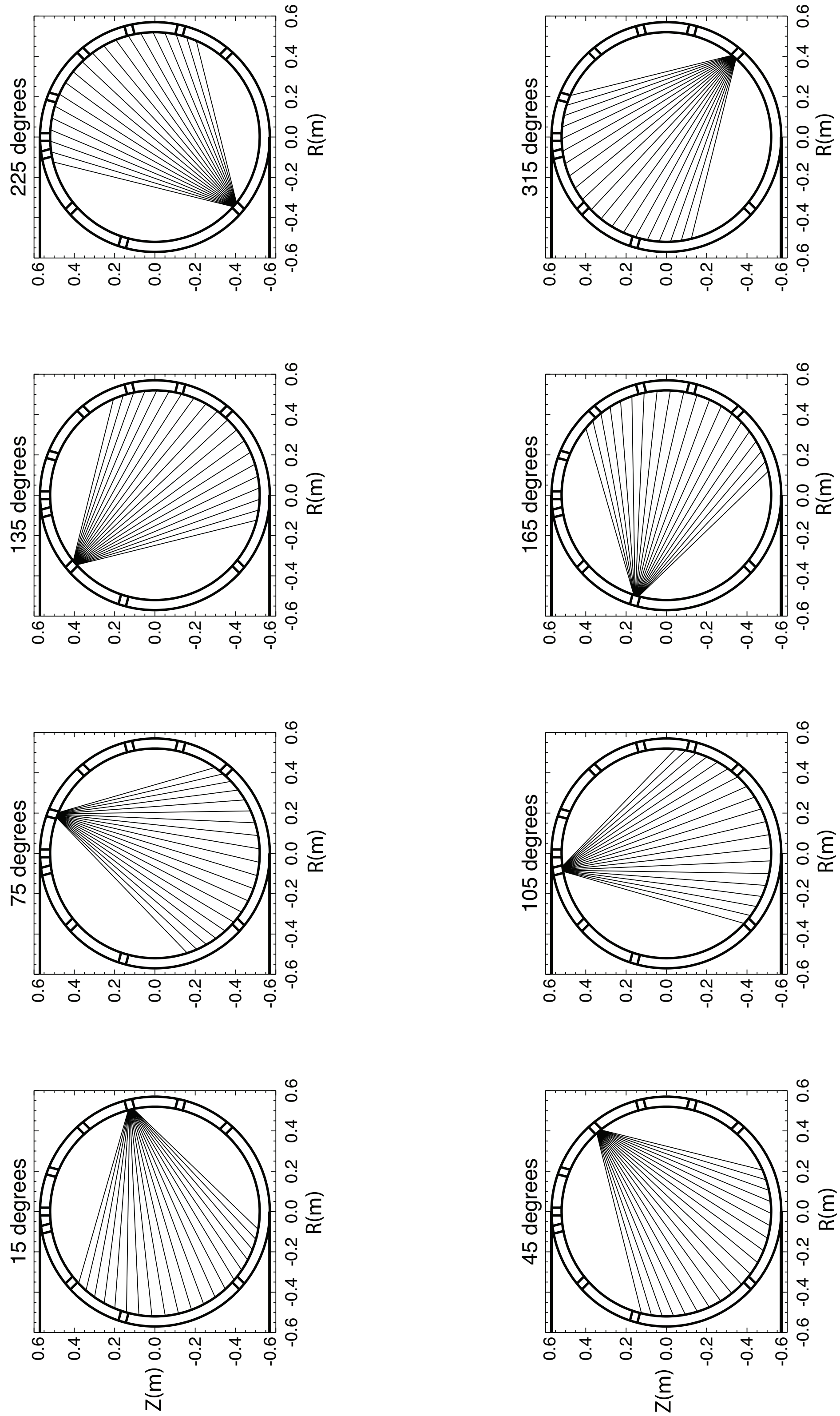

Figure 3.17: Field-of-view for a simulation with the four existing probes plus four additional probes to increase the number of different viewing angles. This geometry also did not eliminate the oscillation, indicating that the existing geometry already has a sufficient number of unique chords.

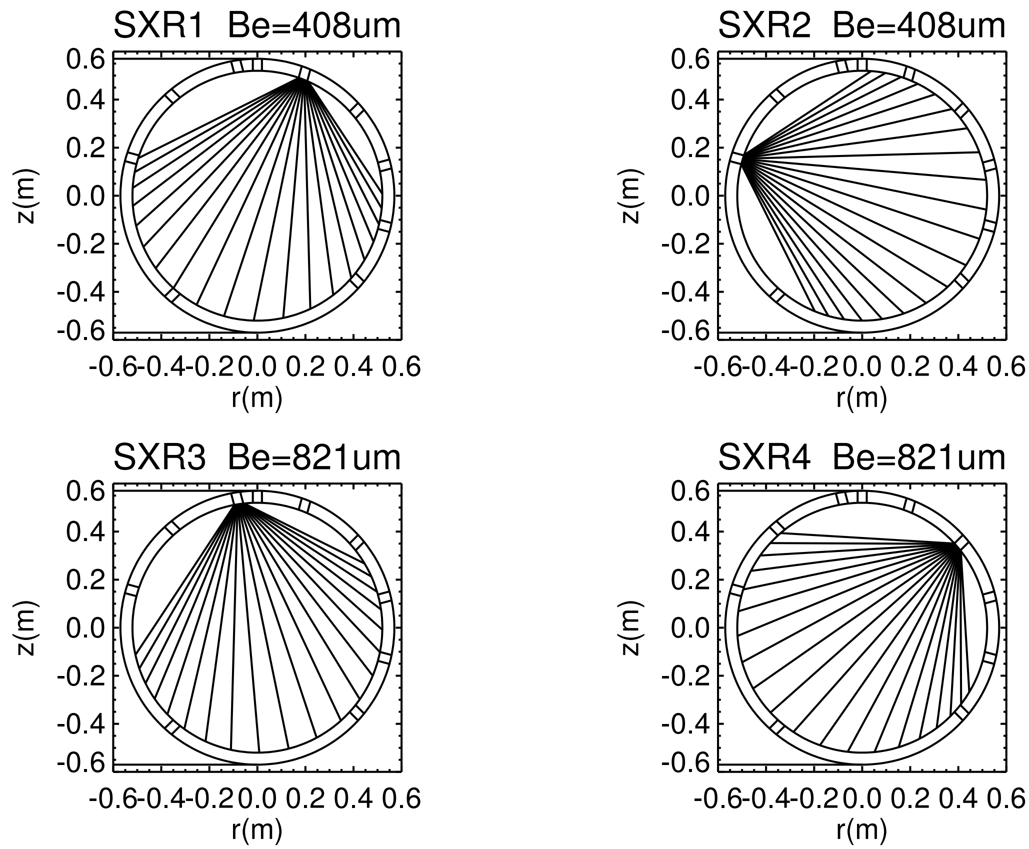

Figure 3.18: Field-of-view for the best simulated geometry at 300° toroidal. This geometry uses the existing probes and the same portholes, but moves the distance from pinhole-to-diode to expand the field-of-view toward the edge of the vessel.

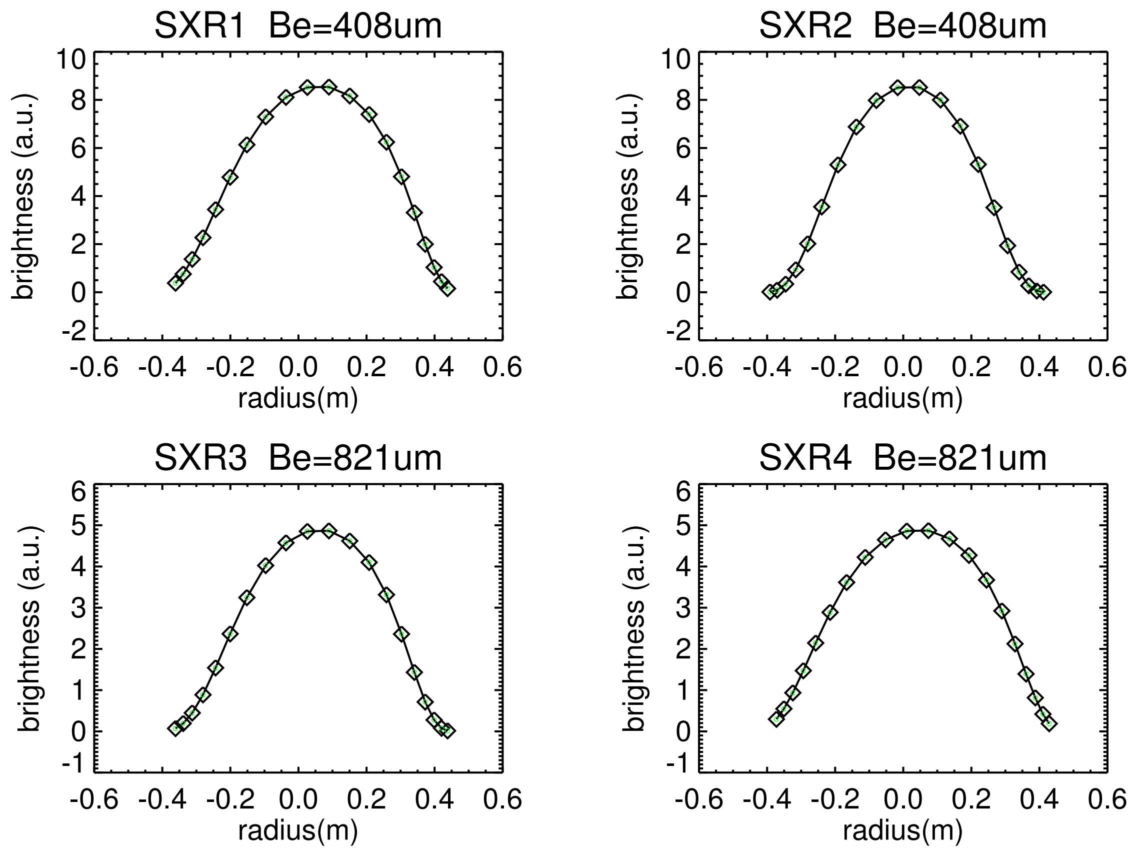

Figure 3.19: Brightness profiles for each probe using the best simulated geometry at 300° toroidal. The simulated profile is shown in black diamonds. The reconstructed emissivity was integrated along each line-of-sight to calculate the reconstructed brightness (green dots). The profile reaches all the way to zero SXR emission for each probe.

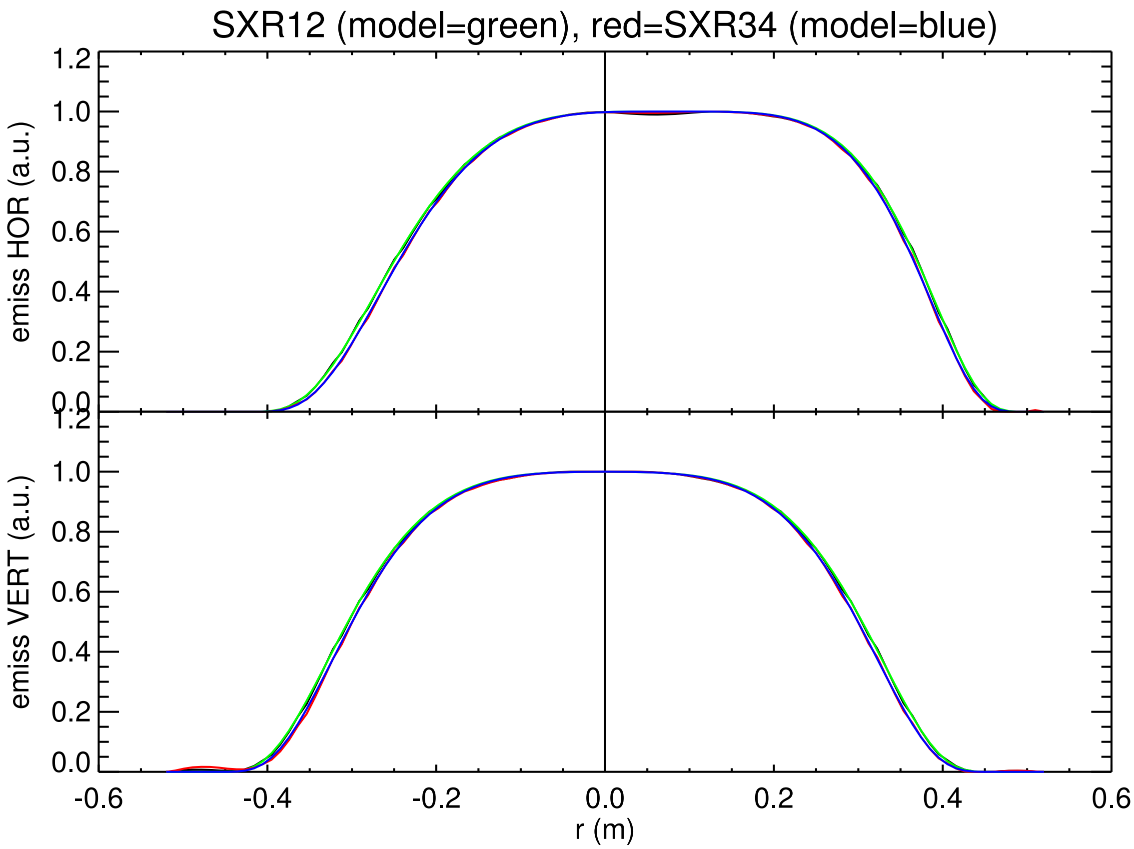

Figure 3.20: Horizontal (top) and vertical (bottom) cross-sections of the reconstructed emissivity for the simulated best geometry at 300° toroidal. In each plot, the emissivity input into the model for the thin filter is green, while the model emissivity through the thick filter is blue. The tomographically reconstruction of SXR-1,2 results in the 'measured' emissivity plotted in black, and the 'measured' emissivity for SXR-3,4 is shown in red. The model and reconstruction match well at both the edge and in the core region because the plasma is well sampled out to zero SXR emission.

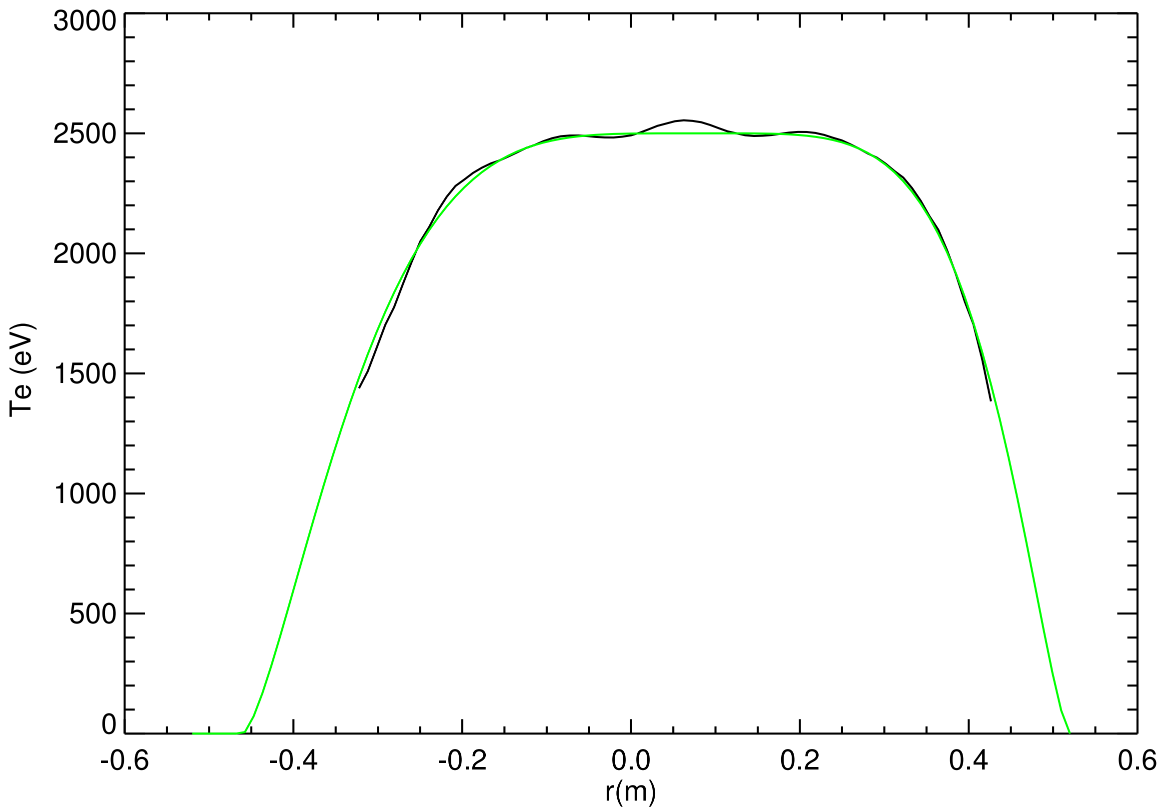

Figure 3.21: Horizontal cross-section of the tomographic temperature for the simulation with the best geometry at 300°. The temperature profile defined by the model input in the simulation is plotted in green. Improved edge coverage of the plasma provides the natural SXR brightness profile all the way to zero, resulting in a smooth emissivity reconstruction. This results in a vastly improved reconstruction of temperature with reduced oscillations.

tomographic T_e cross-section for a model testing this optimized configuration. This geometry gives reasonable emissivity reconstructions for plasmas with island structures as well. As shown in Figure 3.22, emissivity reconstructions of a 2.5keV plasma with a 500eV bean-shaped island is well-resolved at all angles. (This simulation was run with a 500eV island at $r_0/a = 0.13$ with a width of $\delta_r/a = 0.05$ and angular extent $\delta_\theta = 50°$.) SHAX-type islands have even better reconstructed emissivities. In general, islands are well-reconstructed with this geometry so long as their amplitude is a substantial fraction of the equilibrium temperature. For small amplitude islands (i.e. 10% equilibrium temperature), the islands become difficult to properly reconstruct at some angles.

Unfortunately, oscillations in the electron temperature return when island structures are added into the simulation. Figures 3.23 and 3.24 show the reconstructed emissivity and temperature cross-sections for the same bean-shaped island at 135° poloidal. Although the actual island appears in the reconstruction, oscillations are present as well. In fact, the oscillations are the same amplitude as the island in several positions and would make it difficult to correctly identify the island in an experiment. A further problem with this 'best' geometry is that this design is not currently possible at 300° toroidal due to the thick walls of MST. In order to gain the required field-of-view at any location on MST with 1.5 inch portholes, the portholes would need to be scalloped at the inner vessel wall, and the probeheads modified, to allow a pinhole-to-diode distance of 8mm (versus the 15mm distance in the actual hardware).

3.3.4 Optimizing Geometry at 300T

A final test to eliminate temperature oscillations was to create a 'perfect' geometry by having the exact same field-of-view for the thin and thick filters and including

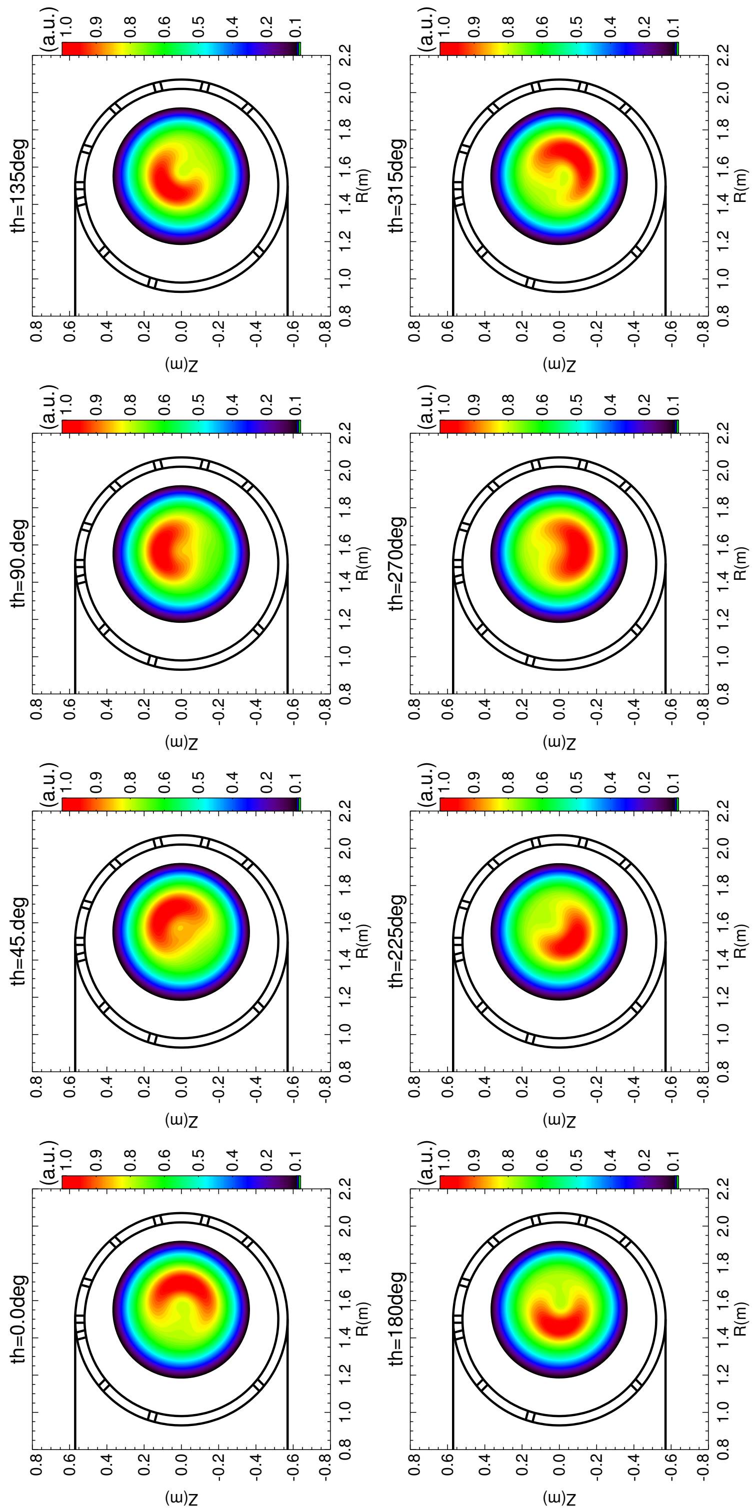

Figure 3.22: Tomographically reconstructed emissivity maps for a bean-shaped island at various poloidal positions, using the best geometry at 300°. The contours are normalized to the highest emissivity in each plot. Considering only the quality of the tomographic reconstruction for emissivity, without measuring temperature, the results are quite reliable.

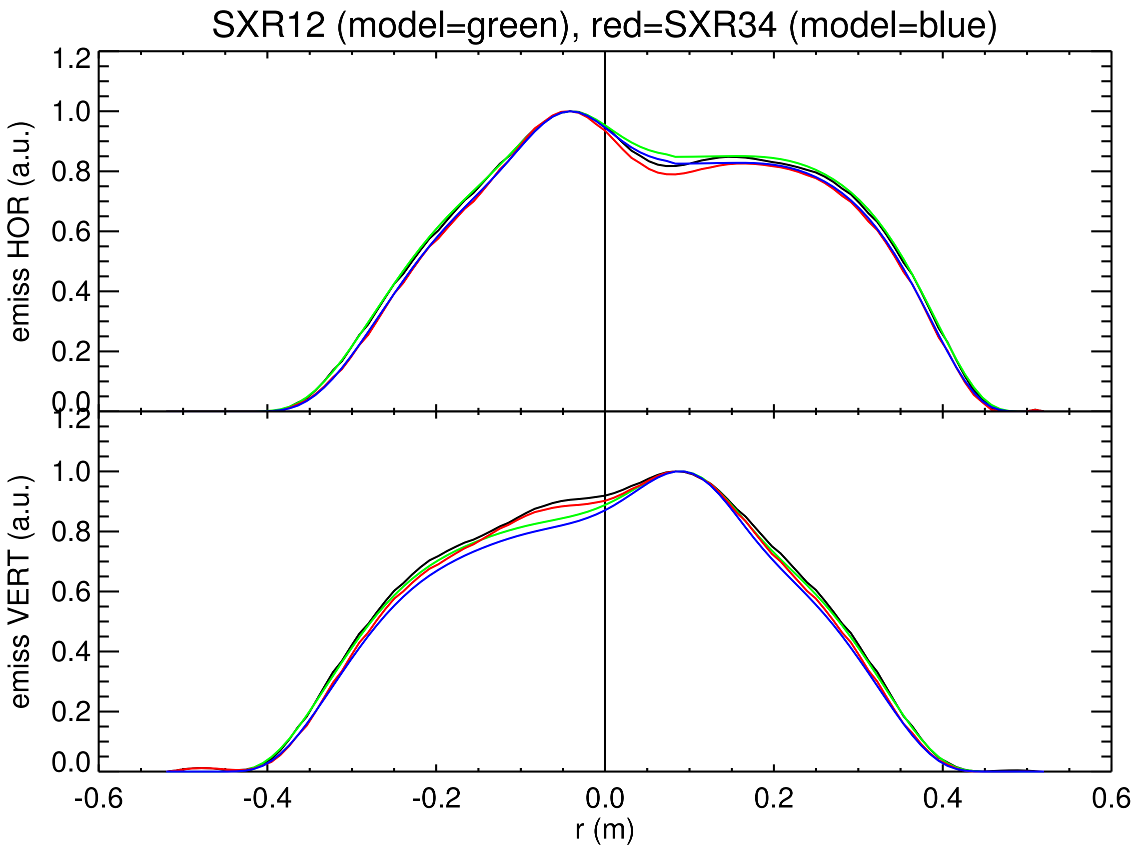

Figure 3.23: Horizontal (top) and vertical (bottom) cross-sections of the reconstructed emissivity for the simulated best geometry at 300° toroidal. In this case, a bean shaped island has been added at 135° poloidal. In each plot, the emissivity input into the model for the thin filter is green, while the model emissivity through the thick filter is blue. The tomographically reconstruction of SXR-1,2 results in the 'measured' emissivity plotted in black, and the 'measured' emissivity for SXR-3,4 is shown in red. The addition of the island again triggers oscillations in the core region, even though the edge emissivity profile is well-behaved.

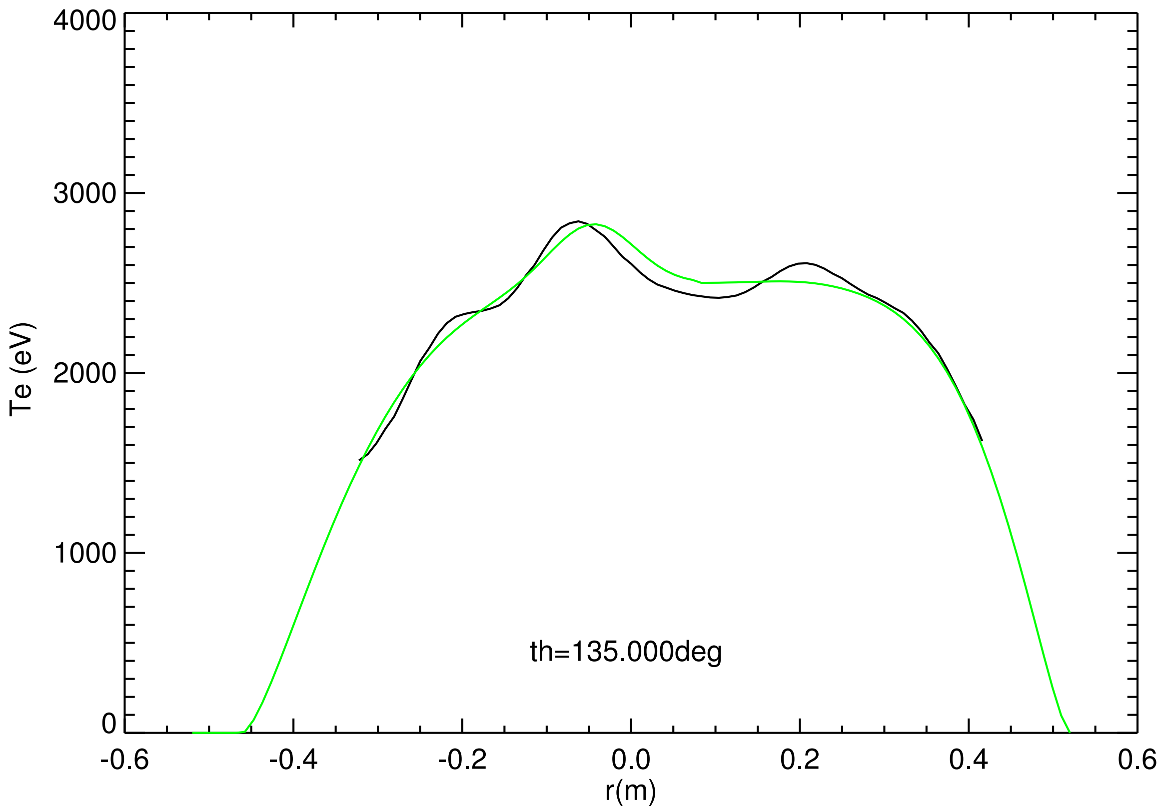

Figure 3.24: Horizontal cross-section of the tomographic temperature for the simulation with the best geometry at 300° , with a bean shaped island at 135° poloidal. The temperature profile defined by the model input in the simulation is plotted in green. The improved edge coverage of the plasma provides the natural SXR brightness profile all the way to zero, stabilizing the emissivity reconstruction at the edges. However, oscillations persist in the core that are nearly as large as the intended island. In real data, it would be difficult to distinguish actual islands from these artifacts.

the extended field-of-view. For this case, the simulation was run for probes in only two portholes, 75° and 165° poloidal, first with thin filters and then with thick filters (Figure 3.25). This is an ideal geometry because the thin and thick filter reconstructions are based on the exact same chords. Therefore, any artifacts in one emissivity should appear in the other as well. The ratio technique would then hopefully damp out these artifacts. Similar to the best geometry at 300° toroidal above, equilibrium plasmas were reconstructed very nicely using this geometry. However, the tomographic inversion has trouble with any type of island. Figures 3.26 and 3.27 show the reconstructed emissivity and temperature of this geometry using with a bean island at 270°. The emissivity cross-sections show clear deviations from the model (recall that the reconstruction black should follow model green, and red should follow model blue). Because the oscillations in the two emissivity reconstructions happen to be in phase in this example, they do somewhat cancel out in the temperature profile. However the T_e oscillation is still too large to distinguish from an actual island. Furthermore, there is no guarantee that in real data, with noise, the oscillations will remain in phase and thus cancel out.

3.4 Conclusions

In general, the Cormack-Bessel tomographic technique works well to reconstruct emissivity. With an optimized geometry, it can combine with the double-foil technique to also reconstruct electron temperature for relatively flat profiles. However, the presence of islands causes large uncertainties in the reconstructed temperature, and cannot be used reliably for all island positions. The difficulty in reconstructing islands occurs because small errors in emissivity are amplified when the ratio is taken. These emissivity errors come from the lack of coverage at the edge of SXR emission, which is constrained by the geometry of the portholes and probe hardware. Addi-

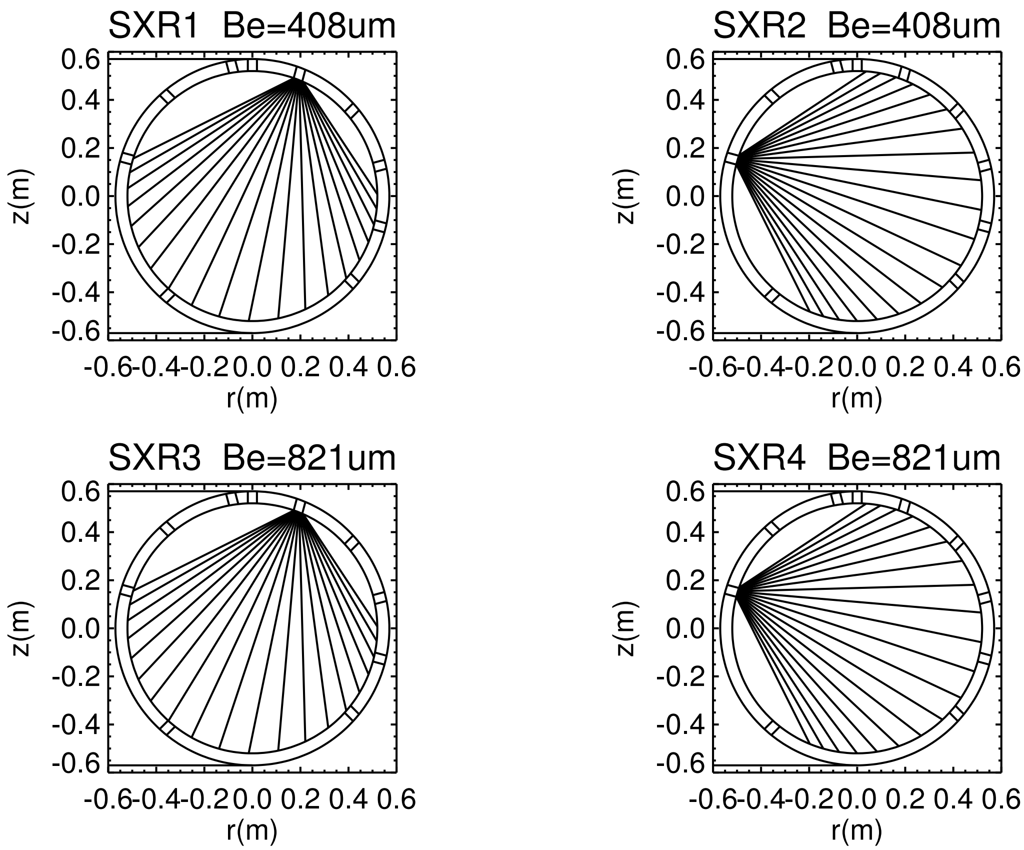

Figure 3.25: Field-of-view for a simulation of the bean-shaped island using the exact same portholes for the two sets of filters (SXR-1 = SXR-3, SXR-2 = SXR-4). This way, the thin and thick filters have identical fields of view. This simulation includes the extended field-of-view introduced in section §3.3.3.

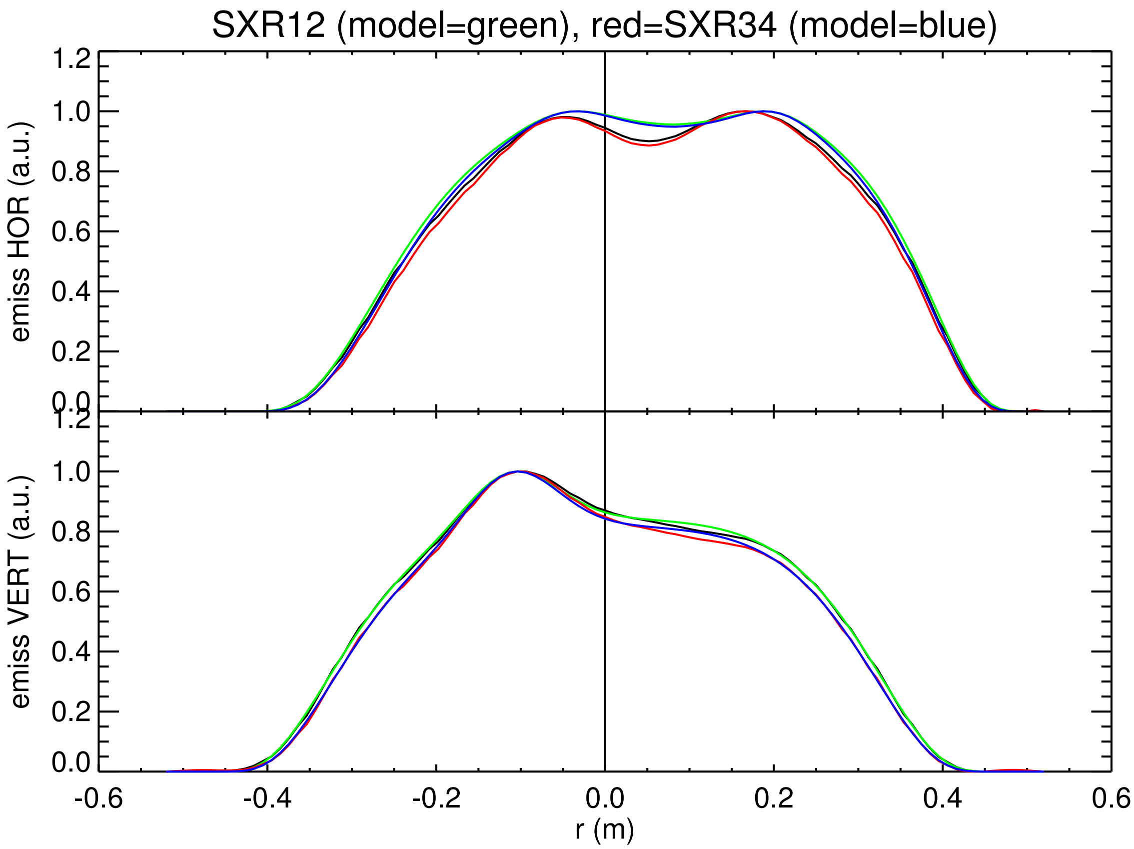

Figure 3.26: Horizontal (top) and vertical (bottom) cross-sections of the reconstructed emissivity for a simulation of the bean-shaped island at 135° poloidal, using the exact same portholes for the two sets of filters (SXR-1 = SXR-3, SXR-2 = SXR-4). In each plot, the emissivity input into the model for the thin filter is green, while the model emissivity through the thick filter is blue. The tomographically reconstruction of SXR-1,2 results in the 'measured' emissivity plotted in black, and the 'measured' emissivity for SXR-3,4 is shown in red. Even with identical geometries between filters, oscillations persist in the core region.

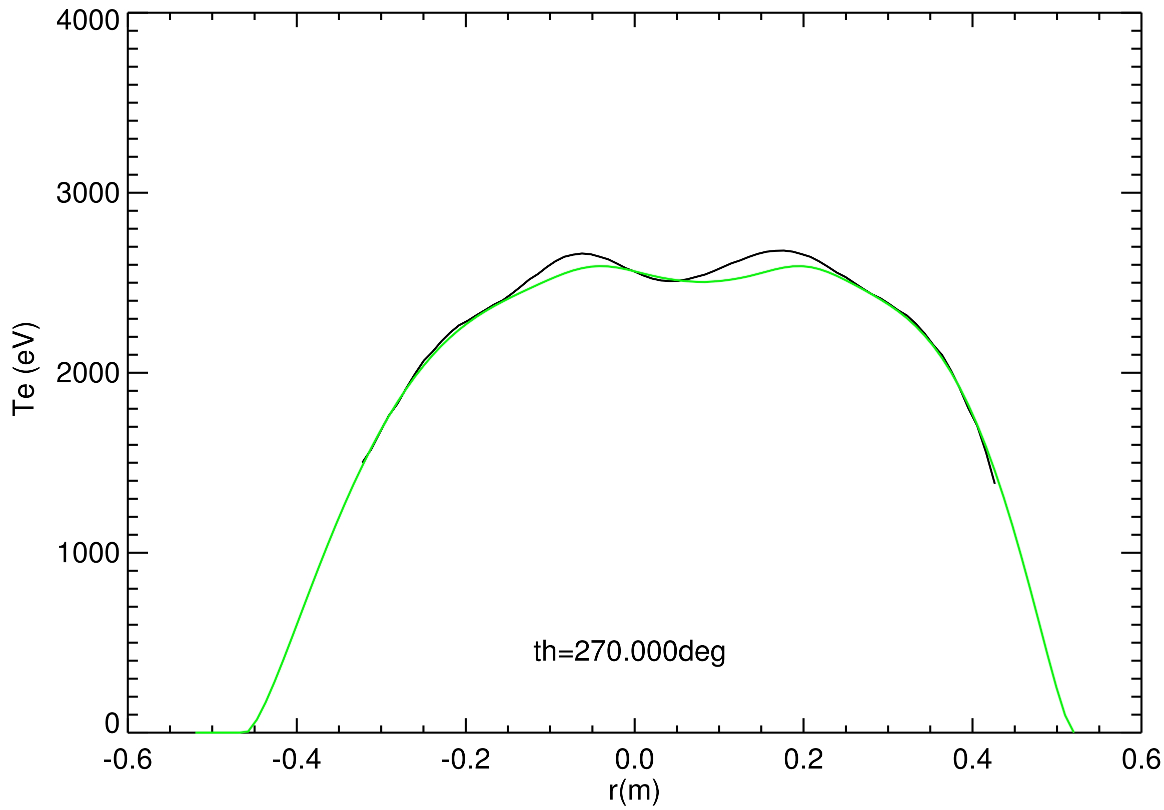

Figure 3.27: Horizontal cross-section of the tomographic temperature for a simulation of the bean-shaped island at 135° poloidal, using the exact same portholes for the two sets of filters (SXR-1 = SXR-3, SXR-2 = SXR-4). The temperature profile defined by the model input in the simulation is plotted in green. The improved edge coverage of the plasma provides the natural SXR brightness profile all the way to zero, stabilizing the emissivity reconstruction at the edges. However, oscillations persist in the core that are nearly as large as the intended island. In real data, it would be difficult to distinguish actual islands from these artifacts.

tional probes or additional chords within the existing field-of-view do not improve the reconstructions. Artificially filling in the missing chords also does not eliminate the oscillations. Some improvement in T_e is seen when thin and thick filters share the same line-of-sight. However, the effect of any amount of instability in the reconstruction is to create artificial T_e 'islands' that can easily be mistaken for true plasma features. In order to measure fluctuations in electron temperature on MST using SXR emission, a different approach is needed.

Chapter 4

The Double Foil Diagnostic: SXR Tomography and a New T_e Measurement

The limitations of electron temperature measurements with the previous SXR tomography diagnostic inspired a major upgrade to a new SXR double-foil (DF) diagnostic [38]. Like the previous version, the DF diagnostic is comprised of four probes separated poloidally at a single toroidal location. Also like the previous version, each probe contains twenty individual channels and uses two thicknesses of beryllium to filter the SXR emission into different energy ranges. However, the double-foil diagnostic includes three major improvements over the previous SXR tomography diagnostic. First, the electronics system has been completely rebuilt to accommodate individual photodiode detectors with differential output, resulting in reduced common mode noise and larger dynamic range. Second, an additional electron temperature measurement capability, the 'direct-brightness' technique, has been added while retaining tomographic capability. Third, the geometry has been improved to increase the field-of-view, which helps reduce spatial oscillations in the tomographic reconstruction. Section §4.1 describes the new diagnostic hardware and electronics. Section §4.2 summarizes the new direct-brightness T_e measurement and the improvements in tomography provided by the new geometry. Section §4.3 details several hurdles encountered during the development of the diagnostic, including both the final design and unsuccessful modifications. Section §4.4 quantifies the level of magnetic pickup on SXR signals in the final design and determines that the pickup can now be ignored at all but 10^9 gain.

4.1 Diagnostic Overview

The new diagnostic utilizes the two-inch portholes at 90° toroidal and is comprised of four units at separate poloidal angles. Two probes are separated poloidally by 180°, at 157.5° (SXR-C) and -22.5° (SXR-D) poloidal. The other two probes are installed on an 8-porthole boxport whose center is located 90° from SXR-C and SXR-D at 67.5° P. All portholes in the boxport are parallel to the center, which is aligned with the magnetic axis. SXR-A occupies the second porthole in the boxport (beginning at the outboard midplane) at 45.5°, while SXR-D occupies the sixth porthole at 87.5°. Figure 4.1 shows the layout for the double-foil SXR system, while Figure 4.2 shows the two probes mounted on the boxport at 90° T. The individual probes are labeled A-D in increasing poloidal angle. Figures 4.3 and 4.4 define the diode numbering using a simulated brightness profile for each probe. Each unit has 10 lines-of-sight, and each line-of-sight is associated with two individual silicon photodiodes (the IRD AXUV4BST from Opto-Diode Corp[1]) each looking through one of two Be foils of different thicknesses. The shared lines-of-sight allow T_e to be calculated directly from SXR brightness. Probes A and B create a nearly horizontal radial profile of T_e, while probes C and D create a nearly vertical profile. For tomographic reconstruction, probes A and B are combined to maximize plasma coverage with vertical chords, while probes C and D are combined for horizontal coverage. The probe hardware has been altered to improve coverage at the edge of the plasma, which has been shown in simulations to reduce spatial oscillations in the reconstructed emissivity and improve

[1] http://www.optodiode.com/products.html#IRD-UV-Photodiodes

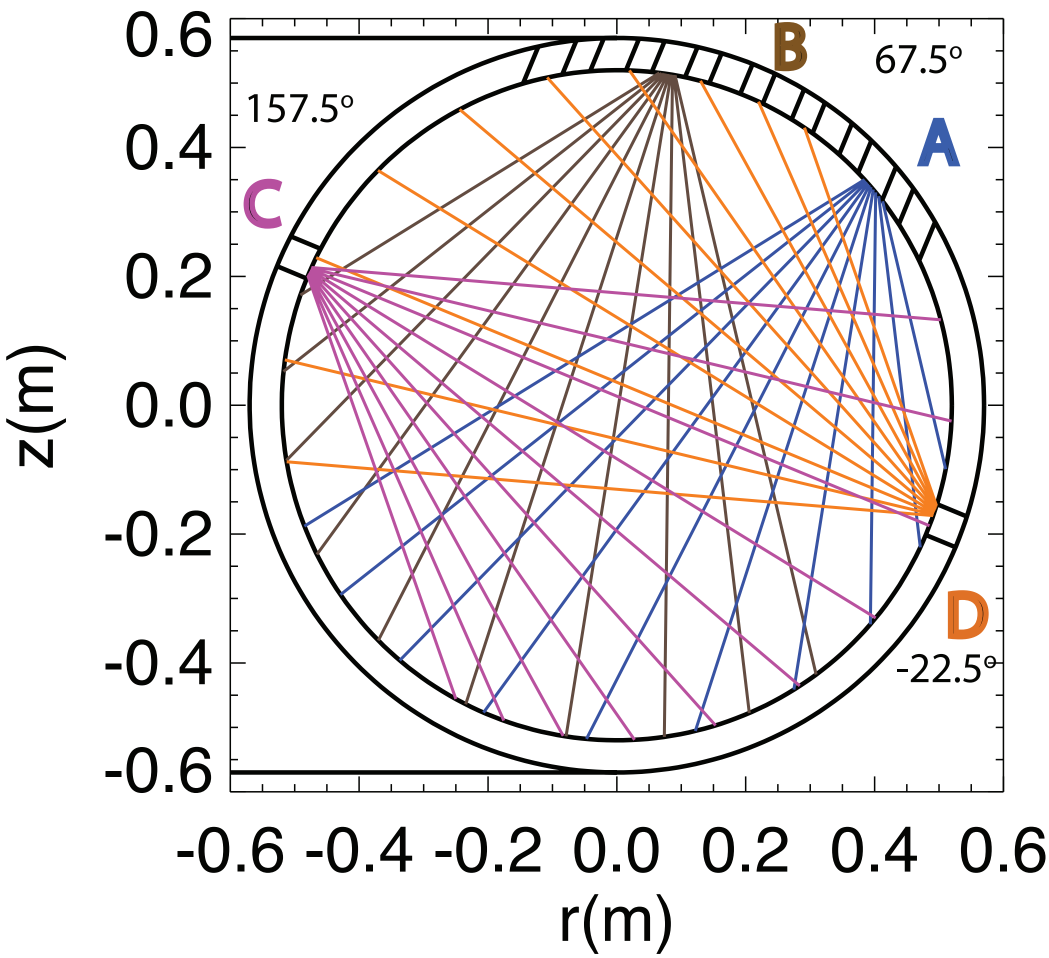

Figure 4.1: Geometry of the diagnostic upgrade, showing the 10 lines-of-sight shared by 20 diodes in each probe. SXR-A and SXR-B are located on the boxport at 67.5° , SXR-C is located at 157.5° , and SXR-D is at -22.5° (where 0° is at the outboard midplane and the angle increases toward the top of MST).

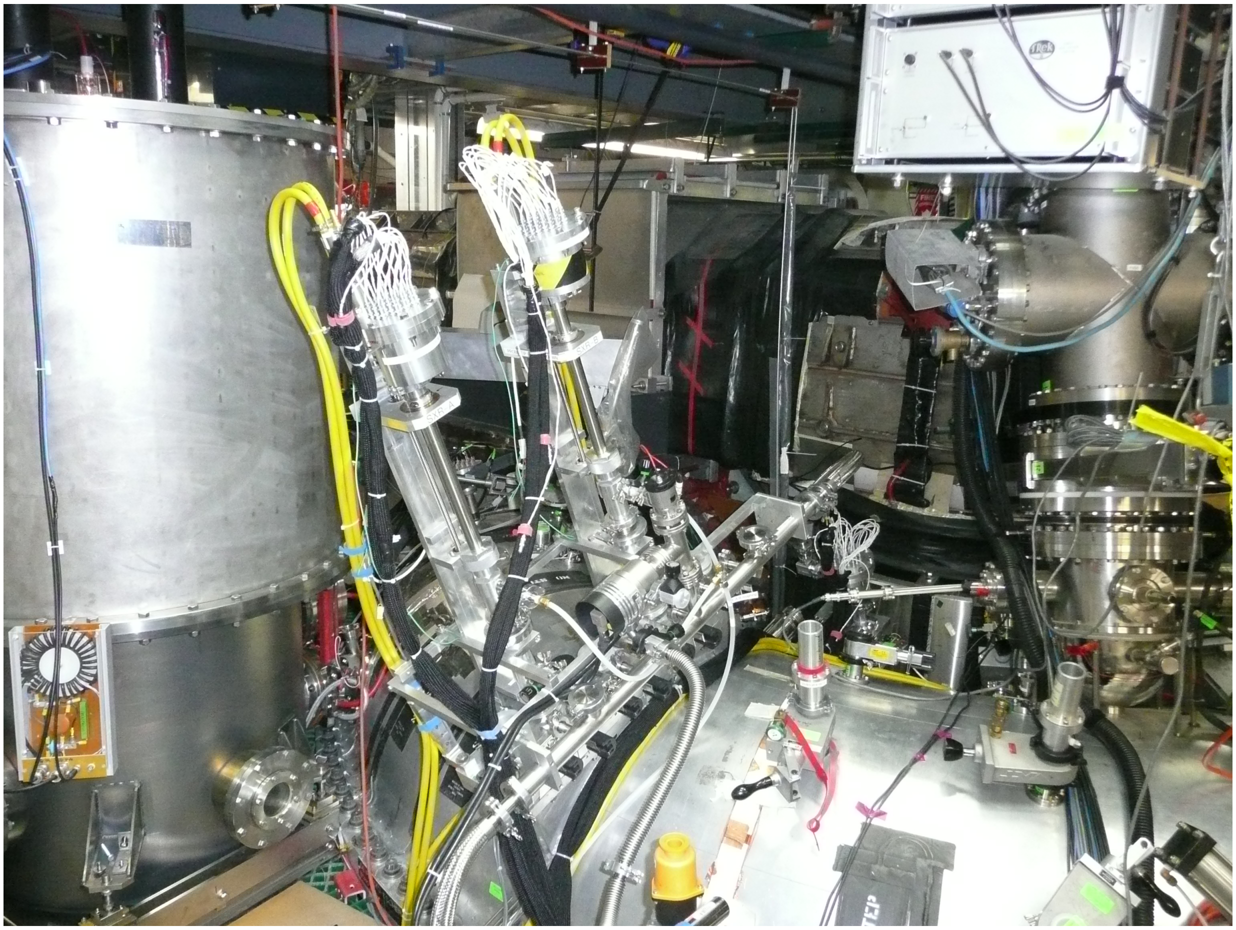

Figure 4.2: Probes A (left) and B (right) mounted on the boxport at 90° T. The top of probe C can be seen near the core.

the resulting tomographic T_e reconstruction.

4.1.1 New Electronics

The double-foil SXR diagnostic is located on 2-inch diameter portholes, which allowed the diameter of the probehead to be increased to 45 mm. As a result, individual photodiodes could be used for the chord array in each probe, rather than an array of diodes with shared grounds as in the old system. The new AXUV4BST photodiodes retain a silicon thickness of 35 μm and an active area of 4 mm^2, like the previous

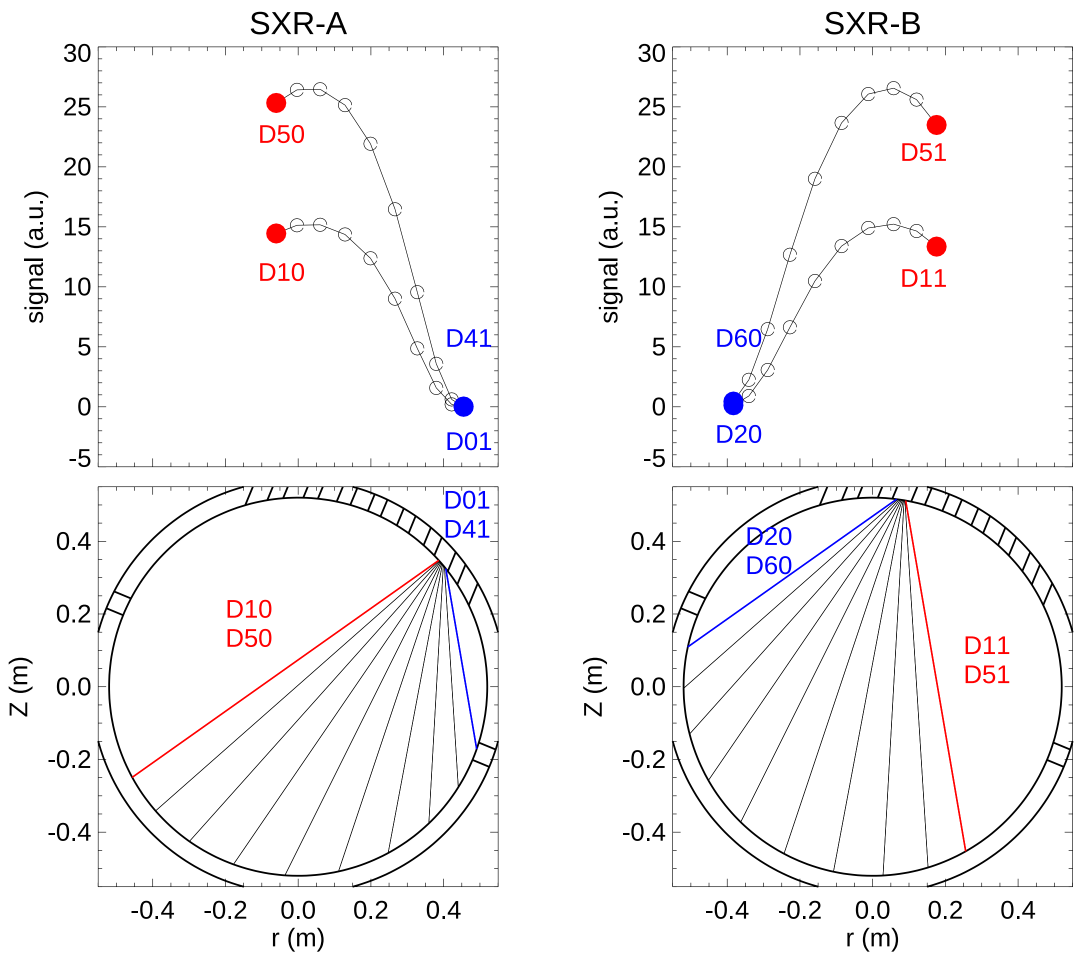

Figure 4.3: Lines-of-sight for SXR-A and SXR-B (bottom left and right) and simulated SXR brightness as viewed by each diode for this geometry (top). Red and blue indicate the logical number of the first and last chord for each probe. Logicals 1-40 are assigned to the thick Be filter diodes, while 41-80 are assigned to the thin filter diodes.

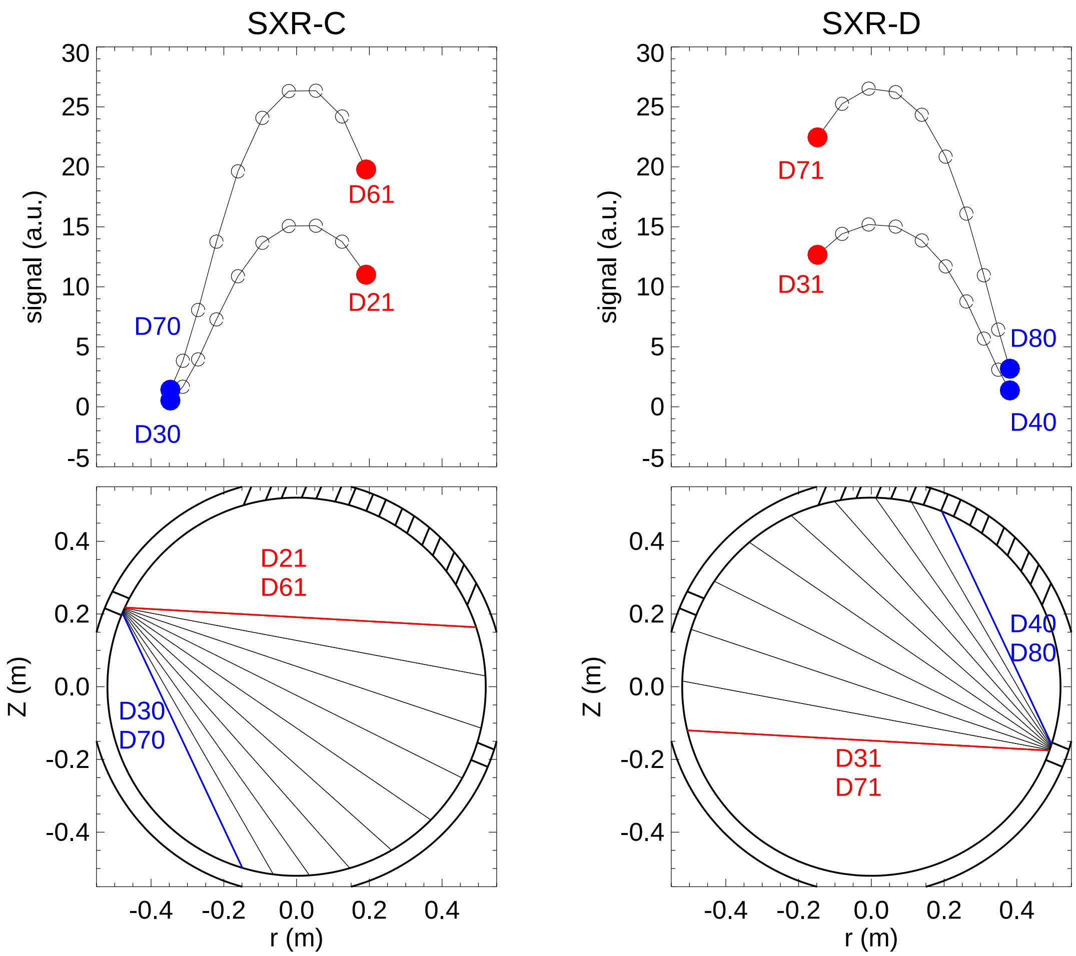

Figure 4.4: Field-of-view for SXR-C and SXR-D (bottom left and right) and simulated SXR brightness as viewed by each diode for this geometry (top). Red and blue indicate the logical number of the first and last chord for each probe. Logicals 1-40 are assigned to the thick Be filter diodes, while 41-80 are assigned to the thin filter diodes.

system. However, due to changes in the pinhole design and placement, the *etendue* of the system is about half that of the previous diagnostic. The new photodiodes are 2 mm by 2 mm and have separate anode and cathode connections for each diode. Figure 4.5 shows individual photodiodes and a fully populated detector for SXR-D. The gold colored base is connected to the diode's anode, while the red wire is connected to the cathode. The diodes have been assembled on a custom designed 5-layer printed circuit board. (See §4.3 and Appendix A for a detailed description of the design). The diodes are attached to the circuit board using a heat-cured conductive silver epoxy (Supreme 10HT/S from Masterbond).

Since each photodiode has a separate anode and cathode wire, the entire electronics chain has been rebuilt as a differential system. A schematic of the electronics layout and grounding system is shown in Figure 4.6. The grounding of the system has been carefully optimized to limit electronic pickup. Beginning with twisted-shielded-pair wire inside the probe, the signals are carried to in-house custom designed differential transimpedance amplifiers (DTIA). The output of the amplifiers is also differential and is sent into Joerger TR1612 digitizers set to low-impedance (100 Ω) differential input. Outside each probe, each bundle of ten signal carrying wires has an additional layer of shielding in the form of a metal braid. Maintaining differential signals all the way to the digitizer improves common-mode rejection and improves the signal-to-noise ratio.

Because of its excellent common-mode rejection, the differential system is much less affected by the programmable power supply (PPS) for the toroidal magnetic field. This is especially important because the power supplies have a switching frequency of 10 kHz, which is near the tearing mode frequency of interest. Figure 4.7 compares the baseline noise and common mode pickup of the original linear transimpedance

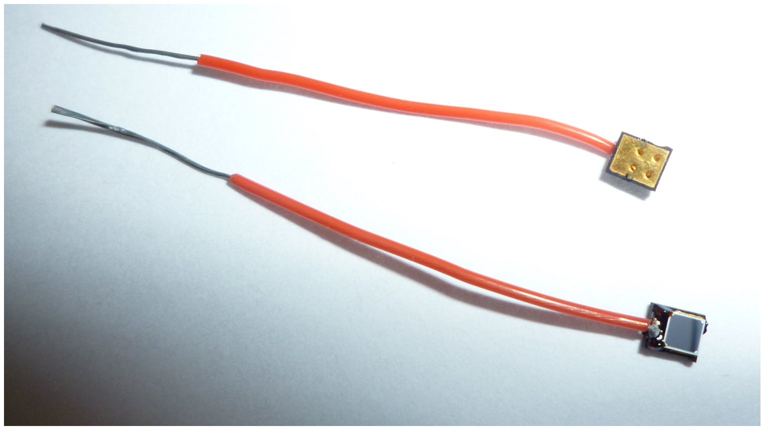

(a) Individual photodiode for DF system - wire is cathode, gold base is anode. When installed in the circuit board, the teflon coating is removed from the cathode wire and the wire is shortened to ∼2mm.

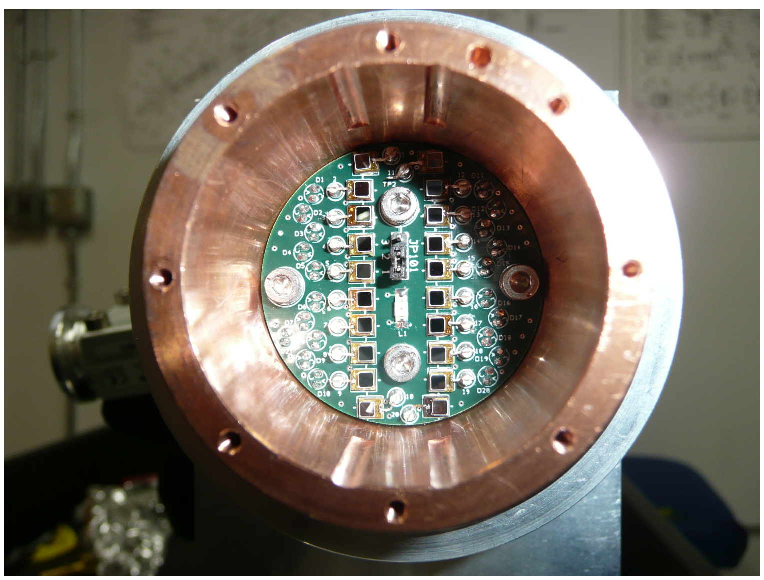

(b) Populated PCB with 20 photodiodes. The anode and cathode signals are both electrically connected to the PCB using heat-cured conductive epoxy.

Figure 4.5: Differential SXR silicon photodiodes

amplifiers (TLA) with the new differential amplifiers. The black traces show the baseline electronic noise for a B_T shot that generates magnetic field via the previous design using simple capacitor discharge. In this 'vacuum' shot, all the capacitor banks are fired and all circuits/diagnostics turned on, but with no plasma. The blue traces show an equivalent vacuum shot using the programmable power supply instead. The left plot shows that the TLA was very sensitive to common mode noise from the experimental area, with signals of ~ 50 mV at 0 ms dramatically increasing to several hundred millivolts during the shot. (Although this was a vacuum shot with no plasma, noise is still generated due to the error correction coil system). The common mode contamination was even worse during shots with the programmable power supplies. In contrast, the new DTIA has a very consistent baseline noise of ~ 100 mV before and during the shot, and their performance is equally good in the presence of switching noise from the PPS.

The DTIA has excellent bandwidth across 5 adjustable gains ranging from 10^5 to 10^9. Figure 4.8 shows the electrical schematic for the final DTIA. Table 4.1 shows the bandwidth, and noise level on the bench at each amplification. In typical MST shots, the dynamic range between the core and edge chords is larger than $10x$ and so at least two gain settings are used across a probe. This range of amplifications enables x-ray studies of high current plasmas (400-600 kA standard, F=0, PPCD) with signals free of aluminum contamination using thick filters for electron temperature measurements (for an explanation of the issue of aluminum contamination, see §2.4). For SXR emissivity studies without T_e measurements, the range of currents can be expanded (250-600 kA standard, F=0, PPCD) using thinner filters for magnetic topology and impurity studies.

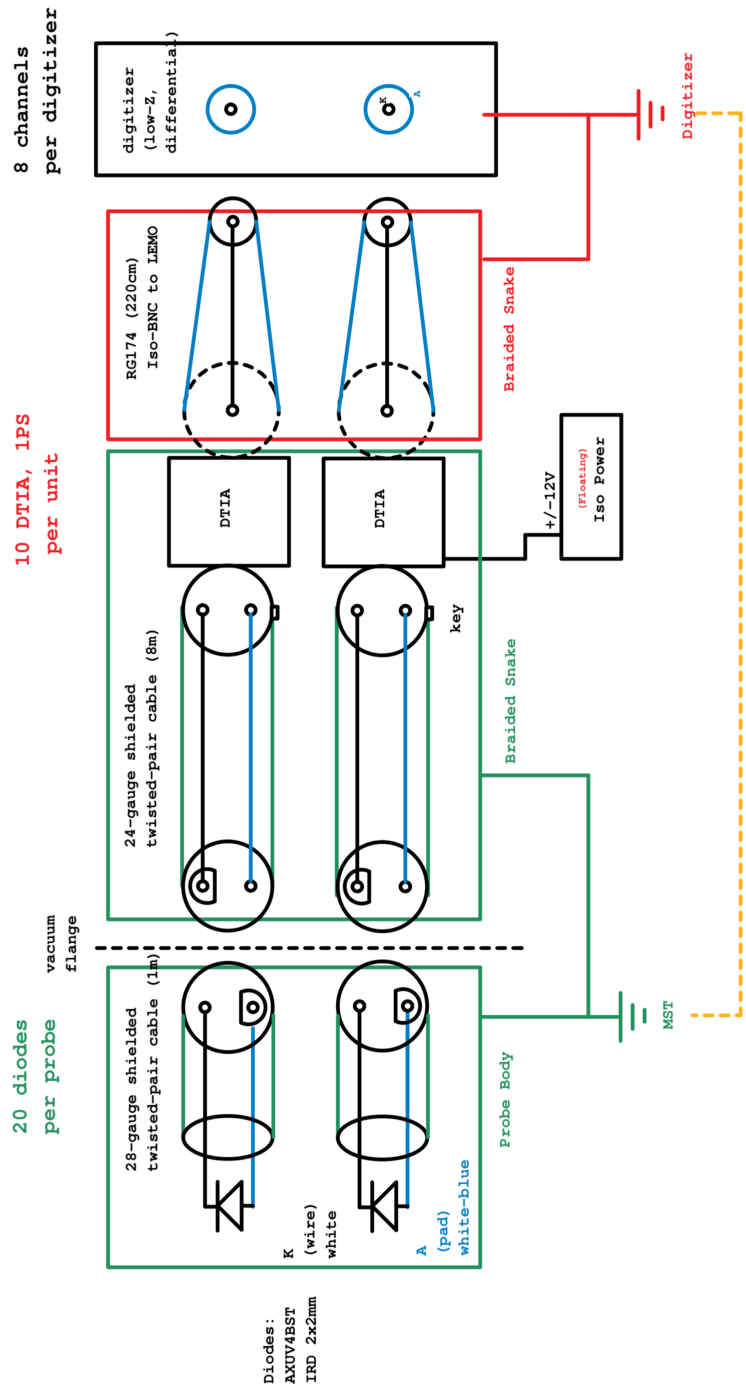

Figure 4.6: Electronics layout and ground schematic for the SXR DF diagnostic. Differential signal is maintained all the way to the digitizer, which is configured for a low-impedance, differential input. The cabling into the DTIA is all twisted-shielded pair. The cable from the DTIA to the digitizer is single-ended BNC, but is isolated so that the shield of the co-axial cable carries the anode signal. Every set of cables has an external copper braid to improve shielding. The differential amplifier (DTIA) is physically housed in the digitizer rack but is electrically isolated and receives its ground from MST.

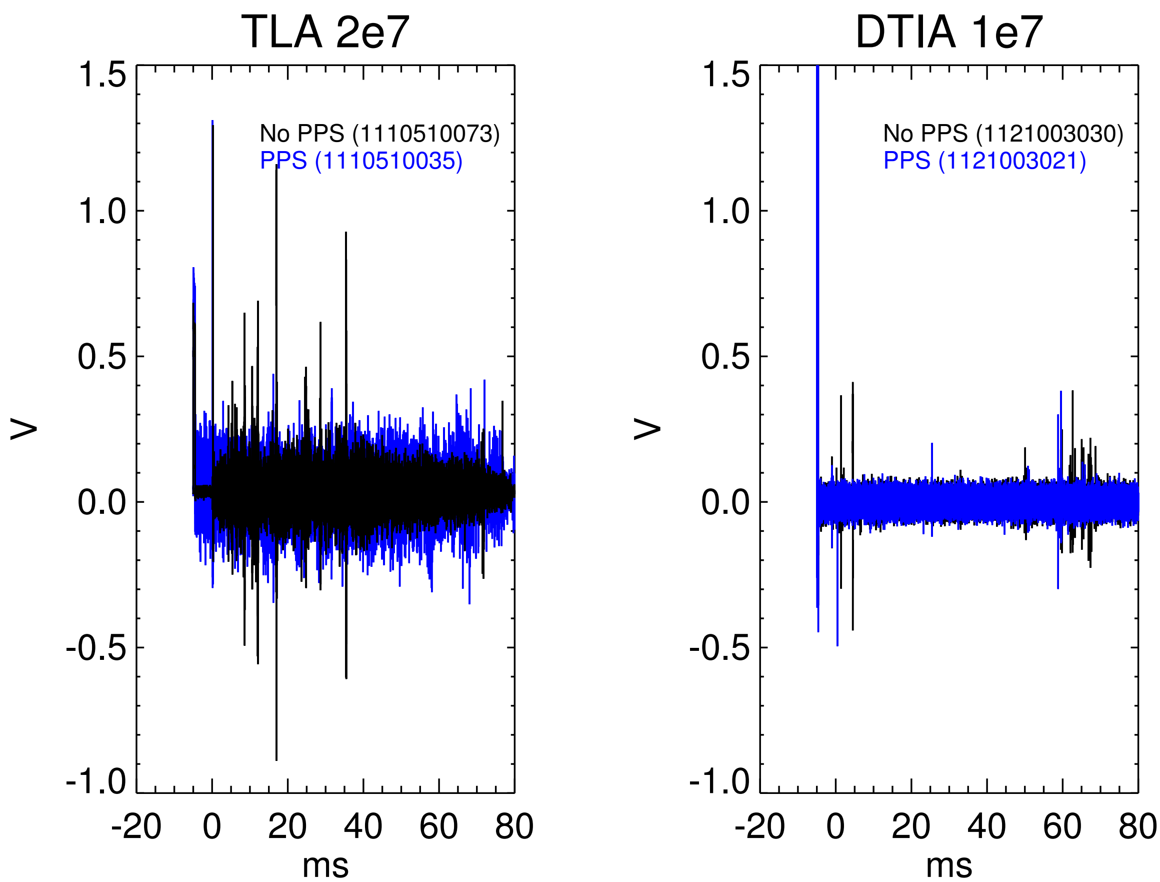

Figure 4.7: Comparison of noise level for TLA (left) versus DTIA (right) in vacuum shots using legacy (black) or PPS (blue) bank configurations. Although the baseline noise on the DTIA is higher than on the TLA, the noise during the shot is lower and there is no significant difference between PPS or legacy mode in terms of pickup. In contrast, the TLA was extremely sensitive to common mode noise from the PPS and other external noise sources during the plasma.

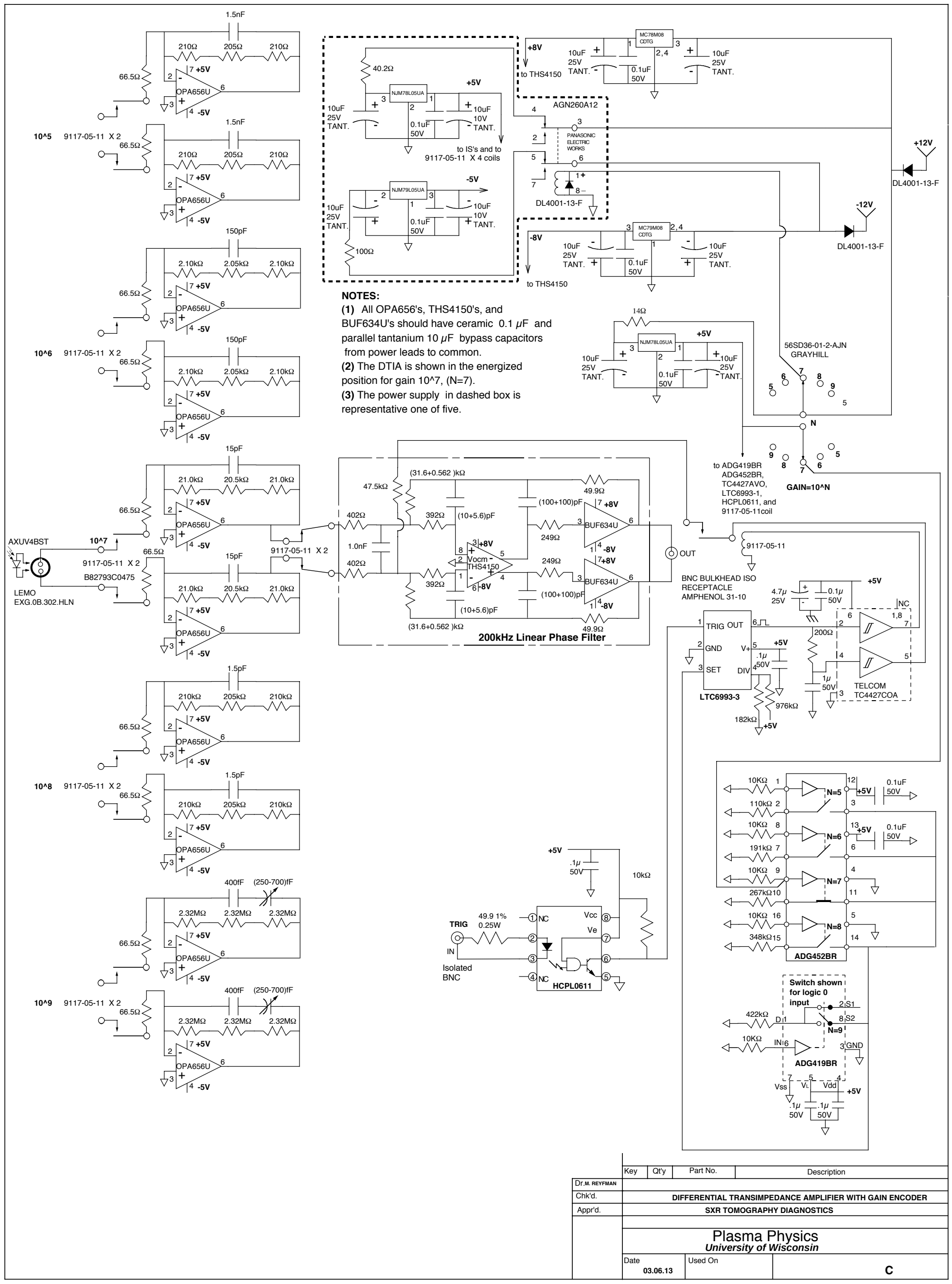

Figure 4.8: Electrical schematic for differential transimpedance amplifiers.

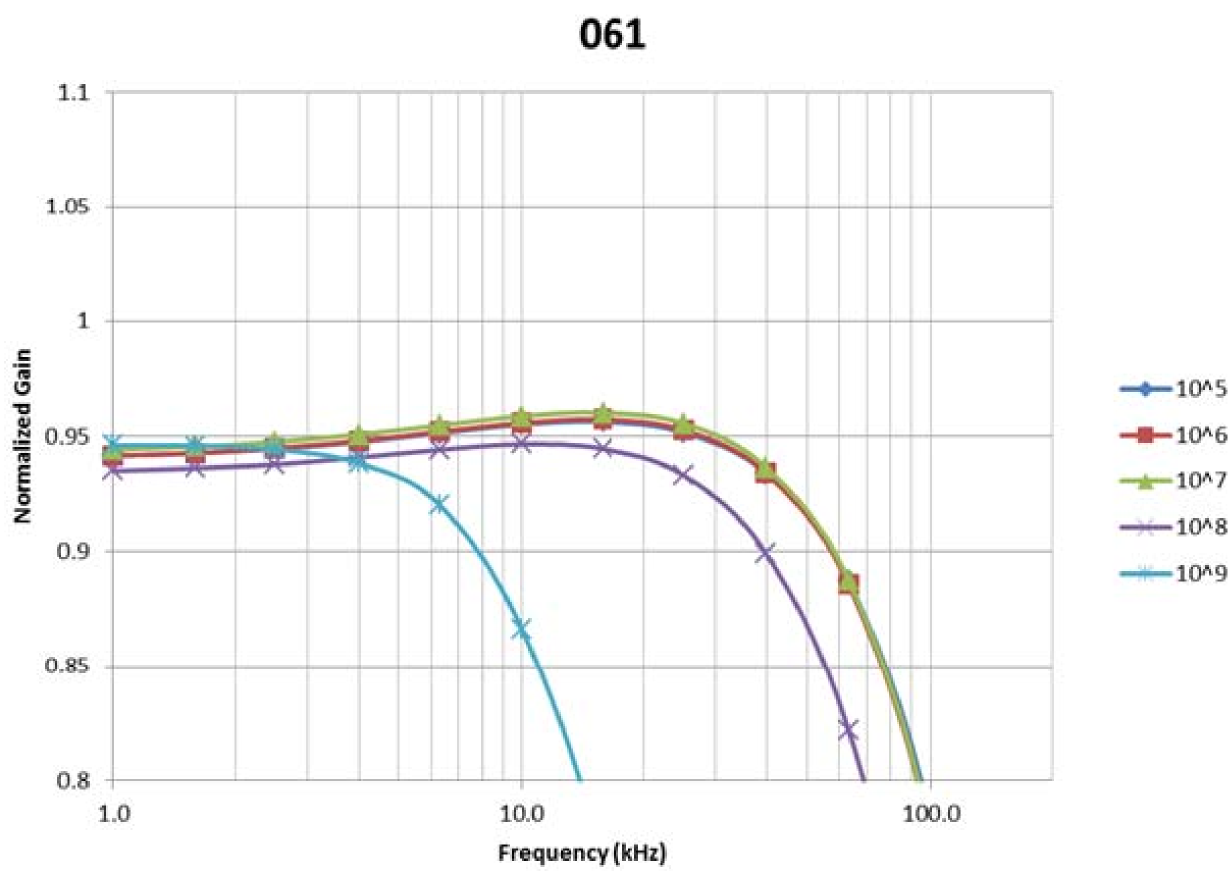

Figure 4.9: Representative frequency response of DTIA for all 5 gains. Normalized gain is approximately 94% the nominal value at all gains.

transimpedance (V/A)	3 dB bandwidth (kHz)	bench noise (mV_{p-p})
10^5	134	80
10^6	134	80
10^7	134	100
10^8	91	120
10^9	27	140

Table 4.1: Amplification specifications for the new DTIA as tested with actual probe and cabling.

4.1.2 Electronics Calibration

The differential transimpedance amplifiers have been calibrated using a pair of HP34401A digital voltmeters and a switchable attenuator providing 10^5- 10^9 A/V differential input to the DTIA. Figure 4.9 shows the normalized frequency response at each gain for a representative DTIA (serial number 061). Actual gains are approximately 94% their nominal value at 1 kHz. The differential signal voltage out of the DTIA at each gain is divided by the voltage input to the attenuator to determine the normalized gain at each setting. Electronic noise from the measurement device is subtracted from all output measurements at each gain. DTIA gains are not stable until the DTIA comes to thermal equilibrium. Due this thermal drift, each gain setting is powered on at least 5 minutes before measurements are taken.

Each amplifier is measured at constant $\delta f/f$ intervals with five steps per decade from 1 kHz to 158 kHz. All amplifiers whose variation in gain is less than $\pm 2\%$ around the mean value of all 100 amplifiers are accepted. All 80 DTIA installed on MST have been individually tested to assure they meet the $\pm 2\%$ requirement at 10^8 (to 60 kHz) and 10^9 gain (to 25 kHz). Gains of 10^5-10^7 have been approved after testing of a subset of 10 amplifiers confirmed the requirement up to 100 kHz. Of the remaining

20 spare amplifiers, 15 do not meet the $\pm 2\%$ requirement for 10^9 gain, but do vary by less than 5%.

To achieve $\pm 2\%$ variation at 10^9 gain, adjustable compensation capacitors had to be added to the circuit. (The 1% variance in the original fixed feedback capacitors was sufficient to skew the output signals due at 10^9 gain). Two 0.25-0.7 pF trimmer capacitors, in series with a 0.4 pF capacitor, allow adjustment of the feedback capacitance in the range of approximately 0.15-0.25 pF. The -3 dB frequency at the first stage of the amplifiers is adjusted to 35 kHz for both halves of the amplifier using the trimmer capacitors and measured with the digital voltmeters. This balancing also optimizes common mode rejection.

4.1.3 Relative Brightness Calibration

Variations within the fabrication of individual probe hardware, diodes and circuit boards, as well as in the thicknesses of individual beryllium foils, introduce systematic variation in the measured SXR brightness profiles. This variation can be measured and corrected by comparing the core-viewing diodes from each profile of the same nominal beryllium thickness. The previous SXR diagnostic had variations of up to 5% with different combinations of probes and foil-stacks. This variation is corrected out of the measurement by normalizing all peak profiles to that of a single probe (for the thin and thick filters separately). Due to its excellent agreement with the Thomson scattering diagnostic in measuring direct-brightness temperature, SXR-C was chosen as the normalizing probe. A statistical study determined the average correction factors for each of the other probes with respect to SXR-C. The database includes all time points (using a 0.5 ms binning window) during PPCD shots where the plasma is rotating (to average out bright spots from magnetic activity) and where there is no plasma-wall interaction. The correction factors for all probes and filters are shown in

Table 4.2.

	SXR-A	SXR-B	SXR-C	SXR-D
857μm	0.947	0.961	1.000	0.989
421μm	0.880	0.855	1.000	0.946

Table 4.2: Brightness correction factors for each profile, thin and thick beryllium filter.

The variation ($< 5\%$) between SXR-C and SXR-D, as well as the variation between SXR-A and SXR-B is considered typical. However, the large variation between A,B and C,D ($> 10\%$) particularly in the thin filter case, is surprising. An explanation for this empirical factor has been sought but not yet found. Figure 4.10 shows the difference in core brightness between probe SXR-A and SXR-B (top) and between SXR-A and SXR-C (bottom) as a function of time. The stability in time indicates this is not a temperature-dependent effect and suggests a problem in the geometry. In fact, it is striking that the fundamental difference between the probes is that SXR-A, B have a centered pinhole geometry while SXR-C, D have an offset pinhole geometry.

Several possible causes have been ruled out by careful measurement or simulation. Uncertainty in the location of individual diode boards with respect to their pinholes (toroidal, poloidal or radial) would have to be measurably large to induce change of this magnitude. The beryllium used in the centered and offset pinholes were made from the same batch and should therefore have the same areal density and purity. The effective difference in silicon thickness due to the angle induced by the offset pinhole contributes a systematic difference of only $\sim$ 1-2% compared with the centered pinhole. The most likely explanation for this difference is either 1) uncertainty in the actual/effective beryllium foil thickness (which could be caused by contaminated foils or by incorrect curvature of the beryllium holder), or 2) a difference in the fabricated *etendue* between the two sets of probetips. The x-ray response using the physical

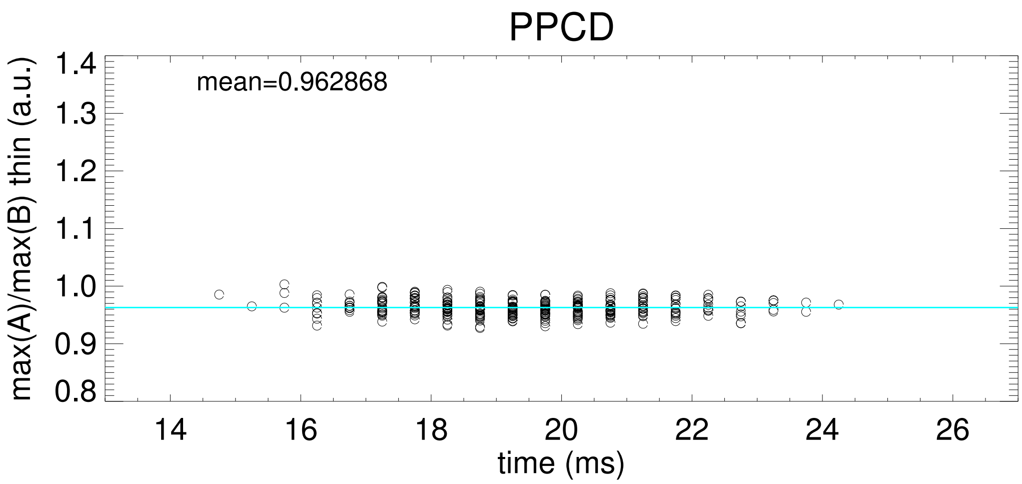

(a) Ratio of thin filter core-viewing diode from SXR-A to that of SXR-B.

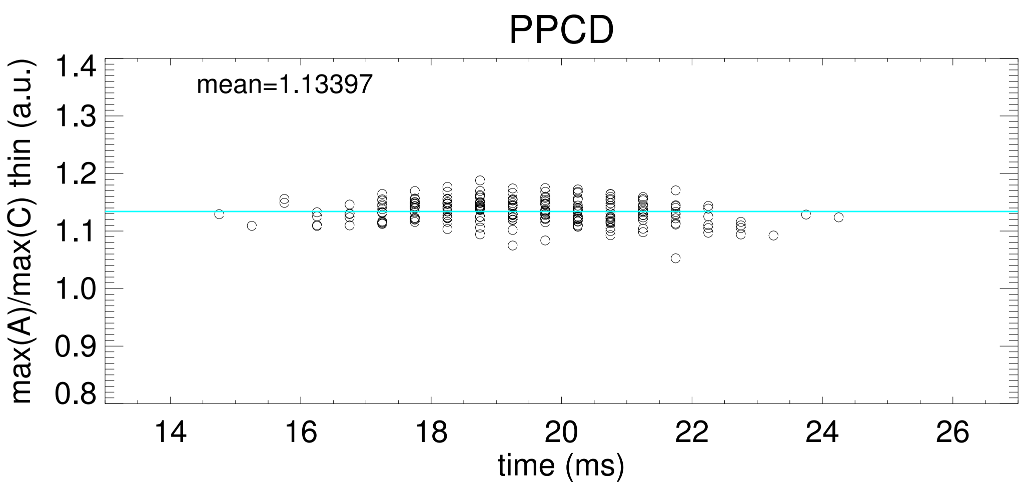

(b) Ratio of thin filter core-viewing diode from SXR-A to that of SXR-C.

Figure 4.10: Comparison of peak signals between probes indicates that signals between the two centered-pinhole probes (SXR-A, SXR-B) vary by about 5%, while signals between the centered (SXR-A) and offset (SXR-C) probes vary by more than 10%. This variation is persistent over a database of samples averaged over 0.5 ms windows during high-current PPCD. This database is used to calculate correction factors for each probe and filter thickness, normalizing to that of SXR-C. Correction factors for all probes and foils are listed in Table 4.2.

geometry of each probe will be investigated once a suitable x-ray source is acquired. This should help to identify the cause of the empirical correction factors.

4.2 Measurement Capabilities

4.2.1 Addition of Direct-Brightness T_e Measurement

The probes are designed to hold two separate filters in the same poloidal geometry so that the direct brightness technique can be used with pairs of diodes. Figure 4.11 shows the layout of (left to right) the diode board, filters, pinholes and probetip for the offset-pinhole geometry utilized for SXR-C and D. Each probe contains two columns of 10 diodes where each column has its own filter and pinhole. (Note that the filters and pinholes for SXR-C and SXR-D are offset from center to optimize the field-of-view, for SXR-A and B the entire geometry is centered). The two columns are separated toroidally by 4 mm at the diode board, which is sufficiently small that the cones-of-sight for each column overlap in the plasma. As a result, each pair of diodes can be considered as viewing the same plasma volume. Two diodes looking at the same plasma through different filters will sample different components of the energy distribution, and their measured brightness can be used directly to calculate electron temperature. This approximately gives the hottest temperature along each line-of-sight, resulting in near-horizontal and near-vertical radial profiles of electron temperature (see §2.3.2 for a detailed description of the direct-brightness technique).

Simulations indicate that the probe geometry will provide good equilibrium temperature profiles. Figure 4.12 shows the calculated T_e (dots) compared with the input to the simulation (line) for all four probes. For equilibrium plasma, the impact parameter is an approximate flux-surface coordinate, and so the temperature at a given impact parameter should be the same for each probe. The temperature curves for the

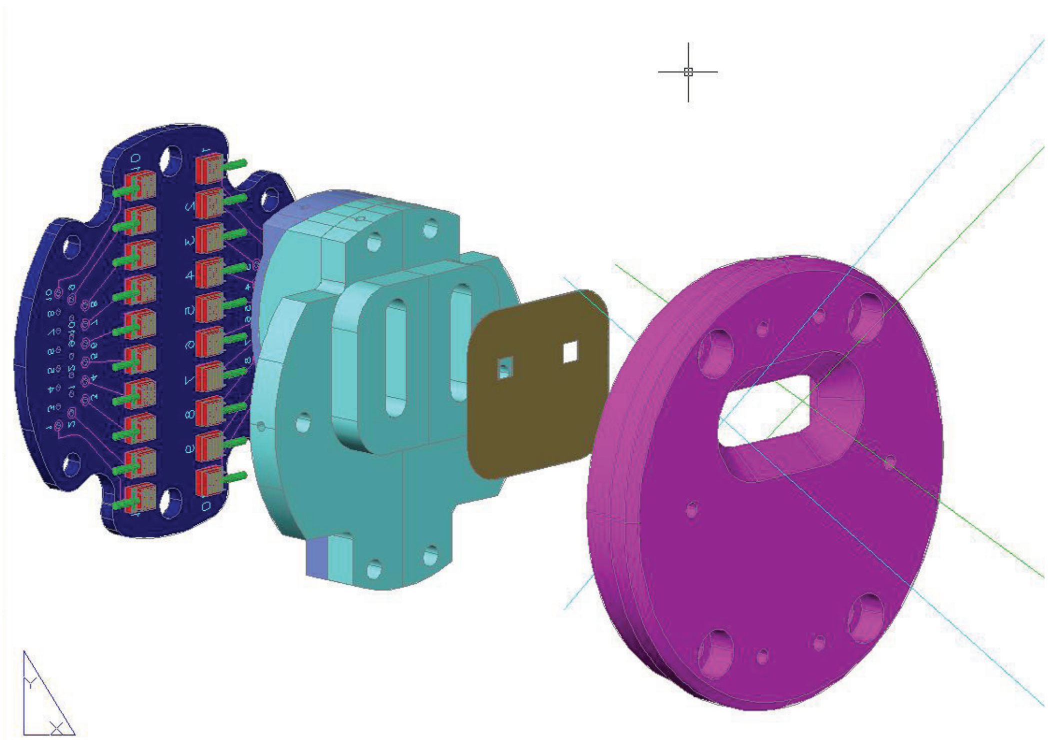

Figure 4.11: Exploded view of probetip with diode board illustrates the shared lines-of-sight between two columns of diodes for the offset-pinhole design. (The final diode board design was modified to reduce the diameter and remove the screw-clearance tabs, however, the diode placement did not change). Beryllium filters are not visible here but are held between the blue frames and the teal filter holders.

four probes line up well. The bottom plot shows that the residual error in the calculation is less than 2%. (This uncertainty is inherent to the mathematical technique and is independent of measurement uncertainties).

The new diagnostic also provides insight into spatial islands through the direct-brightness technique. Figure 4.13 shows the horizontal temperature profiles (from SXR-A, B) versus impact parameter for simulations including a SHAx-type structure for a series of simulations (refer to §1.1.2 for a description of SHAx and island plasmas). A SHAx structure with an amplitude 35% of peak T_e is assumed to be at 135° in the calculation of the $T_e(R)$ curves, while its location in each simulation is varied. The simulations contain a SHAx island at various poloidal angles located with r_0/a=0.2 and δ_r/a=0.3 (refer to §2.1.1 for a description of the model parameters). The green line is the temperature of the simulated plasma, while the black and blue triangles are the calculated values for probes A and B. The direct-brightness technique accurately identifies the temperature and position of the SHAx structure even in cases where it is far from the guess of 135°.

Islands are not measured as accurately as SHAx structures, but are still identified. Figure 4.14 shows the horizontal temperature profiles (SXR-A, B) for simulations with a bean-shaped island. In this simulation, a bean island is assumed at 135° in the $T_e(R)$ calculation. The simulations create an island, (35% of the bulk T_e), for r_0/a=0.2, δ_r/a=0.06, and δ_θ=30°. Unfortunately, although the calculated temperature profile does approximate the simulated island, the amplitude and poloidal location are not accurately measured. As expected, the measured temperature is sometimes cooler than the actual value due to the weighted-average effect of the technique. The incorrect position of the island is due to the sensitivity of bean-island measurements to the $T_e(R)$ assumption of an island at 135°. However, this measurement is still useful

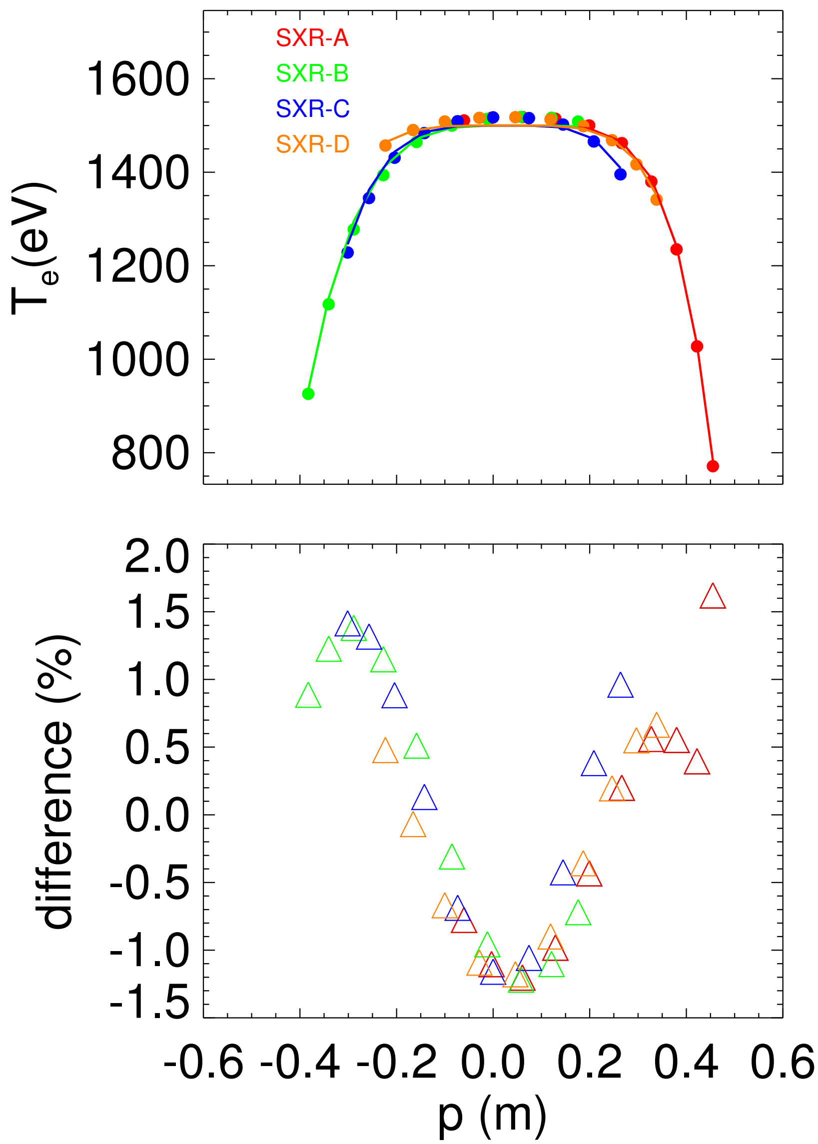

Figure 4.12: (Top) direct-brightness temperature profile for each of the four probes (dots) for a simulated temperature (lines) as a function of impact parameter. (Bottom) percent error between the simulated and calculated T_e is less than 2%.

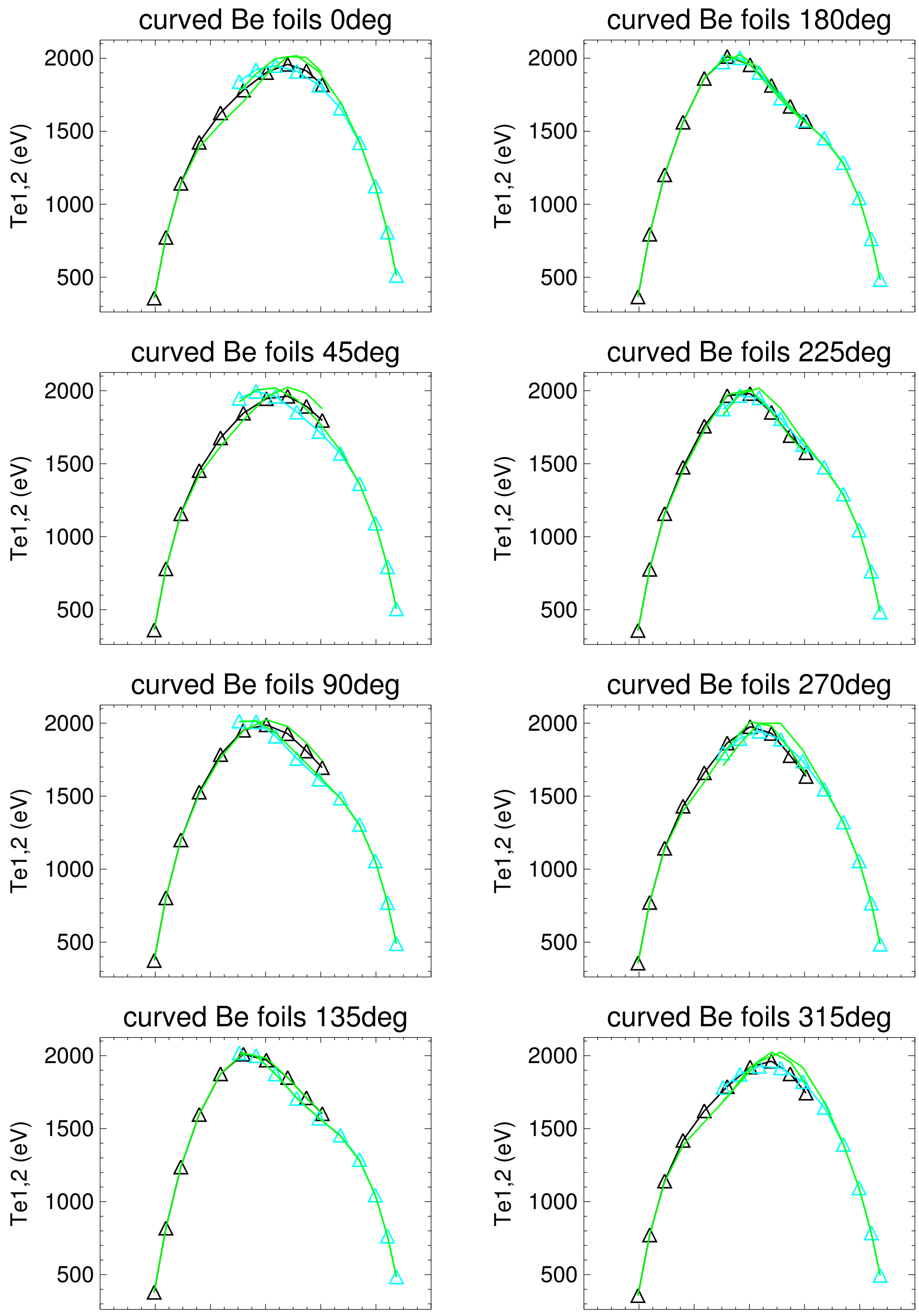

Figure 4.13: DB T_e calculated for a SHAx island at many angles, with the $T_e(R)$ model assuming a SHAx island at 135° poloidal. The black and blue triangles represent the measured brightnesses for SXR-A and SXR-B, while the green lines are the temperature of the input model. The system should be able to reproduce a SHAx profile quite well.

in identifying the existence of an island and approximating its temperature.

4.2.2 Tomographic Reconstruction

The 20 near-vertical and 20 near-horizontal measurements for each foil thickness can be reconstructed into a two-dimensional map of tomographic T_e. In general, the 4-probe tomography system at 90° toroidal has tomographic reconstructions similar in quality to the 300° toroidal ideal case presented in §3.3.4. For example, Figures 4.15 and 4.16 show the reconstructed emissivity cross-section and temperature cross-section for the typical equilibrium plasma case (reconstruction parameters $m = 1, l = 5, svd = 0.01$, refer to §2.2.2 for a description of the reconstruction parameters). The reconstructed temperature matches the model despite small oscillations in emissivity.

For island structures, the tomographic reconstruction is fairly reliable in emissivity but still generates spatial ripples in temperature. Figures 4.17 and 4.18 shows reconstructed emissivity for a series of simulations with a bean-shaped island or a SHAx structure located at 45° intervals. The island position is correctly reconstructed at all locations, although the accuracy of its shape and amplitude are dependent on angle. As with the direct-brightness technique, SHAx islands are more accurately reconstructed than bean-shaped islands.

As seen previously however, once islands are introduced into the system, ripples begin to appear in the reconstructed emissivities. In Figure 4.19, a cross-section of the emissivity map for an island at the worst-case position of 135° shows substantial differences between the model and reconstructed emissivity. The reconstructed temperature, shown in Figure 4.20 continues to be plagued by oscillations. However, these oscillations are still reduced as compared with the 300° toroidal location.

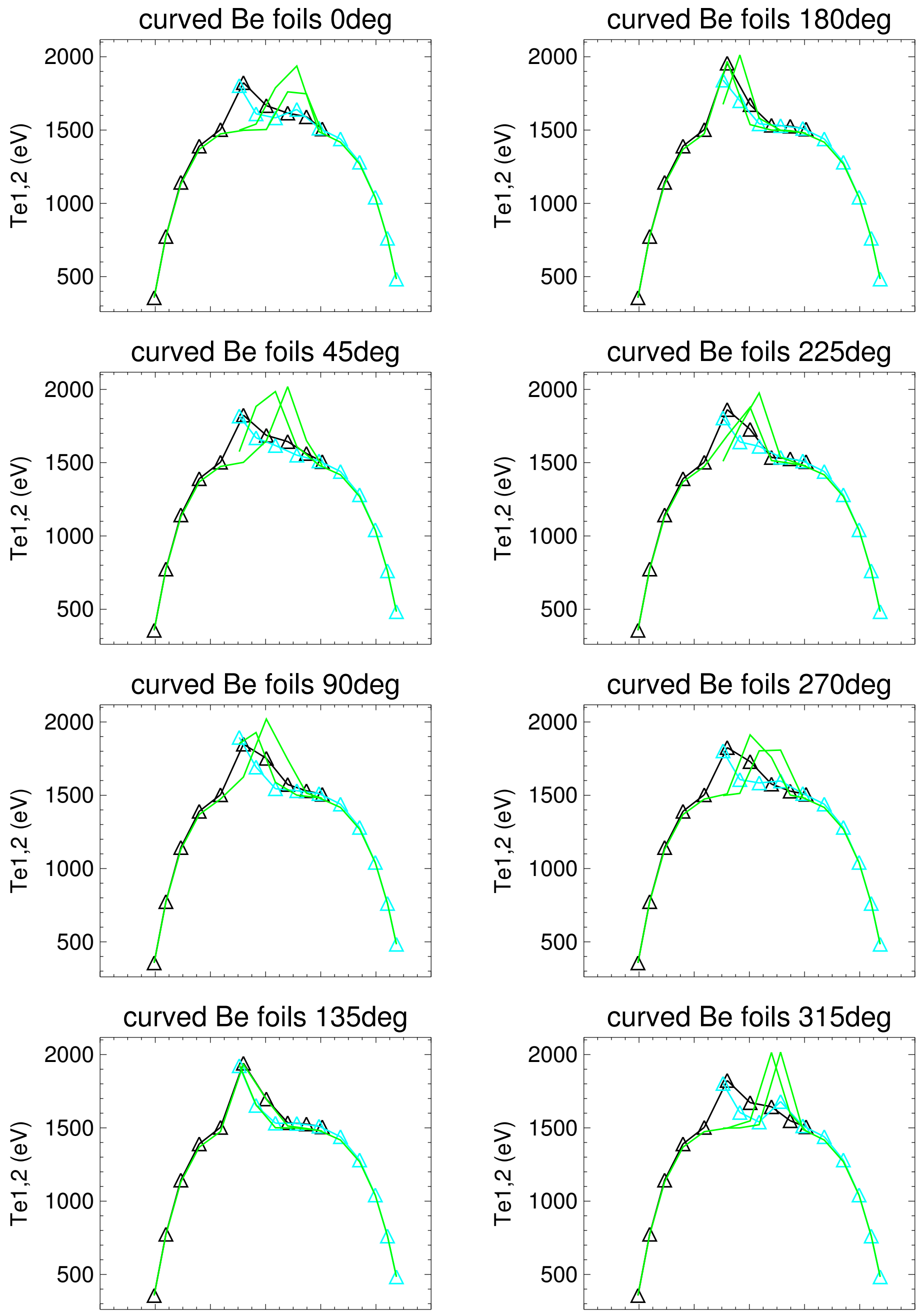

Figure 4.14: Simulation showing T_e calculated for a bean island at many angles, with the $T_e(R)$ model assuming a bean island at 135° poloidal. Again, the black and blue triangles represent the measured brightnesses for SXR-A and SXR-B, while the green lines are the temperature of the input model. The direct-brightness measurement clearly detects an island structure in every case, and the measured amplitude is reasonable (although sometimes under-measured). However, the measured location is strongly dependent on the location of the modeled island and cannot be assumed to be accurate in an experimental dataset.

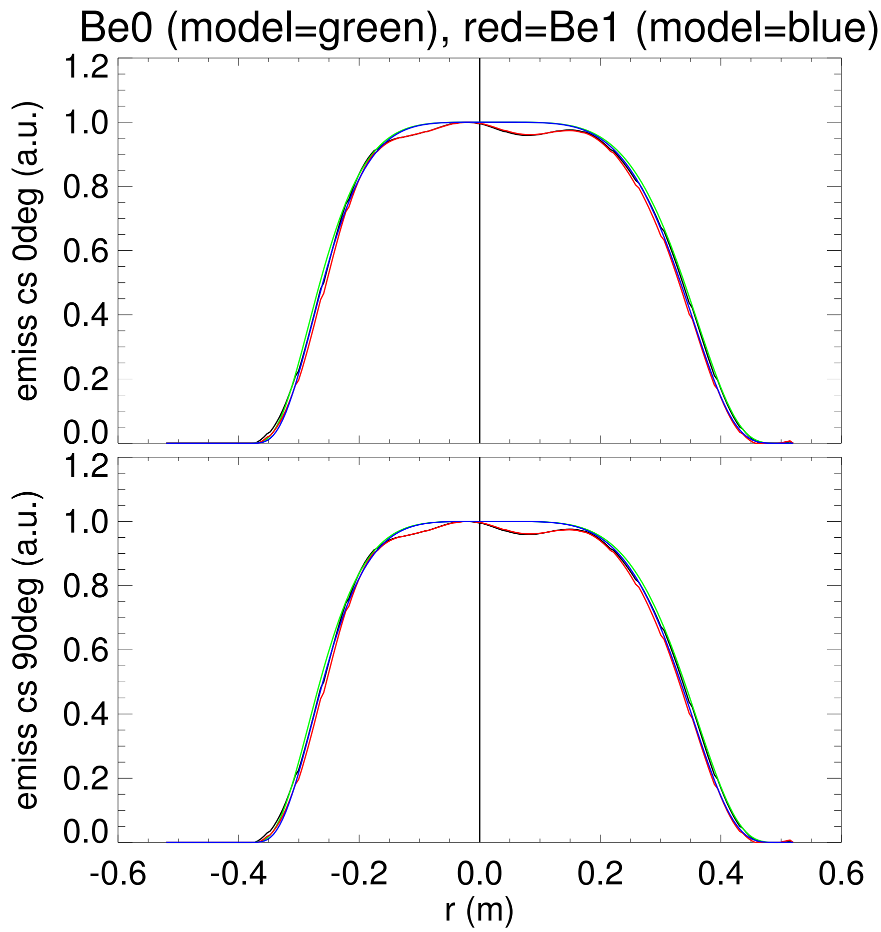

Figure 4.15: SXR-A, B (top) and SXR-C,D (bottom) cross-sections of the reconstructed emissivity based on tomographic reconstruction of the equilibrium plasma at 90° toroidal. In each plot, the emissivity input into the model for the thin filter is green, while the model emissivity through the thick filter is blue. The tomographically reconstruction of thin filter results in the 'measured' emissivity plotted in black, and the 'measured' emissivity for thick filter is shown in red. The model and reconstruction deviate very slightly near the edge of the plasma where the brightness profile is not well-defined.

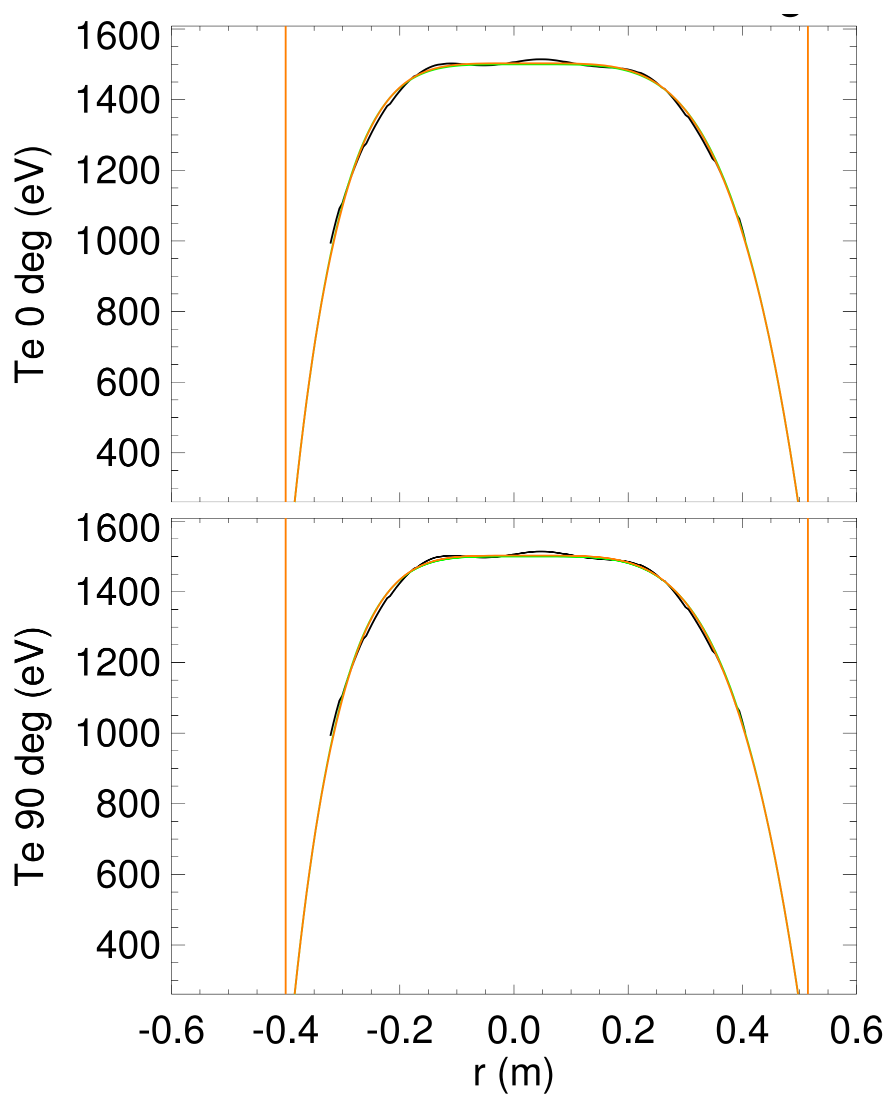

Figure 4.16: A cross-section of the tomographic temperature for this simulation. The full tomographic temperature is a 2D map similar to the emissivity map. For clarity, a horizontal cross-section of this reconstructed temperature is plotted in black. The temperature profile defined by the model input in the simulation is plotted in orange. Although there are still small oscillations in the emissivity profile, they nearly cancel when the ratio is taken to calculate the temperature profile.

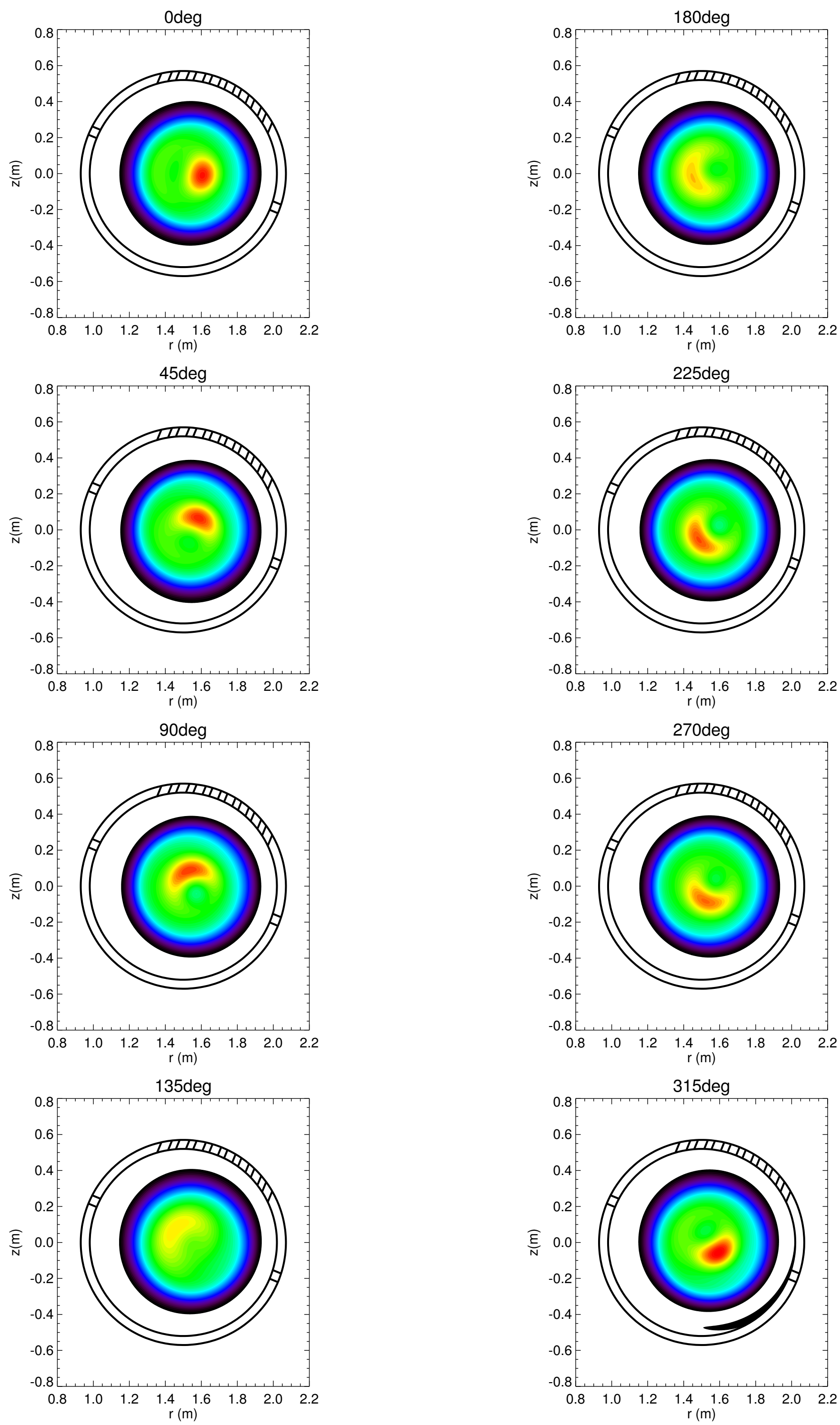

Figure 4.17: Reconstructed emissivity for a bean shaped island at 45° intervals in poloidal angle with the final 4 probe geometry. Accuracy of the reconstructed topology depends on poloidal angle of the island, but the system accurately reconstructs the location for all poloidal angles.

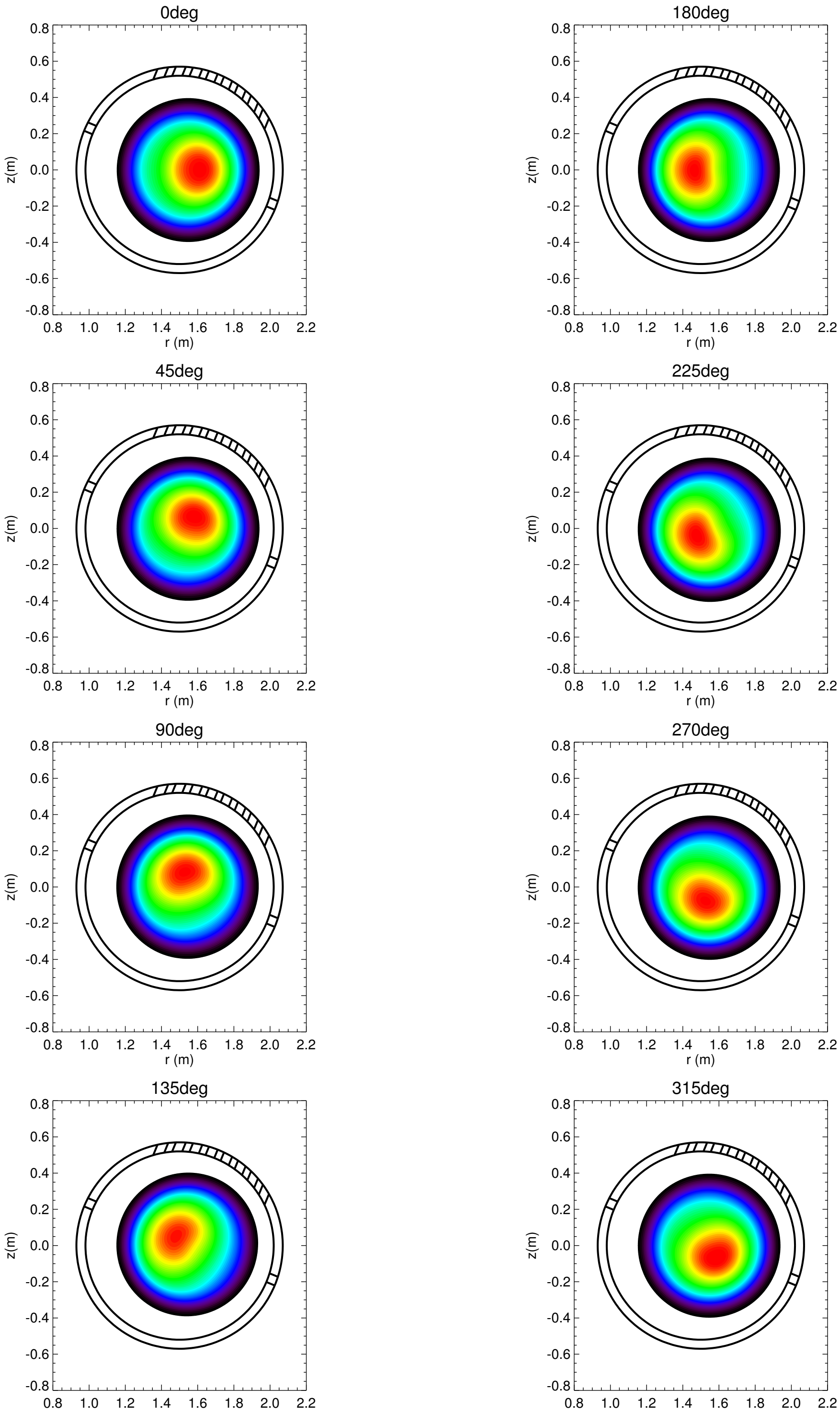

Figure 4.18: Reconstructed emissivity for a SHAx island at 45° intervals in poloidal angle with the final 4 probe geometry. The SHAx shape and location is well-reconstructed at all poloidal angles.

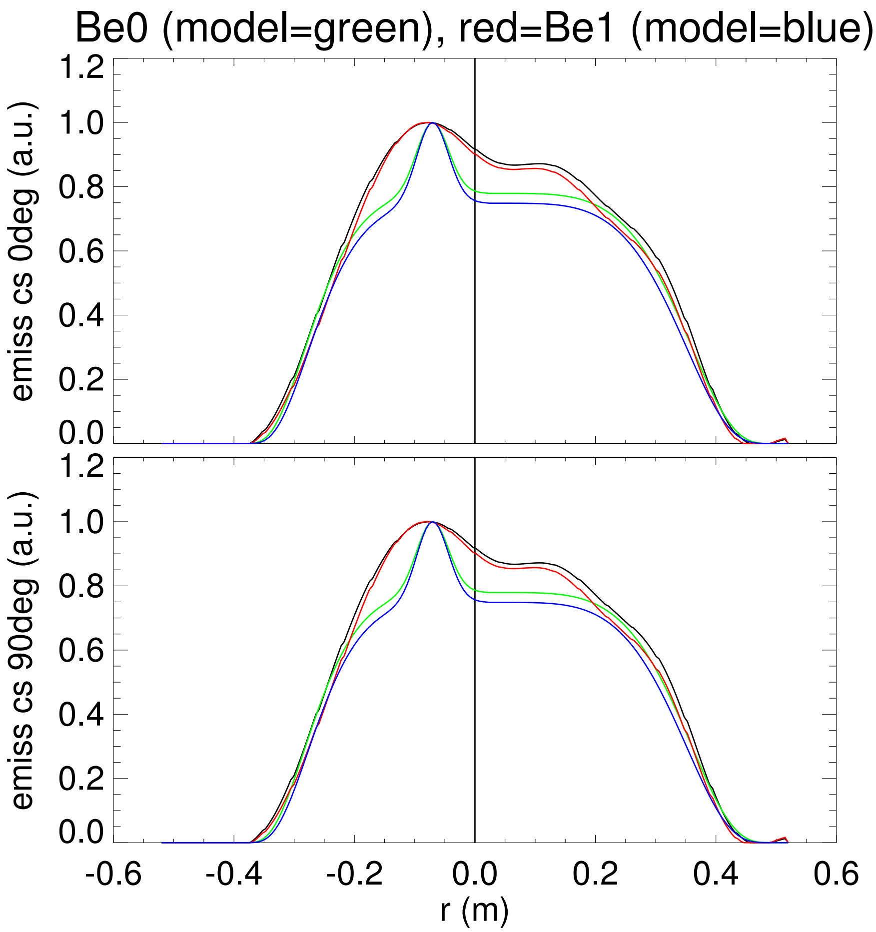

Figure 4.19: SXR-A, B (top) and SXR-C, D (bottom) cross-sections of the reconstructed emissivity based on tomographic reconstruction of a plasma with a bean-shaped island at 135°. In each plot, the emissivity input into the model for the thin filter is green, while the model emissivity through the thick filter is blue. Modeled (green and blue) and reconstructed (black and red) emissivity profiles (for the thin and thick Be filters, respectively).

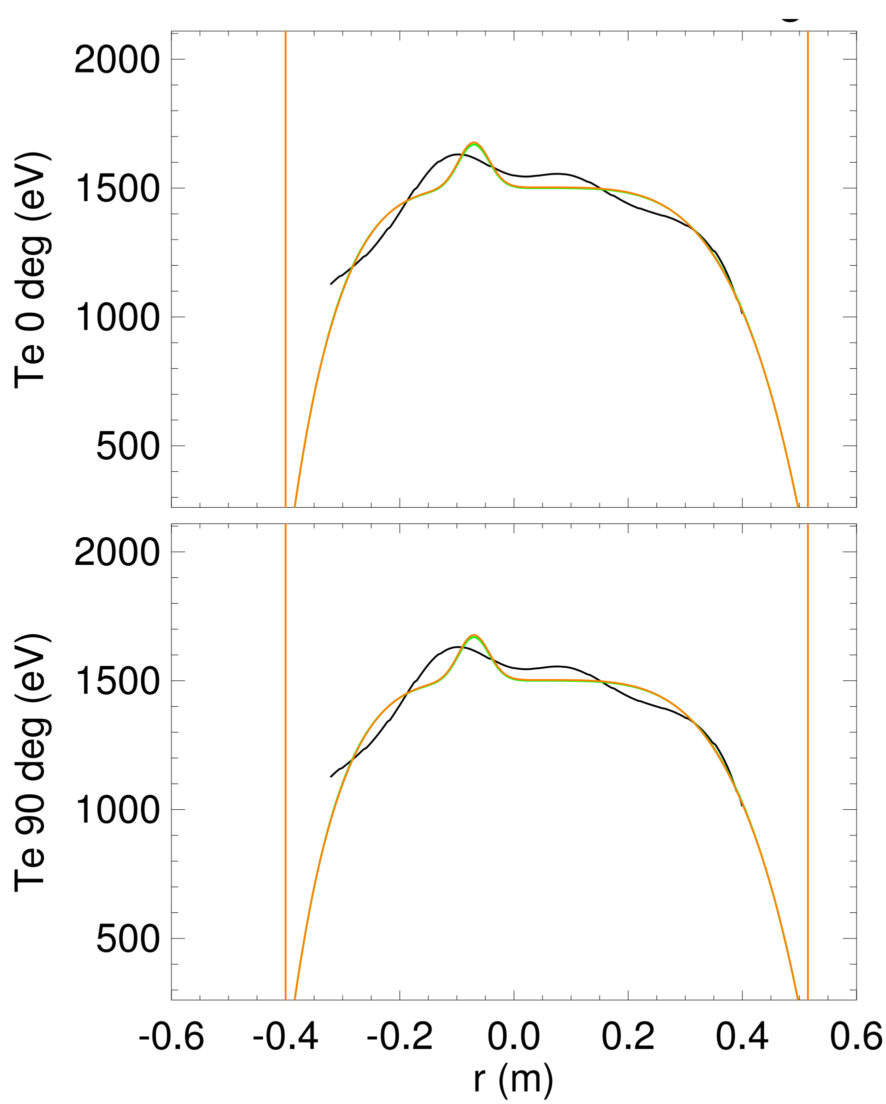

Figure 4.20: A cross-section of the tomographic temperature in a simulation with a bean-shaped island at 135°. For clarity, a horizontal cross-section of this reconstructed temperature is plotted in black. The temperature profile defined by the model input in the simulation is plotted in orange. The introduction of the island creates discrepancies between the modeled and reconstructed emissivity cross-section, which appear as oscillations in the reconstructed temperature profile.

4.2.3 Capability to Add a Fifth Probe

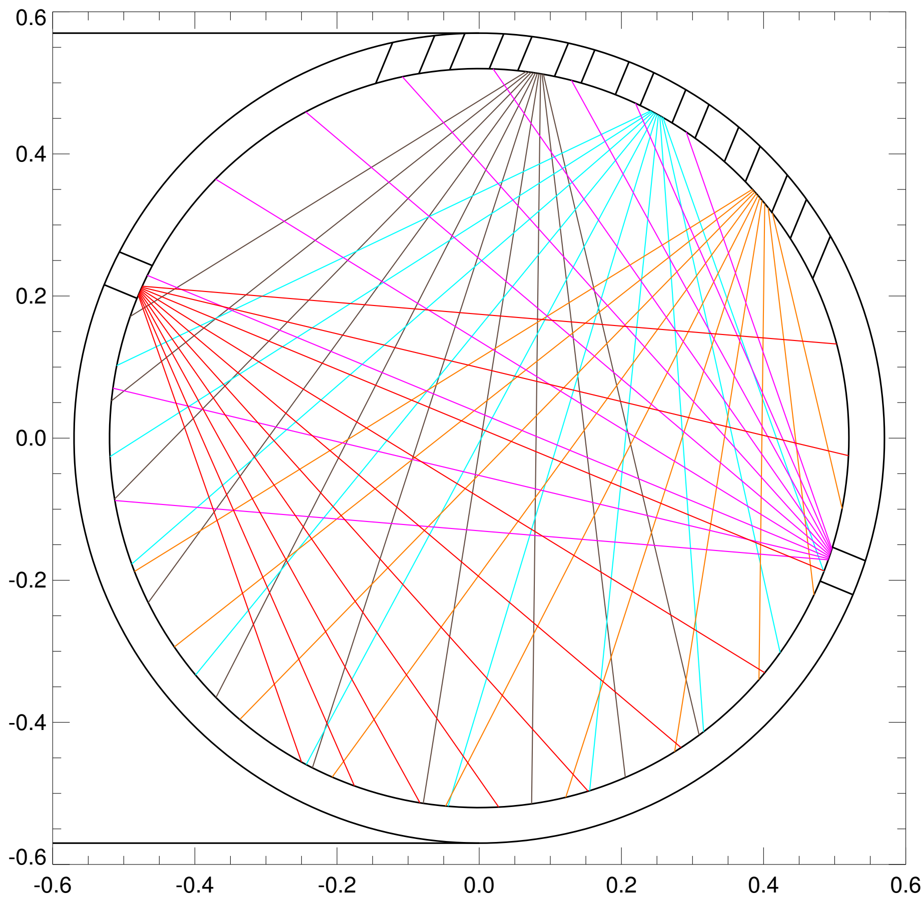

Figure 4.21: A 5-probe geometry continues to use portholes 2, 6, 9 and 10 (where port 1 is the outermost most boxport porthole and 1 and 10 are non-boxport portholes), while adding porthole 4.

A future capability of the 90° toroidal location is space for additional probes. The boxport has eight portholes, of which up to four could potentially be used for the SXR two-color diagnostic. The initial system was built with four probes because the addition of a fifth probe did not substantially improve tomographic reconstructions. In these simulations, the fifth probe was added into the boxport in between

SXR-A and B, as seen in Figure 4.21. Figures 4.22 and 4.23 show tomographically reconstructed emissivities using five probes for the same bean and SHAx-shaped islands that were presented with four probes in Figures 4.17-4.18. The difference in emissivities between the four and five probe bean shaped island case is less than 3% the maximum emissivity, while the SHAx case is even less.

Nevertheless, it is worth considering an expansion of the diagnostic in the future. The resolution of the direct-brightness measurement is directly proportional to the number of lines-of-sight, so adding a fifth probe in the boxport would improve the resolution of the horizontal temperature profile. Alternatively, the addition of probes at other poloidal angles may benefit the tomographic reconstruction. It is possible to improve the reconstruction if an additional probe either stabilizes the mathematical artifacts or increases spatial resolution. For example, a probe in the lower-inboard quadrant might further improve the reconstruction. These alternative porthole possibilities are options for future work.

4.3 Hurdles in Diagnostic Development

Shortly after SXR-D was installed in prototype mode for first-light, a blank was used in place of a pinhole to block all x-rays from entering the detectors during a test of electrical noise. Unfortunately, a clear temporal oscillation was seen in this 'blanked' signal as the problem of magnetic pickup presented itself. The top plot in Figure 4.24 shows an example of this signal measured during a 400 kA $F = 0$ shot. (Recall that $F = 0$ plasmas tend to develop quasi-single helicity states with very large magnetic structures. Therefore $F = 0$ plasmas create some of the strongest magnetic signals). For comparison, the bottom plot shows the poloidal magnetic field coil nearest to the SXR diagnostic (at 87° toroidal, 241° poloidal). Figure 4.25 displays the power spectrum of the SXR signal for the shot, indicating a characteristic frequency around

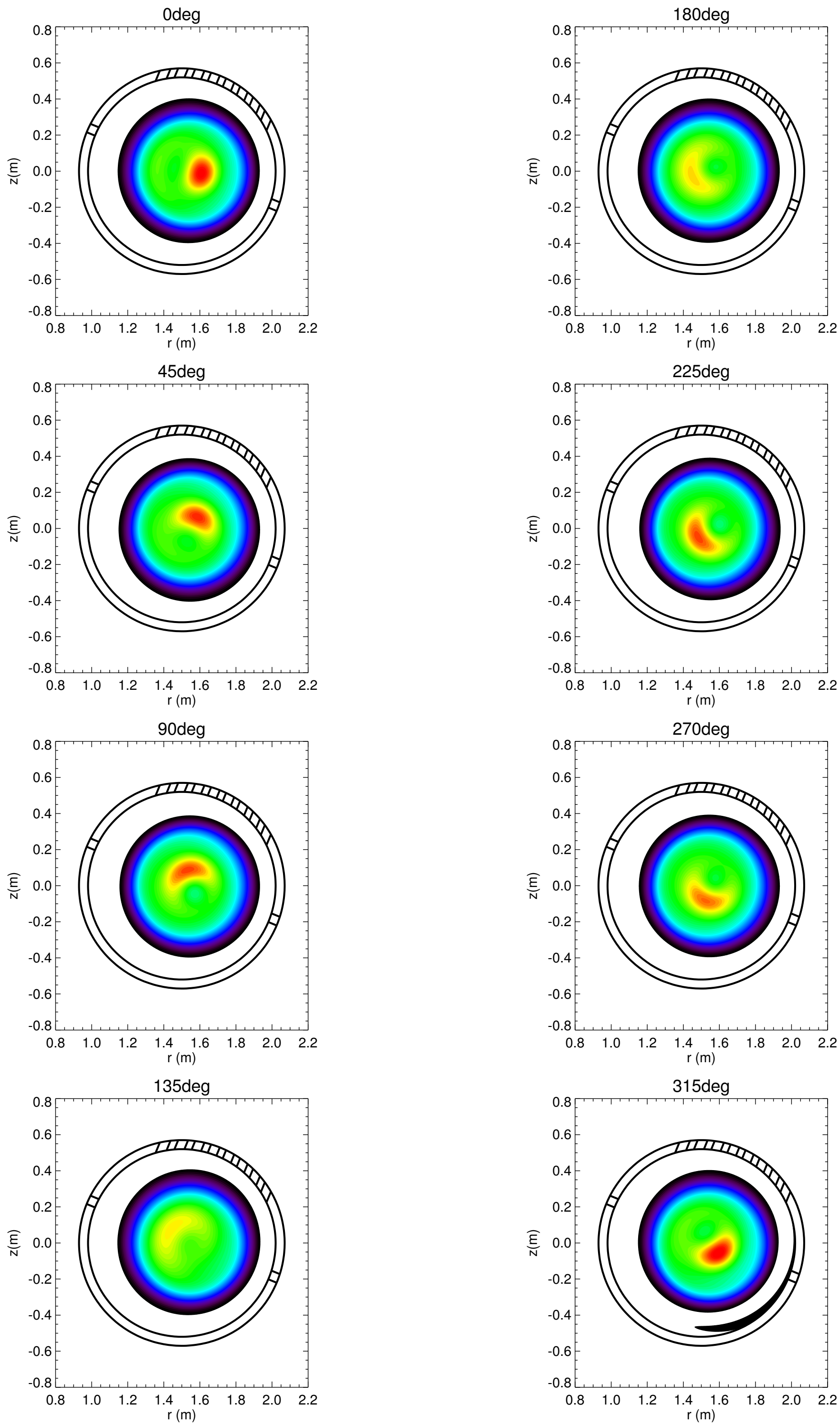

Figure 4.22: Reconstructed emissivity for a plasma with islands at various poloidal locations using a 5-probe tomography system. This system contains the original four probes described throughout this Chapter, plus one additional probe in the center of the boxport. The addition of a fifth probe does not substantially improve the reconstructions.

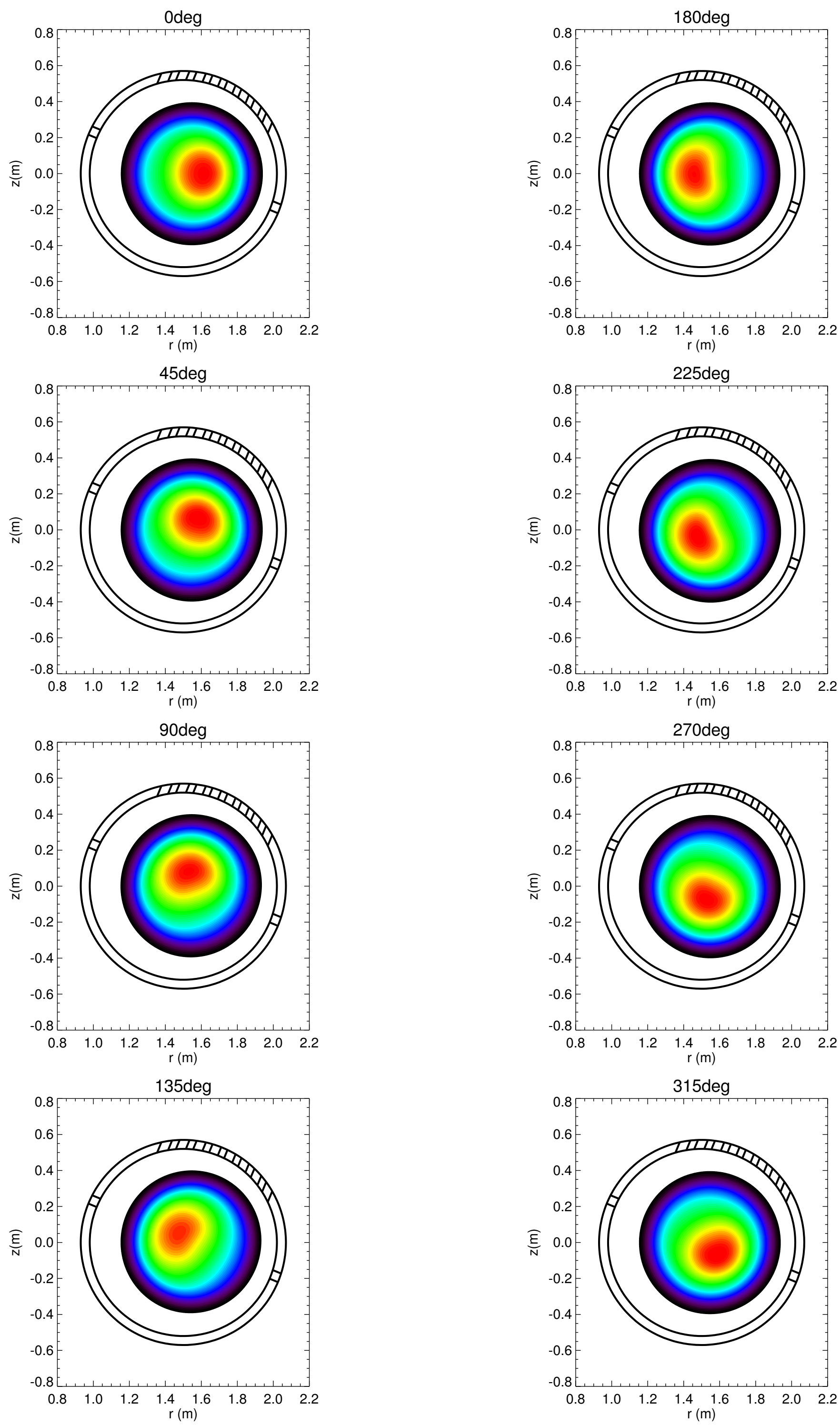

Figure 4.23: Reconstructed emissivities for a SHAx island with a 5 probe system. Again, a 5 probe system does not provide a clear advantage over a 4 probe system.

15 kHz (red). For comparison, a plasma shot with the same parameters but with a magnetic mode with zero rotation velocity (locked) is shown in black. When the plasma locks, the 15 kHz signal in the SXR goes away. The signal is clearly caused by some plasma phenomenon.

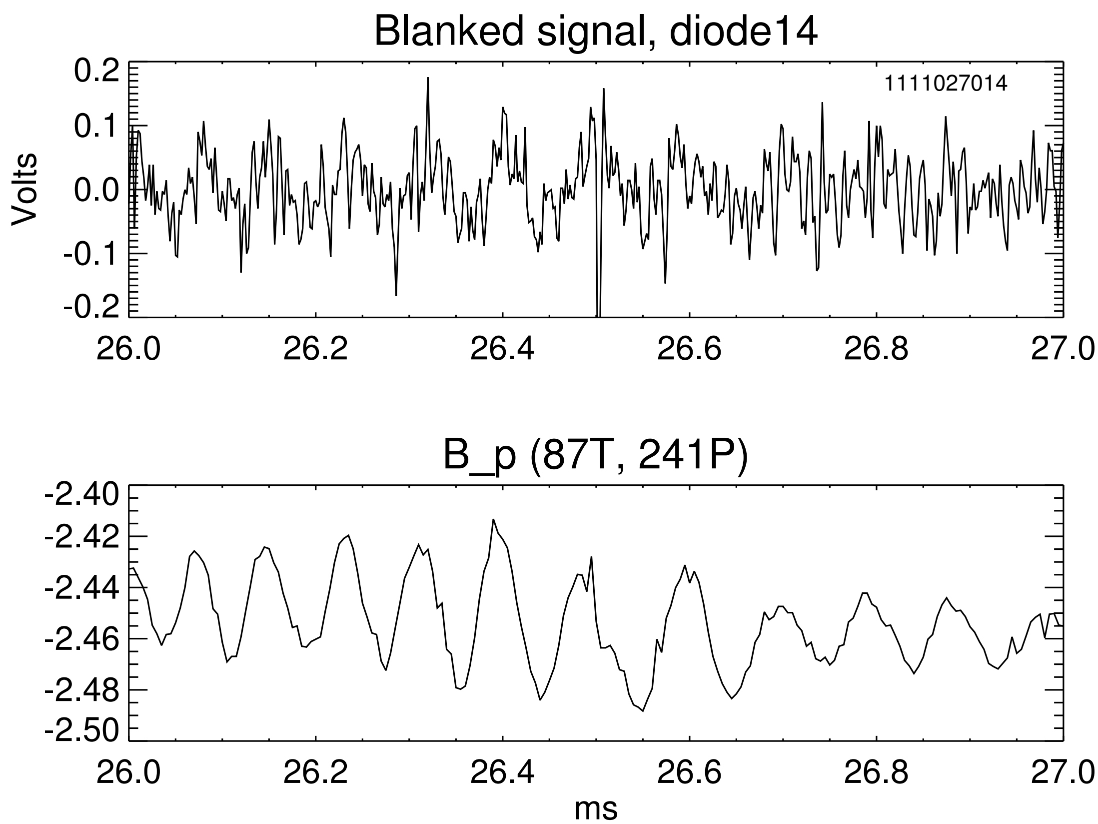

Figure 4.24: (Top) Measurement from a central diode on SXR-D (diode 14) during a plasma when the pinhole is covered so that no x-rays are incident on the detectors. A 15 kHz oscillation is seen in what should be random electronic noise. (Bottom) The poloidal field measurement coil nearest to the probe shows the same 15 kHz signal as seen on SXR-D, suggesting that the oscillation in the signal may be magnetic pickup.

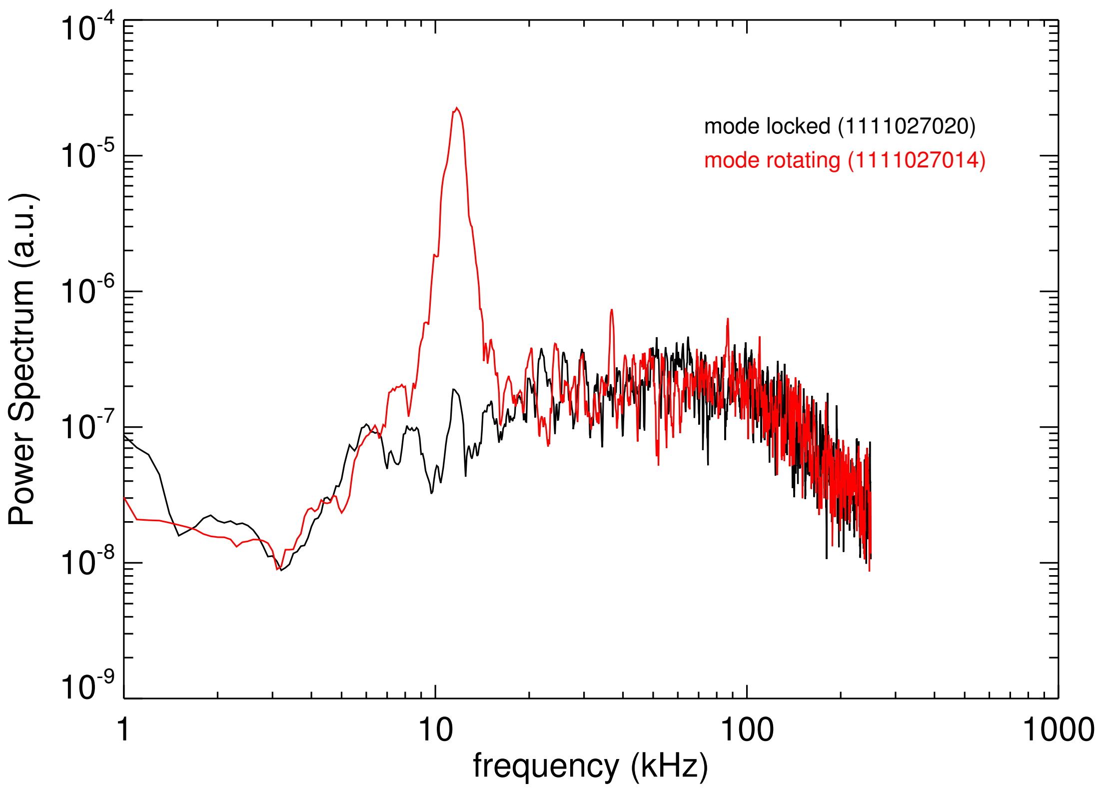

Figure 4.25: Power spectrum of the signal shown in Figure 4.24 (red). This 400 kA F=0 plasma shot has a rotating magnetic structure causing the phantom signal at 15 kHz. For comparison, a similar plasma with a locked magnetic structure is shown in black. There is no evidence of the signal when the mode is locked.

4.3.1 Potential Non-Magnetic Mode Sources

To eliminate the spurious signal, it first had to be correctly identified. One possibility was that x-rays were not being successfully blocked with the blanked pinhole. The probehead was carefully designed to eliminate the possibility of x-ray reflections, but if the x-rays were able to penetrate the 100 μm thick stainless steel cover replacing the pinholes, then a signal would register. Although this possibility is inconsistent with the evidence that the signal oscillates around zero (the x-ray signal is never negative), a double-thick stainless steel blank (250 μm) was installed to rule out the possibility. As expected, this did not affect the signal. Furthermore, the possibility of transmission or cascading of high-energy photons can be calculated using the Stanford Linear Accelerator (SLAC) online electron gamma shower Monte Carlo simulation.[2] Simulations indicate that incident x-ray energies would have to be well over 100 keV before any transmission or cascading through 100 μm of stainless steel would occur.

The other possible source of a spurious signal not tied to the magnetic modes in the plasma would be the active feedback correction coils on MST. The active feedback coils work to null the radial magnetic field at the poloidal gap of the MST vessel and operate with switching power supplies. The power supplies have a switching frequency in the 10-20 kHz range, which is the same frequency region in which the phantom signal occurs. Figure 4.26 shows the relationship between the phase of the SXR-D signal for diode 14 and that of the active feedback correction coil at 88° poloidal. There is no clear correlation between these two signals, so it is unlikely that the spurious signal is magnetic pickup from the active feedback correction system.

---

[2] http://www2.slac.stanford.edu/vvc/egs/basicsimtool.html

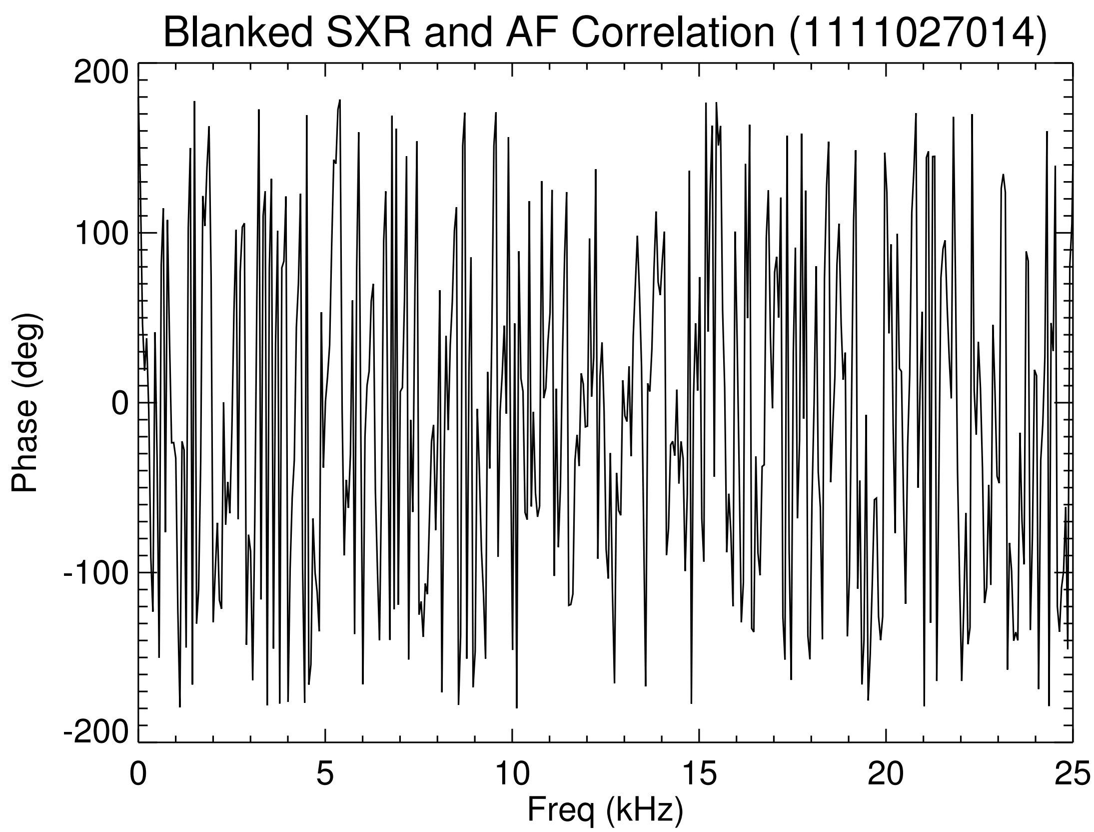

Figure 4.26: Phase correlation between SXR-D diode 14 signal and the active feedback correction coil at 88° poloidal for the same shot shown in Figures 4.24-4.25. The lack of clear phase relationship between the two signals indicates that the spurious signal is not induced by the active feedback system.

4.3.2 Evidence That Signal is Pickup from Magnetic Modes

Applying the same technique to the signals from the MST magnetic field measurement coils shows a clear relationship between the signal on the blanked SXR probe and the magnetic structure in the plasma. The phase correlation between the SXR signal for a rotating plasma and the poloidal magnetic field is shown in Figure 4.27. The SXR signal is clearly correlated to the poloidal magnetic field in MST. As expected, the SXR signal is also correlated to the toroidal component of the magnetic field.

The final indication that the phantom signal seen by the SXR diagnostic is due to the magnetic field of the plasma is that the pickup drops off as the probe is moved away from the plasma. Figure 4.28 contains the power spectra for a series of plasma shots where the probe has been moved successively further from the plasma edge. In the closest position (orange), the probetip is 10 mm beyond the inner wall of MST and is actually acting as a limiter for the plasma. The green case occurs when the probe is in its typical measurement position of 10 mm behind the inner wall. Finally, in the extreme furthest case (light blue), the probe has been retracted all the way to the VAT valve at a distance of -40 mm from the inner wall of MST. This experiment shows a clear drop in pickup amplitude as the detector moves away from the plasma, as expected if the signal is magnetic pickup from the plasma itself. The scan indicates that the probe must be more than 30 mm behind the inner wall of MST before the magnetic pickup is eliminated. However, such a position would completely destroy the diagnostic field-of-view, leaving each probe with only 3 lines-of-sight into the plasma. Therefore, a different approach must be taken to eliminate this magnetic signal.

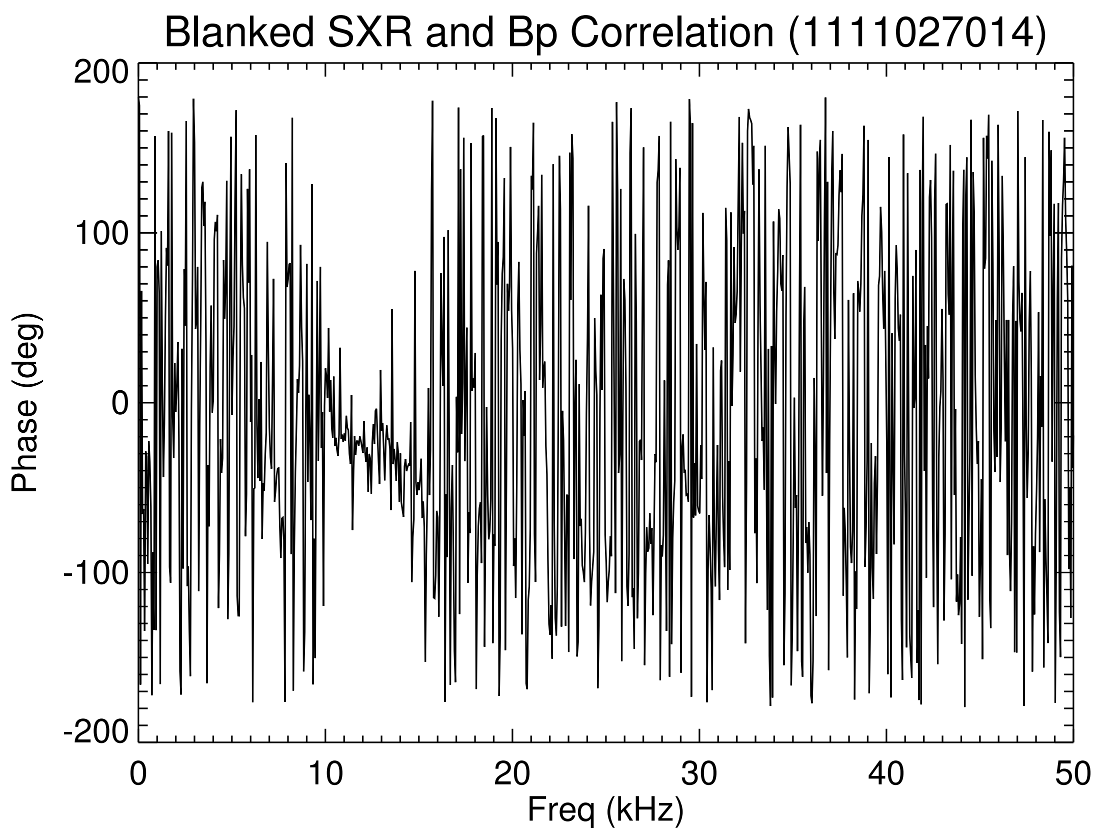

Figure 4.27: Phase correlation between SXR-D diode 14 signal and poloidal magnetic field signal for the same shot shown in Figures 4.24-4.26. In contrast to the active feedback case, there is a clear relationship between the phase of the spurious signal and the phase of the plasma magnetics measured by the magnetic coils in the 10-15 kHz range.

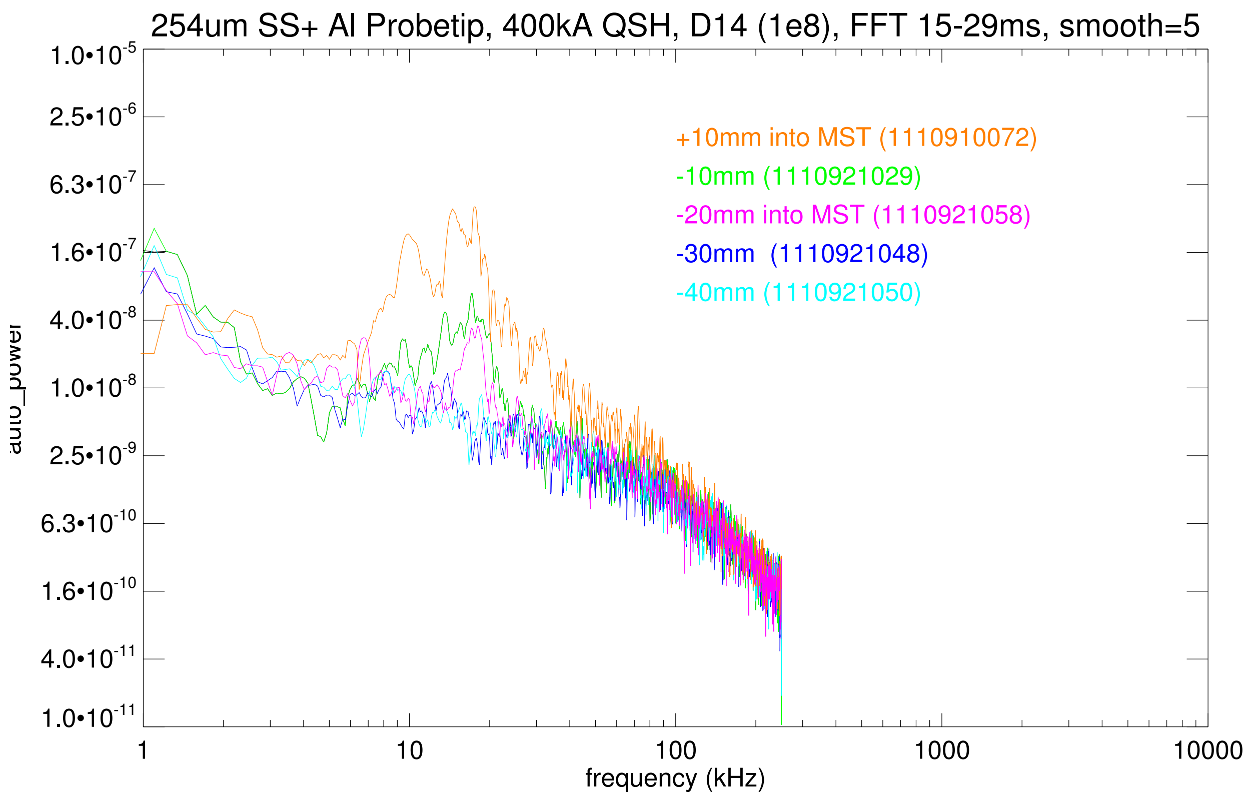

Figure 4.28: Power spectra for the phantom signal as the probe is moved further away from the plasma (+0 mm is the inner wall of MST) in similar 400 kA F=0 plasmas at 10^8 gain. The amplitude of the spurious signal decreases as the probe is moved away, further supporting the hypothesis that it is caused by magnetic pickup from the plasma.

4.4 Magnetic Pickup Mitigation In Final Design

A series of hardware modifications were undertaken to reduce this magnetic pickup. The modifications focused on both reducing loops of enclosed area in the internal wiring of the probe and on improving magnetic shielding around the diodes. A complete description of the hardware modifications, including several tests that did not succeed at reducing the pickup, can be found in Appendix A. The final probehead features minimal loops of enclosed area, a 5-layer diode board with top and bottom shielding ground planes, and a thick-walled copper housing.

There is no evidence of pickup visible to the naked eye or in a power-spectrum analysis for the final design at 10^8 gain. Figure 4.29 shows another example of the power-spectrum of the original design, with blanked diode and aluminum housing, contaminated by magnetic pickup in solid black. The dashed green trace shows a blanked diode using the final design, including new diode board and copper housing, for a similar rotating plasma. The green trace is free of pickup around the tearing mode frequency of 10-15 kHz. Despite this dramatic improvement in the power spectrum however, contamination is still detectable using cross-correlation or wavelet analysis. Figure 4.30 shows a cross-correlation analysis between the Bt87 magnetics signal and 6 diodes on SXR-D for a blanked shot using the final probetip design. Only six diodes were installed during this test in the prototyping phase, but the magnetic pickup is evident on all diodes, despite not being visible by eye or in a power spectrum.

To determine the impact of the pickup on the desired SXR measurement, it is important to quantify the relative amplitudes of the SXR signal, the magnetic pickup, and random electronic noise. A test was performed using the final probehead hardware configuration to determine the magnitude of the magnetic contamination at 10^8 and 10^9 gains. A 300 μm piece of copper was installed covering diodes 2-5

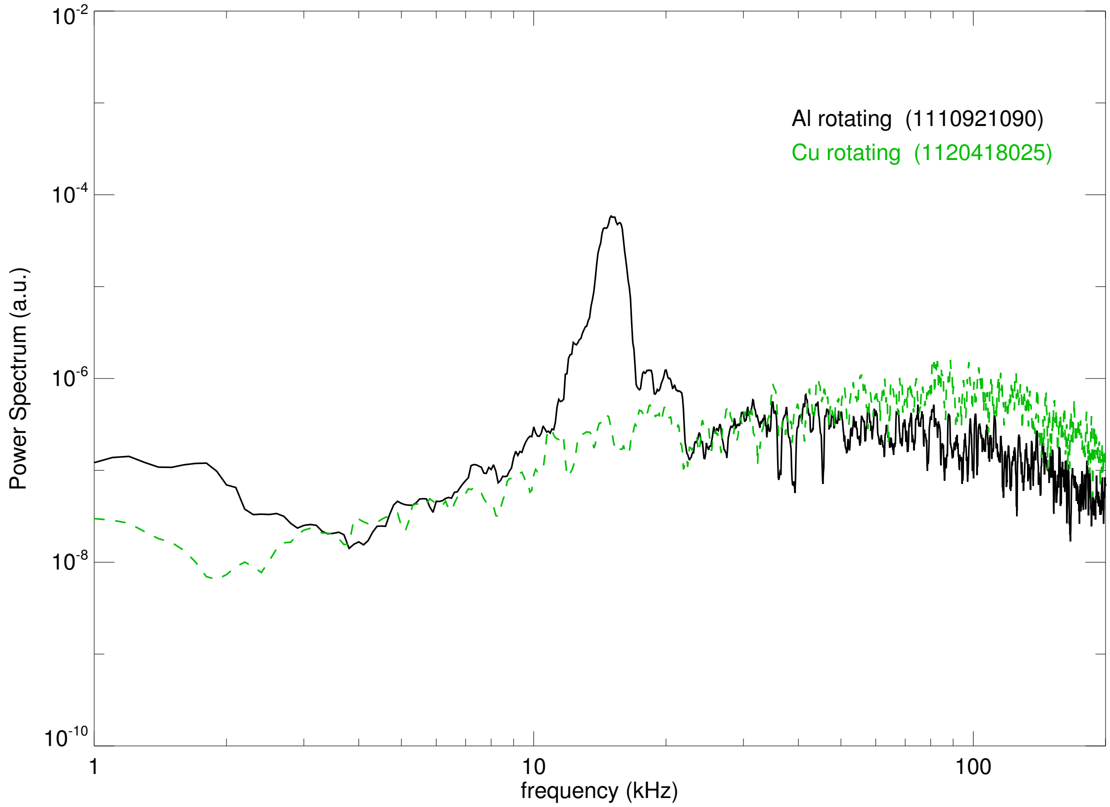

Figure 4.29: Power spectra comparing original probetip made of 1.5mm aluminum (black) to the thick-walled probehead made of 4mm tellurium copper (green) in similar 400 kA F=0 rotating plasmas, using 10^8 amplification. The original design shows a magnetically-induced signal around the plasma rotation frequency of 10-12 kHz. On the other hand, the final thick-walled copper design does not show any magnetic pickup.

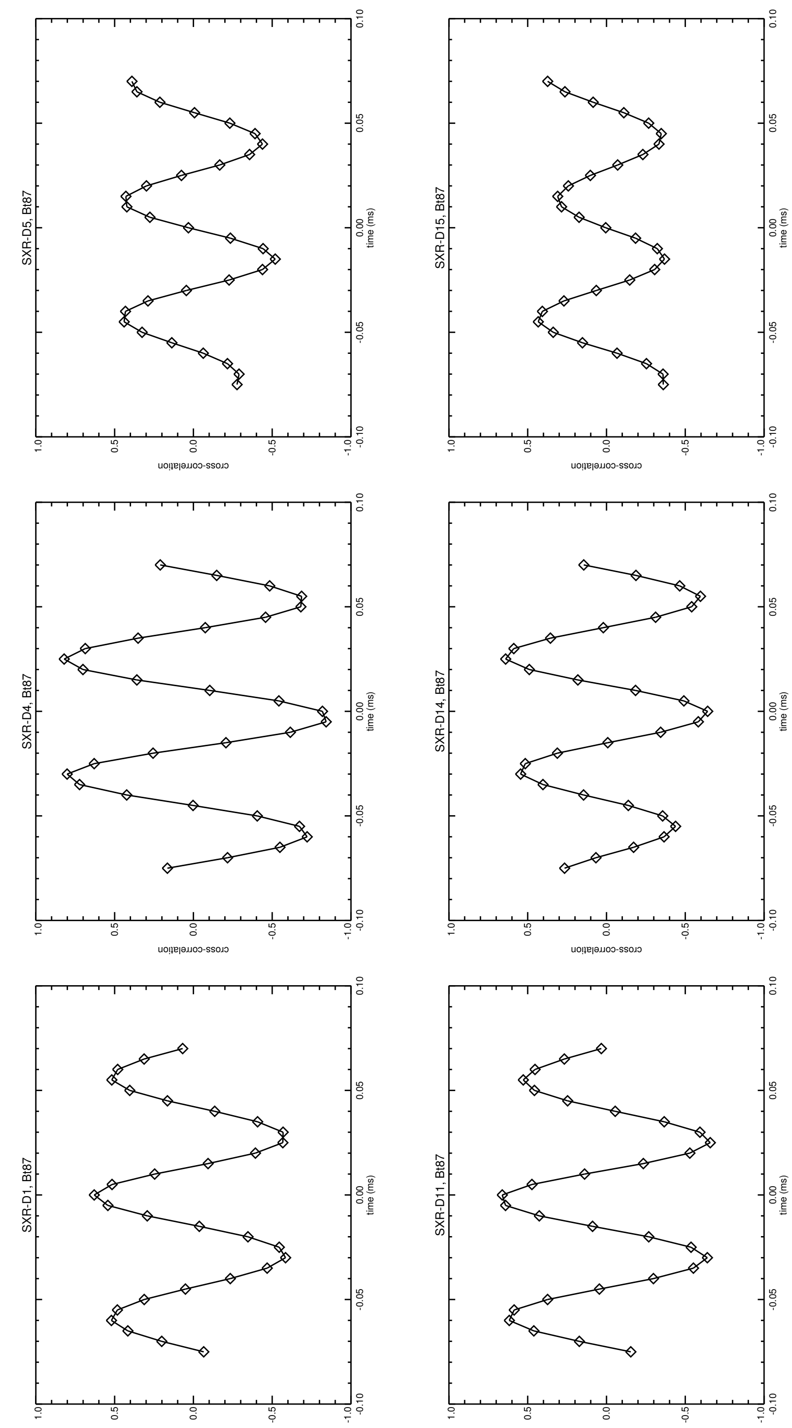

Figure 4.30: Cross-correlation between each SXR-D signal at 10^8 gain and Bt87 magnetics from 22.5-23.5 ms during a 400 kA F=0 shot using the final copper probehead with a blanked probetip (prototype diode board had only 6 diodes installed). The large correlation indicates continued magnetic pickup in the blanked SXR signal.

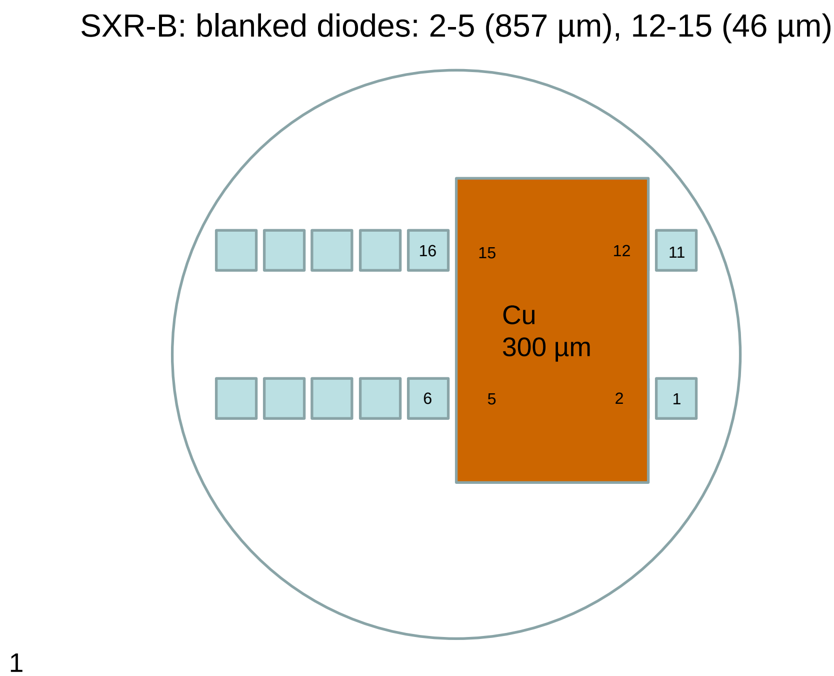

Figure 4.31: Schematic showing the blanked-diode test to measure the amplitude of magnetic pickup. A 300 μm copper sheet covers diodes SXR-B 2-5 and 12-15 so that they can measure only magnetic pickup. Meanwhile the remaining diodes are able to measure SXR signal as well as pickup. Thin Be filters are used to assure good SXR signal in the uncovered diodes.

and 12-15 of SXR-B, while leaving the remaining diodes open. (Although copper could potentially shield out magnetic pickup, tests at 10^9 gain indicate the pickup is still present underneath the copper plate). Figure 4.31 shows a schematic of the experiment. Uncovered diodes 1, 6-10, 11, and 16-20 measure both plasma signal and any magnetic pickup, while diodes 2-5 and 12-15 are covered so that they sensitive only to the magnetic pickup component. Additionally, thin Be filters are installed for diodes 11-20 so that there is ample signal levels on uncovered diodes.

Figure 4.32 compares the signal levels using 10^8 gain between the blanked (B15) and viewing (B16) diodes during a 400 kA F=0 shot with a rotating n=5 dominant mode. The top panel shows the magnetics signal from the Bt87 coil for shot 1121120127. The bottom panel shows a zoom-in of the viewing (black) versus covered (red) diodes through the thin Be filter. This Figure clearly shows a signal matching the magnetic oscillations in the viewing diode, while the amplitude of the oscillation in the covered diode is about 25% as large. Therefore, the majority of the oscillation in the signal seen by a diode at 10^8 gain is caused by true variation in the SXR emission rather than magnetic pickup. In fact, at a gain of 10^8, the level of true signal is approximately 3-4 times the level of magnetic pickup.

At 10^9 gain however, magnetic pickup becomes significant. Figure 4.33 is a zoom of the signals for viewing and covered diodes for a 300 kA F=0 plasma using 10^9 gain. In this case, an oscillation is clearly visible in both the covered (black) and viewing (red) diodes. This demonstrates that at 10^9 gain, the magnetic pickup is dominating the measurement. As a result, any analysis of rotating plasmas using 10^9 gain will likely be contaminated by pickup.

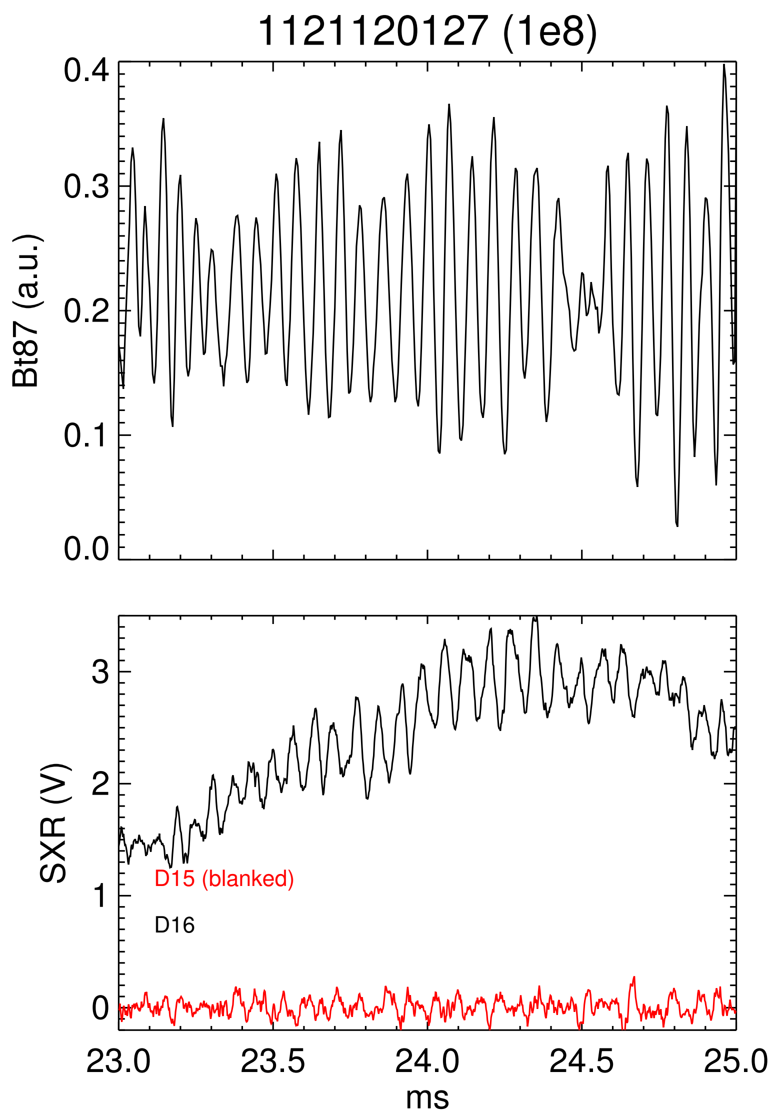

Figure 4.32: Magnetic (top) and SXR measurements for a viewing diode (bottom black) compared with a covered diode (bottom red) using 10^8 amplification. The oscillation seen in the magnetics is much stronger in the SXR viewing diode, indicating that the majority of the oscillation in the SXR emission is from the plasma rather than magnetic pickup contamination.

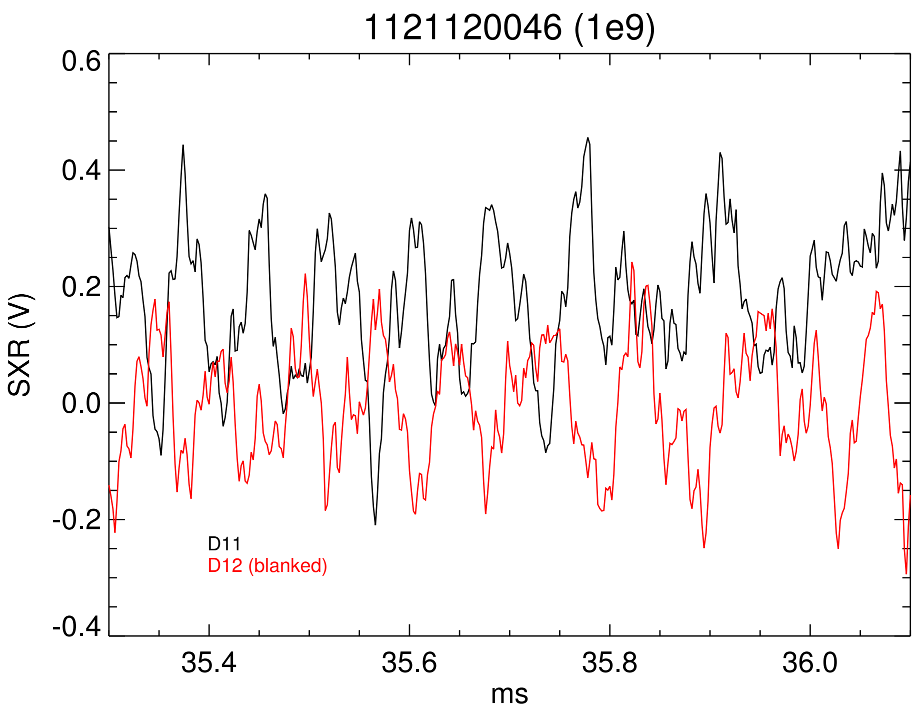

Figure 4.33: SXR measurement for a viewing diode (black) compared with a covered diode (red) at 10^9 amplification for shot 1121120046. An oscillation of equal magnitude is apparent in both diodes, indicating that magnetic contamination is dominating the signal at 10^9 gain.

4.5 Conclusions

A new SXR double-foil diagnostic has been designed for MST that provides improved tomographic emissivity reconstruction and tomographic T_e measurements. In addition, the new diagnostic has two different filters sharing each line-of-sight so that a direct measurement of the temperature along the chord is available. The diagnostic features individual silicon photodiodes with separate anode and cathode signals, facilitating a differential measurement. Fully differential transimpedance amplifiers have been developed for the system with gain of $10^5 - 10^9$ at high bandwidth (27-134 kHz). The differential signal processing provides excellent common-mode rejection so that the diagnostic is not sensitive to noise from switching power-supplies. The new diagnostic is located on 2-inch diameter portholes at 90° toroidal, which provides a better geometry for tomographic reconstruction than the previous location.

During development of the new diagnostic, it was discovered that the SXR measurement is contaminated with magnetic pickup during plasmas with a large rotating tearing mode. The pickup occurs when magnetic field lines at the edge of the plasma induce a current in the photodiodes themselves. These field lines access the diodes by soaking through the thin aluminum walls of the first-iteration probehead. Pickup has been dramatically reduced by minimizing the enclosed area of wire loops in the detectors. Noise has been further reduced by fabricating the probehead out of thick-walled tellurium copper, which has excellent conductivity properties. With these modifications, magnetic pickup is no longer measurable at gains of $10^5 - 10^7$. At 10^8, pickup is only present when the dominant magnetic mode is larger than 3 mT and is typically $\sim$ 3-4 times smaller than the signal level. At 10^9, magnetic contamination is the same order of magnitude as the signal. Therefore, gains $10^5 - 10^8$ can safely be used during all plasmas, while 10^9 gain should be used only when there are no large tearing modes or when the dominant mode is locked. The final diagnostic design provides excellent bandwidth and dynamic range with low noise and good common-mode rejection.

Chapter 5

Soft X-Ray Studies in High Current PPCD Plasmas

The new SXR T_e and tomography diagnostic has been commissioned and used to study the relationship between magnetic structures and electron temperature in improved confinement plasmas. The SXR emissivity regularly indicates the presence of a structure during quasi-single helicity periods of the discharge, where the (1/6) tearing mode locks and grows in amplitude to be substantially larger than the other resonant modes. Section 5.1 describes an integrated data analysis approach that combines SXR brightness with independent measurements of electron density, temperature and magnetic mode amplitude. Section 5.2 discusses general characteristics of 500 kA PPCD discharges as studied using SXR emission. The SXR diagnostic is used to measure the impact of aluminum impurity radiation on the emission spectrum from 2-6 keV. The electron temperature (T_e) profile is characterized in PPCD discharges, and the SXR T_e measurement is benchmarked against Thomson scattering. Additionally, SXR emission is verified to be correlated to the magnetic structure in the plasma. Section 5.3 provides a case study of a strong quasi-single helicity plasma showing indications of a small ($< 15\%$) T_e structure. Section 5.4 contrasts the emission structure seen during QSH with a multiple-helicity example containing a bright emissive ring-structure that is caused by impurity radiation rather than T_e.

5.1 Integrated Data Analysis: Tools and Techniques

The SXR diagnostic provides the most information about the plasma when used in an integrated data analysis framework [60, 61]. Thomson scattering T_e and far-infrared (FIR) interferometer n_e profiles are included in an SXR bremsstrahlung model to create synthetic SXR brightness measurements. Comparing the synthetic brightness to the measured value provides insight into the effective atomic number (Z_{eff}). The role of impurities is further explored with the help of the charge exchange recombination spectroscopy (CHERS) diagnostic. Additionally, the SXR diagnostic measures direct-brightness T_e. External magnetics measurements are used to define magnetic flux surfaces, onto which the SXR emissivity is mapped. The double-foil $T_e(R)$ technique is then applied to the flux-surface-mapped emissivity to make a second T_e measurement from the SXR emission, this time in 2D. Each of these diagnostics provides constraints on aspects of the bremsstrahlung emission that makes up the SXR measurement. A more complete application of integrated data analysis, utilizing Bayesian probability theory, is planned, but even this partial application successfully leverages the available measurements to provide a more complete understanding of the plasma.

5.1.1 FIR n_e and Thomson scattering T_e Diagnostics

The far-infrared, or FIR, diagnostic on MST is a polarimeter-interferometer that can measure plasma electron density, magnetic field, and current density. The FIR is comprised of 5 vertical viewing chords at 250° toroidal (T) and 6 vertical-viewing chords at 255° T that combine to provide a full diameter line-integrated $n_e(r)$ profile with $\sim$ 10 cm radial and 1-4 μs temporal resolution [62, 63]. A single CO_2-pumped laser is split into three beams. Two of the beams are polarized in opposite senses and their phases shift in the presence of a magnetic field. The phase difference between the right-circularly polarized beam and the left-circularly polarized beam determines the line-integrated electron density [64]. Third beam split off the original laser provides the Faraday rotation angle and current density [65]. The line-integrated n_e can also be inverted into a $n_e(r)$ profile measurement using the UCLA shifted-circles inversion technique [66].

Thomson scattering (TS) compliments the capabilities of the SXR T_e measurement and provides an independent measurement of T_e to verify the accuracy of the SXR direct-brightness (DB) T_e technique. SXR T_e complements Thomson scattering because while well-established, TS measures only half of the vertical profile on MST. In contrast, the SXR diagnostic has full-horizontal and vertical profile capabilities and provides 2D T_e contours through flux-surface mapping. Thomson scattering has excellent time resolution but limited temporal coverage, while the SXR diagnostic measures T_e with 20-30 kHz resolution for the entire duration of x-ray emission.

The TS diagnostic measures T_e with a multi-pulse, multi-point laser system. A laser-generated photon incident upon a free electron is absorbed and then re-emitted at a scattering angle [67, 68]. The change in the momentum vector of the photon is a function of the energy of the scattering electron, so the temperature of the electron part of the plasma can be deduced. Thomson scattering photons on MST are generated with two independently triggered Nd:YAG lasers and a 15 m remote-controlled beam line [69]. The scattered light is collected through a lens at (222°T, 20°P) into a radial array of 21 fiber bundles. Figure 5.1 shows the field-of-view of the collection optics. The diagnostic has three modes of operation, including a fast burst mode with 1μs resolution, although the data presented in this thesis has 1 kHz resolution.

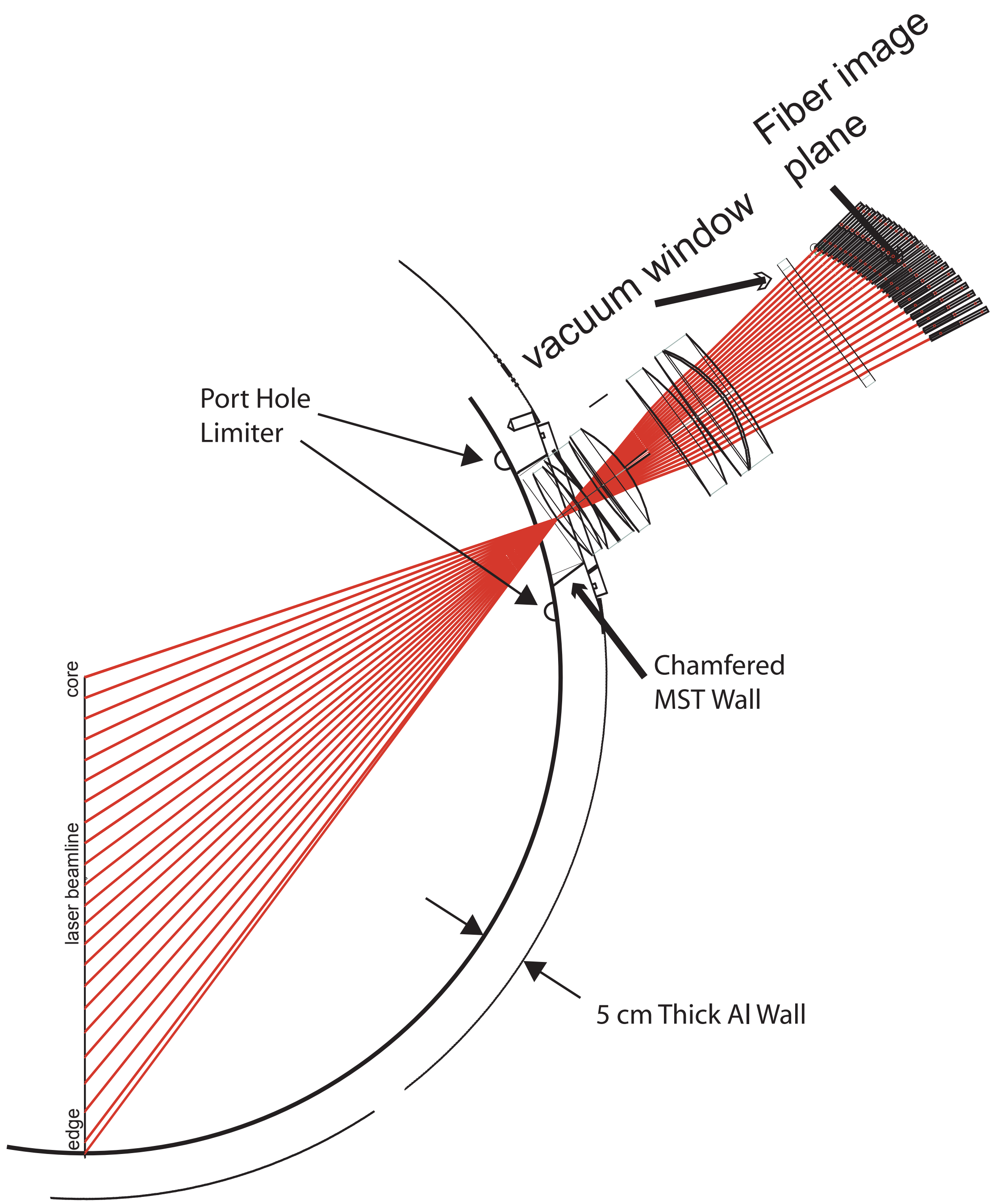

Figure 5.1: Schematic of the Thomson scattering field-of-view in MST. Fiber optic cables sit on the image plane gathering scattered light at 21 locations between the core and edge of MST (courtesy of Rob O'Connell).

5.1.2 Flux Surface Mapping Using the SHEQ Code

An additional tool is now available to aid in the SXR data interpretation by mapping the measurements to magnetic flux coordinates. Magnetic topology reconstruction techniques have been developed at RFX-Mod and adapted for MST using the external magnetics coils to define 3D flux surface coordinates inside the plasma. The SHEq code (described in detail in Ref. [70]) begins by presuming that plasma quantities, such as flux surfaces and magnetic field, are generally comprised of an axisymmetric component (A_0) and a perturbation that are written in coordinates (r, θ, φ) as:

$$A(r,\theta,\varphi) = A_0(r) + \sum_{m,n} a^{m,n}(r)\, e^{i(m\theta - n\varphi)} \tag{5.1}$$

where r, θ, and φ describe the radial, azimuthal, and axial directions in the torus, respectively. The technique uses the Newcomb equation to solve the perturbation as harmonics $\psi_P^{m,n}$ and $\psi_T^{m,n}$ of the poloidal and toroidal flux. The magnetic field in this coordinate system is defined as:

$$\vec{B} = \bigtriangledown\psi_T \times \bigtriangledown\theta - \bigtriangledown\psi_P \times \bigtriangledown\varphi \tag{5.2}$$

From these equations, flux surface coordinates can be written as a function of magnetic mode number (n) as:

$$\chi = m\psi_P - n\psi_T \tag{5.3}$$

Finally, the flux surface coordinates are normalized as:

$$\rho = \sqrt{\frac{\chi - \chi_{min}}{\chi_{max} - \chi_{min}}} \tag{5.4}$$

Quantities that are a flux surface function, such as temperature, can then be

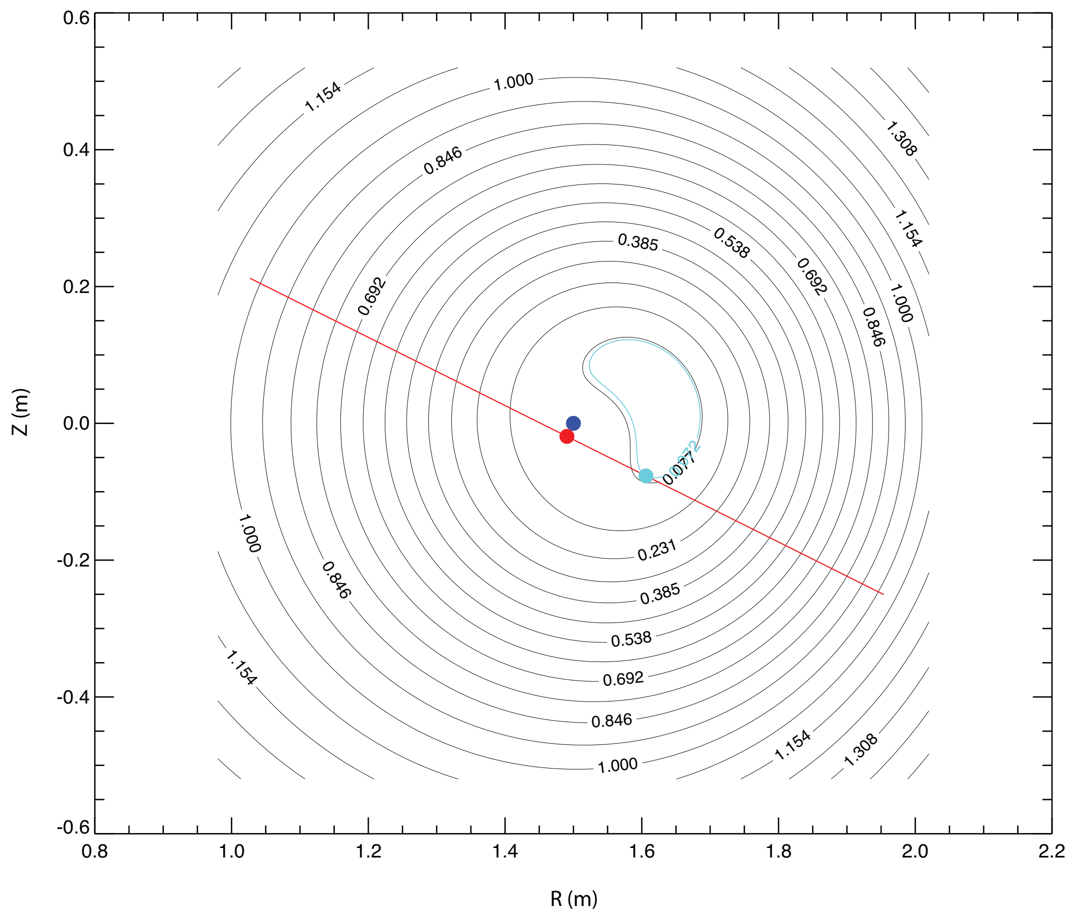

Figure 5.2: Example of the reconstructed magnetic flux coordinates from the SHEq code for a 500 kA PPCD shot (1121203026) with a magnetic island at 18° P. The blue dot is the geometric center. The red line is chord 4 of SXR-C, and the red dot represents the location along the chord closest to the geometric axis, which defines the impact parameter p of the chord. The cyan shows the innermost flux surface that the chord intersects. This is the ρ associated with the direct-brightness T_e for that SXR chord.

mapped to the ρ coordinate. Density from the FIR diagnostic is mapped to φ=252.5°, and T_e from Thomson scattering is mapped to φ=220°. SXR direct-brightness temperature and emissivity are mapped to the ρ coordinate system at φ=90°. The direct-brightness temperature is mapped to flux surface coordinates by finding the minimum flux coordinate that intersects the line-of-sight of the chord, and assigning the chord temperature to that flux surface. Figure 5.2 illustrates the magnetic flux coordinates for an example PPCD shot with an n=6 dominant mode. The black contour lines are reconstructed from the external magnetics measurements and denote the flux surfaces $\rho = 0$ to $\rho = 1$. The blue dot is the geometric center of the machine. The line-of-sight of the SXR-C chord 4 is over-plotted in red. The impact parameter p of chord 4, defined as the closest point along the chord to the geometric axis, is denoted by a red dot. The innermost flux surface that it intersects is highlighted in cyan, this is the ρ that corresponds to the direct-brightness temperature from that chord.

Although SXR emissivity is a flux surface function, it is not measured directly and so must be calculated from the SXR brightness measurement. An initial guess for the emissivity as a function of ρ is made in the form [71]:

$$\epsilon(\rho) = \epsilon_0 \left(1 - \rho^{\alpha}\right)^{\beta} + \epsilon_1 \tag{5.5}$$

The four parameters ϵ_0, ϵ_1, α, β are iteratively varied and the synthetic brightness is calculated at each step. The optimized emissivity profile is determined with a least-squares analysis comparing the synthetic brightness to the measured brightness. An important limitation to this technique is the requirement that the flux surface function be monotonically decreasing. The SHEq reconstructions were designed to be applied to SHAx plasmas, where the magnetic axis has been supplanted by the island and forms a new helical axis. In the SHAx geometry, the flux surfaces naturally follow a monotonically decreasing pattern. However, in PPCD plasmas, the structures are actually a double-axis configuration, so that the magnetic core is retained and the island creates an independent flux surface. In these plasmas, it is possible for SXR emissivity to be high in both the core and the island, but lower in between. Then the emissivity profile is not monotonically decreasing, and Equation 5.5 becomes an approximation.

The flux-surface reconstructed (F.S.R.) emissivity from the thin and thick filter measurements can then be converted to a 2D T_e map using the same $T_e(R)$ double-foil technique as is used to calculate the Cormack-Bessel (C.B.) T_e (see §2.3 for a description of the $T_e(R)$ double-foil technique and its application to the CB emissivity). However, a consequence of a forced monotonically-decreasing emissivity is that any T_e structure calculated from the flux-surface mapped emissivity is underestimated. The F.S.R. emissivity between the core and the island cannot have a dip, and so the region of lower-emission between the two highly emissive regions is averaged with the peaks. Therefore the F.S.R. temperature of the core and the island is likely to be less than the actual value and so the F.S.R. technique puts a lower-limit on ΔT_e.

5.2 General Characteristics of 500kA PPCD Discharges

5.2.1 Plasma Spectrum and Impurities

In addition to measuring SXR brightness, emissivity, and electron temperature, the SXR diagnostic is also capable of measuring the gross plasma spectrum in the soft x-ray energy band. To measure the plasma spectrum, the same point in the plasma is sampled through several different filters. A spectrum measurement was taken on MST with the original SXR tomography diagnostic in multi-color mode to determine the impact of aluminum line radiation on filter thickness choice [42]. In this case, each of the four probes contained a different foil thickness, and the core-viewing line-of-sight of each probe was compared during a single shot. With filter choices of 15, 140, 254, and 478 μm beryllium, the thinnest two filters were clearly contaminated with aluminum radiation.

The new SXR diagnostic is capable of measuring single-shot multi-foil spectra. However, it is also possible to create a spectrum across multiple similar shots if they are properly normalized. This was done during prototype testing using a single probe (SXR-D) in a series of four 500 kA PPCD plasmas. The shots were chosen to have the same plasma current, mode activity, and average core SXR signal (as measured from the core-viewing Be1 diagnostic) signals at the time-point chosen for analysis.

Ideally, shots should be matched for electron and ion density as well, but this was not possible due to variations in machine conditions. To correct for these important effects, the SXR signals have been normalized to the electron and ion densities of the first shot.

$$b_{norm} = \frac{b_{SXR}}{n_e^2} \tag{5.6}$$

$$b_{norm} = \frac{b_{SXR}}{n_e \, n_{Al^{11+}}} \tag{5.7}$$

Equation 5.6 defines the normalization SXR brightness accounting only for n_e, assuming no impurity radiation so that n_i=n_e. Equation 5.7 uses the CHERS Al^{11+} measurement as a proxy for impurity density and normalizes out variation in both n_e and n_i. Figure 5.3 shows the time evolution of the core Al^{11+} density measurements for the four shots. The electron density is measured by the CO_2 interferometer. The ion density is characterized by an Al^{11+} impurity measurement from the charge exchange-recombination spectroscopy (CHERS) diagnostic. (See Ref. [72] for a detailed explanation of aluminum impurity measurements using CHERS). Because both

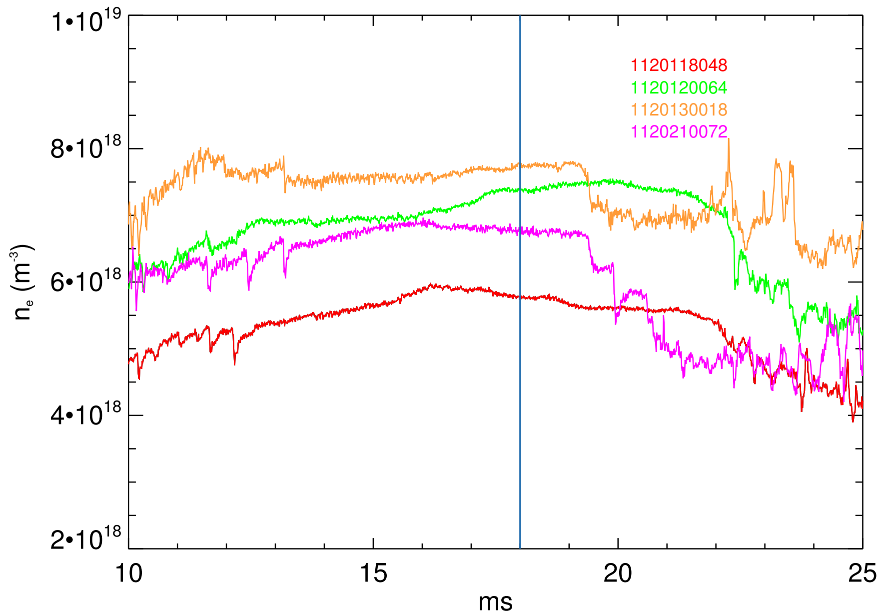

(a) CO_2 n_e

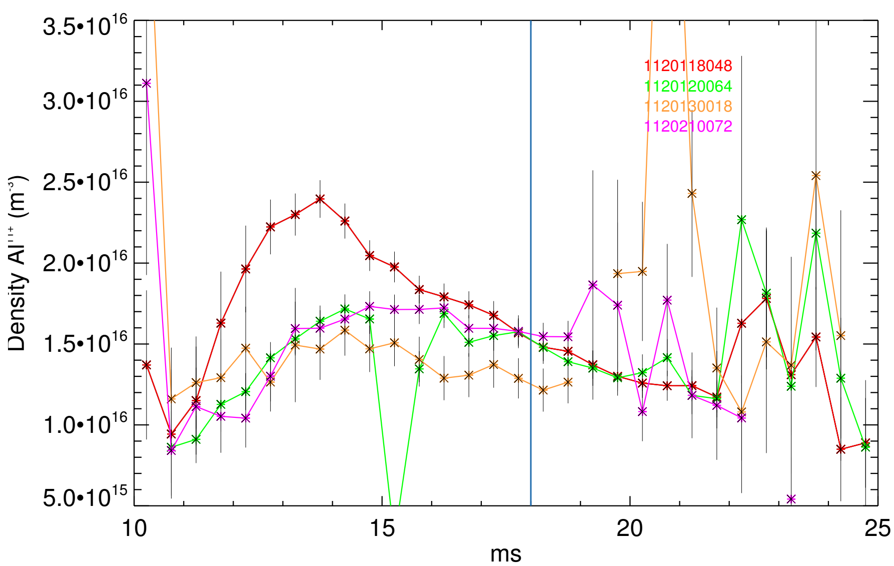

(b) CHERS $n_{Al^{11+}}$

Figure 5.3: Line-averaged electron density (top) and Al^{11+} impurity density (bottom) from core lines-of-sight for 4 shots with similar plasma parameters. The blue line denotes the time point used for calculation of the SXR spectrum, and the window of interest is 0.5 ms wide (maximum resolution of the CHERS diagnostic). SXR brightness measurements are normalized across the 4 shots to account for variation in n_e and n_i.

densities are core-only measurements, the normalization can only be accurately applied to the core SXR chords.

Figures 5.4 and 5.5 show the SXR spectrum as a function of 1/e filter cutoff energy calculated from the four shots, with two distinct Be filter thicknesses used in each shot. Thin filters are color-coded to match the shot number from Figure 5.3. Same-shot filter pairs are [167, 346], [251, 526], [331, 706], and [408, 800] μm. The percent transmission at the hydrogen-like aluminum recombination step (2.3 keV) for each filter cutoff energy is written above each point for reference. The solid black line is the bremsstrahlung-only emission spectrum calculated using DB T_e from the [408, 800] μm data, with red and blue dashed lines representing uncertainty in the temperature measurement. Uncertainty in the brightness measurement is defined as the standard deviation of the signal in a 0.5 ms window around the datapoint. Uncertainty in T_e is calculated by applying the standard deviation in the brightness (f) for the thick filter measurements to the ratio calculation as described in §2.3.4.

In Figure 5.4, the shot-to-shot variation in n_e has been removed, assuming no variation in impurity density. In this case, the SXR data is not well-represented by the calculated bremsstrahlung spectrum. If the shot-to-shot variation in impurity density is accounted for however, the spectrum is much improved. Figure 5.5 shows the spectrum where, for the first time, CHERS Al^{11+} measurements have been used as a proxy for ion density to normalize the impurity component of the bremsstrahlung radiation across shots. This technique allows a more precise treatment of the SXR bremsstrahlung brightness as:

$$f(E) = \frac{n_e\, n_i}{\sqrt{T_e}}\, e^{-E/T_e} \tag{5.8}$$

This treatment does not, of course, account for line and recombination radiation

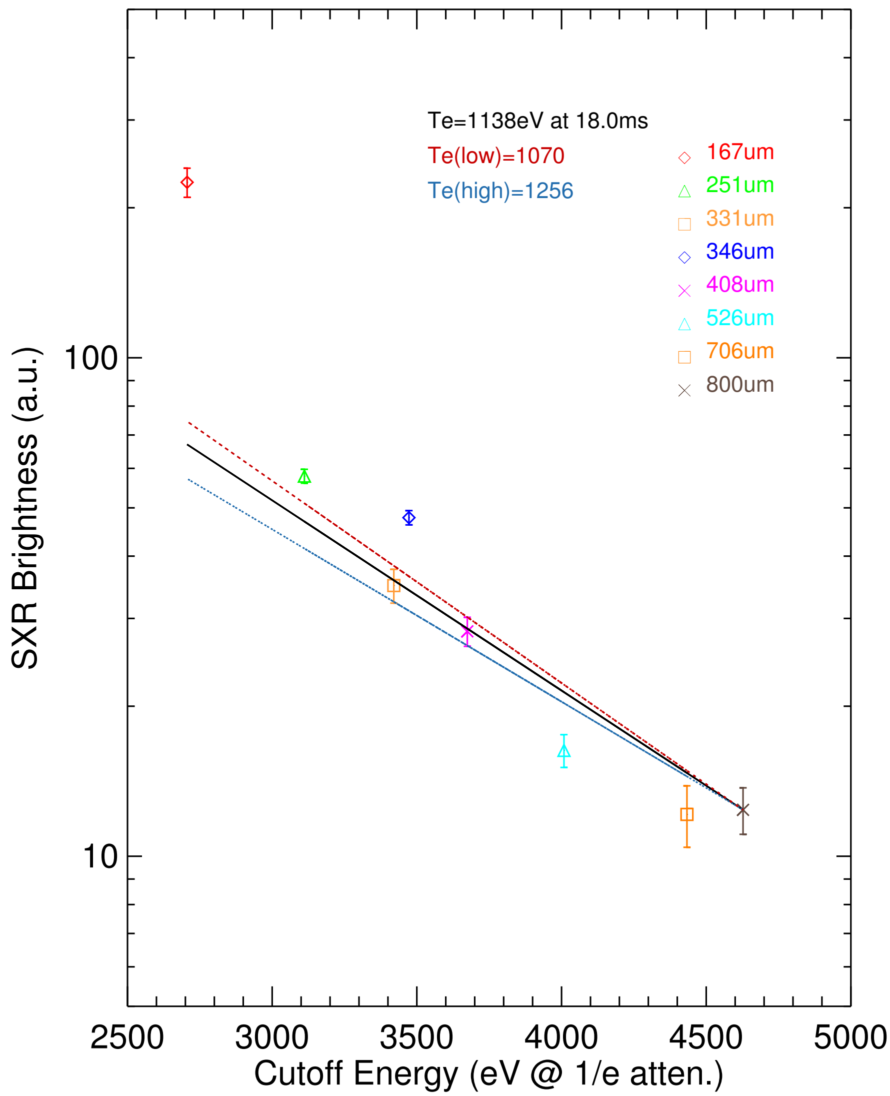

Figure 5.4: SXR brightness as a function of 1/e cutoff energy of the measurement filter, normalizing for shot variation in n_e but not n_i. Thin filters are color-coded to match the shot number from Figure 5.3. Same shot filter pairs are [167, 346], [251, 526], [331, 706], and [408, 800] μm. The solid black line is the bremsstrahlung-only spectrum for a plasma with DB T_e calculated from the [408, 800] μm data, with red and blue dashed lines representing uncertainty in the temperature measurement.

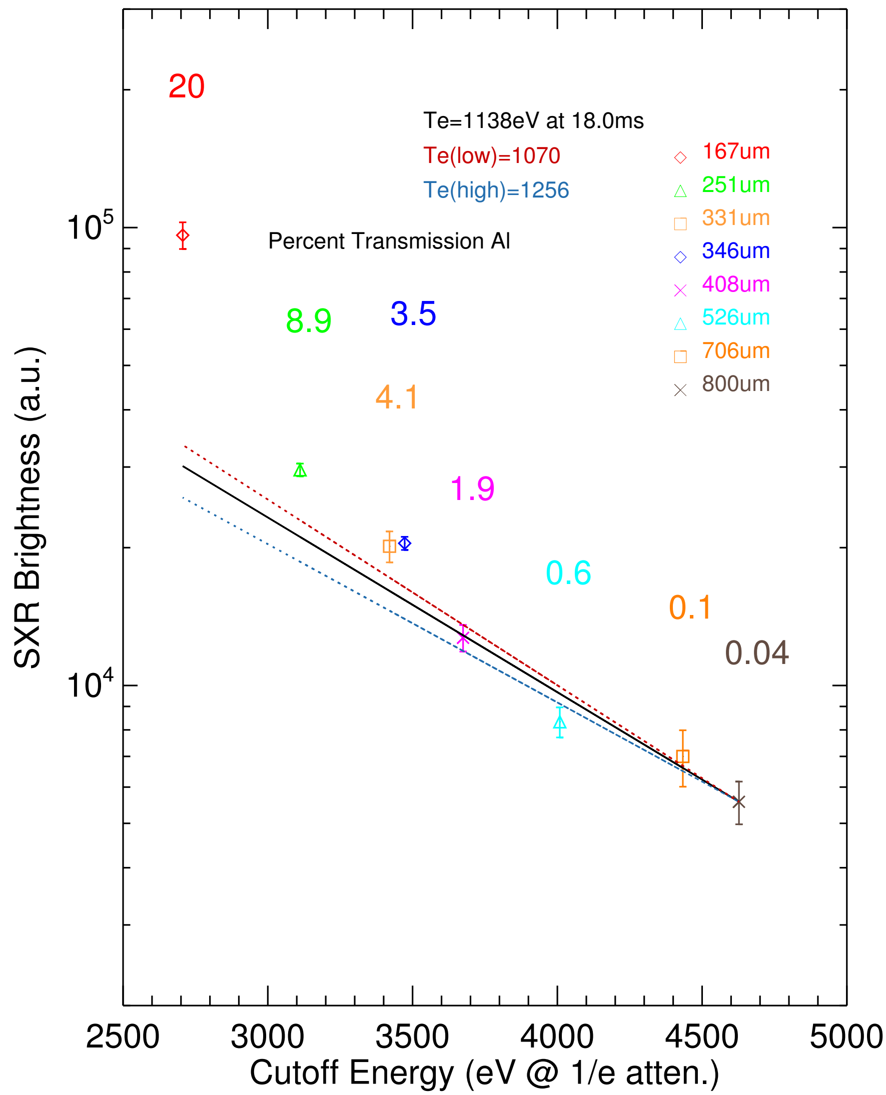

Figure 5.5: SXR brightness as a function of 1/e cutoff energy of the measurement filter accounting for shot variation in both n_e and n_i. Thin filters are color-coded to match the shot number from Figure 5.3. Same shot filter pairs are [167, 346], [251, 526], [331, 706], and [408, 800] μm. The percent transmission of 2.3 keV (last Al recombination step) at each cutoff energy is written above that point for reference. The solid black line is the bremsstrahlung-only spectrum for a plasma with DB T_e calculated from the [408, 800] μm data, with red and blue dashed lines representing uncertainty in the temperature measurement. Note that for filters above 400 μm, aluminum radiation is no longer distorting the measurement.

due to aluminum. In fact, the thin filter measurements begin to deviate from the bremsstrahlung spectrum line due to this additional radiation. For example, the 167 and 251 μm filters have 20% and 9% transmission of the aluminum recombination step at 2.3 keV, and are clearly contaminated by this radiation. The filters in the 300 μm range also likely allow contamination. This experiment confirms that to assure SXR measurements of only bremsstrahlung radiation, filters of at least 400 μm should be used.

In principle, the spectrum measurements can be combined with the aluminum impurity density measurement to more directly quantify the impact of each aluminum line on the SXR emission. However, because the emission region of interest includes two aluminum lines and two recombination steps, a collisional-radiative modeling program is required to separate out the contributions of recombination and line radiation. With this approach, a temperature dependent ratio of n_i/n_e could also be identified for various filter thicknesses, which would provide an operational parameter space where each filter thickness is reliable.

Future work could also expand the spectrum measurements from a static point to a time evolution. Spectrum measurements can be taken by placing different filter thicknesses in each of the four probes for a single shot. The spectrum measurement is restricted to the core region because the diodes in each probe must look at the same part of the plasma. However, it may also be possible to measure the radial profile of the spectrum. This would require the CHERS to be configured to take a profile measurement of the Al^{11+} content and the FIR interferometer to be used to obtain a profile of density. In this case, a single SXR probe could be used over multiple shots with different pairs of foils, normalizing shot-to-shot variation in n_e and n_i as in the example here. This could be an interesting exploration of the impurity distribution and evolution in time.

5.2.2 Comparison of SXR DB T_e with Thomson Scattering T_e

Time-resolved full radial profile DB T_e measurements have been made during 500 kA non-crash heated PPCD plasmas with both SXR and TS simultaneously. Figure 5.6 shows the temperature profiles for both diagnostics, where the SXR data have been binned into a 0.5 ms window. SXR-A (black) and SXR-B (blue) combine to make a horizontal profile measurement, while SXR-C (black) and SXR-D (blue) make a vertical measurement. The Thomson scattering temperature profile (red) most closely matches that of SXR-C in coverage, particularly for the (m/n)=(1/6) mode, which is dominant in high-current PPCD plasmas. In general, the TS T_e profile and all 4 DB T_e measurements are quite consistent. (Note that the DB T_e measurement is artificially forced to 0eV when the SXR brightness signals become small enough that noise overtakes the signal level. Therefore points outside $p/a \sim 0.5$ do not provide a reliable estimate of the slope of the profile).

Figure 5.7 compares the time evolution of the TS and DB T_e measurements in the core region for the same shot. Both SXR and TS traces are taken from core-viewing chords, with TS looking 3 cm below the mid-plane while SXR-C (chord 4) looks 2 cm below the mid-plane. In this shot, Thomson scattering has 1 kHz resolution, and the SXR diagnostic is binned to 0.5 kHz. The two profiles match well within the measurement uncertainties.

Figure 5.8 is a statistical comparison of the core-region T_e for both diagnostics as a function of average shot density. For each shot and diagnostic, the temperature has been estimated by eye looking over the entire core region of the profile during the hottest portion of the shot. Again, SXR DB T_e is shown in black while TS is in red. The two diagnostics agree in T_e to within 100 eV (well within the uncertainties

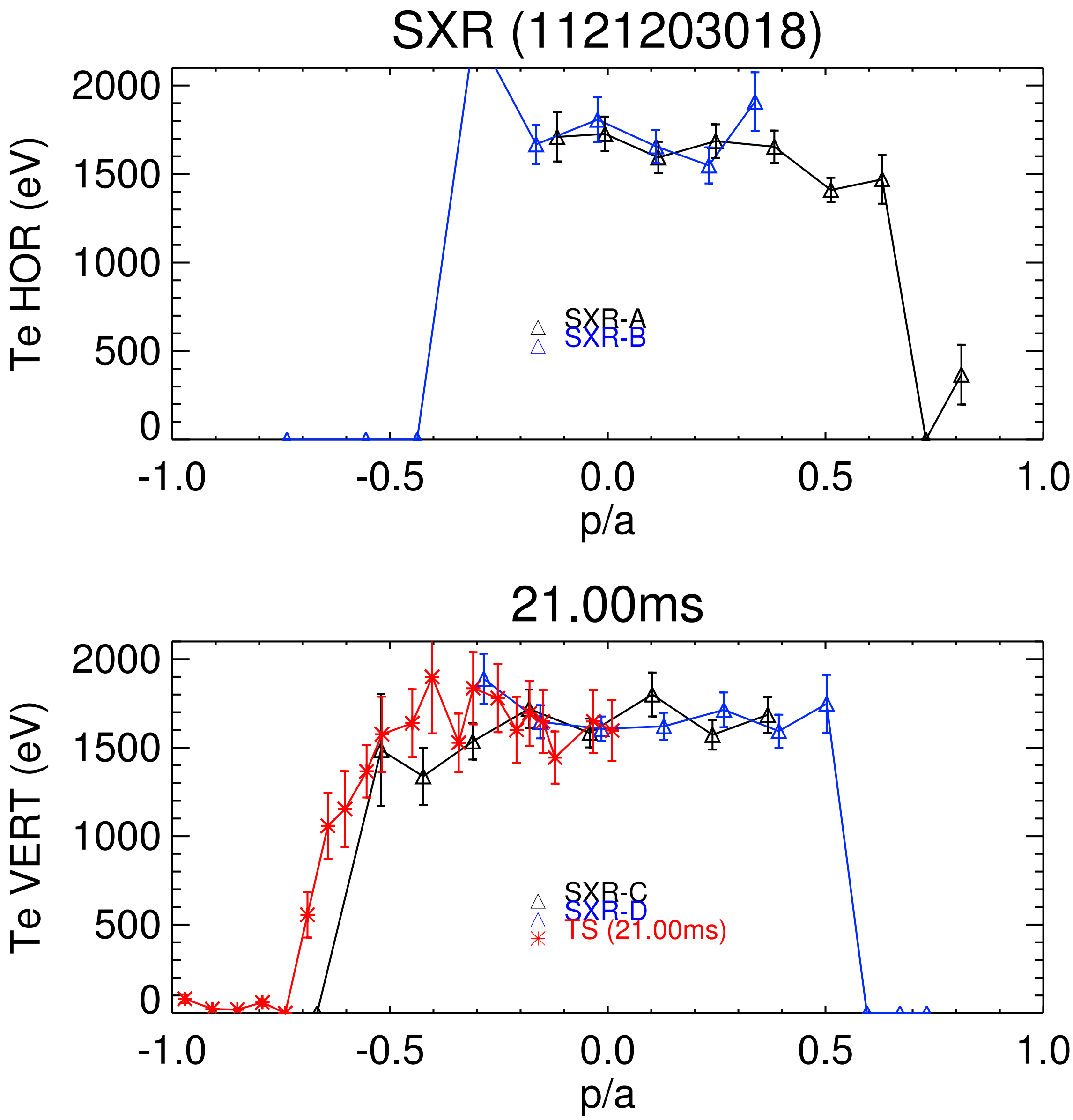

Figure 5.6: Horizontal (top) and vertical (bottom) DB T_e profiles measured during a 500 kA PPCD plasma. SXR-A and SXR-C profiles are black, SXR-B and SXR-D profiles are blue. Thomson scattering T_e for the same shot is overlaid in red. All 5 profiles show good agreement.

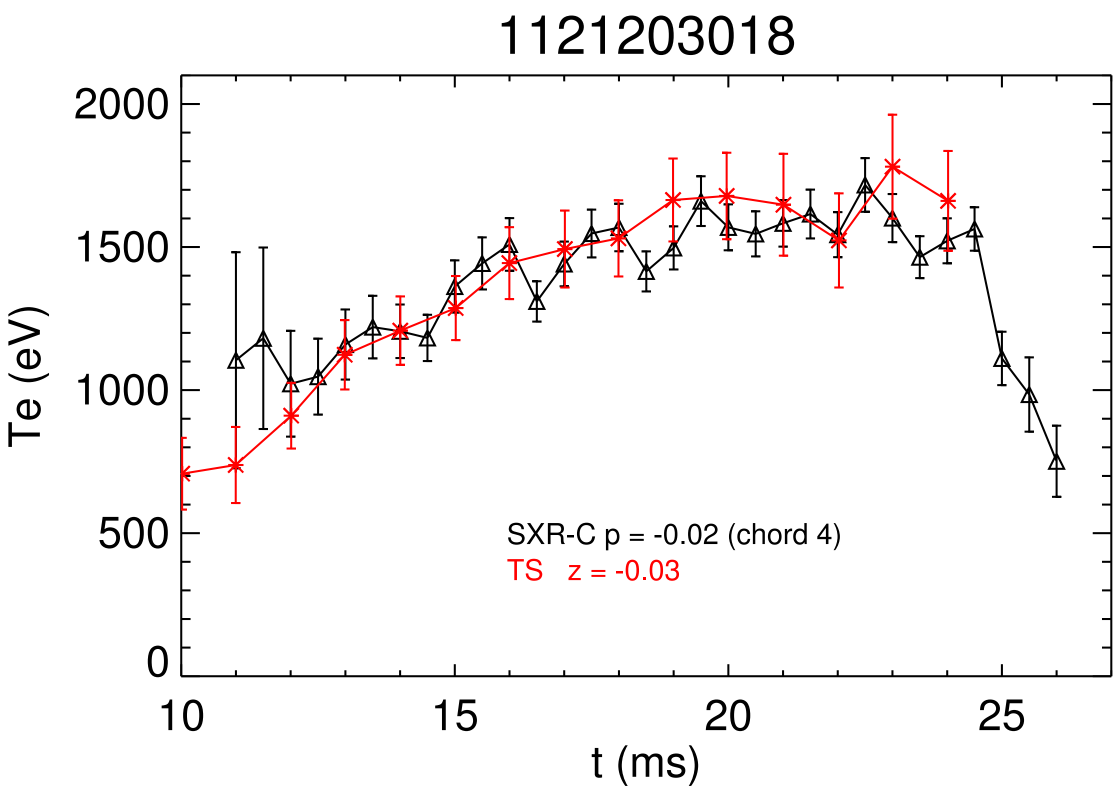

Figure 5.7: Comparison of temporal evolution of DB T_e from a core-viewing chord (black) and a similar Thomson scattering chord (red) indicating good agreement between the two diagnostics.

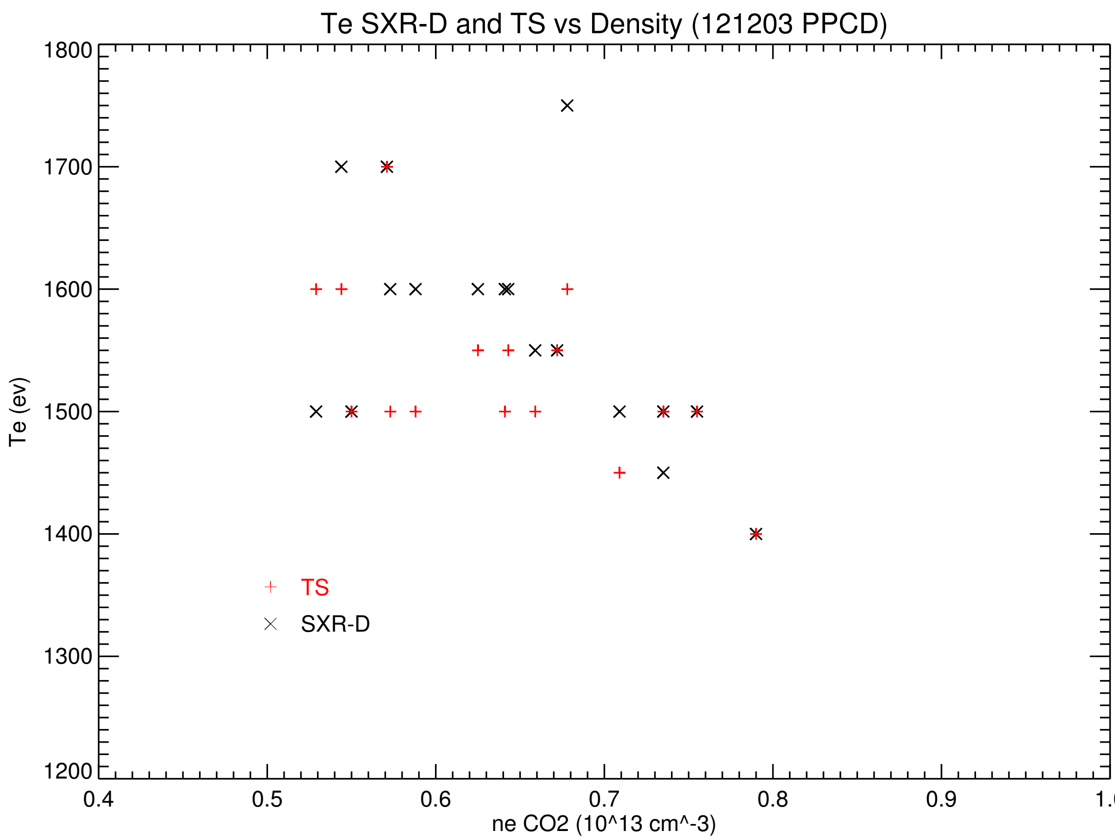

Figure 5.8: Statistical comparison of core T_e from SXR DB (black) and TS (red) for shots with various densities. The two diagnostics made simultaneous measurements for each shot, and demonstrate good agreement.

of both measurements) across a range of temperatures and densities. In fact, electron temperature has been verified on MST to be inversely proportional to electron density.

The full 4-probe SXR diagnostic has now been used to take measurements of approximately 20 good non-crash-heated PPCD plasmas at 500 kA, in addition to several dozen discharges from the commissioning period when between 1 and 3 probes were available. In these plasmas, the canonical DB T_e temperature profile is very flat and extends out to at least $0.5r/a$ before falling off. In general, the direct-brightness T_e measurement consistently matches the Thomson scattering T_e measurement in high current plasmas (the only ones for which it has been benchmarked at the time of writing). The full horizontal and vertical profile coverage of the SXR diagnostic provides a unique capability to measure asymmetries in the temperature profile and are a nice complement to the TS diagnostic.

5.2.3 Correlation of Emissivity Structures to Magnetic Modes

Although parallel current drive reduces tearing mode amplitudes overall, the majority of high-current non-crash-heated PPCD plasma shots still have a single dominant $(m/n) = (1/6)$ mode. This mode is most often locked and has poloidal magnetic field amplitude of between 2-15 Gauss. The magnetic mode spectrum for a typical PPCD QSH plasma with a 15 Gauss, n=6 mode is shown in Figure 5.9. The $n = 6$ island for this shot is located at 175° P at the toroidal location of the SXR diagnostic. Figure 5.10 shows the flux surface contours from the SHEq magnetics reconstruction at the same time. The magnetic flux surface contours can be directly compared with the SXR emissivity. The Cormack Bessel reconstructed SXR emissivity for thin and thick filters in the same shot is shown in Figure 5.11. The reconstructed emissivity clearly contains an emissive structure, and this structure is located at the same poloidal angle as the magnetic structure. The SXR diagnostic resolves an emissive structure for shots

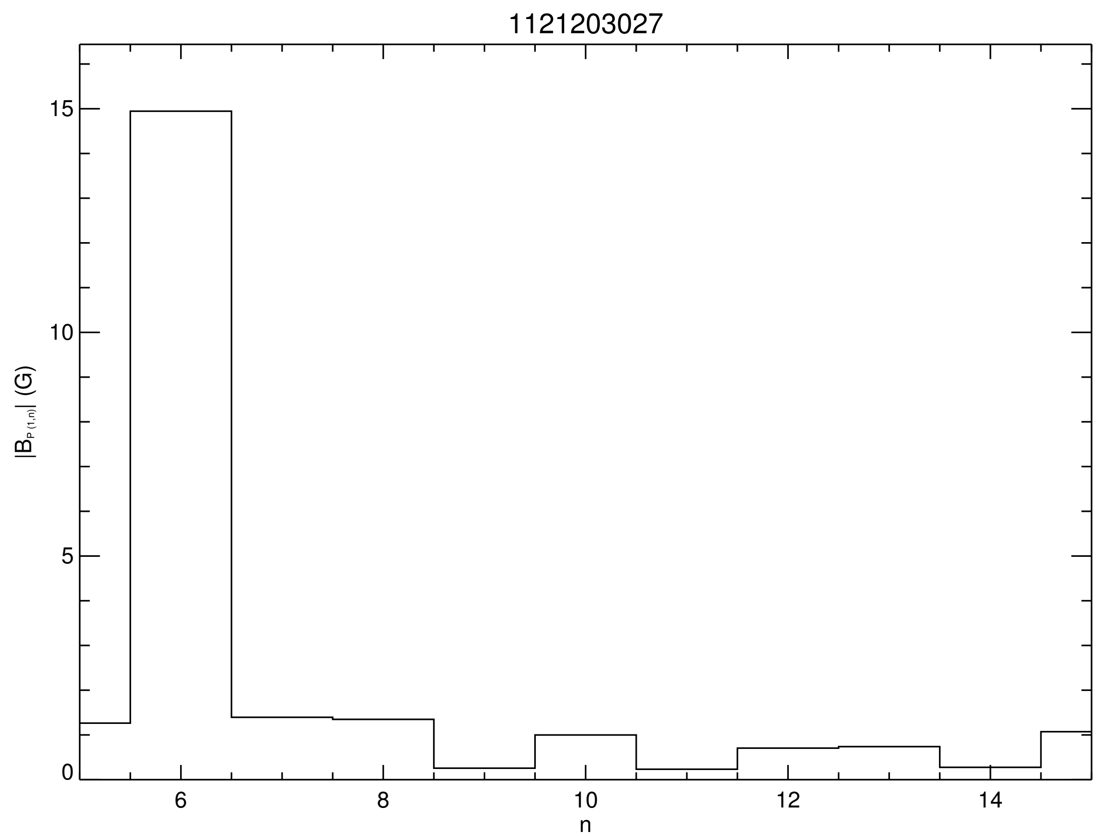

Figure 5.9: B_P amplitude as a function of magnetic mode n number ($m = 1$) for shot 1121203027 at 18 ms. Typical of PPCD QSH, this shot has a dominant n=6 mode and very low amplitudes for the remaining modes. The $n = 6$ mode locks at 175° P at the toroidal location of the SXR diagnostic.

with poloidal mode amplitudes as low as 5 Gauss. The poloidal angle measured by the SXR diagnostic generally agrees with the magnetics to within 50° for (1/6) structures, and when the two measurements do not match, the magnetics is systematically larger in angle than the SXR. The systematic discrepancy between the two measurements is still being investigated, but it is suspected to stem from some inconsistency in the coordinate definitions between the measurements[1]. All locked QSH shots from Dec-3-2012 have dominant modes between $\sim 0 - 180°$, and the most common locking region is between 60-100°.

5.2.4 SXR Emissivity Structures in PPCD During Rotating QSH

The magnetic structure of PPCD QSH plasmas is resolved in SXR emissivity whether the mode is rotating or locked. Figure 5.12 shows the time evolution of the Cormack Bessel emissivity reconstruction of the fluctuating signal at 4 times during the rotation period of the magnetic mode during a high-current PPCD shot where the dominant (1/6) mode is slowing down and $b_p^{1,6} = 10$ Gauss. In this shot, the SXR measurement has been down-sampled to 33 kHz, and then bandpass filtered to look only at emission from 2-7 kHz. The tearing mode is rotating at 4 kHz during the window of interest. Although this discharge occurred during the commissioning phase when only SXR-B and SXR-D probes were available, the reconstruction shows remarkably good agreement with the magnetics. The magnetics indicates that the (1/6) mode should be at 231°, 326°, 82°, and finally 145° at 17.49, 17.64, 17.76, and 17.78ms, respectively. The CB reconstruction shows the island at 220°, 340°, 85° and 180°. The fluctuating component of the emissivity is approximately 10% the total

[1]Although the cause of the inconsistency has not been determined definitively, consider the typical case where the island o-point is defined at a poloidal angle with respect to the magnetic axis at 0° T. Because the island rotates around the magnetic axis, a transformation to 90° T in the geometric coordinate system will necessarily introduce some discrepancy between the calculated poloidal angle and the observed location of the island.

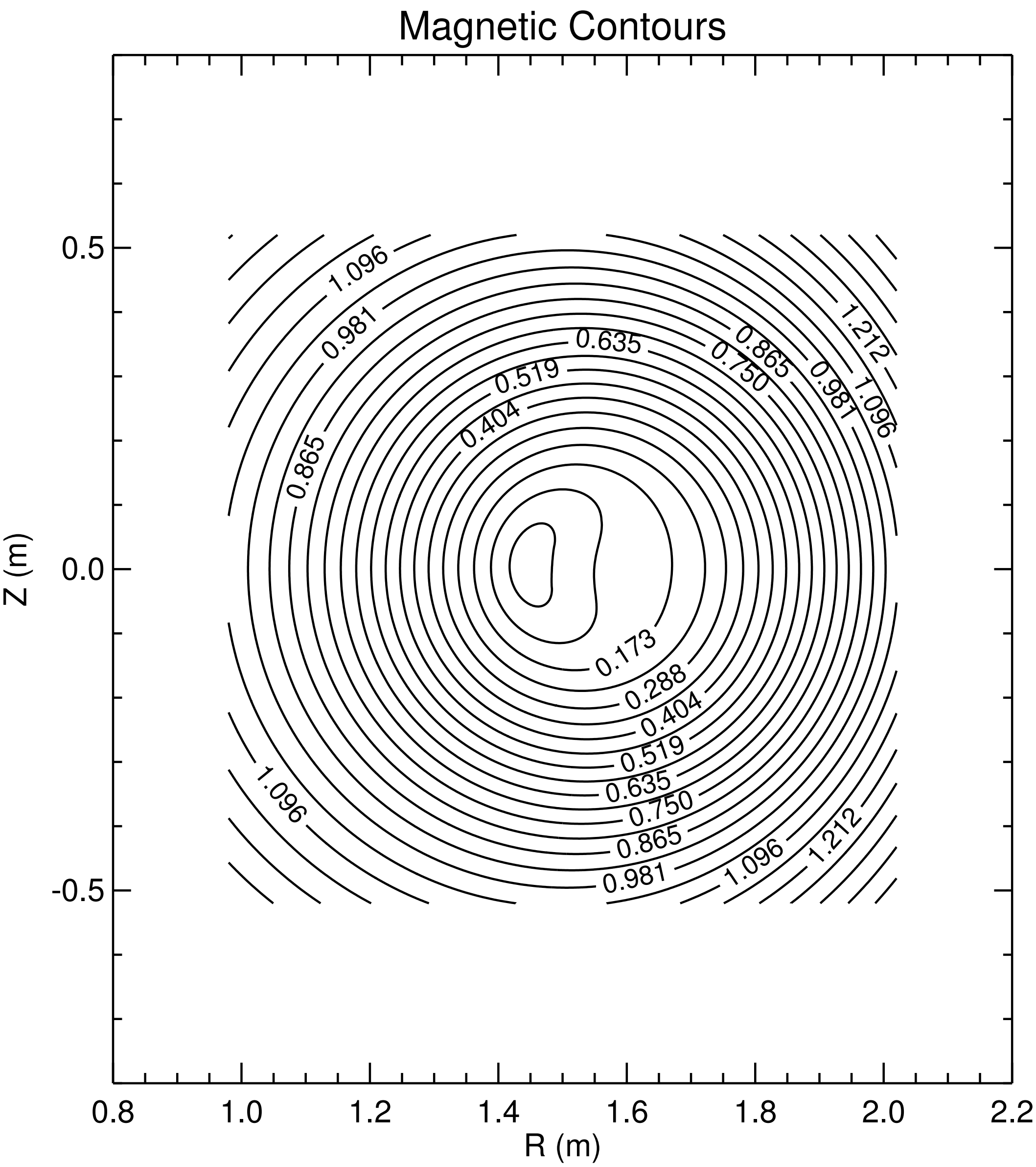

Figure 5.10: Flux surfaces reconstructed from external magnetics for shot 1121203027 at 18 ms show a small island corresponding to the n=6 tearing mode centered at 175° P.

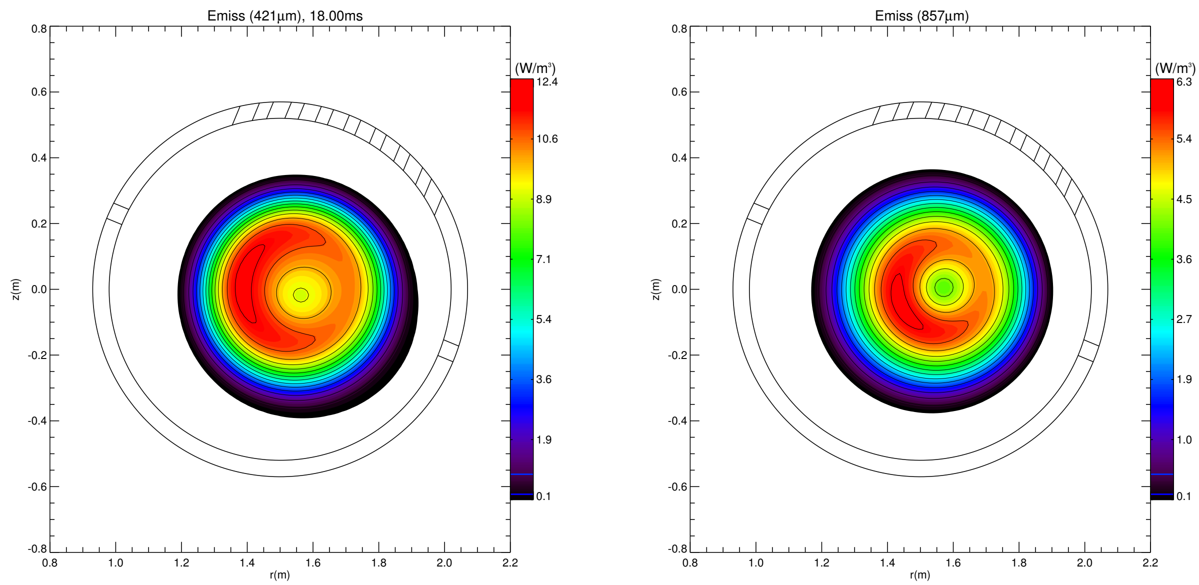

Figure 5.11: Cormack Bessel (CB) reconstructed emissivity contour maps for thin (left) and thick (right) filters on shot 1121203027 at 18.0 ms. Both filters clearly indicate an emissive structure. The location of the island in the reconstruction is consistent with the location of the n=6 magnetic island.

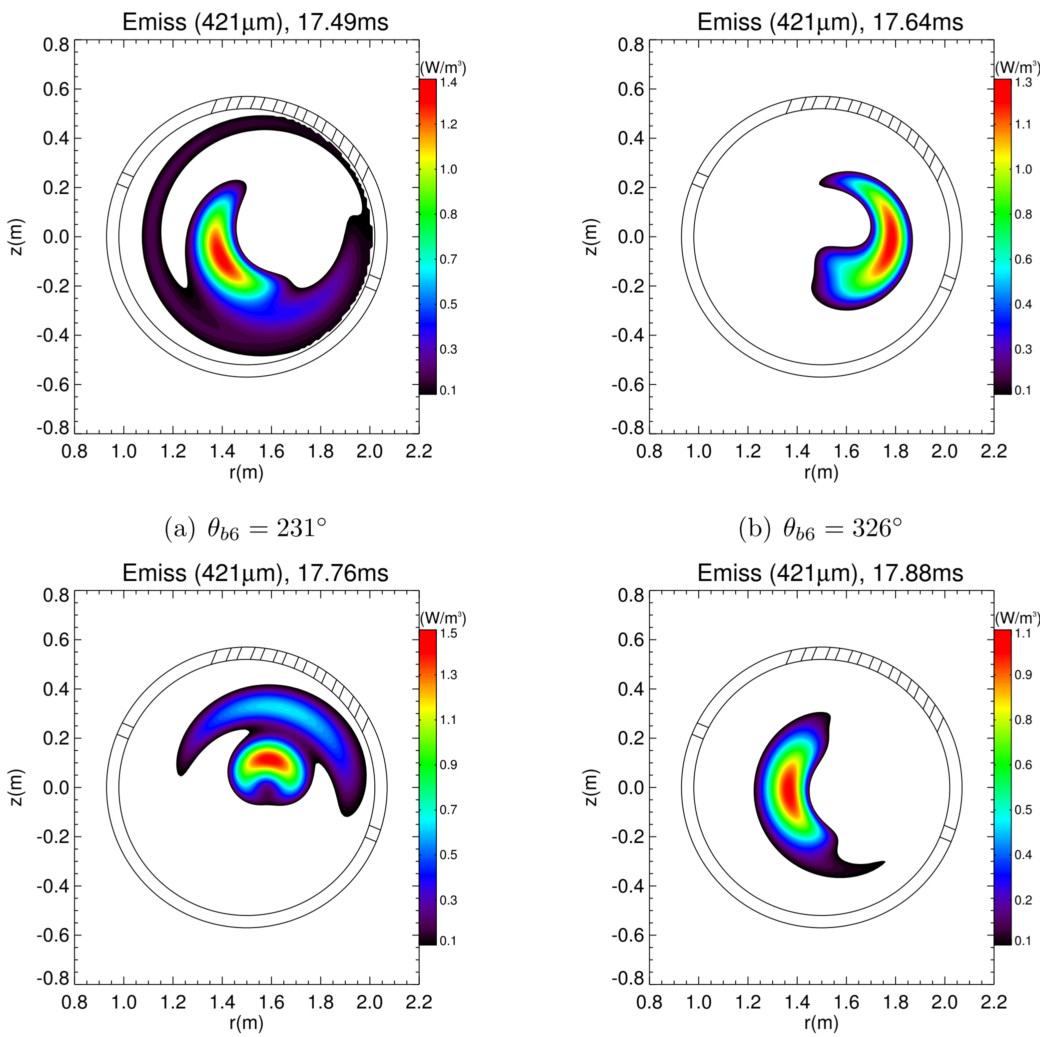

(a) $\theta_{b6} = 231°$

(b) $\theta_{b6} = 326°$

(c) $\theta_{b6} = 82°$

(d) $\theta_{b6} = 145°$

Figure 5.12: Cormack Bessel reconstructed emissivity from fluctuating component of SXR signal for a discharge with $b_p^{1,6}$=10 mode rotating at 4 kHz. Reconstructions are from 2-probe commissioning (only SXR-B and SXR-D), yet trace the rotation of the mode through one period quite well. Mode angle determined from the magnetics is listed below each frame.

signal level. Future analysis of rotating discharges will have higher fidelity tomographic reconstructions with the availability of all 4 probes.

5.3 Case Study: Evidence of T_e Structure during QSH PPCD

SXR brightness profiles and C.B. emissivity reconstructions consistently indicate the presence of emissivity structures in these QSH cases. Because measured SXR emission is a function of T_e, n_e, and Z_{eff}, ($\varepsilon \propto Z_{eff}\, n_e^2\, T_e^{1/2}\, e^{-E/T_e}$) the emissive structure must be caused by a localized increase in one or more of these parameters. Since as a first approximation both T_e and n_e are flux-surface quantities, we consider the case introduced in §5.2.3: a large, locked, dominant n=6 mode (15 Gauss), and determine that a T_e structure contributes to this enhanced emission.

Figure 5.13 shows the plasma parameters for this shot (1121203027), including plasma current I_p, reversal parameter (F), electron density as measured by the CO_2 interferometer, SXR signal from Be1 (black) and SXR-D13 (red), m=0 mode activity, and m=1, n=6-10 toroidal field (where n=6 is in red). Figure 5.14 shows the SXR brightness profiles for the same shot at 18ms (with a 0.5 ms binning window and 5 point downsampling). 421 μm filter profiles are shown in red, while 857 μm filter profiles are shown in blue. The flattened-core region, apparent in all profiles, indicates an emissive structure. The Cormack Bessel reconstructed emissivity for the thin and thick filter are shown in Figure 5.11. The solid lines in the brightness profile indicate the synthetic brightness re-calculated from the emissivity reconstruction. The good match between the reconstructed brightness and the measured brightness further supports the emission island visible in Figure 5.11.

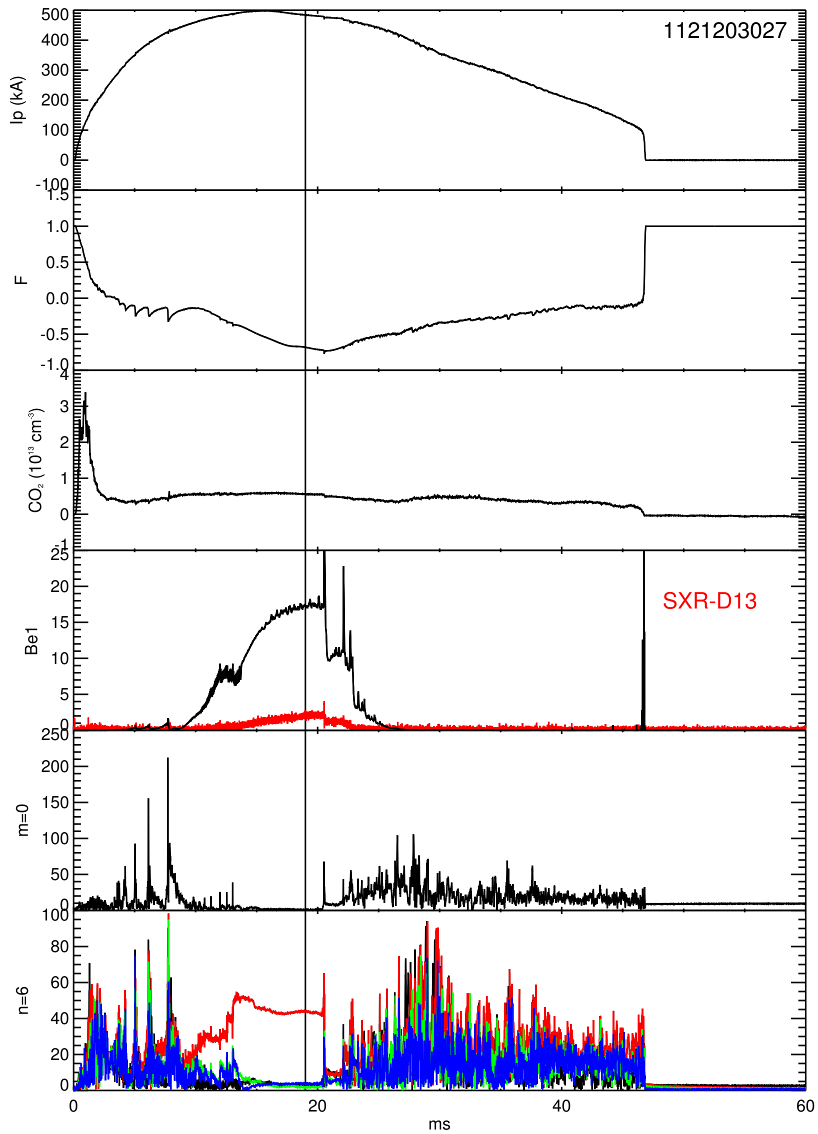

Figure 5.13: Plasma parameters for shot 1121203027. From the top: Plasma current, reversal parameter, electron density, SXR signal (Be1 in black, diode SXR D-13 red), m=0 mode activity, and the toroidal component of n=6-10 mode activity for m=1 (red is n=6). This typical non-crash-heated PPCD shot has a large n=6 dominant mode and is locked from $\sim 15-20$ ms.

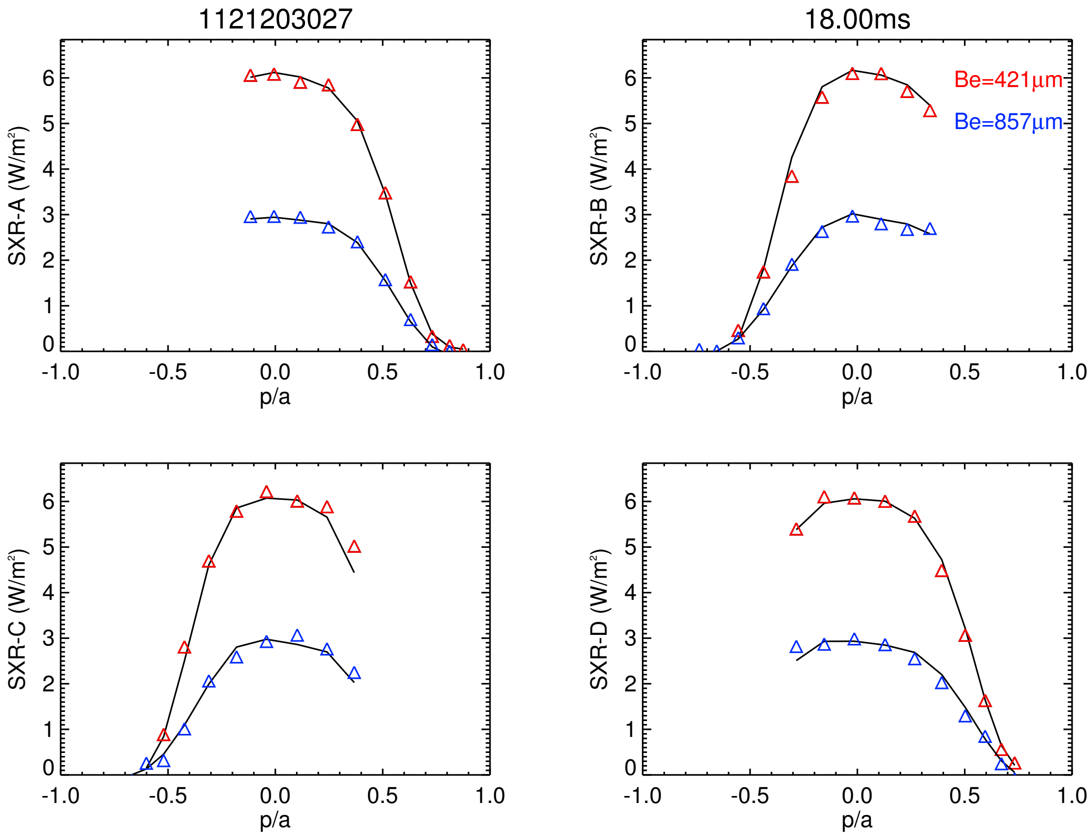

Figure 5.14: SXR brightness profiles as a function of normalized impact parameter for 1121203027 at 18 ms. 421 μm filter is red, 857 μm filter is blue, and synthetic brightness calculated from C.B. reconstructed emissivity (Figure 5.11) is over-plotted in black.

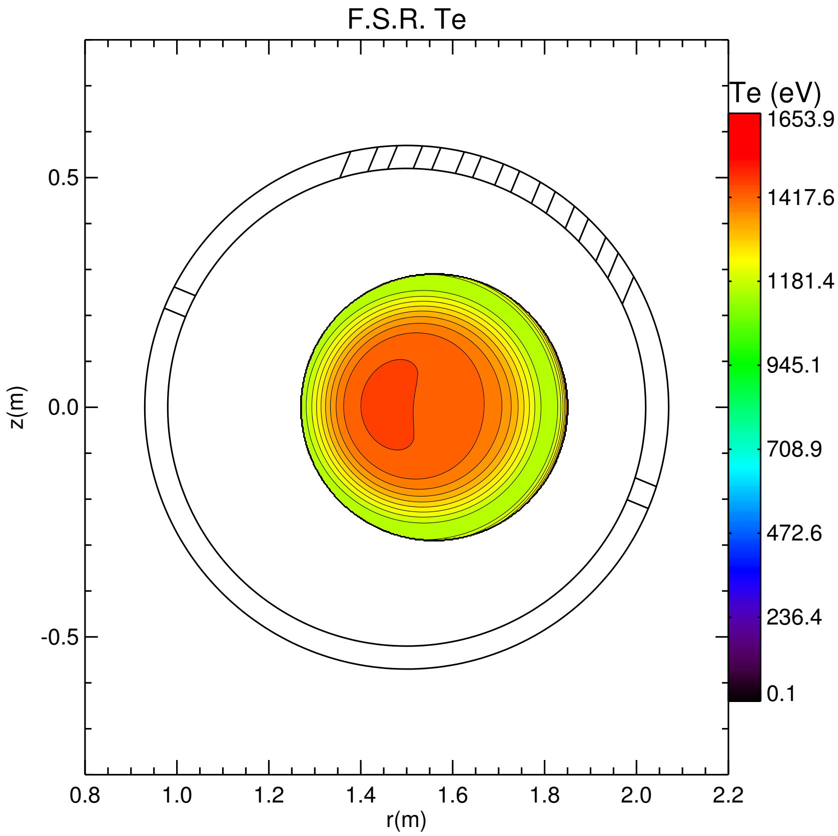

Figure 5.15: Poloidal T_e map as calculated by mapping the thin and thick filter emissivities to flux surface coordinates (Figure 5.10) and then applying the double-foil technique to the ratio of these two emissivity maps. A 20 eV island is visible. This measurement is a lower-bound on the actual island amplitude since the F.S.-mapped emissivities are artificially constrained to be monotonically decreasing.

5.3.1 Evidence Supporting a T_e Structure

The flux surface reconstructed (F.S.R.) T_e, as described in §5.1.2, provides the first indication of a T_e structure. F.S.R. T_e is a particularly useful measurement because it employs the double-foil technique, rendering it independent of n_e and Z_{eff}. Any structure in a F.S.R. T_e map is therefore an indication of temperature alone, in contrast to SXR emissivity. Figure 5.15 shows a 20 eV temperature island in the F.S.R. T_e for shot 1121203027, averaged over a 4ms window centered at 18ms where the plasma parameters are not changing. Because the emissivity profile is artificially constrained to be monotonically decreasing (so that the best emissivity match requires a flattening of emission from the core to the island), this temperature is a lower-bound.

The direct-brightness (DB) temperature further constrains the amplitude of the temperature island. Figure 5.16 plots DB Te as a function of magnetic flux surface coordinate ρ for this shot. Horizontal data from SXR-A and SXR-B are shown in red and pink, while vertical data from SXR-C and SXR-D are in cyan and blue, respectively. Thomson Scattering data is also mapped to flux surface coordinates, accounting for the toroidal shift between the diagnostics and the resulting poloidal shift in n=6 mode angle, shown in black. The point-to-point scatter in both diagnostics is within the uncertainties of the measurements, so no definitive island is visible. However, the lack of a visible island itself provides and upper-limit on potential island amplitude. Combining the size of the error bars with the expected 15% under-estimate of T_e using the direct-brightness technique (refer to §2.3.3), the measurement indicates an upper limit for an island in this discharge of about 250 eV.

A more refined upper-limit on T_e island amplitude for this shot is provided by comparing the measured SXR brightness and emissivity to the SXR emission model described in §2.1. The SXR emission model estimates the T_e island amplitude required

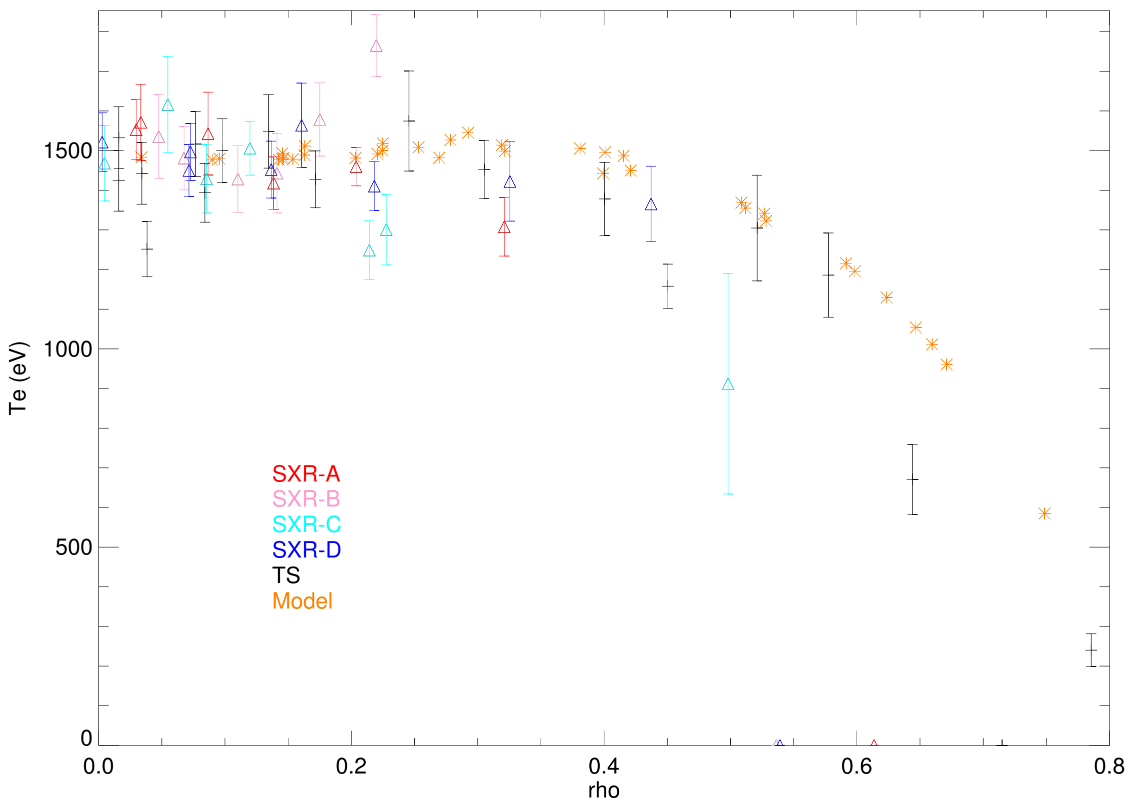

Figure 5.16: SXR DB T_e (triangles) and TS T_e (black crosses) plotted in magnetic flux coordinates (ρ) for shot 1121203027 at 18 ms with a 4 ms binning window. The horizontal profile of SXR-A and SXR-B is plotted in red and pink, while the vertical profile of SXR-C and SXR-D is plotted in cyan and blue. A modeled $T_e + \Delta T_e$ profile for the best fit to the SXR brightness data (ΔT_e near $\rho = 0.3$, orange stars), indicates that the expected island would be smaller than the uncertainties in the measurement, and provides an upper-bound of $\Delta T_{isl} \sim 180$ eV.

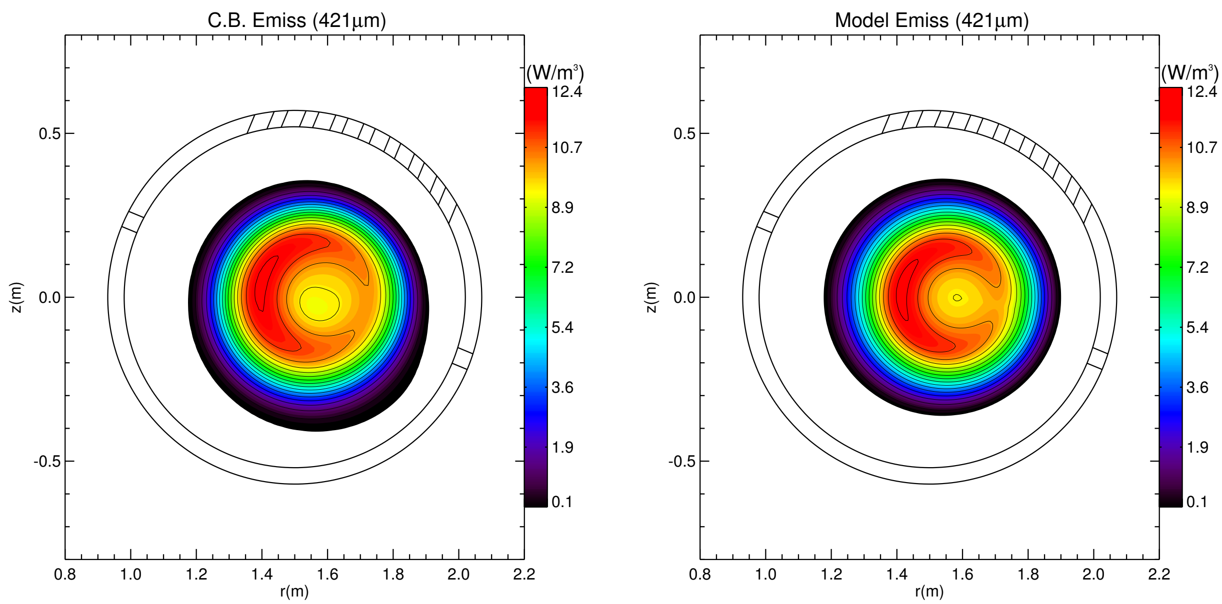

Figure 5.17: Measured thin-filter SXR emissivity from Cormack-Bessel reconstruction (left) and modeled SXR emissivity (right) assuming the source of emission is a 180±10 eV T_e island with parameters $T_e(0) = 1350$ eV, $\alpha = 8.0$, $\beta = 8.0$, $\delta r_{Te} = 0.18$ m, $\delta\theta = 170°$, $\Delta r_{Te} = 0.06$ m and $\Delta\theta = 130°$.

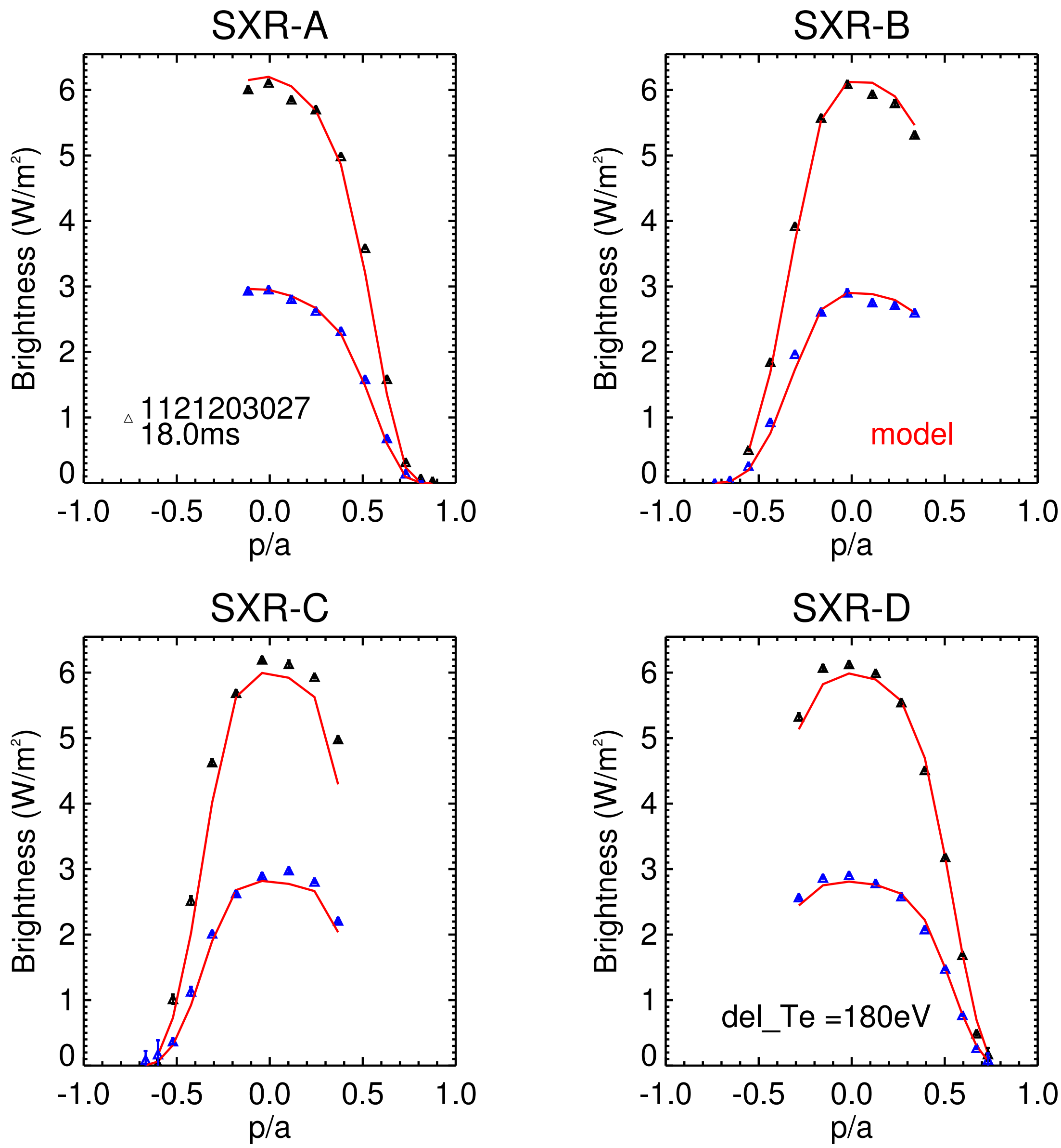

Figure 5.18: Measured thin (black) and thick (blue) filter SXR brightness profiles as a function of impact parameter, compared with the synthetic brightness from the SXR T_e-only model with a 180 eV island (red) for shot 1121203027 at 18 ms. The model provides a reasonably good match to the flattened core-regions of the brightness profiles.

for the resulting synthetic emissivity map to match the CB reconstructed emissivity. Figure 5.17 compares the measured CB reconstructed emissivity for the thin filter (left) to the synthetic emissivity (right) for a model with a temperature island of the form:

$$T_e(r) = T_e(0)\,(1-(r/a)^{\alpha})^{\beta} + \Delta T_e\, e^{-(\delta r_T - r)^2/2\Delta r_T^2}\, e^{-(\delta\theta-\theta)^2/\Delta\theta^2} \tag{5.9}$$

Shot 1121203027	Model Case:		
Parameter	ΔT_e	Δn_e	ΔZ_{eff}
$T_e(0)$	1350	1450	1450
α_T	8.0	8.0	8.0
β_T	8.0	8.0	8.0
$n_e(0)$ ($10^{19}\,m^{-3}$)	0.865	0.821	0.865
α_n	4.2	3.5	4.2
β_n	4.0	2.5	4.0
ΔT (eV)	180	0	0
Δn ($10^{19}\,m^{-3}$)	0	0.18	0
δr (m)	0.18	0.20	–
$\delta\theta$ (° P)	170	170	–
Δr (m)	0.06	0.06	–
$\Delta\theta$ (° P)	130	130	–
Z_{eff} enhanc	0	0	[0.32, 0.32]
$[r_1, r_2, r_3, r_4]$	–	–	[0.06, 0.14, 0.22, 0.24]
Δa (m)	0.075	0.075	0.075

Table 5.1: SXR model parameters for limiting cases T_e, n_e, or Z_{eff} structures in shot 1121203027 at 18 ms.

The island is $\Delta T_e = 180 \pm 10$ eV on top of a background $T_e(0) = 1350$ eV, at $\delta r_{Te} = 0.18$ m, $\delta\theta = 170°$. Uncertainty in the island amplitude comes from matching the island emission relative to the core emission. All model parameters are listed in Table 5.1. The synthetic line-integrated brightness (red) is compared with the

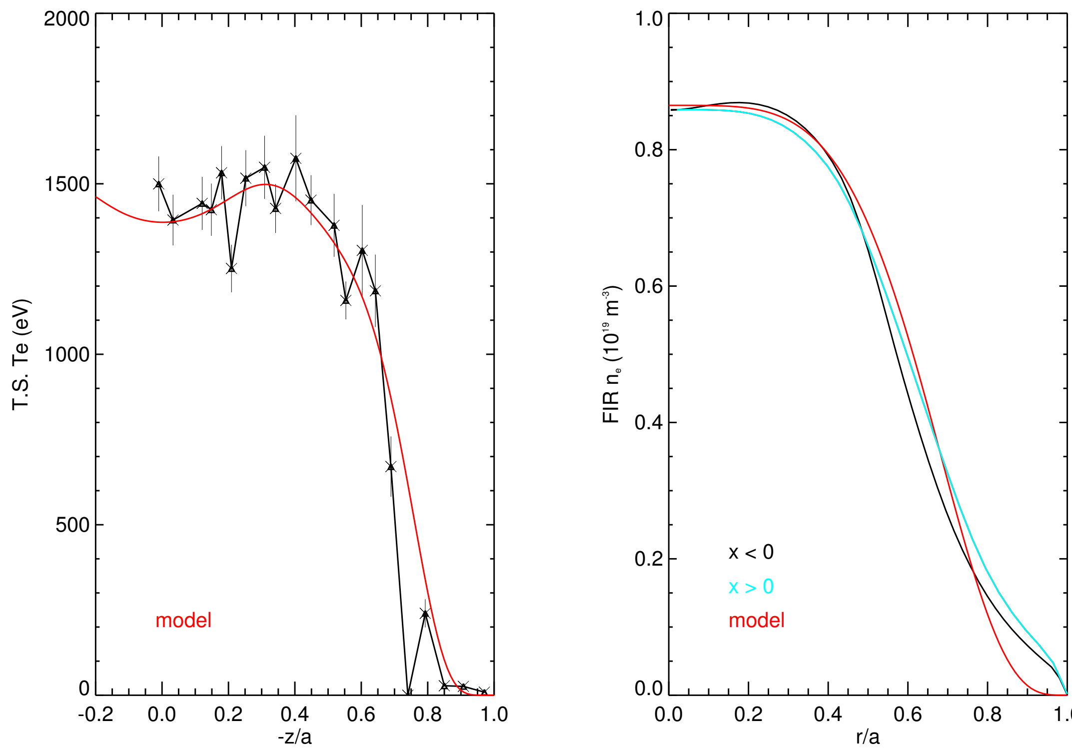

Figure 5.19: Thomson scattering T_e (left) and FIR n_e (right) for measured data binned over 4ms (black, cyan) and synthetic model (red) described in Table 5.1, assuming ΔT_e=180 eV and $\Delta n_e = 0$ for shot 1121203027 at 18.0 ms. Both modeled T_e and n_e match the data reasonably well.

measured thin and thick brightness profiles (black and blue) as a function of impact parameter in Figure 5.18. The synthetic brightness is a reasonable approximation of the measured profiles and shares the characteristic flattening in the core region.

Figure 5.19 compares the modeled temperature and density profiles with the Thomson scattering (left) and FIR (right) inverted measurements. The modeled values are shown in red, while the experimental values are shown in black. The cyan portion of the density profile represents the inboard half of the measurement (cyan is the outboard half). The modeled n_e profile averages the inboard and outboard halves of the FIR profile. Although a flat-profile will also fit the TS data within 1-σ error, the modeled $T_e + \Delta T_e$ profile, which was optimized based only on the SXR emissivity, is an excellent match. A flat density model matches the UCLA reconstructed n_e reasonably well, considering the uncertainty in the core region of the n_e inversion can easily reach 10%. Although the density profiles diverge somewhat at the edge, there is no SXR emission outside r/a=0.7, so this does not impact the comparison to SXR measurements.

Figure 5.16 maps the modeled $T_e + \Delta T_e$ profile onto flux coordinates as orange stars. The island is located around $\rho = 0.3$ and has a projected DB amplitude of < 100 eV. Although the actual island amplitude in the model is larger, the DB T_e technique provides an under-estimate (refer to §2.3.2 for a detailed explanation). Comparison to both the measured DB T_e and Thomson scattering diagnostic indicates that the radial location of the island is not well-sampled by the two diagnostics. Furthermore, the amplitude of the island is smaller than the experimental uncertainties, therefore it is unsurprising that no clear island is seen in the measurements. This T_e-only model for the source of the x-ray emission therefore provides an upper-bound on the amplitude of any temperature island as $\Delta T_e \leq 180$eV.

In the case where an emissive structure cannot be definitively ascribed to T_e, n_e and Z_{eff} should also be considered as sources of SXR emission. A localized increase of n_e or Z_{eff} would not manifest as a T_e island in the double-foil technique, so it is unlikely that either n_e or Z_{eff} alone offers a complete description of the plasma. Nonetheless, some insight can be derived from the limiting cases where the enhanced emission is due solely to n_e or solely to Z_{eff}, and there is no T_e contribution.

5.3.2 Limit: Pure n_e Structure

As the second limiting case, consider the possibility that the enhanced emission is due to n_e alone. To describe the emission from electron density, a Δn_e=0.18x10^{19}

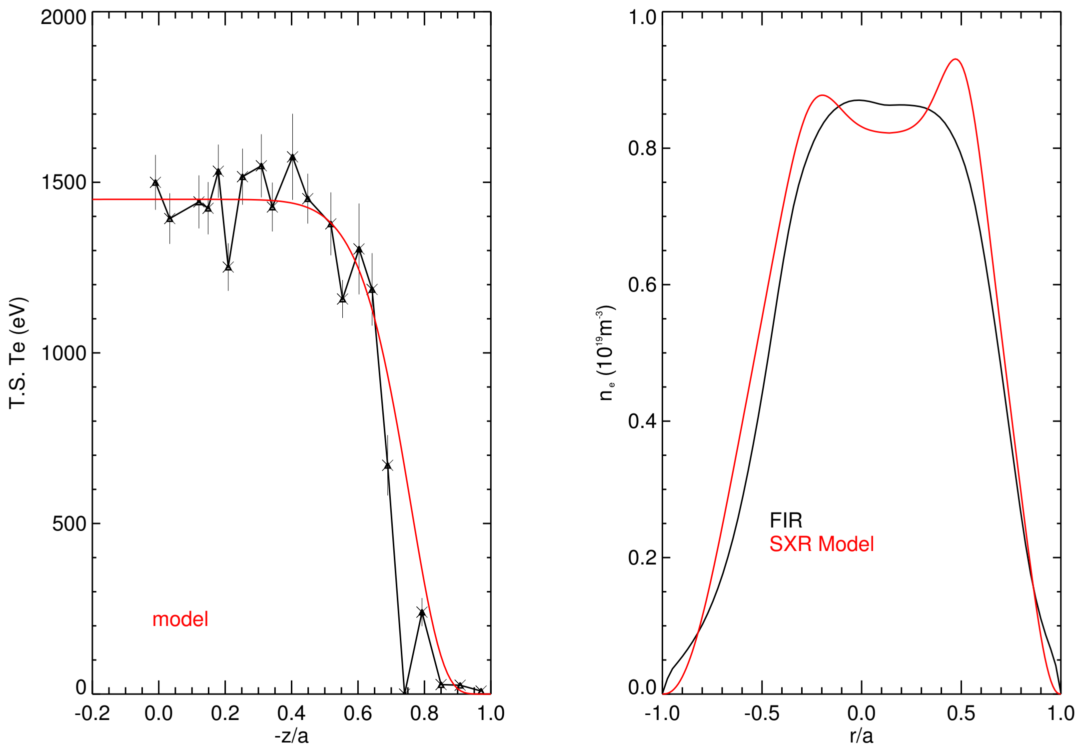

Figure 5.20: Thomson scattering T_e (left) and FIR n_e (right) for measured data binned over 4ms (black) and the model (red) described in Table 5.1, assuming ΔT_e=0 eV and Δn_e=0.18x10^{19} m^{-3} for shot 1121203027 at 18.0 ms. The TS profile can be described as flat within the measurement errors.

m^{-3} structure is required. Complete parameters for this fit are listed in Table 5.1. The simulated SXR emissivity and brightness profiles look just the same as for the T_e case (Figure 5.18). The simulated T_e and n_e profiles are compared with their measured values in Figure 5.20. The Thomson Scattering uncertainties are large enough that either the previous island or this flat profile could describe the data. However, the density island required for the SXR model to match the CB emissivity is not consistent with the FIR inverted n_e. The 21% increase in n_e required to explain the SXR emission is larger than the uncertainty in the inverted FIR profile.

Figure 5.21 shows the line-integrated FIR n_e profile measurement (black), compared with a synthetic line-integrated density calculated from the model profile described by Figure 5.20 (red). The uncertainty in the line-integrated n_e on the FIR is quite small, on the scale of the plot-symbol size. Because the n_e model has been defined from the SXR emission, and there is no SXR emission much beyond mid-radius (vertical lines), it is unsurprising that the model and measurement do not match at the edge. However, any additional emission added to the edge-region would propagate to increase the overall line-integrated signals of the core-viewing chords, further exacerbating the overestimate of the model amplitude compared with the FIR. The synthetic line-integrated measurement also indicates an asymmetry in the core region, peaking near r/a=-0.2 and r/a=+0.4, that is not present in the data. The FIR measurement is therefore not consistent with a model using electron density alone to describe the SXR emission structure.

5.3.3 Limit: Pure Z_{eff} Structure

The third case to consider is that of a localized increase in Z_{eff} generating enhanced SXR emission. Recent experiments at Alcator C-Mod have identified magnetic structures confining impurities similar in topology to MST QSH structures [73]. Recall

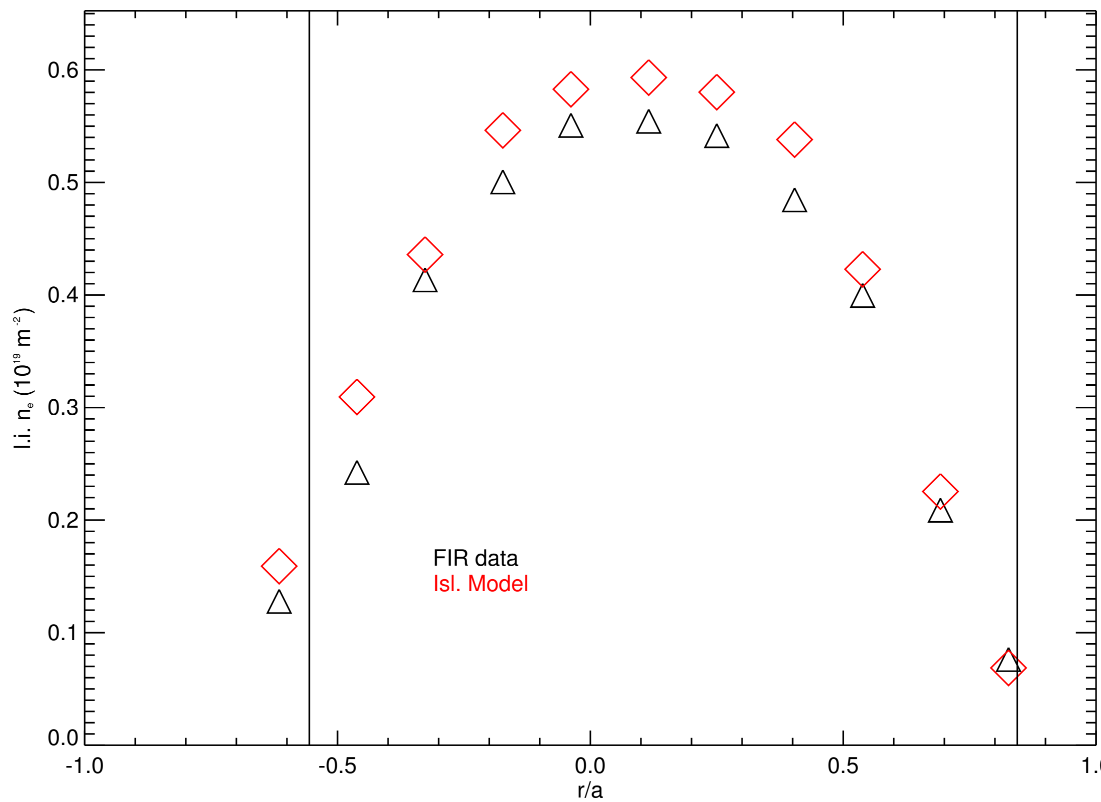

Figure 5.21: Line-integrated n_e measured by FIR (black triangles) and simulated from the $n_e + \Delta n_e$ model described by Figure 5.20 (red diamonds). The model is not optimized outside the region of SXR emission (vertical lines). Nonetheless, the discrepancy is asymmetric between the inboard and outboard sides. This indicates that the density structure required to explain the SXR emission in the n_e-only model is not consistent with the FIR n_e measurement.

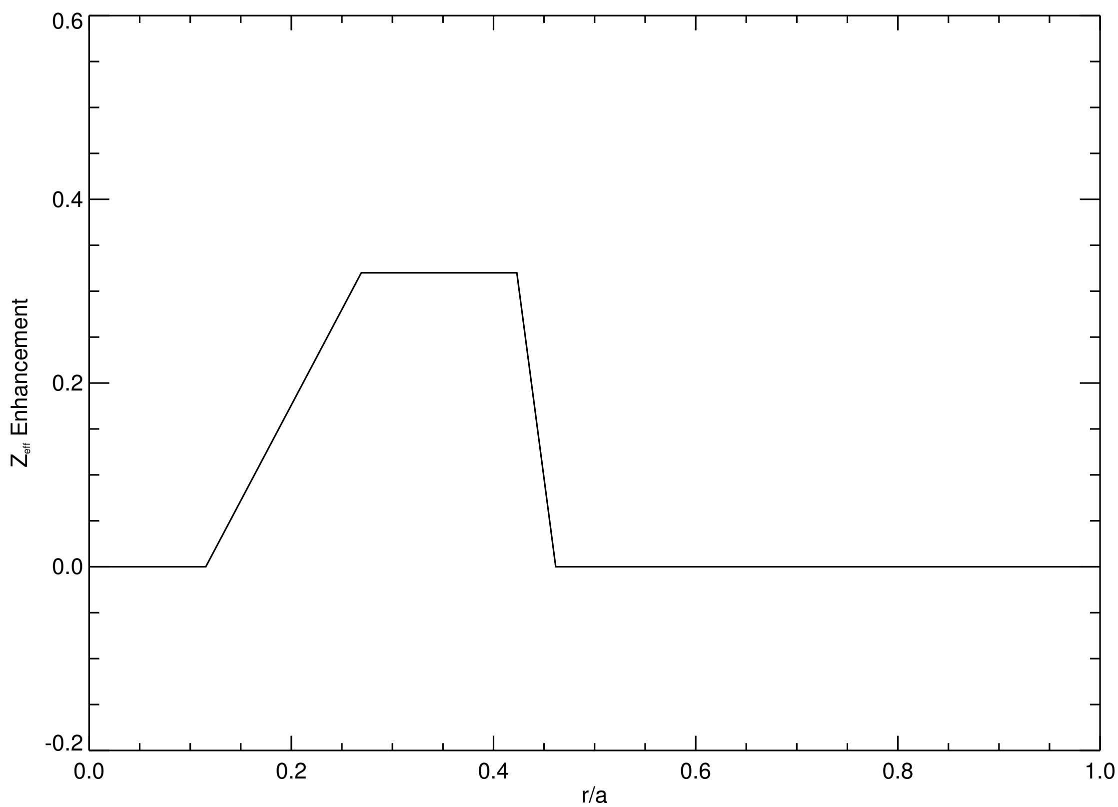

Figure 5.22: The relative enhancement profile used to model the emission as being caused by Z_{eff}. The enhancement factor is applied as $e^{ln(1+ENH)}$ so that for this case there is a 32% enhancement in the island compared with the core region.

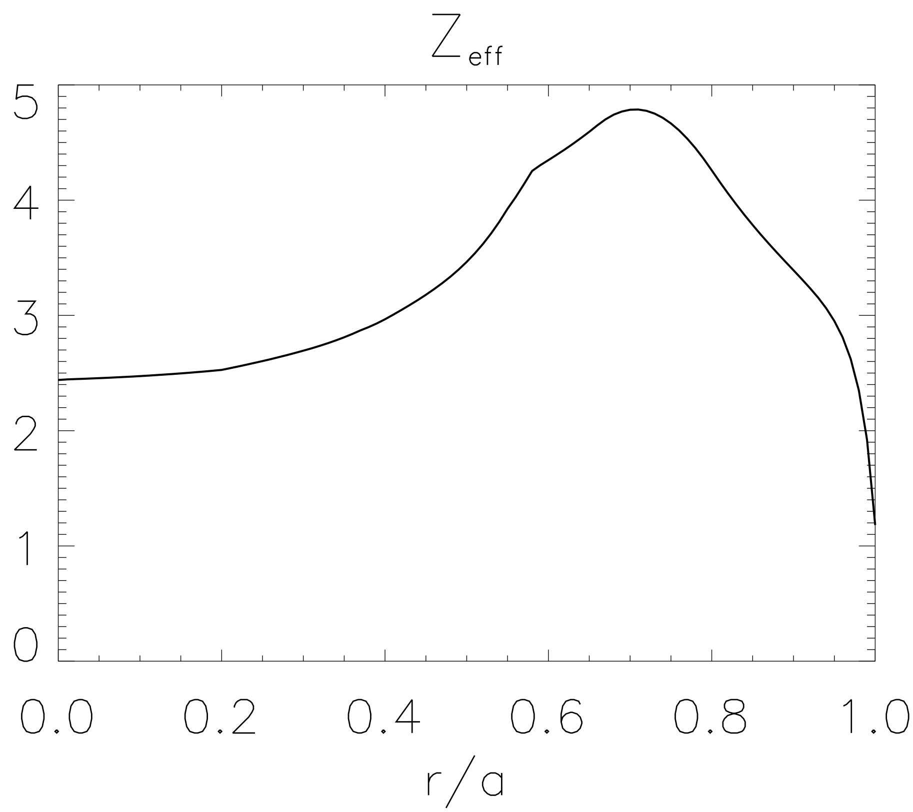

Figure 5.23: Canonical Z_{eff} profile during 500 kA crash-heated PPCD, calculated by combining CHERS impurity data with a collisional-radiative transport model (courtesy of T. Barbui [75].)

that the beryllium filters have been carefully chosen to block out impurity line radiation. Recall from Equation 2.1 that pure bremsstrahlung radiation is also a function of effective atomic number, and so a localized increase in emission can potentially be explained by this mechanism. SXR emission is directly proportional to Z_{eff}, so to explain a $\sim 30\%$ increase in SXR emission, a $\sim 30\%$ increase is required in Z_{eff} as well. The Z_{eff} enhancement profile defined by the parameters in Table 5.1 is shown in Figure 5.22 (where enhancement is defined as $e^{ln(1+ENH)}$, see §2.1.3 for a full description).

A general Z_{eff} profile for high-current PPCD plasma has been estimated by combining impurity line profiles measured by the CHERS diagnostic with an RFX model that applies collisional radiative effects to hydrodynamic evolution of the plasma [74, 75]. This Z_{eff} profile is shown in Figure 5.23. This model suggests a core value of $Z_{eff} = 2.4$, meaning that the local Z_{eff} at r/a=0.34 in this case study would have to be $Z_{eff} \sim 3.1$ to explain the SXR emission. Note that the Z_{eff} profile presented here is taken from analysis of a 500 kA crash-heated PPCD plasma, rather than the non-crash-heated plasmas used for the SXR analysis. Crash-heated PPCD plasmas tend to have higher T_e and lower magnetic mode amplitudes ($b_p^{1,6}$=4 G in this case), so a direct match is not necessarily expected. Furthermore, the peak Z_{eff} in the profile (Figure 5.23) occurs at r/a=0.7. SXR emission falls off dramatically around r/a=0.5 due to the gradients in $T_e(r)$ and $n_e(r)$, so the $Z_{eff}(r/a = 0.34)$ does not constrain the peak of the Z_{eff} profile. Therefore, the required Z_{eff} at the island radius required to fully explain the SXR emission is plausible.

5.3.4 T_e Structure: Discussion

Shot 1121203027 has a locked (1/6) magnetic structure at 175° poloidal (at the toroidal location of the SXR diagnostic). The tearing mode has a poloidal magnetic amplitude of 15 Gauss, which is quite large for a high-current non-crash-heated PPCD plasma. A corresponding structure is seen in both SXR emissivity and flux-surface-reconstructed T_e. The flux surface reconstructed T_e provides a minimum amplitude for the structure of 20 eV. The absence of a visible structure in the direct-brightness T_e profile provides an upper bound on the structure of $\sim$ 250 eV, or <20% of the core T_e.

The SXR emission model is used to examine the limiting cases that describe SXR emission as being due to solely T_e, n_e, or Z_{eff}. The T_e-only case reduces the upper-limit on ΔT_e to 180 eV. A n_e-only model for the emission can be ruled out because the resulting line-integrated synthetic density is inconsistent with the measurement from the FIR diagnostic. Contribution of an enhanced Z_{eff} to the region is plausible and cannot be ruled out. A 32% increase in Z_{eff} relative to the core is sufficient to explain the structure without any requirement for T_e or n_e contributions. An increase in Z_{eff} toward mid-radius has been observed in other PPCD plasmas due to ion-screening, further supporting the plausibility of Z_{eff} [74]. Perhaps the most likely explanation for the enhanced SXR emission is that it is due to a combination of T_e and Z_{eff}, and possibly n_e as well.

This large amplitude quasi-single helicity PPCD shot (1121203027) is a somewhat unique example. Of the 60 good-PPCD shots taken over three run days in these conditions, only 10 have magnetic amplitudes $>$ 10 Gauss. (Interestingly, all of the large-magnetic amplitude shots are locked). Unfortunately, the shot analyzed here is the only example in this dataset for which there is data from all four SXR probes, FIR, and TS. Of the 9 locked shots with complete diagnostic data, the discharge presented here is the only one that has reasonable evidence for ΔT_e in the flux-surface reconstructions. There are two shots with F.S.R. ΔT_e=4-6 eV, and the remaining six shots do not indicate a T_e structure in the flux surface reconstructions.

5.4 Case Study: Evidence of Z_{eff} Structure During MH PPCD

A contrasting example that highlights the SXR diagnostic capabilities is found by examining a PPCD discharge where all magnetic tearing modes are suppressed. The conventional wisdom is that during multiple helicity (MH) plasmas, the overall mode reduction leads to axisymmetric flux surfaces and improved confinement. This is manifested in SXR emission by symmetric reconstructed emissivity, as can be seen for an example shot during 2-probe commissioning in Figure 5.24. (Figure 5.25 shows

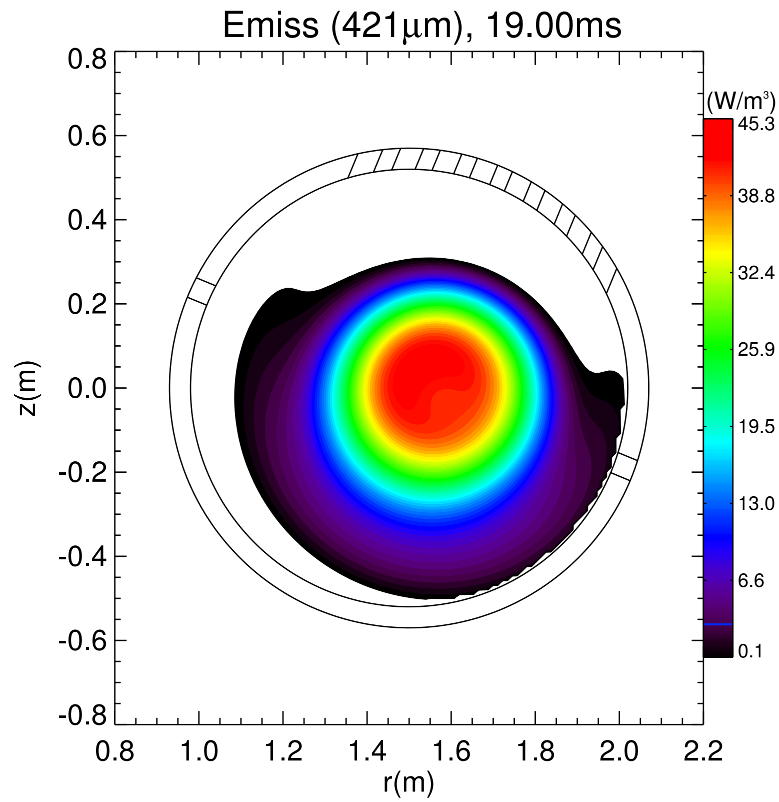

Figure 5.24: Thin filter Cormack-Bessel reconstructed emissivity for a 'typical' multiple-helicity PPCD discharge where all the tearing modes have been suppressed (1121015040 at 19 ms). In a canonical MH plasma, the SXR emission is quite axisymmetric, even in this example where only SXR-B and SXR-D were available for the reconstruction (the reduced coverage causes the slight vertical shift).

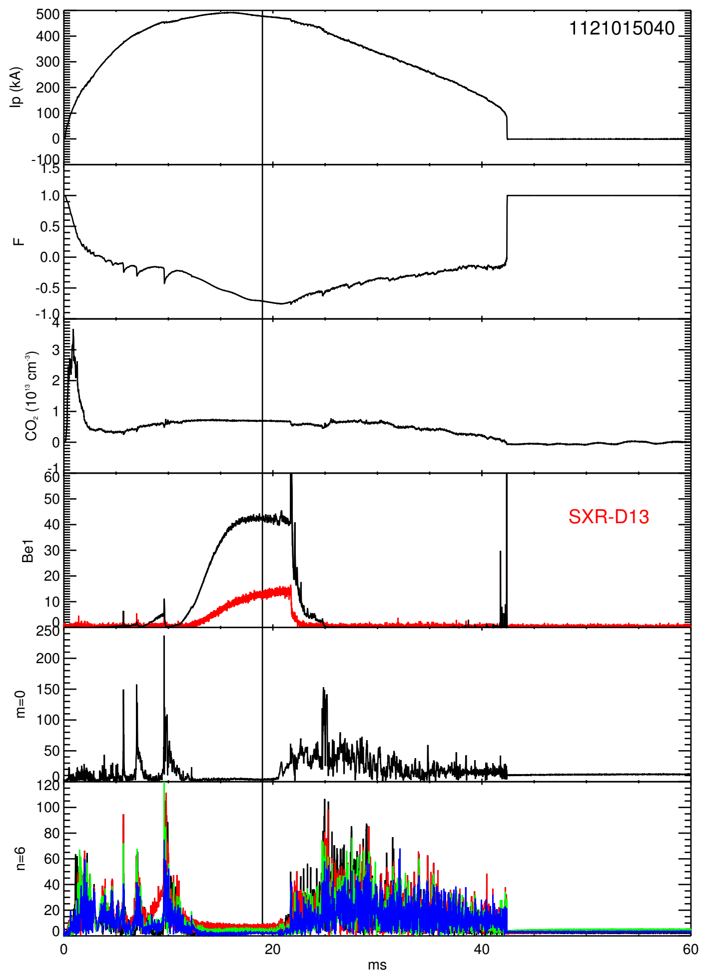

Figure 5.25: Plasma parameters for a 'typical' multiple-helicity PPCD discharge (1121015040). From the top: Plasma current, reversal parameter, electron density, SXR signal (Be1 in black, diode SXR D-13 red), m=0 mode activity, and the toroidal component of n=6-10 mode activity for m=1 (red is n=6). This MH plasma has very low toroidal mode amplitudes for all n.

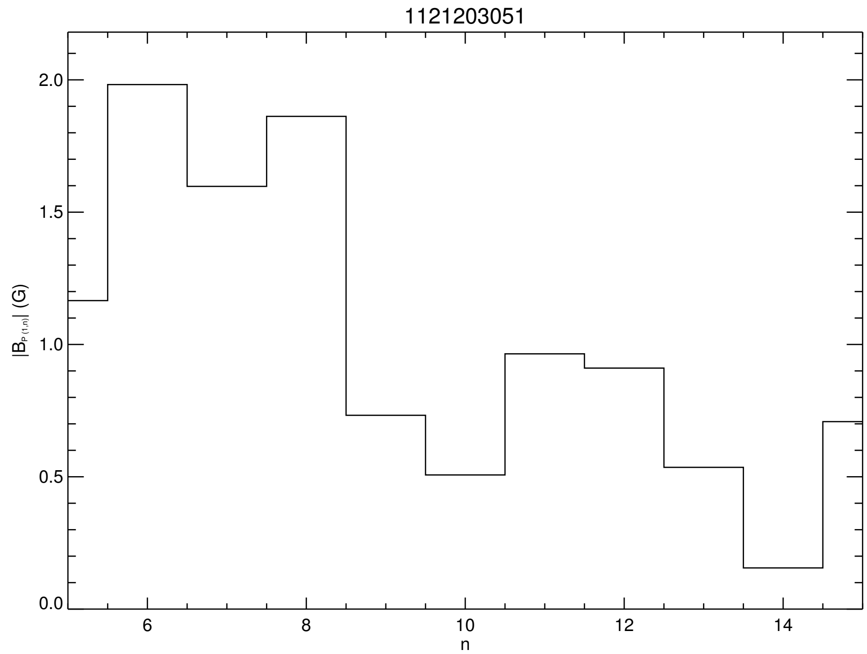

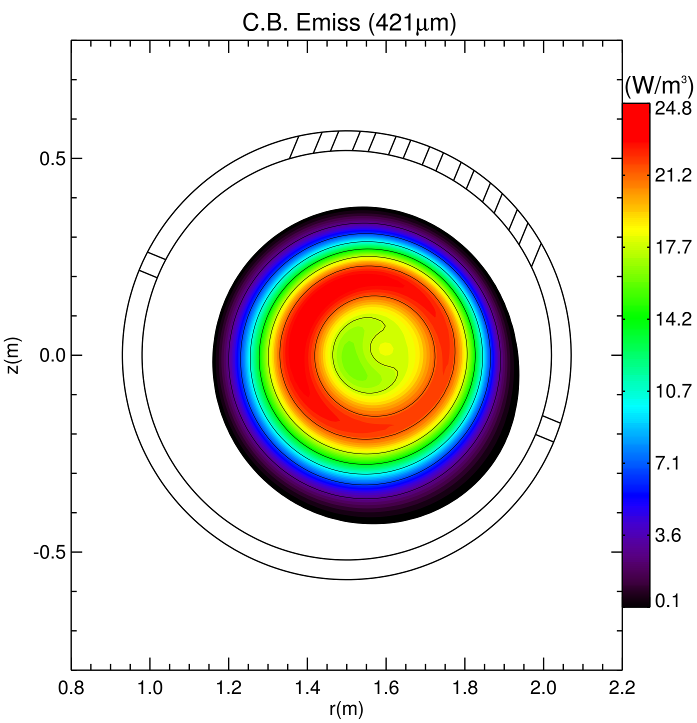

Figure 5.26: Magnetic mode spectrum and Cormack-Bessel reconstructed thin filter SXR emissivity for an 'atypical' MH discharge with an emissive ring structure (shot 1121203051 at 19 ms). The SXR emission is quite different from the MH case shown in Figure 5.24 despite an equivalent magnetic geometry.

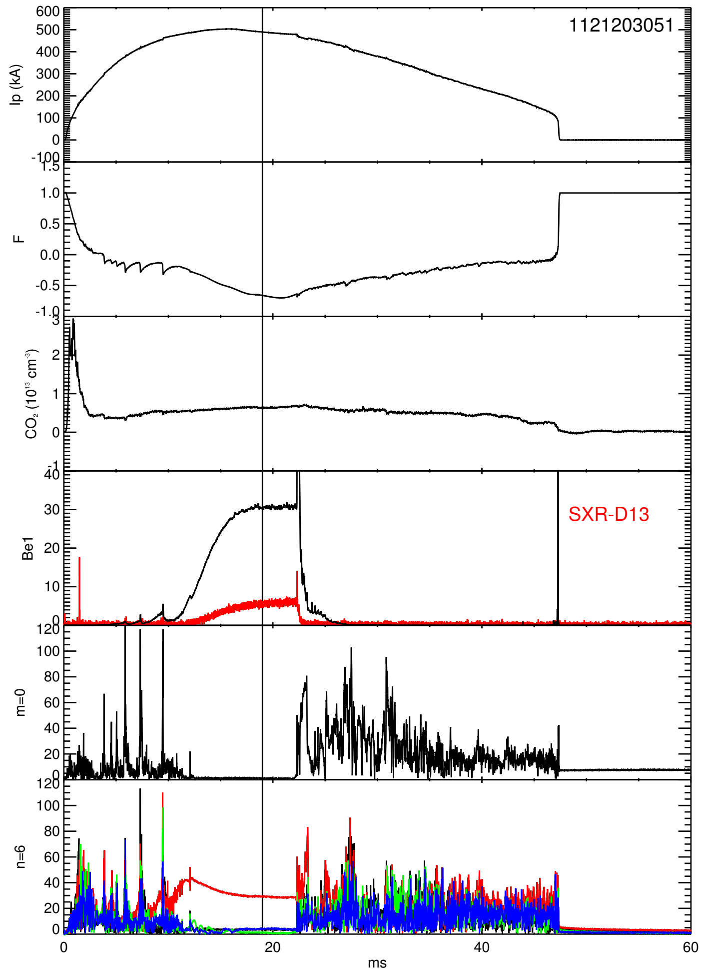

Figure 5.27: Plasma parameters for a multiple-helicity PPCD discharge showing a ring-structure (1121203051). From the top: Plasma current, reversal parameter, electron density, SXR signal (Be1 in black, diode SXR D-13 red), m=0 mode activity, and the toroidal component of n=6-10 mode activity for m=1 (red is n=6). This MH plasma has a slightly larger n=6 toroidal magnetic mode compared with higher order n, but is still small. The poloidal mode amplitudes are all equivalently small (Figure 5.26).

the plasma parameters for this discharge). In this good PPCD shot, the SXR and TS T_e profiles are consistent and the emissivity map can be explained without invoking any additional emission beyond the axisymmetric T_e profile.

However, SXR emissivity sometimes indicates an 'atypical' emissivity structure featuring a prominent ring of emission during discharges with a similar multiple-helicity magnetic mode spectrum. The magnetic mode spectrum and thin filter reconstructed emissivity for an example of this ring-MH discharge (1121203051) are shown in Figure 5.26. (Plasma parameters for this shot are shown in Figure 5.27.) As with the QSH example, the enhanced SXR emission can potentially be caused by variation in T_e, n_e, or Z_{eff}. Table 5.2 lists the modeling parameters required to match the enhanced SXR emission for the limiting cases where all the emission is caused by each one of these three components.

5.4.1 Limit: Pure T_e Structure

In this discharge, T_e measurements suggest the emission is likely not caused by a local increase in T_e. Figure 5.28 shows the direct-brightness and Thomson scattering T_e mapped in flux surface coordinates (top), as well as the flux-surface reconstructed T_e (bottom). $T_e(\rho)$ is over-plotted in orange stars for the $T_e + \Delta T_e$ model. The $T_e(\rho)$ measurements again lack any clear indication of an island structure around $\rho = 0.4$. If anything, the measured values suggest a decrease in T_e in that region, rather than an increase. The flux-surface-reconstructed T_e is very flat and also lacks an indication of structure. A model with a T_e-only structure is also not a good fit to the data. A direct comparison between the model and the Thomson Scattering profile (as well asthe FIR n_e) for this model are shown in Figure 5.29. Here again, the model is not particularly consistent with the Thomson Scattering profile, particularly in the core region. The T_e model is not well-matched to the data for this ring-MH plasma.

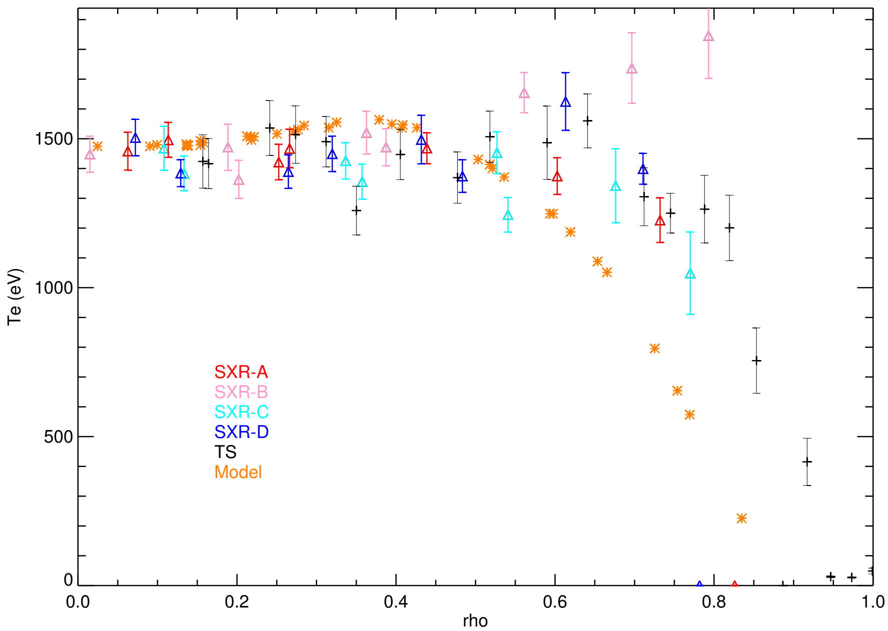

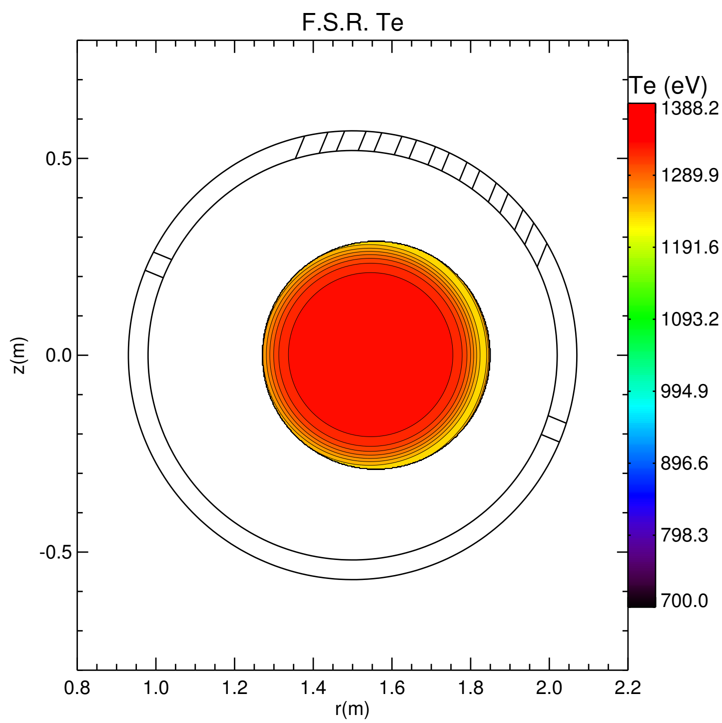

Figure 5.28: *Ring-MH discharge* (1121203051 at 19ms, with at 2ms binning window) Top: Direct-brightness (triangles) and Thomson Scattering (pluses) $T_e(\rho)$. The horizontal profile from SXR-A and SXR-B is plotted in red and pink, while the vertical profile from SXR-C and SXR-D is plotted in cyan and blue. A modeled $T_e + \Delta T_e$ profile for the best fit to the SXR brightness data (ΔT_e near $\rho = 0.4$, orange stars) is not a good match in T_e. Bottom: Flux-surface-reconstructed T_e contours are very flat and do not show evidence of structure.

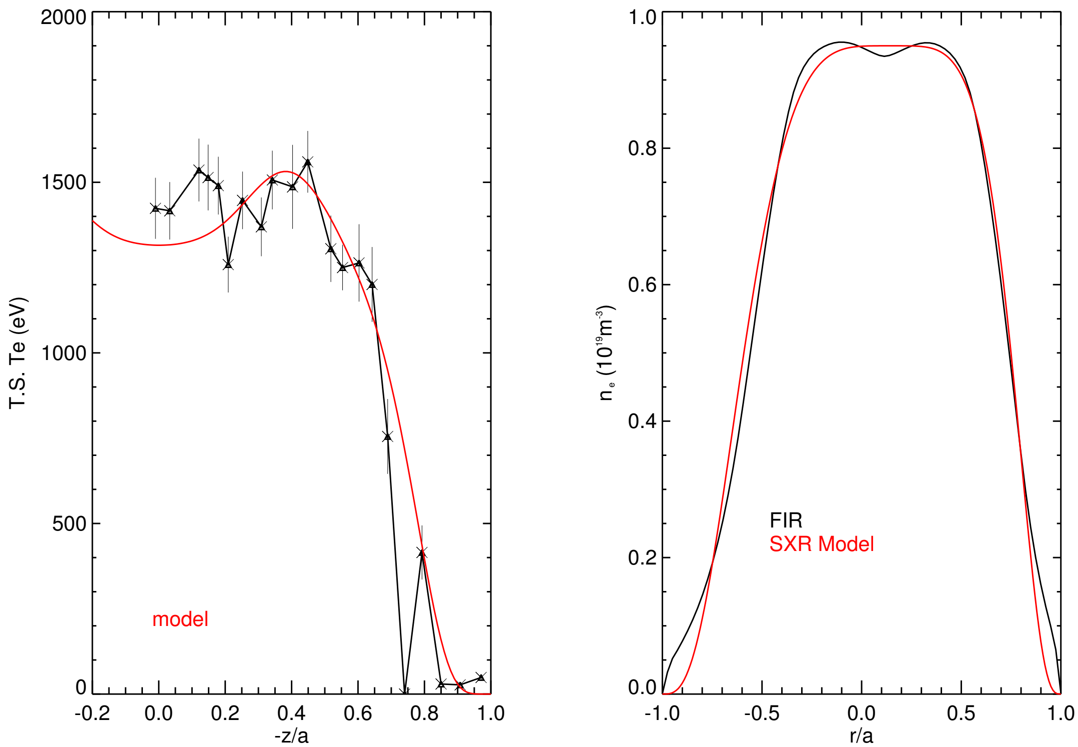

Figure 5.29: Comparison of the modeled T_e and n_e (red) to the experimental profiles (black) from the FIR (left) and Thomson Scattering (right) diagnostics for discharge 1121203051 assuming a T_e-only model. The T_e model profile is not a good fit to the Thomson Scattering measurement.

	Model Case:			
Parameter	ΔT_e	Δn_e	ΔZ_{eff}	Barbui ΔZ_{eff} Model
$T_e(0)$	1300	1400	1400	1400
α_T	8.5	8.5	8.5	8.5
β_T	7.2	7.2	7.2	7.2
$n_e(0)$ ($10^{19}\, m^{-3}$)	0.95	0.883	0.95	0.95
α_n	4.4	3.8	4.4	4.4
β_n	3.4	2.3	3.4	3.4
ΔT (eV)	250	0	0	0
Δn ($10^{19}\, m^{-3}$)	0	0.21	0	0
δr (m)	0.21	0.21	–	–
$\delta\theta$ (°P)	130	–	–	–
Δr (m)	0.06	0.06	–	–
$\Delta\theta$ (°P)	360	–	–	–
Z_{eff} enhanc	0	0	[0.58, 0.58]	[1.0, 1.0]
$[r_1, r_2, r_3, r_4]$	–	–	[0.09, 0.19, 0.22, 0.34]	[0.10, 0.34, 0.39, 0.49]
Δa (m)	0.07	0.07	0.07	0.07

Table 5.2: SXR model parameters for limiting cases T_e, n_e, or Z_{eff}-only structures in shot 1121203051 at 19 ms. The final column uses the equilibrium T_e and n_e models along with an approximation of the Z_{eff} profile measured for PPCD plasmas by Barbui [75] to see how well the canonical Z_{eff} matches the SXR emission from this discharge. The n_e-only structure has no angular dependence because it is modeled as a ring.

5.4.2 Limit: Pure n_e Structure

The enhanced SXR emission is also not well-described in the limit where all of the emission is due to n_e. Figure 5.30 compares the model temperature and density profiles required to explain the SXR emission in the n_e-only case (red) with the Thomson Scattering T_e and FIR n_e profiles for the actual shot (black). Figure 5.31 shows the synthetic line-integrated model (red), again compared with the measured line-integrated FIR profile (black). In order to match the SXR emissivity profile, the density profile must include a structure that is larger in amplitude than the FIR measurement identifies, even within the 10% uncertainty in the inverted FIR profile. Moreover, comparison of the line-integrated model and FIR measurements shows a particularly large discrepancy at -0.2 and +0.4 r/a. The uncertainty in the line-integrated FIR measurement is very small (the size of the plot symbols), and the discrepancy induced by the SXR emission structure is outside this uncertainty. Therefore, a SXR emission model assuming a structure caused by enhanced n_e is inconsistent with the measured density profile.

5.4.3 Limit: Pure Z_{eff} Structure

The limiting cases explaining the SXR enhancement using Δn_e or ΔT_e alone are not convincing. Instead, consider a model using the estimated example PPCD Z_{eff} profile from the CHERS measurements, along with the $\Delta n_e, \Delta T_e = 0$ (Figures 5.29 and 5.30, respectively). Figure 5.32 shows a normalized approximation of the T. Barbui Z_{eff} profile in Figure 5.23, where the shape has been approximated to the limitations of the SXR model Z_{eff}. The model captures the ratio of peak-to-core Z_{eff}, the radial location of the peak, and the general slope on either side of the peak, although it does not match the detailed gradient of the Barbui profile in the mid-radius region. The red star represents the Z_{eff} enhancement required at the center of the emissivity ring to fully explain the SXR emission as due to impurity radiation.

Despite the underestimate of Z_{eff} in the ring compared with the core, the Barbui estimate is generally plausible. Figure 5.33 shows the thin-filter CB reconstructed emissivity contours (left) compared with this model (right), and Figure 5.34 illustrates the radial cross-sections of these two emissivities (black and red, respectively). The Barbui profile resultes in an emission ring in the same mid-radius region, with steep reduction of emissivity beyond r/a = 0.5. The modeled emissivity ring extends

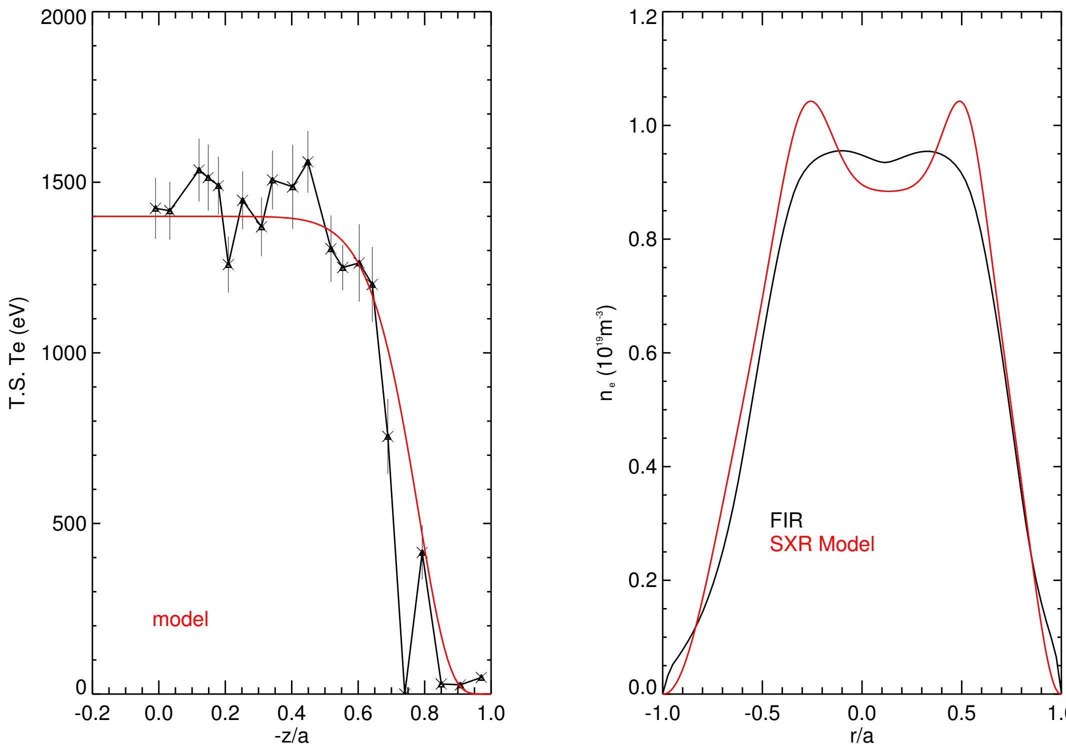

Figure 5.30: Comparison of the modeled T_e and n_e(red) to the experimental profiles (black) from the FIR (left) and Thomson Scattering (right) diagnostics for discharge 1121203051 assuming a n_e-only model. The amplitude of the density structure required for the SXR model to match the measured emissivity is much larger than the measured n_e profile from the FIR. In contrast, a flat model is a reasonable estimate for the T_e profile.

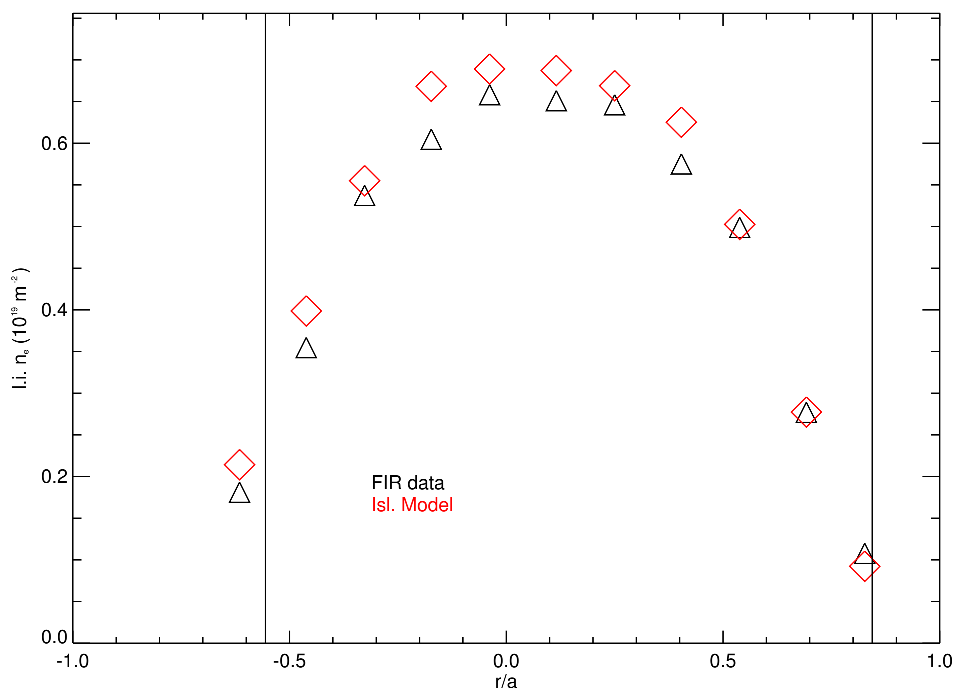

Figure 5.31: Line-integrated n_e from the FIR measurement (black triangles) and the synthetic SXR model (red diamonds) for the n_e-only case on discharge 1121203051. In matching the SXR emissivity profile, the model (shown in Figure 5.30) over-estimates emission in the core region. In particular, the chords at -0.2 and +0.4 r/a should have a relative increase in signal if the ring is due to n_e.

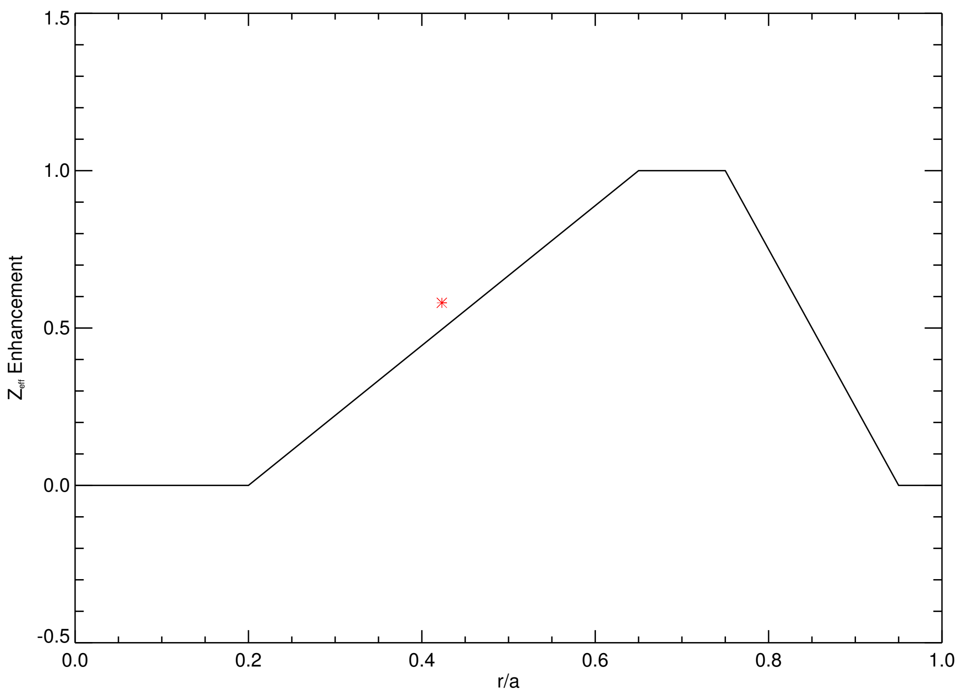

Figure 5.32: Normalized approximation of example PPCD Z_{eff} profile calculated by T. Barbui in Ref. [75] (and shown in Figure 5.23), matched within the limitations of the SXR Model Z_{eff} profile. The red star represents the value and location of Z_{eff} required to match the SXR emissivity reconstruction, which is slightly larger than the Barbui profile estimate.

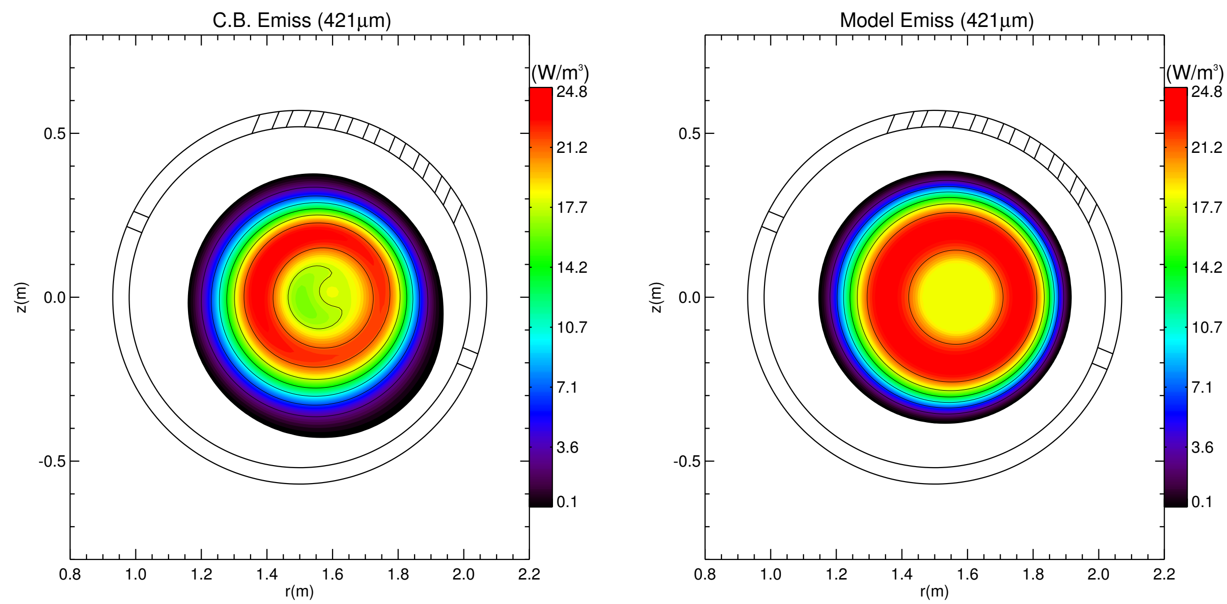

Figure 5.33: CB reconstructed (left) and modeled (right) thin-filter emissivities assuming $\Delta n_e, \Delta T_e = 0$ and the Barbui Z_{eff} profile modeled in Figure 5.32. The emission is over-estimated on the inboard side of the ring, where the model is not a good match to the Barbui profile. The Barbui model also results in slightly smaller Z_{eff} in the ring relative to the core than the CB emissivity suggests.

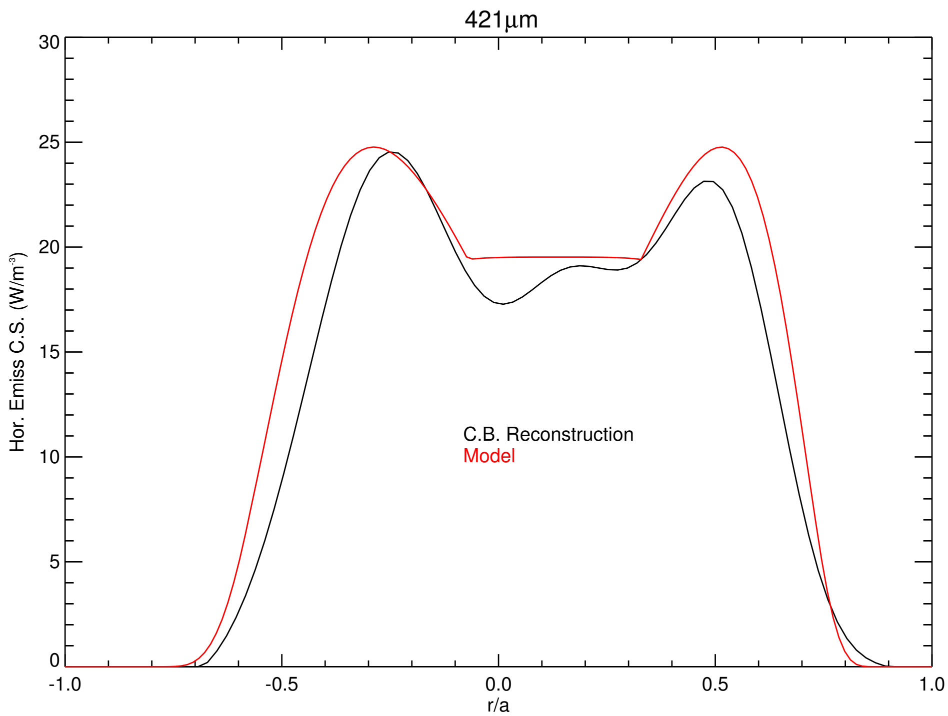

Figure 5.34: Radial cross-section of CB reconstructed (black) and Barbui Z_{eff} profile model (red) emissivities. The profile indicates generally good agreement, although the modeled emission extends about 10% further out in radius than the CB emissivity. The relative increase in emission in the ring compared with the core is slightly underestimated with the Barbui profile. Nonetheless, the profiles are quite similar and the discrepancies could be due to shot-to-shot variation.

about 10% further outward than the CB reconstruction, but the dropoff in emission is dominated by the negative n_e and T_e gradients despite Z_{eff} continuing to increase out to r/a=0.7. That the model ring extends further toward the core than the CB reconstruction is primarily due to the crudeness of the Z_{eff} model such that it does not closely match the Barbui profile in the mid-radius region. The underestimate of ring-to-core emission could be easily compensated by slightly adjusting the slope of Z_{eff} between 0.2-0.6 r/a. Finally, the Barbui profile is not a measurement of Z_{eff} in this particular PPCD plasma, but a shot-averaged example. Shot-to-shot variation may well account for the discrepancies between the profile and this discharge. More precisely, a Z_{eff} model that is 58% larger in the structure than in the core is sufficient to entirely explain the enhancement in SXR emission, with no additional contribution from T_e or n_e. For a PPCD plasma with $Z_{eff}(0) \sim 2.4$, this corresponds to Z_{eff}=3.8 at r/a=0.4. In fact, Alcator C-Mod has measured helical snake structures with ΔZ_{eff} = 60-70% $Z_{eff}(0)$[73].

5.5 Conclusions

The new SXR T_e and tomography diagnostic has been fully commissioned and is available for plasma studies at high current and improved confinement. A suite of diagnostics provide the opportunity to leverage the SXR brightness and emissivity measurements using integrated data analysis. Thomson Scattering T_e and FIR n_e profiles provide constraints to help understand SXR emissivity in general. A new analysis technique that uses external magnetics measurements to reconstruct the plasma flux surfaces is paired with the SXR measurements to make contour maps of T_e.

Using a series of different beryllium foils for core-viewing diodes, the SXR diagnostic has been used to measure the plasma spectrum in the soft x-ray energy band. In particular, this study confirms the existence of substantial x-ray emission due to aluminum radiation in MST. For the first time, CHERS impurity measurements have been used to normalize the impurity component of the SXR emission across shots, allowing a more precise treatment of the SXR brightness. This study demonstrates that the SXR diagnostic must be equipped with beryllium foils that are more than 400 μm thick to reliably measure T_e with the double-foil technique.

Measurements from the SXR system have been compared with other MST diagnostics. The direct-brightness T_e technique has been benchmarked against Thomson Scattering in high-current non-crash-heated PPCD, and the two diagnostics show excellent agreement. Both the spatial profile and the temporal evolution of T_e are consistent between the two measurements. Island-shaped structures in SXR emissivity are correlated to the poloidal angle of the dominant magnetic tearing mode. The Cormack-Bessel reconstructed SXR emissivity structure can be tracked during mode rotation as well. Filtering the signal around the dominant mode frequency indicates that the fluctuating component is $\sim 10\%$ of the measured SXR emission.

The SXR double-foil diagnostic has been used to search for T_e structures during locked PPCD discharges. A case study of a large magnetic mode amplitude QSH plasma indicates a small T_e structure. The exact amplitude of ΔT_e has not been measured, but it may be as large as 180 eV, or $\sim 10-15\%$ $T_e(0)$. Future current-profile measurements will indicate whether the result of the island is to modify the current profile or to improve the local confinement. A contribution to the SXR emission by n_e and Z_{eff}, resulting in $\Delta T_e < 180$ eV cannot be ruled out. Concurrent Z_{eff} and $J(r)$ profile measurements will help to disentangle the competing effects of T_e and Z_{eff} on energy confinement.

A contrasting example of an atypical multiple helicity PPCD discharge suggests that ring-like emissive structures in SXR emission are best explained by impurity accumulation. The emission in this case is not well-described by either T_e or n_e structures, whereas a local ΔZ_{eff}=0.58 $Z_{eff}(0)$ is sufficient to entirely explain the SXR emission and is consistent with previous calculations of Z_{eff} during PPCD. This measurement provides further evidence that temperature screening results in classical impurity transport out of the core region [74]. This example is also an illustration of the usefulness of the SXR T_e and tomography diagnostic in non-ΔT_e studies.

The SXR T_e and tomography diagnostic has proven to be reliable and accurate during high current discharges. T_e profile measurements indicate that a locked dominant tearing mode during PPCD does not generally result in a T_e island. However, T_e structures are possible and may be triggered at a critical amplitude of the dominant tearing mode. More research is needed to quantify the conditions required for improved confinement through magnetic islands.

Chapter 6

Conclusions and Future Work

An innovative new soft x-ray (SXR) diagnostic has been developed for MST that provides tomographic emissivity and also measures electron temperature using the double-foil technique. Two measurements of electron temperature from SXR emission are available, one from the ratio of the emissivities through thin and thick filters as mapped onto magnetic flux surfaces, and the other directly from the ratio of two foils sharing a single line-of-sight. The SXR tomography and T_e diagnostic is used to investigate the source of emissive structures seen during high-current improved confinement discharges and distinguish between localized electron temperature enhancement and impurity accumulation. Sections 6.1 and 6.2 summarize the work presented in this thesis, and Section 6.3 suggests future experiments.

6.1 A New SXR T_e and Tomography Diagnostic

The previous SXR tomography diagnostic on MST provided Cormack-Bessel tomographic reconstructions of SXR emissivity from line-integrated brightness. Although the diagnostic was used to successfully study SXR emission structures in a variety of plasmas, measurements of T_e from the reconstruction were valid only in the core. The design of the original diagnostic required tomographic reconstruction of thin filter measurements from one set of poloidal angles and reconstruction of thick filter measurements from a second set of angles. The uncertainties inherent in the emission reconstructions overwhelmed the T_e measurement outside the core region due to the sensitivity of the double-foil technique to the small signal-to-noise typical of the emission edge. Additionally, the maximum gain of the original noise-sensitive linear transimpedance amplifiers was 10^7, limiting application of the diagnostic during thick-filter measurements.

To improve tomographic reconstruction and facilitate T_e measurements, a new diagnostic has been designed, built, and implemented on MST. The new diagnostic marries improved tomographic capability with new shared line-of-sight two-filter measurements to maximize scientific output of the device. Two probes are located 180° apart at -22.5 and 157.5° P. The other two probes are located on a boxport 90° away whose portholes are parallel to its center at 67.5° P. This geometry provides excellent tomographically reconstructed SXR emissivity. The double-foil technique is applied directly to the shared line-of-sight brightnesses to measure full $T_e(r)$ profiles in the vertical and horizontal planes. Additionally, SXR brightness is converted to a 2D T_e contour of the poloidal cross-section by reconstructing the thin and thick filter emissivities through flux-surface mapping and then applying the double-foil technique.

The new diagnostic is fully differential from the diode output all the way through to the digitizers. It features innovative custom differential current-to-voltage transimpedance amplifiers. The amplifiers have user-selectable gain ranging from 10^5-10^9. Bandwidth at 10^5 is 130 kHz, while 25 kHz is retained even at 10^9, all with low noise. The system is insensitive to common-mode noise generated by switching power supplies.

Although the diagnostic is insensitive to external noise, it is highly sensitive to changing magnetic fields at the MST wall. At 10^9 gain, induced EMF current as small as 1 nano-amp at the diode is converted to 1 Volt of signal at the digitizer, which is on the order of the SXR signal being measured. Substantial design modifications were implemented to reduce magnetic pickup from the plasma, such as minimization of untwisted portions of the differential signal path, use of thick-walled copper housing, and development of a 5-layer circuit board with upper and lower ground planes shielding the signals. In the final configuration, magnetic pickup is not measured at gains $10^5 - 10^7$. At 10^8, the pickup is present only in discharges with large amplitude rotating tearing modes, and pickup is $\sim 25\%$ typical signal levels. At 10^9, the diagnostic must be restricted in use to locked discharges, as pickup can be nearly as large as the expected signal.

6.2 Physics Results

The SXR direct-brightness and tomographic T_e measurements have been benchmarked against Thomson Scattering T_e during high current, improved confinement discharges, and show excellent agreement. The SXR direct-brightness T_e profiles complement the Thomson Scattering T_e by providing vertical and horizontal profile measurements on both sides of the midplane. With up to $\sim$ 30 kHz sampling resolution throughout the entire period of enhanced confinement, direct-brightness T_e has more temporal coverage than the Thomson Scattering diagnostic. Furthermore, lower-frequency 'equilibrium' flux-surface-reconstructed T_e provides 2D contour maps of T_e with sub-millisecond resolution. Finally, tomographic emissivity measurements are also available with sufficient frequency resolution to track SXR emission from rotating magnetic modes. SXR emissivity structures match the poloidal location of the dominant tearing mode to within 45°.

SXR brightness measurements of the core region through 8 different filter thicknesses during similar plasmas results in a measurement of the SXR spectrum from

2.5-5.0 keV. For the first time, CHERS Al^{11+} impurity measurements have been used to normalize the aluminum contribution to the SXR emission. Shot-to-shot variation in n_e has also been normalized using the CO_2 interferometer. As a result, the impact of aluminum line radiation on the SXR measurement has been measured for each foil thickness. Beryllium foils thicker than 400μm that have 2% or less transmission of aluminum line radiation and these are shown to be reliable measurements free of line-radiation.

The impact of locked dominant tearing modes on high current improved confinement discharges has been investigated. The majority of non-crash-heated plasmas have a locked magnetic mode at high current, with mode amplitudes ranging from 5-15 Gauss. Dominant tearing modes seen in the magnetics are consistently reflected as bean-shaped structures in the SXR emissivity reconstruction. Direct-brightness T_e measurements do not typically show a clear corresponding T_e structure, indicating a general upper limit of $\sim 15-20\%$ on any possible ΔT_e. In most shots, the flux-surface reconstructed T_e shows no indication of a ΔT_e. However, in one discharge with a very large tearing mode amplitude (15 Gauss), F.S.R. T_e indicates a structure of at least 20 eV.

An integrated data analysis approach, combining SXR measurements with n_e from FIR, T_e from Thomson Scattering, and $|B|$ from external magnetics, provides further insight into the m/n= (1/6) 15 Gauss QSH discharge. Modeling of the SXR emission assuming the emissivity structure is caused by a localized enhancement in T_e, with no change to n_e or Z_{eff} results in an estimate of $\Delta T_e = 180$ eV. The radial T_e profile is consistent with the Thomson Scattering measurement in this case and the magnetic structure locks in the viewing region of the Thomson Scattering optics. A similar study, assuming a structure caused by n_e enhancement rather than T_e requires an electron density profile that is inconsistent with the FIR measurement. A pure Z_{eff} structure requires a 32% enhancement in the island, which is not implausible. It can be concluded that in this example, a local electron temperature structure correlated to the dominant tearing mode is present and has an amplitude between 20-180 eV. The emissive structure corresponds to a thermal transport barrier, and may also be trapping impurities.

In shots where all tearing modes are suppressed, impurities are sometimes driven out of the core region only to accumulate at mid-radius. A second case study with a multiple-helicity mode spectrum indicates a ring of enhanced SXR emission at 0.4 r/a. F.S.R. T_e does not show any structure. Explaining the emission solely due to T_e would require a 20% island with $\Delta T_e = 250$ eV. Modeling indicates an island of this magnitude should be visible in the $T_e(\rho)$ profile and is inconclusive but unlikely. An explanation for the emission using an enhancement of n_e alone is excluded due to inconsistencies between the modeled and measured n_e. Therefore, the emissive structure is required to have an enhancement of impurities. If caused by impurities alone, this corresponds to a 58% increase in Z_{eff} compared with the core region. Measurements of impurity profiles with CHERS, combined with radiative-transport modeling for similar high-current plasmas indicate that a change to Z_{eff} of this magnitude is very plausible.

6.3 Future Work

The new SXR tomography and T_e diagnostic has a great deal of as-yet untapped potential. The inclusion of additional diagnostic measurements in the integrated data analysis approach will improve our understanding of confinement during high current non-crash-heated PPCD plasmas. Additionally, several run campaigns during the commissioning phase looking at other types of plasmas could benefit from followup with the full 4-probe system.

6.3.1 Integrated Data Analysis

SXR analysis will benefit from further improvements to the integrated data analysis approach. In particular, the large number of diagnostics with semi-independent uncertainties would benefit from a Bayesian approach to error analysis. Bayesian analysis uses all available constraints to calculate the likelihood that a given solution is the correct solution [77]. This approach is useful because the likely amplitude of the T_e structures is within the statistical uncertainty of both the SXR and Thomson Scattering diagnostics, yet qualitative information from reconstructed emissivity and FIR measurements offer additional constraints to the estimate that are not reflected in the statistical approach.

Additionally, the SXR measurements can become more quantitative by further developing analysis tools based on flux-surface reconstructions. The current F.S.R. parameterization for SXR brightness is a simple function with a monotonically decreasing slope. It is well known that in the case of a dominant magnetic tearing island, SXR emission can have two separate flux surface regions of peaked emission: one corresponding to the magnetic core, and the other to the magnetic axis of the island. The current equation was optimized for SHAx plasmas, where the core and island combine into a single helical geometry and so it is not the ideal model for an island geometry. Parameterizing the SXR brightness with a more consistent flux function will improve the fidelity of the resulting F.S.R. T_e so that it represents a true estimate of island temperature rather than a lower-bound.

6.3.2 T_e Structure in High-Current PPCD

An obvious interest is to more fully explore locked dominant-mode plasmas during PPCD. Is the 15 Gauss QSH example an indication that T_e structures regularly arise at some magnetic amplitude threshold? Or is there something unique about this case that leads to a ΔT_e that is not tied to the large magnetic perturbation? To answer this question, further run campaigns are required, since less than 5% of PPCD discharges have locked plasmas with dominant mode amplitude > 10 Gauss. Furthermore, concurrent measurements of $Z_{eff}(r)$ (from the hard and soft x-ray array) and the $J(r)$ (from the FIR in 3-beam interferometry mode) will provide an opportunity to estimate local energy confinement in the island region.

6.3.3 Crash-Heated PPCD Discharges

A second type of improved-confinement plasma, crash-heated PPCD, can also be investigated using the SXR diagnostic. Crash-heated PPCD plasmas reach much higher core electron temperatures than non-crash-heated (up to 2.5 keV), and they are more likely to have multiple-helicity magnetic configurations where all tearing modes are suppressed. The mechanisms that differentiate crash-heated and non-crash-heated PPCD are not well-understood. Are the temperatures hotter because energy confinement is improved or because the initial ion temperature is hotter, providing an additional source of energy? Why is the magnetic spectrum more suppressed in crash-heated PPCD than in non-crash-heated? Is there a correlation between mode amplitude and core T_e? Is there any indication of T_e structure in the QSH variety of crash-heated PPCD?

Interestingly, crash-heated PPCD discharges are also more likely to have rotating modes. Does mode rotation indicate improved plasma stability? Are there T_e island structures in rotating discharges? Correlating the SXR D.B. T_e measurements to the magnetics offers a method of searching for islands in rotating plasmas.

6.3.4 T_e Structure in SHAx Plasmas

Finally, MST is frequently run in a configuration where the toroidal component of the magnetic field is forced to zero at the edge (F=0 discharges). In these plasmas, the dominant magnetic tearing mode frequently grows in amplitude until it saturates around $\sim$ 75 Gauss. It has been shown that in these SHAx plasmas, a new helical magnetic geometry is formed [16]. Furthermore, on RFX this helical axis has been measured to have an enhanced T_e [78]. The T_e characteristics of SHAx plasmas have not yet been measured on MST. Single-probe SXR profile measurements from the commissioning phase of the diagnostic suggest the existence of a temperature enhancement. Figure 6.1 shows an example of a brightness profile (top) and DB T_e profile (bottom) from SXR-D using a symmetric pinhole. The T_e profile appears asymmetric suggesting a ΔT_e structure below the mid-plane. This is consistent with the location of the magnetic mode at 305° P, which has a poloidal amplitude of 25 Gauss at 18.5ms. However, this data was taken with prototype single-gain 10^9 amplifiers that were not calibrated, so uncertainty estimates are not available for this shot.

With the final system, more data will be needed to make an equivalent measurement. Because the user-selectable gain amplifiers have 5 gain settings, the overall increase to the circuit complexity means that the electronic noise is substantially larger than in the commissioning-phase example. Additionally, the SXR signal levels during F=0 plasmas are very low, often approaching the 0.5 W/m^2 noise-limit on the thick filters. To properly investigate SHAx plasmas, an ensemble of shots is required to improve the signal-to-noise ratio. SXR ensembling further requires all of the data to be locked at the same poloidal angle, so a dataset spanning several days would be needed to gain enough statistical certainty.

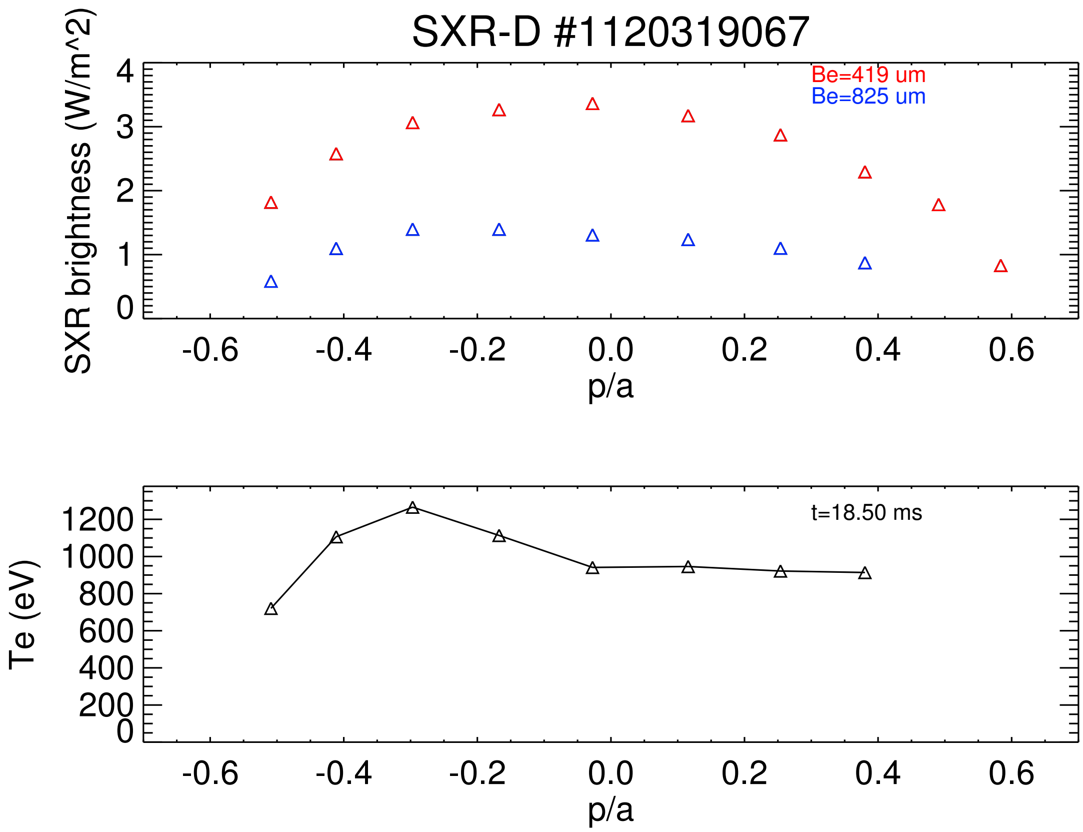

Figure 6.1: SXR-D brightness profile measurement (top) of a locked SHAx structure during 600kA F=0 plasma. During the commissioning phase, SXR-D had a centered pinhole and fixed gain 10^9 prototype amplifiers. The magnetic structure is locked at 305° P. Negative impact parameter (p) looks below the mid-plane. D.B. T_e (bottom) suggests a structure, although uncertainties are large and have not been quantified for this shot.

Bibliography

[1] F. F. Chen, *Introduction to Plasma Physics and Controlled Fusion*, Plenum Press, **1984**

[2] S. C. Prager, "Transport and Fluctuations in Reversed Field Pinches," *Plasma Phys. Control. Fusion*, vol. 32, p. 903, **1990**

[3] S. Ortolani and D. Schnack, *Magnetohydrodynamics of Plasma Relaxation*, World Scientific, **1993**

[4] J. T. Chapman, *Spectroscopic Measurement of the MHD Dynamo in the MST Reversed Field Pinch*, Ph.D. thesis, University of Wisconsin - Madison, **1998**

[5] D. Craig, *Magnetic Mode Analysis in MST*, http://hackserver.physics.wisc.edu/wiki/index.php/Toroidal_Magnetic_Array_(Mode_Analysis), MST Internal Document, **2005**

[6] T. D. Tharp, *Measurements of Nonlinear Hall-Driven Reconnection in the Reversed Field Pinch*, Ph.D. thesis, University of Wisconsin - Madison, **2010**

[7] J. A. Beckstead, *Sawteeth in the MST Reversed Field Pinch*, Ph.D. thesis, University of Wisconsin - Madison, **1990**

[8] S. Hokin, A. Almagri, S. Assadi, J. Beckstead, G. Chartas, N. Crocker, M. Cudzinovic, D. J. Den Hartog, R. N. Dexter, D. Holly, S. Prager, T. Rempel,

J. Sarff, E. Scime, W. Shen, C. Spragins, C. Sprott, G. Starr, M. Stoneking, and C. Watts, "Global Confinement and Discrete Dynamo Activity in the MST Reversed-Field Pinch," *Physics of Fluids B*, vol. 3, p. 2241, **1991**

[9] M. R. Stoneking, N. E. Lanier, S. C. Prager, J. S. Sarff, and D. Sinitsyn, "Five-fold Confinement Time Increases in the Madison Symmetric Torus Using Inductive Poloidal Current Drive," *Phys. Plasmas*, vol. 4, p. 1632, **1997**

[10] C. R. Sovinec and S. C. Prager, "Magnetohydrodynamic Effects of Current Profile Control in Reversed Field Pinches", *Nucl. Fusion*, vol. 39, p.777 **1999**

[11] J. Sarff, S. Hokin, H. Ji, S. Prager, and C. Sovinec, "Fluctuation and Transport Reduction in a Reversed Field Pinch by Inductive Poloidal Current Drive", *Phys. Rev. Lett.*, vol. 72, p. 3670, **1994**

[12] B. E. Chapman, J. W. Ahn, A. F. Almagri, J. K. Anderson, F. Bonomo, D. L. Brower, D. R. Burke, K. Caspary, D. J. Clayton, S. K. Combs, W. A. Cox, D. Craig, B. H. Deng, D. J. D. Hartog, W. X. Ding, F. Ebrahimi, D. A. Ennis, G. Fiksel, C. B. Forest, C. R. Foust, P. Franz, S. Gangadhara, J. A. Goetz, M. C. Kaufman, J. G. Kulpin, A. Kuritsyn, R. M. Magee, M. C. Miller, V. V. Mirnov, P. D. Nonn, R. O'Connell, S. P. Oliva, S. C. Prager, J. A. Reusch, J. S. Sarff, H. D. Stephens, M. D. Wyman, and T. Yates, "Improved-Confinement Plasmas at High Temperature and High Beta in the MST RFP", *Nucl. Fusion*, vol. 49, p. 104020, **2009**

[13] P. Martin, L. Marrelli, G. Spizzo, P. Franz, P. Piovesan, I. Predebon, T. Bolzonella, S. Cappello, A. Cravotta, D.F. Escande, L. Frassinetti, S. Ortolani, R. Paccagnella, D. Terranova, the RFX team, B. E. Chapman, D. Craig, S. C. Prager, J. S. Sarff, the MST team, P. Brunsell, J.-A. Malmberg, J. Drake, the

EXTRAP T2R team, Y. Yagi, H. Koguchi, Y. Hirano, the TPE-RX team, R. B. White, C. Sovinec, C. Xiao, R. A. Nebel and D. D. Schnack, "Overview of Quasi-Single Helicity Experiments in Reversed Field Pinches," *Nucl. Fusion*, vol. 43, p.1855, **2003**

[14] R. Lorenzini, D. Terranova, A. Alfier, P. Innocente, E. Martines, R. Pasqualotto and P. Zanca, "Single-Helical-Axis States in Reversed-Field-Pinch Plasmas," *Phys. Rev. Lett.*, vol. 101, no. 2, p. 025005, **2008**

[15] R. Lorenzini, M. Agostinin, A. Alfier, V. Antoni, L. Apolloni, F. Auriemma, O. Barana, M. Baruzzo, P. Bettini, D. Bonfiglio, T. Bolzonella, F. Bonomo, M. Brombin, A. Buffa, A. Canton, S. Cappello, L. Carraro, R. Cavazzana, G. Chitarin, S. Dal Bello, A. De Lorenzi, G. De Masi, D. F. Escande, A. Fassina, P. Franz, E. Gaio, E. Gazza, L. Giudicotti, F. Gnesotto, M. Gobbin, L. Grando, S. C. Guo, P. Innocente, A. Luchetta, G. Manduchi, G. Marchiori, D. Marcuzzi, L. Marrelli, P. Martin, S. Martini, E. Martines, F. Milani, M. Moresco, L. Novello, S. Ortolani, R. Paccagnella, R. Pasqualotto, S. Peruzzo, R. Piovan, P. Piovesan, L. Piron, A. Pizzimenti, N. Pomaro, I. Predebon, M. E. Puiatti, G. Rostagni, F. Sattin, P. Scarin, G. Serianni, P. Sonato, E. Spada, A. Soppelsa, S. Spagnolo, G. Spizzo, M. Spolaore, C. Taliercio, D. Terranova, V. Toigo, M. Valisa, P. Veltri, N. Vianello, P. Zaccaria, B. Zaniol, L. Zanotto, E. Zilli, and M. Zuin, "Improvement of the Magnetic Configuration in the Reversed Field Pinch Through Successive Bifurcations," *Phys. Plasmas*, vol. 16, p. 056109, **2009**

[16] W. F. Bergerson, F. Auriemma, B. E. Chapman, W. X. Ding, P. Zanca, D. L. Brower, P. Innocente, L. Lin, R. Lorenzini, E. Martines, B. Momo, J. S. Sarff and D. Terranova,"Bifurcation to 3D Helical Magnetic Equilibrium in an

Axisymmetric Toroidal Device", *Phys. Rev. Lett.*, vol. 107, no. 25, p. 255001, **2011**

[17] F. Auriemma, P. Zanca, W. F. Bergerson, B. E. Chapman, W. X. Ding, D. L. Brower, P. Franz, P. Innocente, R. Lorenzini, B. Momo and D. Terranova, "Magnetic Reconstruction of Nonaxisymmetric Quasi-single-helicity Configurations in the Madison Symmetric Torus", *Plasma Phys. Contr. F.*, vol. 53, p. 105006, **2011**

[18] G. B. Rybicki and A. P. Lightman, *Radiative Processes in Astrophysics*, WILEY-VCH Verlag GmbH and Co. KGaA, **2004**

[19] S. von Goeler, W. Stodiek and N. Sauthoff, "Studies of Internal Disruptions and m=1 Oscillations in Tokamak Discharges with Soft-X-Ray Techniques," *Phys. Rev. Lett.*, vol. 33, no. 20, p. 1201, **1974**

[20] F. C. Jahoda, E. M. Little, W. E. Quinn, G. A. Sawyer, and T. F. Stratton, "Continuum Radiation in the X-Ray and Visible Regions from a Magnetically Compressed Plasma (Scylla)," *Phys. Rev.*, vol. 119, no. 3, p. 843, **1960**

[21] T. P. Donaldson, "Theory of Foil-Absorption Techniques for Plasma X-Ray Continuum Measurements," *Plasma Physics*, vol. 20, p. 1279, **1978**

[22] P. Martin, A. Murari and L. Marrelli, "Electron Temperature Measurements with High Time Resolution in RFX," *Plasma Phys. Contr. F.*, vol 38, p. 1023, **1996**

[23] G. T. Herman, *Fundamentals of Computerized Tomography*, Springer Dordrecht Heidelberg, **2009**

[24] M. A. Dubois, D. A. Marty, A. Pochelon, "Method of Cartography of q=1 Islands During Sawtooth Activity in Tokamaks," *Nucl. Fusion*, vol. 20, no.11, p. 1355, **1980**

[25] P. Smeulders, "Evolution of the m=1 Tearing Mode During Internal Sawtooth Disruption," *Nucl. Fusion*, vol. 23, no. 4, p. 529, **1983**

[26] N. R. Sauthoff, K. M. McGuire, and S. von Goeler, "Reconstruction of m=1 MHD Modes from Projections," *Rev. Sci. Instrum.*, vol. 57, no. 8, p. 2139, **1986**

[27] R. S. Granetz and J. F. Camacho, "X-Ray Tomography on Alcator C," *Nucl. Fusion*, vol. 25, no. 6, p. 727, **1985**

[28] R. S. Granetz and P. Smeulders, "X-Ray Tomography on JET," *Nucl. Fusion*, vol. 28, no. 3, p. 457, **1988**

[29] N. Asakura, Y. Nagayama, S. Shinohara, H. Toyama, K. Miyamoto, and N. Inoue, "Soft X-ray Measurements on the REPUTE-1 Reversed Field Pinch," *Nucl. Fusion*, vol. 29, no. 6, p. 893, **1989**

[30] A. P. Navarro, M. A. Ochando, and A. Weller, "Equilibrium-Based Iterative Tomography Technique for Soft X-ray in Stellarators," *IEEE T Plasma Sci*, vol. 19, no. 4, p. 569, **1991**

[31] G. A. Chartas, *Manifestations of the MHD and Kinetic Dynamo Through Soft X-rays*, Ph.D. thesis, University of Wisconsin - Madison, **1991**

[32] J. Kiraly, M. Bitter, P. Efthimion, S. von Goeler, B. Grek, K. W. Hill, D. Johnson, K. McGuire, N.Sauthoff, S. Sesnic, F. Stauffer, G. Tait, and G. Taylor,

"Multichord Time Resolved Electron Temperature Measurements by the X-ray Absorber Foil Method on TFTR," *Nucl. Fusion*, vol. 27, no. 3, p. 397, **1987**

[33] A. Murari, P. Franz, L. Zabeo, R. Bartiromo, L. Carraro, G. Gadani, L. Marrelli, P. Martin, R. Pasqualotto, and M. Valisa, "An Optimized Multifoil Soft X-ray Spectrometer for the Determination of Electron Temperature with High Time Resolution," *Rev. Sci. Instrum.*, vol. 70, no. 1, p. 581, **1999**

[34] F. Bonomo, P. Franz, A. Murari, G. Gadani, A. Alfier, and R. Pasqualotto, "A Multi Chord Soft X-ray Diagnostic for Electron Temperature Profile Measurements in RFX-Mod," *Rev. Sci. Instrum.*, vol. 77, p. 10F313, **2006**

[35] L. F. Delgado-Aparicio, D. Stutman, K. Tritz, M. Finkenthal, R. Bell, J. Hosea, R. Kaita, B. LeBlanc, L. Roquemore, and J. R. Wilson, "Fast Electron Temperature Measurements Using a Multicolor Optical Soft X-ray Array," *J. Appl. Phys.*, vol. 102, p. 073304, **2007**

[36] P. Franz, F. Bonomo, G. Gadani, L. Marrelli, P. Martin, P. Piovesan, G. Spizzo, B. E. Chapman, and M. Reyfman, "High Resolution Soft X-ray Tomography in the Madison Symmetric Torus," *Rev. Sci. Instrum.*, vol. 75, no. 10, p. 4013, **2004**

[37] P. Franz, F. Bonomo, L, Marrelli, P. Martin, P. Piovesan, G. Spizzo, B. E. Chapman, D. Craig, D. J. Den Hartog, J. A. Goetz, R. O'Connell, S. C. Prager, M. Reyfman, and J. S. Sarff, "Two-dimensional Time Resolved Measurements of the Electron Temperature in MST", *Rev. Sci. Instrum.*, vol. 77, p. 10F318, **2006**

[38] M. B. McGarry, P. Franz, D. J. Den Hartog, and J. A. Goetz, "A New Double-foil Soft X-ray Array to Measure Te on the MST Reversed Field Pinch", *Rev. Sci. Instrum.*, vol. 81, p. 10E516, **2010**

[39] M.B. McGarry, P. Franz, D. J. Den Hartog, J. A. Goetz, M. A. Thomas, M. Reyfman and S. T. A. Kumar, "High-Performance Double-Fliter Soft X-ray Diagnostic for Measurement of Electron Temperature Structure and Dynamics", *Rev. Sci. Instrum.*, vol. 83, p. 10E129, **2012**

[40] R. O'Connell, D. J. Den Hartog, C. B. Fores, and R. W. Harvey, "Measurement of Fast Electron Distribution Using a Flexible, High Time Resolution Hard X-ray Spectrometer", *Rev. Sci. Instrum.*, vol. 74, no. 3, p. 2001, **2003**

[41] B. E. Chapman, A. F. Almagri, J. K. Anderson, T. M. Biewer, P. K. Chattopadhyay, C.-S. Chiang, D. J. Den Hartog, G. Fiskel, C. B. Forest, A. K. Hansen, D. Holly, N. E. Lanier, R. O'Connell, S. C. Prager, J. C. Reardon, J. S. Sarff, M. D. Wyman, D. L. Brower, W. X. Ding, Y. Jiang, S. D. Terry, P. Franz, L. Marrelli, and P. Martin, "High Confinement Plasmas in the Madison Symmetric Torus Reversed-Field Pinch", *Phys. Plasmas*, vol. 9, no. 5, p. 2061, **2002**

[42] F. Bonomo, *Experimental Measurements of Soft X-Ray Emissivity Distribution and Electron Temperature Profile in Reversed Field Pinch Plasmas*, Ph.D. thesis, Universita Delgi Studi di Padova, RFX - Italy, **2008**

[43] F. Bonomo, A. Alfier, M. Gobbin, F. Auriemma, P. Franz, L. Marrelli, R. Pasqualotto, G. Spizzo, and D. Terranova, "2D Characterization of Core Thermal Topology Changes in Controlled RFX-mod QSH States", *Nucl. Fusion*, vol. 49, p. 045011, **2009**

[44] M. Valisa, T. Bolzonella, P. Buratti, L. Carraro, R. Cavazzana, S. Dal Bello, P. Martin, R. Pasqualotto, J. S. Sarff, M. Spolaore, P. Zanca, L. Zanotto, M. Agostini, A. Alfier, V. Antoni, L. Apolloni, F. Auriemma, O. Barana, M. Baruzzo, P. Bettini, D. Bonfiglio, F. Bonomo, M. Brombin, A. Buffa, A. Canton, S. Cappello, M. Cavinato, G. Chitarin, A. De Lorenzi, G. De Masi, D. F. Escande, A. Fassina, P. Franz, E. Gaio, E. Gazza, L. Giudicotti, F. Gnesotto, M. Gobbin, L. Grando, L. Guazzotto, S. C. Guo, V. Igochine, P. Innocente, R. Lorenzini, A. Luchetta, G. Manduchi, G. Marchiori, D. Marcuzzi, L. Marrelli, S. Martini, E. Martines, K. McCollam, F. Milani, M. Moresco, L. Novello, S. Ortolani, R. Paccagnella, S. Peruzzo, R. Piovan, L. Piron, A. Pizzimenti, P. Piovesan, N. Pomaro, I. Predebon, M.E. Puiatti, G. Rostagni, F. Sattin, P. Scarin, G. Serianni, P. Sonato, E. Spada, A. Soppelsa, S. Spagnolo, G. Spizzo, C. Taliercio, D. Terranova, V. Toigo, N. Vianello, D. Yadikin, P. Zaccaria, B. Zaniol, E. Zilli and M. Zuin, "High Current Regimes in RFX-mod", *Plasma Phys. Control. Fusion*, vol. 50, p. 124031, **2008**

[45] D. Gregoratto, L. Garzotti, P. Innocente, S. Martini, and A. Canton, "Behaviour of Electron Density Profiles and Particle Transport Analysis in the RFX Reversed Field Pinch", *Nucl. Fusion*, vol. 38, no. 8, p. 1199, **1998**

[46] A. Thompson, I. Lindau, D. Attwood, P. Pianetta, E. Gullikson, A. Robinson, M. Howells, J. Scofield, K. J. Kim, J. Underwood, J. Kirz, D. Vaughan, J. Kortright, G. Williams, H. Winick, *X-Ray Data Booklet*, *Center for X-Ray Optics Advanced Light Source*, Lawrence Berkeley National Laboratory, Berkeley, California, **2001**

[47] D. J. Clayton, *Fast Electron Transport in Improved-Confinement RFP Plasmas*,

Ph.D. thesis, University of Wisconsin - Madison, **2010**

[48] R. O'Connell, D. J. Den Hartog, C. B. Forest, J. K. Anderson, T. M. Biewer, B. E. Chapman, D. Craig, G. Fiksel, S. C. Prager, J. S. Sarff, and S. D. Terry, "Observation of Velocity-Independent Electron Transport in the Reversed Field Pinch", *Phys. Rev. Lett.*, vol. 91, no. 4, p. 045002, **2003**

[49] P. Franz, L. Marrelli, P. Piovesan, I. Predebon, F. Bonomo, L. Frassinetti, P. Martin, G. Spizzo, B. E. Chapman, D. Craig, and J. S. Sarff, "Tomographic Imaging of Resistive Mode Dynamics in the Madison Symmetric Torus Reversed-field Pinch", *Phys Plasmas*, vol. 13, p. 012510, **2006**

[50] R. Bardet, "Cofefficients D'Attenuation Massiques Des Rayons X", *Association Euratom-CEA*, Internal Document (DPh-PFC-SIG, EUR-CEA-FC-885), Grenoble, France, **1977**

[51] A. M. Cormack, "Representation of a Function by its Line Integrals, with some Radiological Applications",*J. Appl. Phys.* vol. 34, p. 2722, **1963**

[52] A. M. Cormack, "Representation of a Function by its Line Integrals, with some Radiological Applications. II",*J. Appl. Phys.* vol. 35, p. 2908, **1964**

[53] "Tomography of m=1 Mode Structure in Tokamak Plasma Using Least-square-fitting Method and FourierBessel Expansions", *J. Appl. Phys.* vol. 62, p. 2702 **1987**

[54] L. Wang and R. S. Granetz, "An Analytical Expression for the Radon Transform of Bessel Basis Function in Tomography", *Rev. Sci. Instrum.*, vol. 62, p. 1115, **1991**

[55] L. Marrelli, P. Martin, A. Murari and G. Spizzo, “Total Radiation Losses and Emissivity Profiles in RFX ”, *Nucl. Fusion*, vol. 38, p. 649, **1998**

[56] P. Franz, L. Marrelli, A. Murari, G. Spizzo, and P. Martin,“ Soft X-ray Tomographic Imaging in the RFX Reversed Field Pinch”, *Nucl. Fusion*, vol. 41, no. 6, p. 695, **2001**

[57] P. Franz, G. Gadani, R. Pasqualotto, L. Marrelli, P. Martin, G. Spizzo, P. Brunsell, B.E. Chapman, F. Paganuccio, P. Rossetti, and C. Xiao, “Compact Soft X-ray Multichord Camera: Design and Initial Operation”, *Rev. Sci. Instrum.*, vol 74, no. 3, p. 2152, **2003**

[58] C. Xiao, P. Franz, B. E. Chapman, D. Craig, W. X. Ding, G. Gadani, L. Marrelli, P. Martin, R. Pasqualotto, G. Spizzo, J. S. Sarff, and S. D. Terry, “ Soft X-ray Emission, Plasma Equilibrium, and Fluctuation Studies on Madison Symmetric Torus”, *Rev. Sci. Instrum.*, vol. 74, no. 3, p.2157, **2003**

[59] P. Franz, L. Marrelli, P. Piovesan, B. E. Chapman, P. Martin, I. Predebon, G. Spizzo, R. B. White, and C. Xiao, “Observations of Multiple Magnetic Islands in the Core of a Reversed Field Pinch”, *Phys. Rev. Lett.*, vol. 92, no. 12, p. 125001-1, **2004**

[60] R. Fischer and A. Dinklage, “Integrated Data Analysis of Fusion Diagnostics by Means of the Bayesian Probability Theory”, *Rev. Sci. Instrum.*, vol. 75, no. 10, p. 4237, **2004**

[61] G. Verdoolaege, R. Fischer, G. Van Oost, and JET-EFDA Contributors, “Potential of a Bayesian Integrated Determination of the Ion Effective Charge

via Bremsstrahlung and Charge Exchange Spectroscopy in Tokamak Plasmas", *IEEE T. Plasma Sci.*, vol. 38. no. 11, p. 3168, **2010**

[62] D. L. Brower, W. X. Ding, S. D. Terry, J. K. Anderson, T. M. Biewer, B. E. Chapman, D. Craig, C. B. Forest, S. C. Prager and J. S. Sarff, "Laser Polarimetric Measurement of EQuilibrium and Fluctuating Fields in a Reversed Field Pinch," *Rev. Sci. Instrum.*, vol 74, no. 3, p. 1534, **2003**

[63] W. X. Ding, D. L. Brower, W. F. Bergerson and L. Lin, "Upgrade of Far-infrared Laser-based Faraday Rotation Measurement on MST," *Rev. Sci. Instrum.*, vol. 81, p. 10D508, **2010**

[64] G. Dodel and W. Kunz, "A Far-Infrared 'Polari-Interferometer' for Simultaneous Electron Density and Magnetic Field Measurements in Plasmas", *Infrared Phys.*,vol. 18, p. 773, **1978**

[65] D. L. Brower, W. X. Ding, S. D. Terry, J. K. Anderson, T. M. Biewer, B. E. Chapman, D. Craig. C. B. Forest, S. C. Prager and J. S. Sarff, "Measurement of the Current-Density Profile and Plasma Dynamics in the Reversed-Field Pinch," *Phys. Rev. Lett.*, vol. 88, n. 18, pp. 185005-1, **2002**

[66] H. K. Park, "A New Asymmetric Abel-Inversion Method for Plasma Interferometry in Tokamaks," *Plasma Phys. Control. Fusion*, vol. 31, no. 13, p. 2035, **1989**

[67] I. H. Hutchinson, *Principles of Plasma Diagnostics*, Ch. 7.2. Cambridge University Press, second ed., **2002**

[68] J. Sheffield, *Plasma Scattering of Electromagnetic Radiation*, New York: Academic Press, **1975**

[69] H. D. Stephens, *Electron Temperature Structures Associated with Magnetic Tearing Modes in the Madison Symmetric Torus*, Ph.D. thesis, University of Wisconsin - Madison, **2010**

[70] B. Momo, E. Martines, D. F. Escande and M. Gobbin, "Magnetic Coordinate Systems for Helical SHAx States in Reversed Field Pinch Plasmas", *Plasma Phys. Control. Fusion*, vol. 53, p. 0125004, **2011**

[71] E. Martines, R. Lorenzini, B. Momo, D. Terranova, P. Zanca, A. Alfier, F. Bonomo, A. Canton, A. Fassina, P. Franz and P. Innocente, "Equilibrium Reconstruction for Single Helical Axis Reversed Field Pinch Plasmas", *Plasma Phys. Control. Fusion*, vol. 53, p. 035015, **2011**

[72] S. T. A. Kumar, D. J. Den Hartog, B. E. Chapman, M. O'Mullane, M. Nornberg, D. Craig, S. Eilerman, G. Fiksel, E. Parke and J. Reusch, "High Resolution Charge-exchange Spectroscopic Measurements of Aluminum Impurity Ions in a High Temperature Plasma", *Plasma Phys. Control. Fusion*, vol. 54, p. 012002, **2012**

[73] L. Delgado-Aparicio, L. Sugiyama, R. Granetz, D. A. Gates, J. E. Rice, M. L. Reinke, M. Bitter, E. Fredrickson, C. Gao, M. Greenwald, K. Hill, A. Hubbard, J. W. Hughes, E. Marmar, N. Pablant, Y. Podpaly, S. Scott, R. Wilson, W. Wolfe, and S. Wukitch, "Formation and Stability of Impurity 'Snakes' in Tokamak Plasmas," *Phys. Rev. Lett.*, vol. 110, p. 065006, **2013**

[74] S. T. A. Kumar, D. J. Den Hartog, V. V. Mirnov, K. J. Caspary, R. M. Magee, D. L. Brower, B. E. Chapman, D. Craig, W. X. Ding, S. Eilerman, G. Fiskel, L. Lin, M. Nornberg, E. Parke, J. A. Reusch and J. S. Sarff, "Classical Confinement

and Outward Convection of Impurity Ions in the MST RFP," *Phys. Plasmas*, vol. 19, p. 056121, **2012**

[75] T. Barbui, "Impurity Transport Analysis on MST Using A Collisional-Radiative and Transport Code," submitted to *Plasma Phys. Control. Fusion*, **2013**

[76] M. Wyman, "The Physics of High Density, High-Beta Reversed-Field Pinch Plasmas," Ph.D. thesis, University of Wisconsin - Madison, **2007**

[77] D. S. Sivia, *Data Analysis: A Bayesian Tutorial*, Oxford Science Publications, **1996**

[78] P. Franz, M. Gobbin, L. Marrelli, A. Ruzzon, F. Bonomo, A. Fassina, E. Martines and G. Spizzo, "Experimental Investigation of Temperature Dynamics of Helical States in the RFX-Mod Reversed Field Pinch," *Nucl. Fusion*, vol. 53, p. 053011, **2013**

[79] P. J. Fimognari, A. F. Almagri, J. K. Anderson, D. R. Demers, J. S. Sarff, V. Tangri, and J. Waksman, "Port Hole Perturbations to the Magnetic Field in MST", *Plasma Phys. Control. Fusion*, vol. 52, no. 9, p. 5002, **2010**

Appendix A

Reducing Magnetic Pickup

Chapter 4 describes the presence of magnetic pickup that was found to be contaminating the SXR signals in the new diagnostic at high gain. This Appendix describes a series of design modifications to reduce the pickup. Some modifications were quite effective, while those that did not work nonetheless provided insight into eventual solutions. Two parallel approaches were taken to reduce this magnetic pickup - reducing the area enclosed by current-carrying wires and increasing the electrical thickness of the housing.

Table A.1 summarizes the improvements in pickup resulting from the reduction in area and improved shielding implemented in the final design of the SXR diagnostic. The 'Estimated Improvement' column shows how much change should occur due to each contribution of pickup. In contrast, the 'Measured Improvement' column shows the net effect of the design changes, which may not be precisely accounted for in the estimations. A third source of induced current that is not accounted for in these modifications is that due to the field-lines entering directly through the viewing aperture. Therefore, although the 4mm copper walls reduce the soak-through pickup by a factor of 10^4, the contribution of soak-through to the total pickup is small and so the measured improvement is dominated by direct-entrance field lines. The following sections explain these steps more fully.

	Initial Design	Final Design	Estimated Improvement	Measured Improvement
Area	70 mm^2	7 mm^2	10x	20x
Wall Thick	1.5 mm	4.0 mm		
Skin Depth	0.69 mm	0.40 mm	10^4	10^2

Table A.1: Improvements to enclosed area and inner surface current density from initial design to final design. The reduction in enclosed area is an estimate. The measured improvement comes from two tests that were not as cleanly delineated as the table: Figure A.6 showing results from the reduction in area plus added ground planes in circuit board, and Figure 4.29 showing results from the sreduced area and thick Cu walls combined. One outstanding source of pickup, field lines entering directly through the aperture, has not been addressed in this table.

A.1 Magnetic Pickup Amplitude

The SXR probe bodies are made of aluminum and the probeheads are tellurium copper, which provide both electrostatic and electromagnetic shielding. A conductor in the presence of an oscillating field (angular frequency ω) will develop a surface (eddy) current in response to the emf. The attenuation of current density (J) improves as thickness (d) increases, as described by the skin depth (δ):

$$\vec{J} = \vec{J}_0\, e^{-d/\delta} \tag{A.1}$$

$$\delta = \sqrt{\frac{2}{\mu\sigma\omega}} \tag{A.2}$$

where μ and σ are the magnetic permeability and electrical conductivity of the conductor. If the wall is not sufficiently thick, then the inner wall of the conductor will have a non-zero current density. Additionally, because the probehead is not a single piece of metal, electrical gaps exist between the probetip and probehead. If this contact is poor then eddy currents flow directly to the inner wall of the conductor without attenuation, propagating the field into the enclosure.

If a magnetic field B penetrates beyond the inner wall of the probe by either means, it will induce an εmf in any loop of wire that it passes through:

$$\varepsilon mf = -\frac{d\Phi_B}{dt} \tag{A.3}$$

$$\Phi_B = \int \vec{B} \cdot d\vec{A} \tag{A.4}$$

Φ_B is the magnetic flux through a loop of area A. If the area (A) enclosed by the current loop is known, an estimate can be made for the induced current (I) inside the diode due to the time-varying magnetic field ($\vec{B} = \vec{B_0}\, e^{-i\omega t}$):

$$I = \frac{\omega |B_0|\, A}{Z_{RC}} \tag{A.5}$$

where B_0 is the magnetic field at the diode board, A is the enclosed area, and Z_{RC} is the impedance of the diode circuit. This current, referred to colloquially as 'magnetic pickup', is then amplified by the high-gain current-to-voltage transimpedance amplifiers. As a result, very small fluctuating magnetic fields are magnified up to nine orders of magnitude and are seen in the SXR diagnostic as a signal correlated to the magnetic fields.

In the original probe design, there was $\sim$70 mm^2 of area available to enclose magnetic field lines inside the probe. The circuit impedance for the differential diode and twisted-shielded pair wire is not straightforward, but can be approximated as $Z_{RC} \sim 10^4 - 10^5\ \Omega$ depending on whether the diode and wire are treated as being in parallel or in series (R_{wire}=1.87 Ω, C_{wire}=1200 pF, C_{diode}=100 pF). Finally, Figure 4.28 indicates that the pickup (and therefore the magnetic field amplitude) when the probe is at the measurement position is about an order of magnitude smaller than at wall. Therefore, for a magnetic mode of ~ 2 mT at the wall of MST, rotating at 15 kHz, and including the field attenuation provided by the 1.5mm aluminum probe wall, currents of 10-100 nano-amps can be induced in the diode circuit.

At an amplification of 10^8, this translates into magnetic pickup signals of more than a volt, which is on the order of the expected signal. For 10^9 amplification, this level of pickup threatens to completely overwhelm the signal. Figure A.1 shows the signal for the magnetic pickup seen on the first diode board design, where the pinhole is covered so that no x-rays are included. This plot shows three different amplifications ($10^6 - 10^8$) for a single 400 kA F=0 plasma shot, filtered around the pickup frequency of 15 kHz. The magnetic pickup is about 100-200 mV at 10^8, about 10 times smaller than predicted but still sufficient to corrupt the signal. This underestimation is likely due to the uncertainties in the total impedance of the circuit.

A.2 Enclosed Area

A very effective strategy for minimizing magnetic pickup was to reduce the area enclosed by current carrying wires in the detectors The original design of the diode board had not been well-optimized for avoiding magnetic pickup. Figure A.2 show the first-generation detector layout from the top and bottom of the circuit board. On the top of the circuit board, the red wires running from each diode to the cable-connector created loops of enclosed area. This red wire is the cathode of the diode, while the anode of the diode is a trace on the circuit board below it. This loop contributed an enclosed area up to 10 mm^2. On the bottom of the circuit board, the cable-connector assembly created another set of loops. The anode signal (white-blue) and cathode signal (white) for each diode had to be unshielded and untwisted in order to solder the wires into the connector. These loops had an area of approximately 60 mm^2.

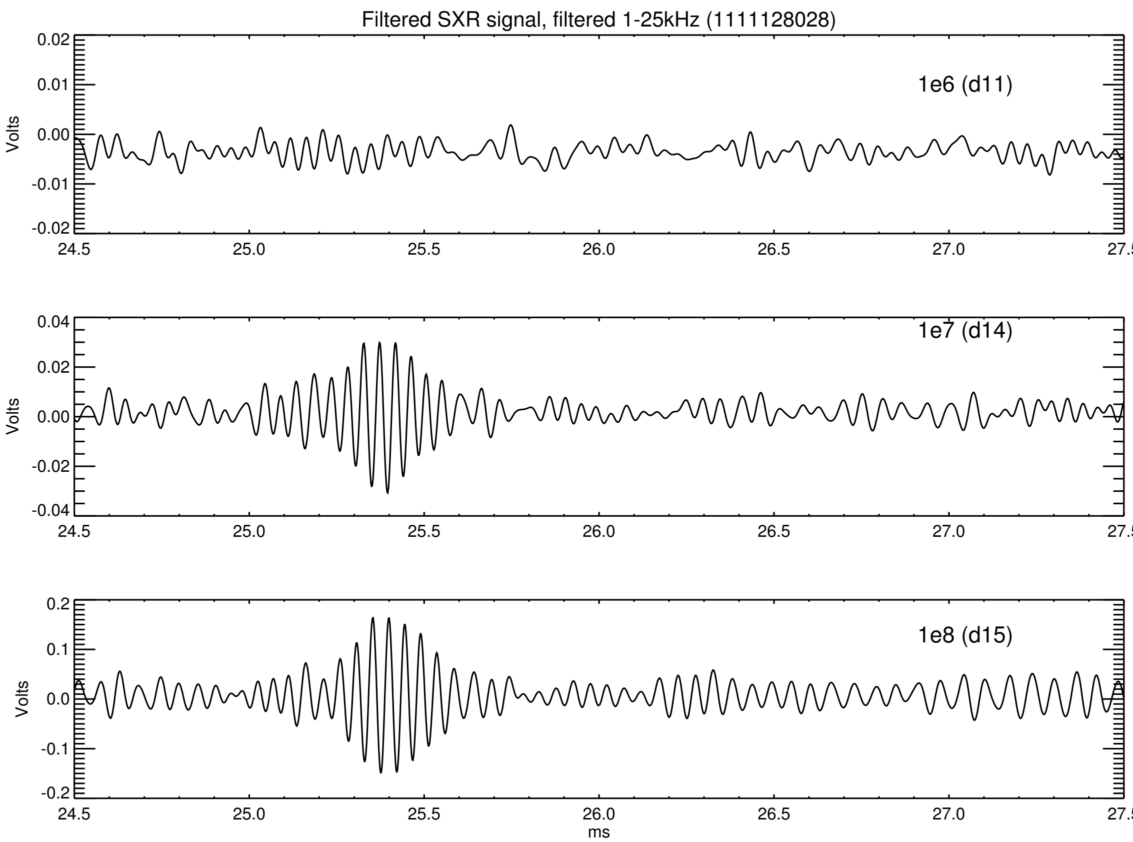

Figure A.1: Signals from a single 400 kA F=0 plasma filtered to show the magnetic pickup component using different amplifications. The pinhole is blanked so that no x-rays are present and any signal is due to magnetic pickup. At 10^8, the pickup is more than 10% the level of the expected signal.

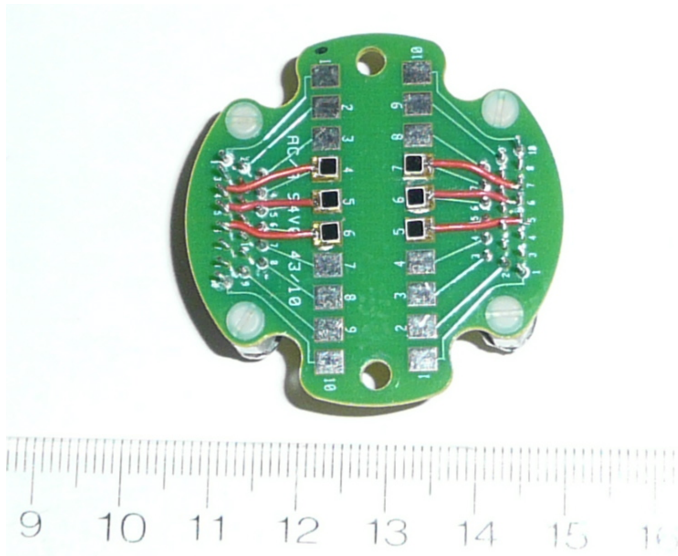

(a) First version of the detector board has a long cathode wire that creates a loop with the anode signal on the board.

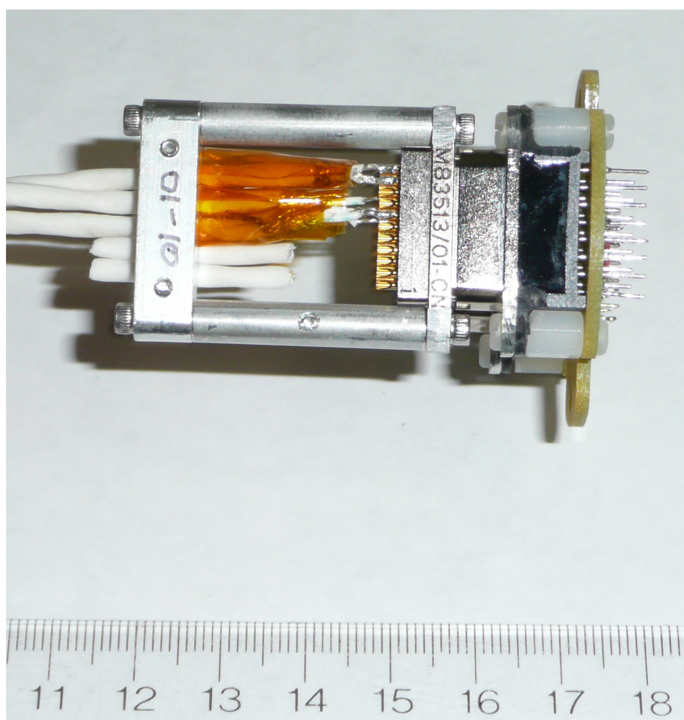

(b) Cable connectors on back of detector board are another source of enclosed area that is susceptible to magnetic pickup.

Figure A.2: The first detector design was not optimized to eliminate loops of enclosed area.

The total area enclosed was substantially reduced by creating an improved circuit board that eliminated the D-pin connector that attached the wires to the board. The final board has small metal turrets near each diode that the cathode wire attaches to directly, then these turrets carry the signal down into the board. The board is designed with 5 layers, including an upper and lower ground plane, as well as separate layers for the anode and cathode signal. The anode (light green) and cathode (dark green) signals thus run directly on top of one another in the board, as seen in Figure A.3, with a thickness of $\sim$400 μm between the layers. Figure A.4 shows the electrical schematic for the diode board. A board-mounted LED at the center of the board is connected to the D21 cable to provide visible-light illumination for electronics testing. The design has a 3-pin jumper at the midplane to allow for different grounding configurations. The standard configuration connects the left-pin (3) to the center-pin (2), tying the ground plane of the board to the strain relief (the strain relief is then connected to MST using a drain wire from the LED cable shield). Alternatively, connecting the center-pin (2) to the right-pin (1) ties the PCB ground-plane to MST through the probehead screws, leaving the strain relief floating.

To reduce the open area caused by the cable connector, the cable connector was removed and the cables are now soldered directly to the board. This reduces the length of unshielded wire from 10 mm to 2 mm. The photos in Figure A.5 show the final circuit board with the turrets and internal layers, as well as the cabling soldered directly to the board. Figure A.6 contains the power spectra of the original printed circuit board (v1) and the final board, with (v2) and without (v3b) the cable-connector (all with a thin-walled aluminum probehead). In each case, a 400 kA F=0 plasma was run while the pinhole was covered with a blank so that the detectors would see only magnetic pickup. Each plot includes three sets of comparable shots to demonstrate

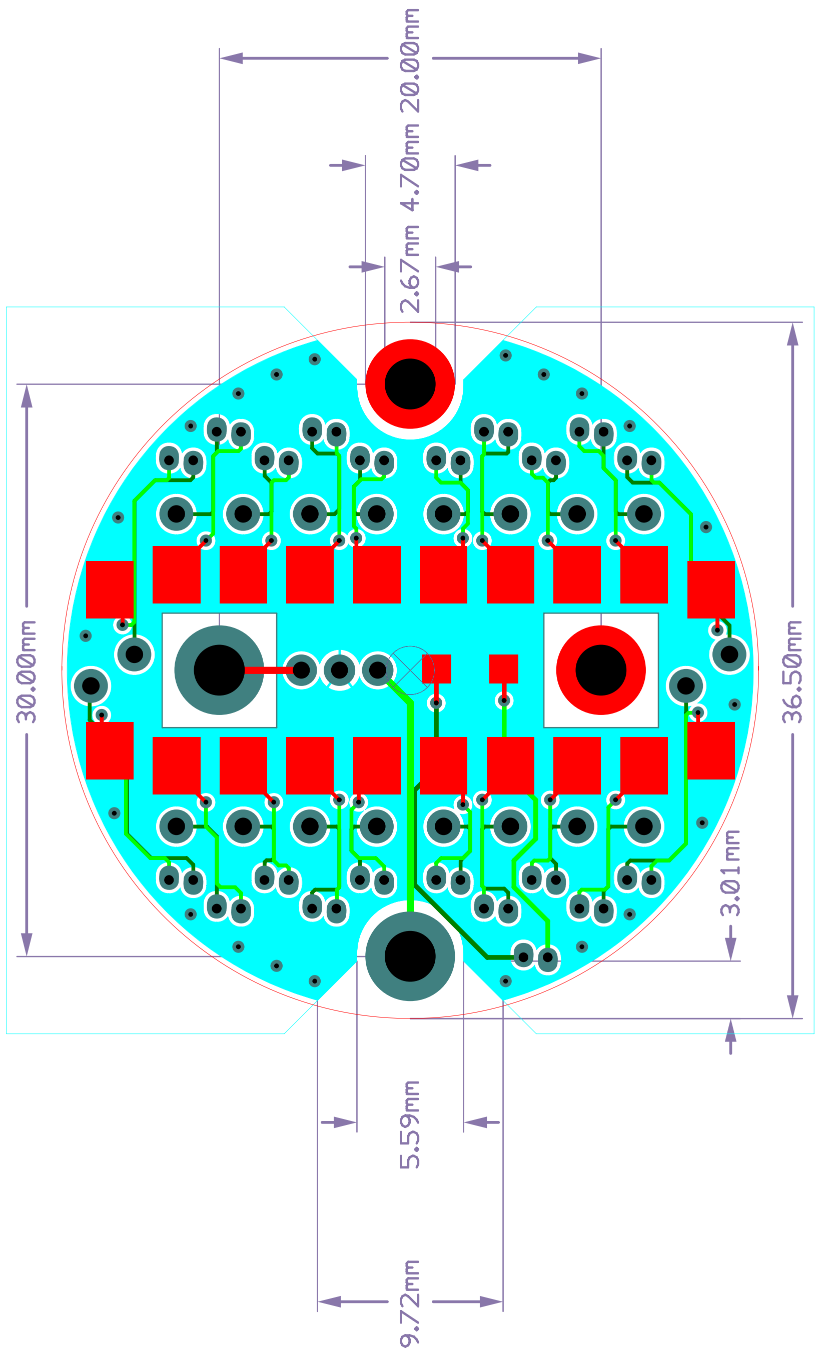

Figure A.3: Final circuit board design with layers for diodes (red), anode (lt. green), cathode (drk. green), and ground plane (blue), where traces overlay to minimize enclosed area. Horizontal screw holes are used for strain relief, while vertical screw holes attach to the probe.

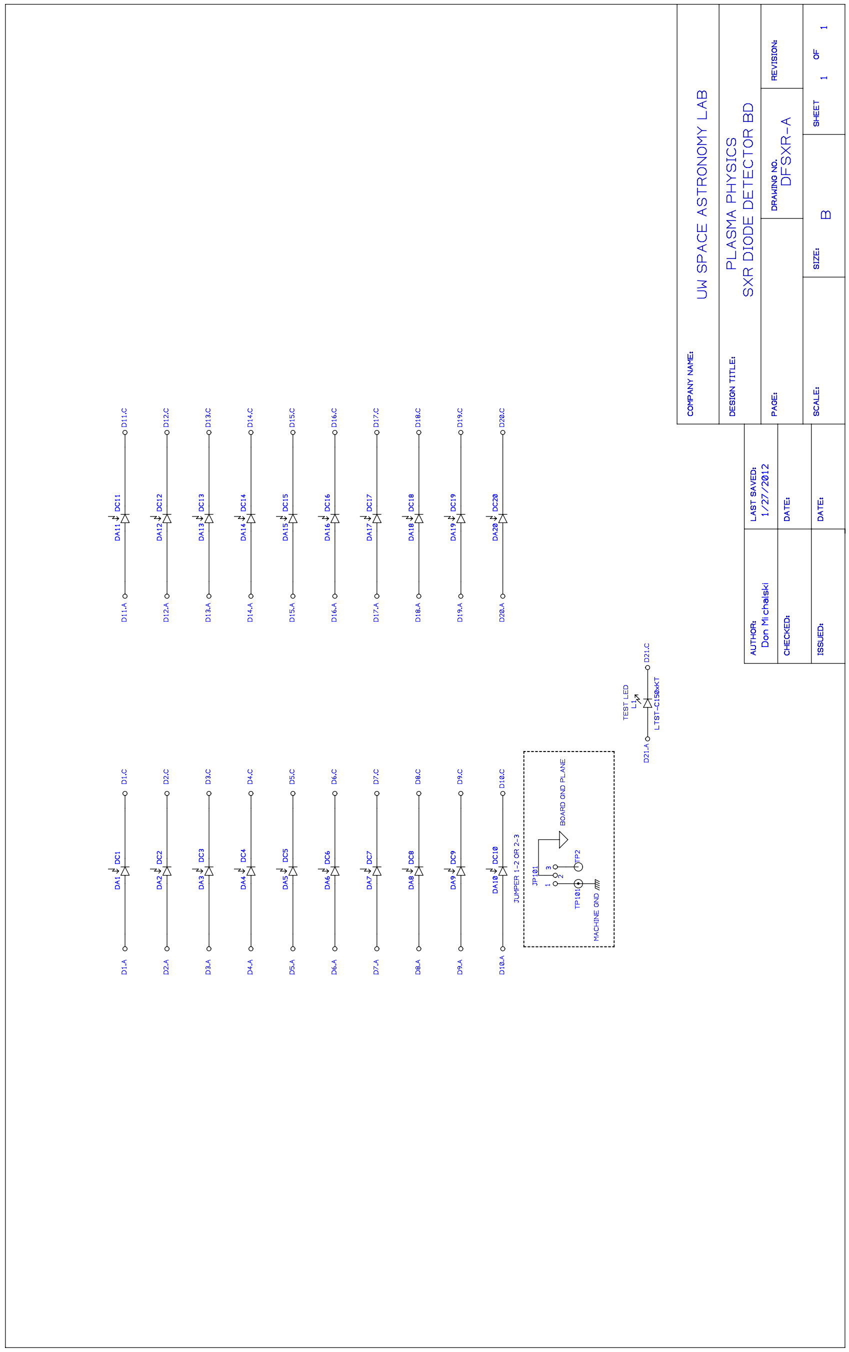

Figure A.4: Circuit schematic for final detector board showing electrical layout of diodes.

that the reduction of magnetic pickup is reproducible. Eliminating the cable connector improved signals dramatically, by approximately 2 orders of magnitude. The circuit board improvements with the minimized signal traces also improved signals somewhat.

A.3 Probe Tip Design

Although the probe body should act as a shield against magnetic fields, the measured pickup indicated the probe was not sufficiently well-shielded. Several modifications to the probehead and probetip were made to optimize geometry and material. In the first test, a probetip was made from mild steel and a blanked pinhole made of μ-metal were installed with the idea that magnetic materials would improve magnetic shielding. (The probehead remained the original aluminum design.) In theory, a ferromagnetic material should soak in the field lines and trap them within the material so that the enclosed region is free of field. Figure A.7 shows the power spectra for 300 kA F=0 plasmas comparing the original aluminum probetip design (with a stainless steel blanked pinhole) versus the mild steel and μ-metal probetip. Unfortunately, the mild steel probetip (black) is actually much noisier than the original aluminum case (blue). In fact, the mild steel probetip did not work because it increased the magnetic flux density near it, effectively drawing the field into the probehead on the back face of the probetip. The timescales and amplitudes of the changing magnetic fields on MST are strong enough to saturate magnetic materials and make them ineffective.

There was also concern that the aluminum probetip was not in good electrical contact with the probehead, which would circumvent the shielding function of the design. The theory that stray field lines entered the probe directly at the gap between the probetip and probehead, (which can be seen in Figure 4.11), led to the second modification of the probehead. Specifically, if the two pieces do not have good electrical contact due to the resistance created by oxidization of aluminum, then eddy currents

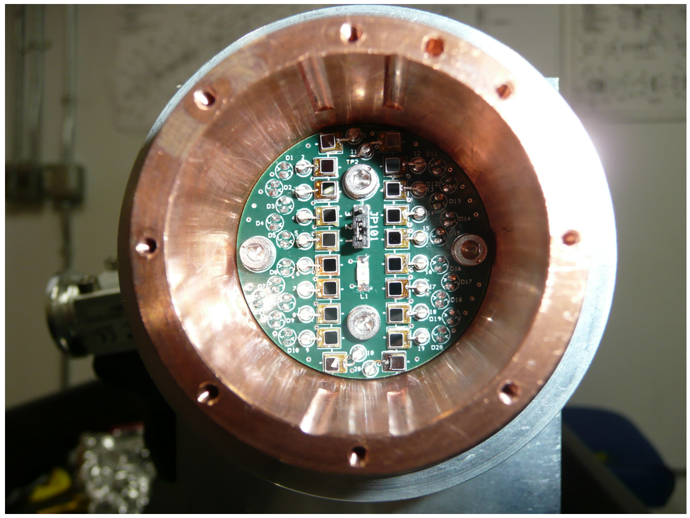

(a) Final probe design: PCB detector layout and 4 mm thick-walled copper probehead (aluminum visible is the KF flange that mounts to MST).

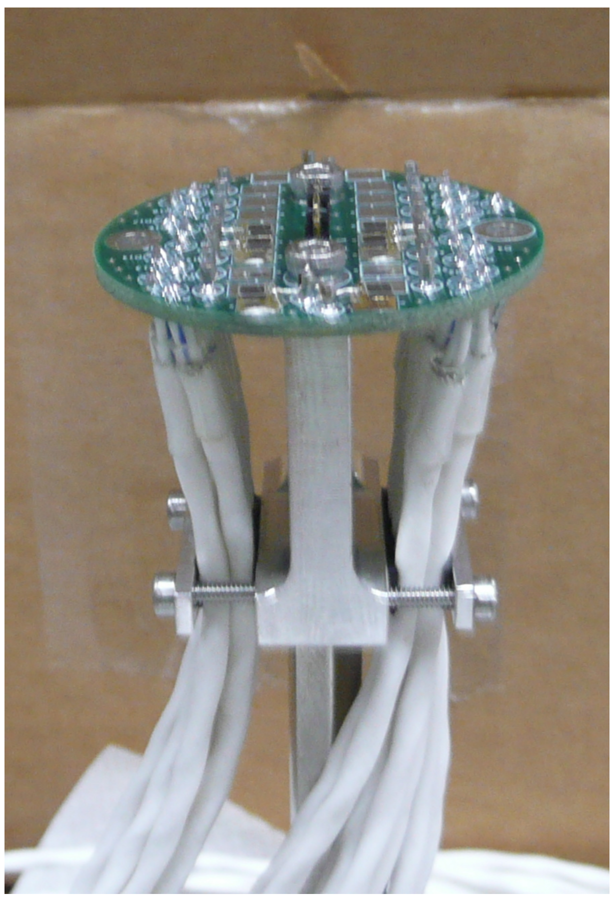

(b) Cables and strain-relief on back of detector board.

Figure A.5: The final detector design was optimized to eliminate loops of enclosed area both above and below the detectors. The PCB ground plane is grounded to the strain-relief, which is in turn grounded to MST through a drain wire attached to the LED shield.

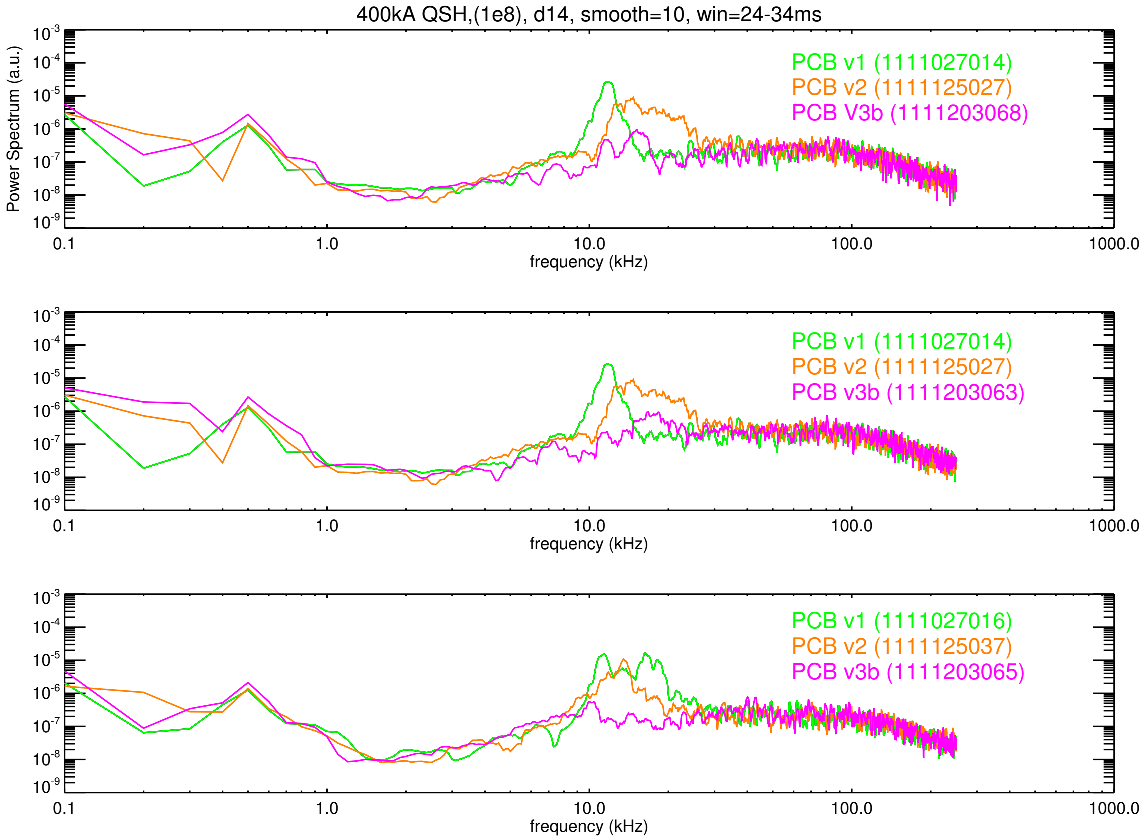

Figure A.6: Power spectra for similar plasmas with three iterations of detector layout. V1 (green) is the original PCB design, V2 (orange) is the 5-layer PCB with the glenair connector, and V3 (magenta) is the final 5-layer PCB design with cables soldered directly to the PCB. (All examples use a thin-walled aluminum probehead, in contrast to the final thick-walled copper probehead). Improvements to the PCB design dramatically reduce the magnetic pickup visible in the FFT.

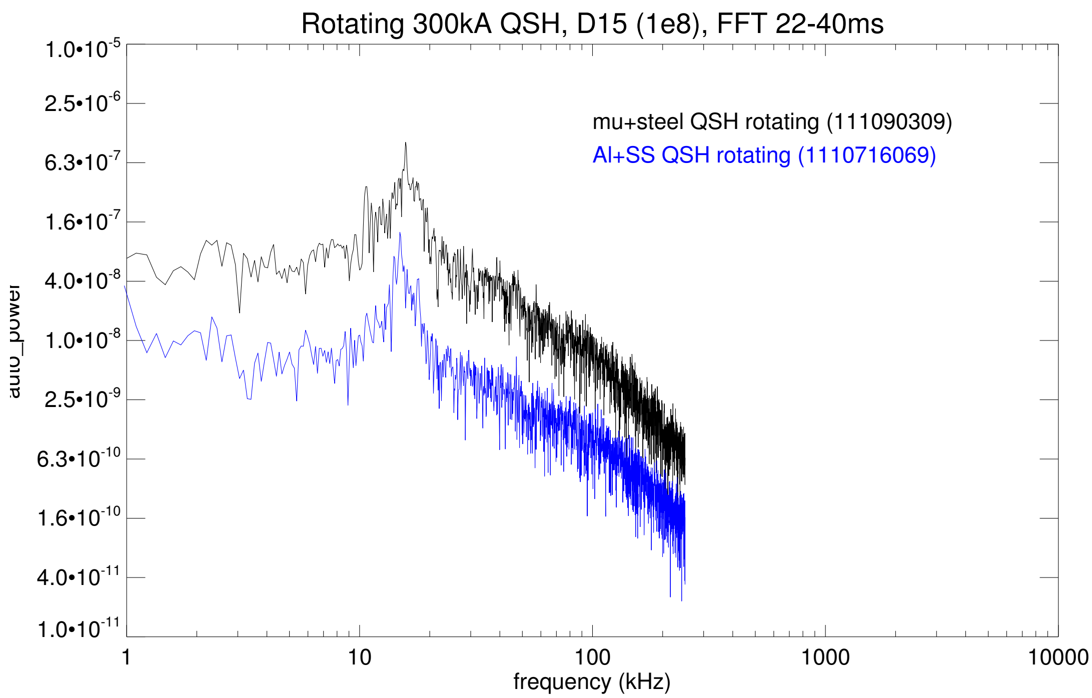

Figure A.7: Power spectra when the probe has a mild-steel probetip (black) compared to an aluminum probetip (blue). Both the noise floor and the magnetic pickup in the mild steel probetip are worse than the aluminum case.

generated in the probetip will flow across the back of the tip, and introduce magnetic field inside the probehead. To address this issue, a probetip was designed with an extended cap that moved the gap further away from the plasma. When the current path to return across the back of the probetip becomes longer than the current path to return cylindrically along the cap wall, then the eddy currents will flow along the cylindrical outer surface of the walls rather than inside the probe. Figure A.8 shows the extended cap design, with cap walls and probehead walls each 0.7 mm thick to combine for nearly the original thickness of 1.5 mm. The gap between the probetip and probehead is moved from 7.0 mm from the face of the probe to 30.0 mm.

Figure A.9 compares the power spectrum signal through the original probetip design (black) compared with the extended cap design (green) for three pairs of comparable 400 kA F=0 plasmas on MST. Unfortunately, no significant improvement was seen in the pickup. This test indicates that the original probetip and probehead were already in good electrical contact. Because the probetip cap design was more difficult to fabricate and made the Be foil holders less accessible, this design was then abandoned.

A.4 Probehead Walls

The failed modifications to the probetip suggest that the main source of magnetic field penetration is not at the probetip but rather through the walls of the probehead. The skin depth for aluminum is 0.69 mm, which means that with 1.5 mm walls, $\sim 11\%$ of the surface current density propagates to the inner wall of the probehead at 15 kHz. This inner surface current density can be reduced by increasing wall thickness and choosing a material with better electrical conductivity σ. Increasing the wall thickness to 4 mm and using tellurium copper ($\sigma = 5.21x10^7\ \Omega^{-1}m^{-1}$) instead of aluminum ($\sigma = 3.54x10^7\ \Omega^{-1}m^{-1}$), the skin depth drops to 0.4 mm. In this case, the

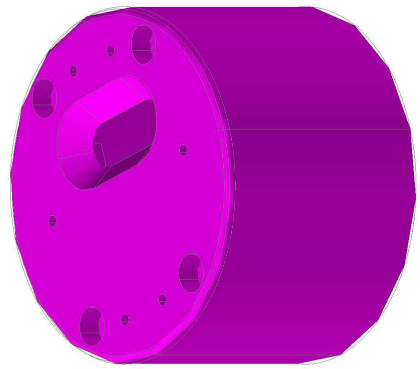

Figure A.8: Extended probetip design includes a cap 3 cm long with 0.7 mm thick walls. (Note: actual face of probetip is round, appears to be a polygon solely due to pdf rendering.)

inner current density is $4x10^{-4}$ times the original aluminum case.

The final probehead is shown in Figure A.5(a). The final design has 4 mm thick tellurium copper walls. (The tellurium copper alloy features the desirable conductive properties of copper and is easier to machine than other copper alloys.) The probetip is also made of tellurium copper (with the same 3-7 mm thickness of the original design), and has a 0.1 mm coating of molybdenum to prevent sputtering in the plasma. Figure 4.29 compares the power spectrum of the original (1.5 mm thin-walled) aluminum probehead (black) to the final (4.0 mm thick-walled) copper probehead (green). In both cases, the pinhole of the diagnostic is covered so that no x-rays are measured, and any resulting signal is the result of magnetic pickup. Both cases look at 400 kA F=0 rotating plasmas and use 10^8 gain amplification. As seen previously, data from the original design shows clear magnetic pickup around the plasma rotation frequency of 10-12 kHz. On the other hand, final probehead design has no magnetic pickup at all in this example.

The final probe design does not show evidence of magnetic pickup in an FFT of

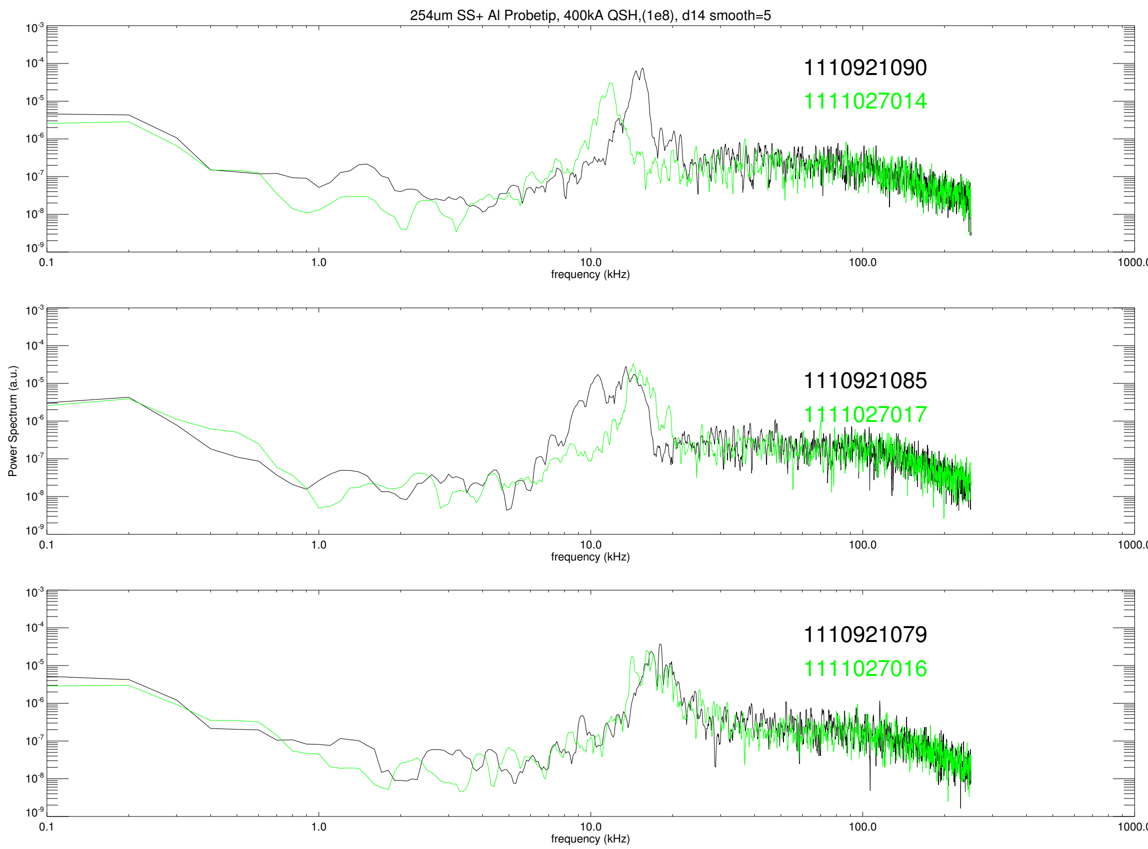

Figure A.9: Power spectra for three sets of similar shots comparing original probetip design (black) to extended probetip (green) demonstrates no reduction in magnetic pickup.

the blanked signal, or in a phase correlation with the B_p magnetic signal for gains of 10^5-10^7. At 10^8 and 10^9 gain, there is no visible magnetic pickup when the dominant magnetic field is less than 3.0 mT. There is some evidence of magnetic pickup above 3.0 mT, but in most conditions the plasma locks before the dominant mode reaches this amplitude. At 10^8, pickup amplitude is of order $40 - 60$ mV_{p-p}, which is below the electronic noise floor (see Table 4.1 for amplifier noise characteristics).

However, cross-correlation analysis still indicates the presence of magnetic pickup. Figure 4.30 shows a cross-correlation analysis between the Bt87 magnetics signal and the SXR-D for a shot using the final probetip design (and a blanked pinhole). Only six diodes were installed during this test in the prototyping phase, but the magnetic pickup is clear on all diodes, despite not being visible by eye or in a power spectrum. Fortunately, further tests (detailed in §4.4) indicate that the amplitude of the pickup $\sim 10x$ smaller than typical signal levels for 10^8 gain and can be ignored. At 10^9 gain however, pickup is still significant at ~ 400 mV_{p-p}, and this data cannot be reliably used during plasma rotation unless the magnetic and SXR contributions to the signal are somehow decoupled.

A.5 Future Design Improvement

Despite substantial improvement from the modifications described previously, the level of magnetic pickup at 10^9 gain is still unacceptably high, sometimes overwhelming the desired SXR signal. Measurements of pickup with an open probetip but covered diodes, described in §4.4, indicates that the primary source of pickup is now the probe's viewing aperture itself. The original viewing aperture was designed to be larger than necessary, with ease-of-machining as the primary criteria. To test this theory, an experiment was done using a completely solid tellurium copper probetip (thickness 7.1 mm) with no viewing aperture on SXR-B during 400 kA F=0 plasmas

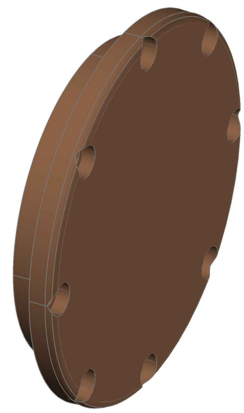

Figure A.10: Solid copper probetip (7.1 mm thick) for blanked probetip experiments. Installed on SXR-B, this experiment showed the primary remaining source of pickup to be through the viewing aperture.

at 10^8 gain (as seen in Figure A.10). While this is clearly an extreme test, it confirms that the magnetic pickup enters the probehead primarily through the field-of-view aperture. Figure A.11 shows the cross-correlation of magnetics and SXR signal in this solid probehead case (this test used the final diode board in SXR-B, so all 19 working diodes are included). Comparing with the final implemented design (Figure 4.30 demonstrates that although copper design reduces pickup through the walls, there is still some magnetic pickup on the diodes. The solid probetip case indicates that a reduction in open viewing area can further improve magnetic pickup. Of course the viewing aperture cannot be completely eliminated, but its extent could be substantially reduced. If scientific goals demand reduced pickup in future experiments, reduction of viewing aperture is a good candidate approach.

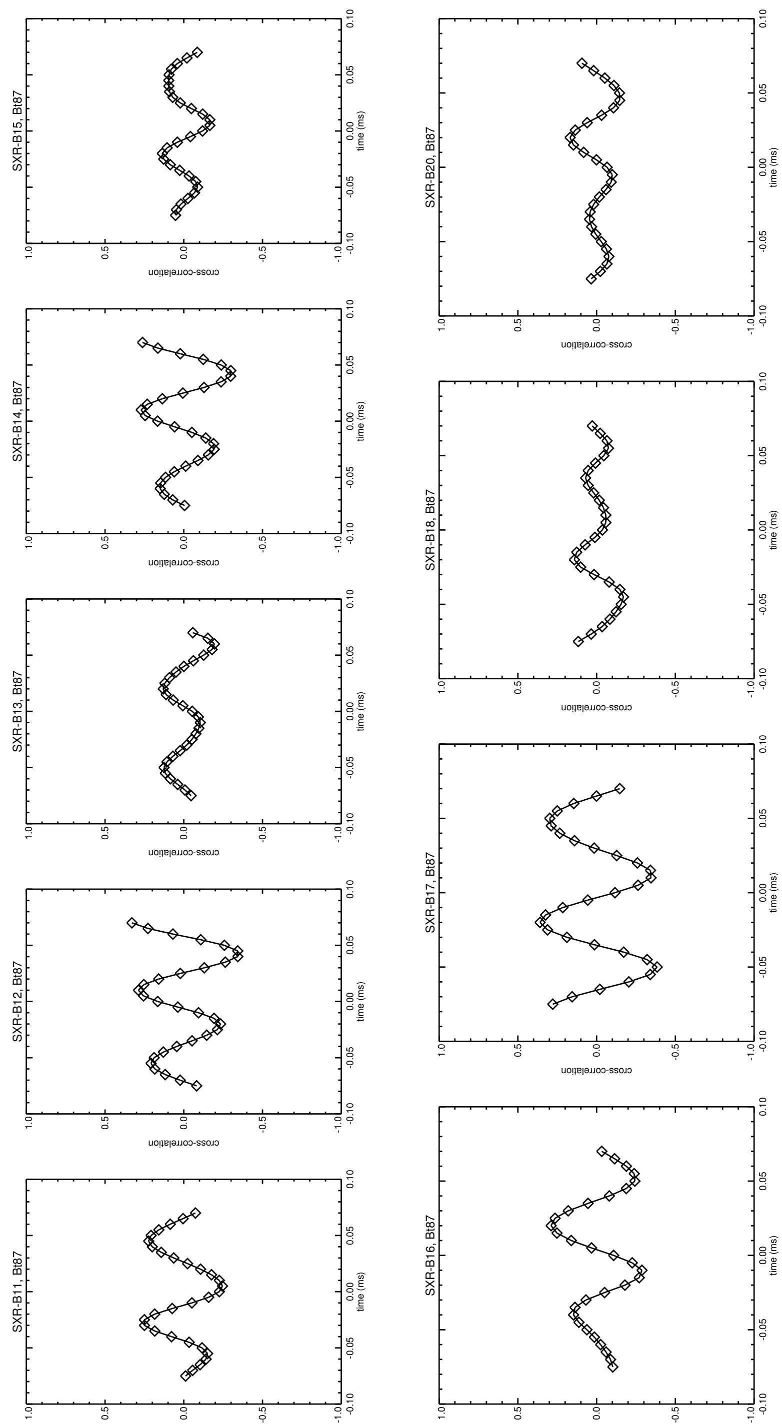

Figure A.11: Cross-correlation between each SXR-B signal at 10^8 gain and Bt87 magnetics from 22.5-23.5 ms during a 400 kA F=0 shot (1121110048) using the final copper probehead with a solid copper probetip that has no viewing aperture. The correlation is greatly reduced compared with the case in Figure 4.30, confirming that the pickup primarily enters through the viewing aperture.